frontiers | Research Topics

Advances in electromagnetic geophysical exploration

Edited by
Jin Li, James Gong and Cong Zhou

Coordinated by
Xian Zhang

Published in
Frontiers in Earth Science

ISSN 1664-8714
ISBN 978-2-8325-4306-1
DOI 10.3389/978-2-8325-4306-1

About Frontiers

Frontiers is more than just an open access publisher of scholarly articles: it is a pioneering approach to the world of academia, radically improving the way scholarly research is managed. The grand vision of Frontiers is a world where all people have an equal opportunity to seek, share and generate knowledge. Frontiers provides immediate and permanent online open access to all its publications, but this alone is not enough to realize our grand goals.

Frontiers journal series

The Frontiers journal series is a multi-tier and interdisciplinary set of open-access, online journals, promising a paradigm shift from the current review, selection and dissemination processes in academic publishing. All Frontiers journals are driven by researchers for researchers; therefore, they constitute a service to the scholarly community. At the same time, the *Frontiers journal series* operates on a revolutionary invention, the tiered publishing system, initially addressing specific communities of scholars, and gradually climbing up to broader public understanding, thus serving the interests of the lay society, too.

Dedication to quality

Each Frontiers article is a landmark of the highest quality, thanks to genuinely collaborative interactions between authors and review editors, who include some of the world's best academicians. Research must be certified by peers before entering a stream of knowledge that may eventually reach the public - and shape society; therefore, Frontiers only applies the most rigorous and unbiased reviews. Frontiers revolutionizes research publishing by freely delivering the most outstanding research, evaluated with no bias from both the academic and social point of view. By applying the most advanced information technologies, Frontiers is catapulting scholarly publishing into a new generation.

What are Frontiers Research Topics?

Frontiers Research Topics are very popular trademarks of the *Frontiers journals series*: they are collections of at least ten articles, all centered on a particular subject. With their unique mix of varied contributions from Original Research to Review Articles, Frontiers Research Topics unify the most influential researchers, the latest key findings and historical advances in a hot research area.

Find out more on how to host your own Frontiers Research Topic or contribute to one as an author by contacting the Frontiers editorial office: frontiersin.org/about/contact

Advances in electromagnetic geophysical exploration

Topic editors
Jin Li — Hunan Normal University, China
James Gong — Deakin University, Australia
Cong Zhou — East China University of Technology, China

Topic Coordinator
Xian Zhang — Hunan University of Finance and Economics, China

Citation
Li, J., Gong, J., Zhou, C., Zhang, X., eds. (2024). *Advances in electromagnetic geophysical exploration*. Lausanne: Frontiers Media SA.
doi: 10.3389/978-2-8325-4306-1

Table of contents

frontiers | Frontiers in Earth Science

TYPE Editorial
PUBLISHED 05 January 2024
DOI 10.3389/feart.2023.1356280

OPEN ACCESS

EDITED AND REVIEWED BY
Kenneth Philip Kodama,
Lehigh University, United States

*CORRESPONDENCE
Jin Li,
geologylj@163.com

RECEIVED 15 December 2023
ACCEPTED 19 December 2023
PUBLISHED 05 January 2024

CITATION
Li J, Gong J, Zhou C and Zhang X (2024), Editorial: Advances in electromagnetic geophysical exploration.
Front. Earth Sci. 11:1356280.
doi: 10.3389/feart.2023.1356280

Editorial: Advances in electromagnetic geophysical exploration

Jin Li[1]*, James Gong[2], Cong Zhou[3] and Xian Zhang[4]

[1]College of Information Science and Engineering, Hunan Normal University, Changsha, China, [2]School of Engineering, Deakin University, Geelong Waurn Ponds Campus, Geelong, VIC, Australia, [3]State Key Laboratory of Nuclear Resources and Environment, East China University of Technology, Nanchang, China, [4]School of Information Technology and Management, Hunan University of Finance and Economics, Changsha, China

KEYWORDS

electromagnetic method, data processing, forward modelling, inversion, calculation method

Editorial on the Research Topic
Advances in electromagnetic geophysical exploration

Introduction

Geophysical exploration is an effective way to build a national resource security system and carry out "deep exploration of blindness" (Di et al., 2019). The application of advanced scientific and technological means to extract deep geological information has become the development direction of contemporary geophysical research. Electromagnetic exploration is one of the earliest and most widely used geophysical techniques for mineral resource exploration. Electromagnetic methods, such as magnetotelluric (MT), audio magnetotelluric (AMT), transient electromagnetic method (TEM), and controlled source electromagnetic method (CSEM), have made a great contribution to industrialization and urbanization by discovering underground deposits of various resources (Tikhonov, 1950; Cagniard, 1953; He, 2010; Tang et al., 2015; Liu et al., 2019).

Driven by the latest progress in electronics and intelligent algorithms, electromagnetic exploration is developing at a high speed. Many challenges faced by traditional geophysical methods are now solvable. Emerging sensing technologies and signal processing technologies can significantly improve the accuracy of data analysis in many applications (Zhang et al., 2021; Li et al., 2023). At the same time, new technologies are promoting the development of new geophysical theories and methods. This Research Topic brings together articles reporting the latest progress in MT denoising, data processing, forward modelling, and inversion methods.

Advances in electromagnetic geophysical exploration

The articles in this Research Topic synthesise advanced techniques across electromagnetic data processing, 1D/2D/3D forward modelling, and inversion methods, covering a broad range of applications of the electromagnetic method.

Wang et al. presented a novel approach to analyse MT time series based on forward modelling and the correspondence between frequency- and time-domain electromagnetic fields. The study focused on the electromagnetic responses of a given numerical model to two

orthogonal polarization sources. The randomness of the polarization of natural field sources was simulated by a linear combination of the two polarization sources. The novel approach provides a technical basis to transform the forward modeling of electromagnetic responses from the frequency domain to the time domain. Moreover, time series not derived from the inversion model can be separated to study the distribution of noise.

Zhan et al. reported a new MT data processing method based on cepstral analysis, which can suppress different types of MT noise, and obtain smoother and more continuous apparent resistivity curves, this method shows better performance than EMD method in handing MT data.

Chen et al. combined the analyses of three new parameters (the amplitude ratio predicted amplitude ratio, the linear coherence between the predicted and observed electric fields and the dispersion degree of the magnetic polarization direction) to detect noisy data, and developed an automatic pre-selection strategy for MT single-site data processing. The results showed that these parameters can be used to identify contaminated data, and a reliable response function can be obtained.

Tong et al. introduced a new efficient spectral element approach originally developed by Patera to solve 2D MT forward problems based on Gauss-Lobatto-Legendre polynomials. It has implied the spectral element method on a resistivity half-space model to obtain a simple analytical solution and find that the magnetic field solutions simulated by the spectral element approach matched closely to the exact solutions. Moreover, the method can compute the two-dimensional magnetotelluric responses of the boundary problem without measuring Earth's curvature.

Zhu et al. proposed a rapid 3D MT forward modelling approach for arbitrary anisotropic conductivity in the Fourier domain. The study verified the classical 1D anisotropy model, calculated the 3D anisotropic model of land and ocean, and analysed the influence characteristics of the anisotropic medium on the MT response.

Li et al. reported a generic 3D forward modelling solver for CSEMs with multitype sources and operating environments. The numerical results showed that frequency domain CSEMs with a wire source were more suitable for detecting deep anomalies than time domain CSEMs with a loop source.

Ge and Li presented a finite difference algorithm for simulating the ocean wave-induced electromagnetic fields with variable seawater conductivity. The study revealed the impacts of variable seawater conductivity on the electromagnetic fields induced by the wind waves and swell as well as mixed ocean waves.

Su et al. reported a high-resolution 2D inversion method based on weighted horizontal and vertical constraints. The method ensured the horizontal continuity of resistivity and recovers the inclined strata, and improved the vertical resolution. The TEM data processing and inversion results were consistent with known geological information.

Tian et al. reported a new calculation method of arbitrary orientation single component electric field for the wide field electromagnetic method (WFEM). The study showed that the new method could reduce the influence of the azimuthal difference on the apparent resistivity parameters and thus improve the accuracy of interpretation.

Summary and outlook

The articles cover new methods in data processing, forward modelling, and inversion methods for electromagnetic exploration. These new electromagnetic processing methods can effectively analyse the characteristics of electromagnetic fields, improving the interpretation accuracy, and expand the applicability and flexibility of electromagnetic methods in the presence of complex environmental/topographical/geological conditions. Advances in electromagnetic geophysical exploration will contribute to the sustainable development of People-Earth system in the future.

Author contributions

JL: Supervision, Writing–review and editing. JG: Supervision, Writing–review and editing. CZ: Supervision, Writing–review and editing. XZ: Supervision, Writing–review and editing.

Conflict of interest

The authors declare that the research was conducted in the absence of any commercial or financial relationships that could be construed as a potential conflict of interest.

Publisher's note

References

Cagniard, L. (1953). Basic theory of the magnetotelluric method of geophysical prospecting. *Geophysics* 18 (3), 605–635. doi:10.1190/1.1437915

Di, Q. Y., Zhu, R. X., Xue, G. Q., Yin, C. C., and Li, X. (2019). New development of the Electromagnetic (EM) methods for deep exploration. *Chin. J. Geophys.* 62 (6), 2128–2138. (in Chinese). doi:10.6038/cjg2019M0633

He, J. S. (2010). Wide field electromagnetic sounding methods. *J. Central South Univ. Sci. Technol.* 41, 1065–1072.

Li, J., Liu, Y. C., Tang, J. T., Peng, Y. Q., Zhang, X., and Li, Y. (2023). Magnetotelluric data denoising method combining two deep-learning-based models. *Geophysics* 88 (1), E13–E28. doi:10.1190/geo2021-0449.1

Liu, J. X., Zhao, R., and Guo, Z. W. (2019). Research progress of electromagnetic methods in the exploration of metal deposits. *Prog. Geophys. (in Chinese)* 34 (1), 151–160. doi:10.6038/pg2019CC0222

Tang, J. T., Ren, Z. Y., Zhou, C., Zhang, L. C., Yuan, Y., and Xiao, X. (2015). Frequency-domain electromagnetic methods for exploration of the shallow subsurface:A review. *Chinese Journal of Geophysics* 58 (8), 2681–2705. (in Chinese). doi:10.6038/cjg20150807

Tikhonov, A. N. (1950). On determining electrical characteristics of the deep layers of the Earth's crust. *Dokl. Akad. Nauk. SSSR.* 73 (2), 295–297.

Zhang, X., Li, J., Li, D. Q., Li, Y., Liu, B., and Hu, Y. F. (2021). Separation of magnetotelluric signals based on refined composite multiscale dispersion entropy and orthogonal matching pursuit. *Earth Planets and Space* 73 (1), 76. doi:10.1186/s40623-021-01399-z

frontiers | Frontiers in Earth Science

TYPE Original Research
PUBLISHED 09 February 2023
DOI 10.3389/feart.2023.1086749

OPEN ACCESS

EDITED BY
Jin Li,
Hunan Normal University, China

REVIEWED BY
Hongzhu Cai,
China University of Geosciences Wuhan, China
Yunhe Liu,
Jilin University, China

*CORRESPONDENCE
Xiaobin Chen,
cxb@pku.edu.cn

SPECIALTY SECTION
This article was submitted to Geomagnetism and Paleomagnetism, a section of the journal Frontiers in Earth Science

RECEIVED 01 November 2022
ACCEPTED 24 January 2023
PUBLISHED 09 February 2023

CITATION
Wang P, Chen X and Zhang Y (2023), Synthesizing magnetotelluric time series based on forward modeling.
Front. Earth Sci. 11:1086749.
doi: 10.3389/feart.2023.1086749

Synthesizing magnetotelluric time series based on forward modeling

Peijie Wang[1], Xiaobin Chen[2]* and Yunyun Zhang[2]

[1]State Key Laboratory of Earthquake Dynamics, Institute of Geology, China Earthquake Administration, Beijing, China, [2]National Institute of Natural Hazards, Ministry of Emergency Management of China, Beijing, China

The validity of magnetotelluric time-series processing methods has been lacking reasonable testing criteria. Since the time series synthesized by existing techniques are not fully derived from a given model, they are not reliable. In this paper, we present a novel approach to synthesize magnetotelluric time series based on forward modeling and the correspondence between frequency and time domain electromagnetic fields. In this approach, we obtain the electromagnetic response of two orthogonal polarization sources for a given model by magnetotelluric forward modeling, and simulate the randomness of the polarization of the natural field source by a linear combination of the two polarization sources. Based on the correspondence between the frequency and time domain electromagnetic fields, the electromagnetic fields obtained by forward modeling in the frequency domain are transformed into the time domain, and finally the time series are synthesized. The test results on 1D and 3D models validate the effectiveness of the proposed method and the correctness of the procedure. After adding noise to the synthesized time series, we can test the performance of each method by comparing the results of the time series processing methods with the response of the given model. Therefore, the method presented in this paper can be used to construct standard magnetotelluric time series, which can be used as a carrier to construct synthetic data satisfying various noise distributions, and for the study of related methods. This method can also be used to synthesize time series of other frequency-domain electromagnetic methods.

KEYWORDS

magnetotelluric, electromagnetic theory, forward modeling, synthesize time series, data processing

Introduction

The magnetotelluric (MT) method is widely used in the surface geological survey, mineral resources exploration, earthquake, volcano, and continental dynamics by detecting subsurface electrical structures (Cai et al., 2017; Jiang et al., 2022). The time series of the electric and magnetic fields are collected simultaneously at the surface and the MT response is subsequently obtained by Fourier transform and transfer function estimation. High quality transfer function estimation is a prerequisite for reliable detection of subsurface structures. With the development of industrialization, MT hardware devices have been perfected to collect reliable raw data. However, industrialization also makes artificial noise increase, which seriously affects the quality of measurement data and limits the application of MT method (Szarka, 1988; Junge, 1996; Banks, 1998). Existing time series processing techniques, such as the least-square method (Sims et al., 1971), remote reference method (Goubau et al., 1978; Gamble et al., 1979b; Gamble et al., 1979a), robust estimation method (Egbert and Booker, 1986; Chave et al., 1987; Larsen et al., 1996; Smirnov, 2003; Chave and Thomson, 2004), maximum likelihood estimation method (Chave, 2014; Chave, 2017), and others methods based on wavelet transform,

Hilbert-Huang transform, variational mode decomposition, and inter-station transfer function (Kappler, 2012; Cai, 2014; Campanya et al., 2014; Cai and Chen, 2015; Carbonari et al., 2017; Wang et al., 2017), have different processing performance for different kinds of noise. For example, the least-square method performs poorly in the presence of outliers (Egbert and Booker, 1986), and the remote reference method does not work when noise is correlated at the local and remote sites (Shalivahan and Bhattacharya, 2002; Pomposiello et al., 2009), and the robust estimation method usually fails to work when MT data are contaminated by persistent or coherent noises (Escalas et al., 2013; Carbonari et al., 2017; Li et al., 2020a; Li et al., 2020c; Zhou et al., 2022; Zhang et al., 2022). New time series processing methods for various types of noise are the focus of current research, but there is a lack of criteria to evaluate the effectiveness of various MT time series processing methods in existing studies. The traditional evaluation method based on curve continuity is proved to be unreliable (Sutarno, 2005). Many studies take the measured low-noise data as the standard data, but because the real response is unknown, it is insufficient to prove the effectiveness of the time series processing method (Li et al., 2020a; Li et al., 2020b; Guo et al., 2022; Zhou et al., 2022). Therefore, reliable standard time series are urgently needed to test the effectiveness of various time series processing methods.

In geophysical inversion, the validity of the inversion method is assessed by comparing the inversion results with a given evaluation model. Similarly, if the time series of the evaluated model are available, they can be used to test the performance of different time series processing methods. Several studies have proposed techniques for synthesizing time series of simple models. For example, Varentsov and Sokolova (1995) and Loddo et al. (2002) realized the synthetic time series techniques based on inverse Fourier transform and convolution. These techniques take the measured low-noise magnetic field data or random number sequences as the synthetic magnetic field time series, and then use the impedance of a one-dimensional (1D) or two-dimensional (2D) model to calculate the electric field time series. However, the given time series may be noisy and its true model is unknown or even non-existent, so their synthetic time series are unreliable. Moreover, these techniques are also difficult to simulate the variability of the actual natural sources of the electromagnetic field. Kelbert et al. (2017) predicted the geoelectric field from the impedance of the 3D model and the time series of the magnetic storm, which was highly consistent with the measured data. This is a nice advance for synthesizing time series of complex models, but the method also relies on a given time series.

In this paper, we propose a method to synthesize MT time series based on forward modeling. All five-channel time series are generated by forward modeling, which accurately reflects the spatial distribution and temporal variability properties of the electromagnetic fields in the model. The transfer function can be obtained by processing synthetic time series using common software, so that the actual observed time series can be adequately simulated. In the following paper, the basic principles and implementation of the method are detailed. The time series of the 1D and 3D models are then synthesized in this way. Commercial and open-source software is used to process and analyze the synthetic time series. The processing results of the time series and the response of a given model are compared to verify the reliability of the synthetic time series. Finally, noise is added to the synthetic time series to test the performance of different data processing methods, demonstrating that the synthetic time series can be used as an evaluation criterion for data processing techniques.

Methodology

Theory of synthesizing time series

The time domain form of the single-frequency electromagnetic field is (detailed derivation is in the **Supplementary Material S1**):

$$\begin{cases} \mathbf{e}(\omega,t) = \mathbf{A}_e \cos\left(\omega t + \Phi_e\right) \\ \mathbf{h}(\omega,t) = \mathbf{A}_h \cos\left(\omega t + \Phi_h\right) \end{cases}, \tag{1}$$

where ω denotes the angular frequency. $\mathbf{A}_e = |\mathbf{E}(\omega)|$, $\mathbf{A}_h = |\mathbf{H}(\omega)|, \Phi_e = Arg(\mathbf{E}(\omega)), \Phi_h = Arg(\mathbf{H}(\omega))$. $\mathbf{E}(\omega)$ and $\mathbf{H}(\omega)$ are the electromagnetic fields in the frequency domain, which can be calculated by MT forward modeling. Thus, Eq. 1 provides a new approach to synthesize MT time series. By MT forward modeling, $\mathbf{E}(\omega)$ and $\mathbf{H}(\omega)$ is calculated, which is substituted into Eq. 1 to calculate the time series of single frequency. Time series containing N frequencies can be synthesized according to the superposition principle of electromagnetic fields:

$$\begin{cases} \mathbf{e}(t) = \sum_{k=1}^{N} \mathbf{e}(\omega,t) \\ \mathbf{h}(t) = \sum_{k=1}^{N} \mathbf{h}(\omega,t) \end{cases}. \tag{2}$$

Following the above theory, we can design any complex model and synthesize time series by forward modeling. The synthesized time series can be used to test the effectiveness of data processing methods.

MT forward modeling

In the approach of this paper, MT forward modeling is a prerequisite for synthesizing time series. MT forward modeling has become highly mature after several decades. Numerical simulation methods such as finite difference, finite element, integral equation, and even deep learning can solve the forward calculation of various complex models (Wang et al., 2021). Kelbert et al. (2014) developed ModEM, an open-source 3D magnetotelluric and controlled-source electromagnetic forward and inversion system, which was used for forward modeling of the 3D model in this method. We have made minor modifications to ModEM by adding an output interface for the electromagnetic field.

The transfer functions include the impedance and tipper, which are defined as follows:

$$\begin{cases} E_x(\omega) = Z_{xx}(\omega) H_x(\omega) + Z_{xy}(\omega) H_y(\omega) \\ E_y(\omega) = Z_{yx}(\omega) H_x(\omega) + Z_{yy}(\omega) H_y(\omega) \\ H_z(\omega) = T_{zx}(\omega) H_x(\omega) + T_{zy}(\omega) H_y(\omega) \end{cases}. \tag{3}$$

Eq. 3 can be abbreviated as $\mathbf{E} = \mathbf{ZH}$ and $H_z = \mathbf{TH}$, where $\mathbf{Z}$ is the MT impedance tensor and $\mathbf{T}$ is the tipper vector. $\mathbf{E}$ and $\mathbf{H}$ is horizontal electric and magnetic field component. H_z is vertical magnetic field. The above three equations are independent and solving them requires at least two linearly independent sets of electromagnetic fields. In the forward modeling of MT, we solve the governing equations with two different polarization sources as boundary conditions and obtain two sets of fields:

Polarization 1: $E_x^1(\omega)$, $E_y^1(\omega)$, $H_x^1(\omega)$, $H_y^1(\omega)$, $H_z^1(\omega)$,
Polarization 2: $E_x^2(\omega)$, $E_y^2(\omega)$, $H_x^2(\omega)$, $H_y^2(\omega)$, $H_z^2(\omega)$.

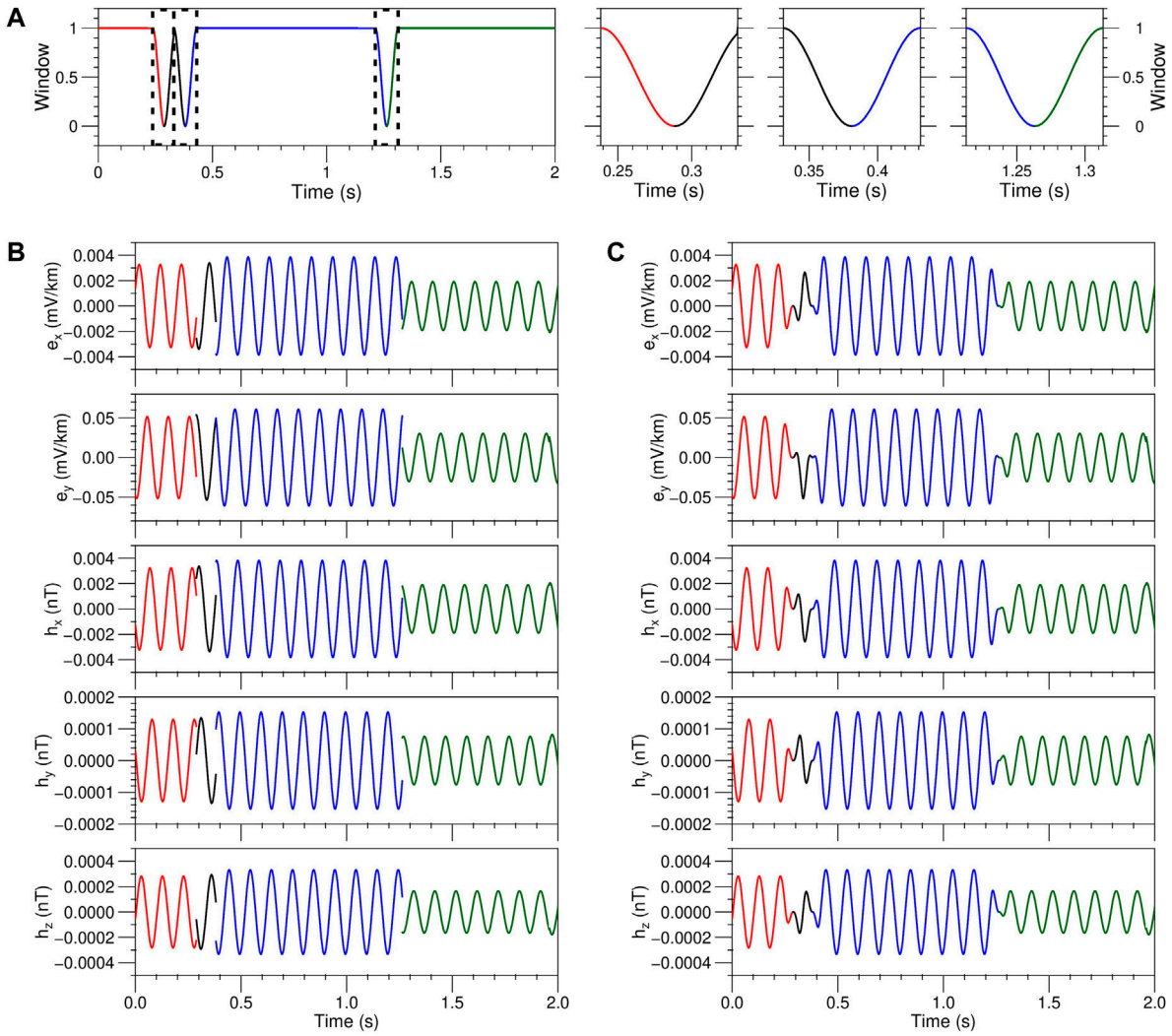

FIGURE 1
Time series splice diagram of a single frequency. The frequency is 10 Hz, the direction of source polarization is X, and the sampling rate is 2,400 Hz. **(A)** Window function time series, **(B)** original time series, and **(C)** windowed time series.

Then combined into transfer functions:

$$\begin{cases} Z_{xy}(\omega) = \dfrac{E_x^2(\omega)H_x^1(\omega) - E_x^1(\omega)H_x^2(\omega)}{H_x^1(\omega)H_y^2(\omega) - H_x^2(\omega)H_y^1(\omega)} \\ Z_{xx}(\omega) = \dfrac{E_x^1(\omega)H_y^2(\omega) - E_x^2(\omega)H_y^1(\omega)}{H_x^1(\omega)H_y^2(\omega) - H_x^2(\omega)H_y^1(\omega)} \\ Z_{yx}(\omega) = \dfrac{E_y^1(\omega)H_y^2(\omega) - E_y^2(\omega)H_y^1(\omega)}{H_x^1(\omega)H_y^2(\omega) - H_x^2(\omega)H_y^1(\omega)} \\ Z_{yy}(\omega) = \dfrac{E_y^2(\omega)H_x^1(\omega) - E_y^1(\omega)H_x^2(\omega)}{H_x^1(\omega)H_y^2(\omega) - H_x^2(\omega)H_y^1(\omega)} \\ T_{zx}(\omega) = \dfrac{H_z^1(\omega)H_y^2(\omega) - H_z^2(\omega)H_y^1(\omega)}{H_x^1(\omega)H_y^2(\omega) - H_x^2(\omega)H_y^1(\omega)} \\ T_{zy}(\omega) = \dfrac{H_z^2(\omega)H_x^1(\omega) - H_z^1(\omega)H_x^2(\omega)}{H_x^1(\omega)H_y^2(\omega) - H_x^2(\omega)H_y^1(\omega)} \end{cases} . \quad (4)$$

In practical MT, the time series of electromagnetic fields are collected, and divided into segments (L). For a given frequency, L groups of electromagnetic fields are obtained by Fourier transform of the time series segments. And the transfer functions can be estimated from this L groups of electromagnetic fields by estimation methods, such as the least-square method. The purpose of MT data processing is to obtain transfer functions for multiple discrete frequencies. Therefore, only time series containing the given frequencies need to be synthesized for the study of data processing methods. MT transfer function estimation requires that these sets of electromagnetic fields to be linearly independent, which is easily satisfied by the fact that the polarization direction of the natural electromagnetic field source varies with time. And this time-varying polarization needs be simulated in synthetic time series by segmentation and concatenation.

Source simulation

In the forward modeling, only the fields of two different polarization sources are calculated. The natural sources are time-varying, and the sources at different moments can be simulated by combining the two sources described above.

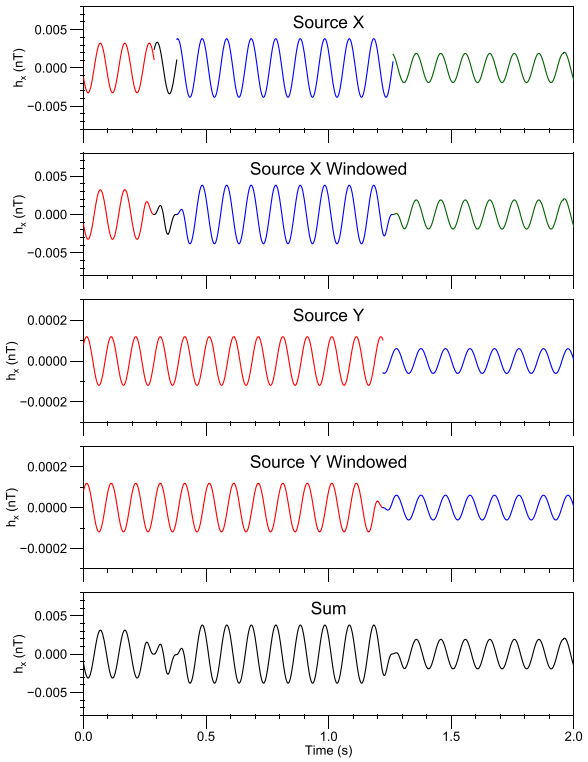

FIGURE 2
Synthesis a single frequency time series. The frequency is 10 Hz, the sampling rate is 2,400 Hz, and the field component is H_x.

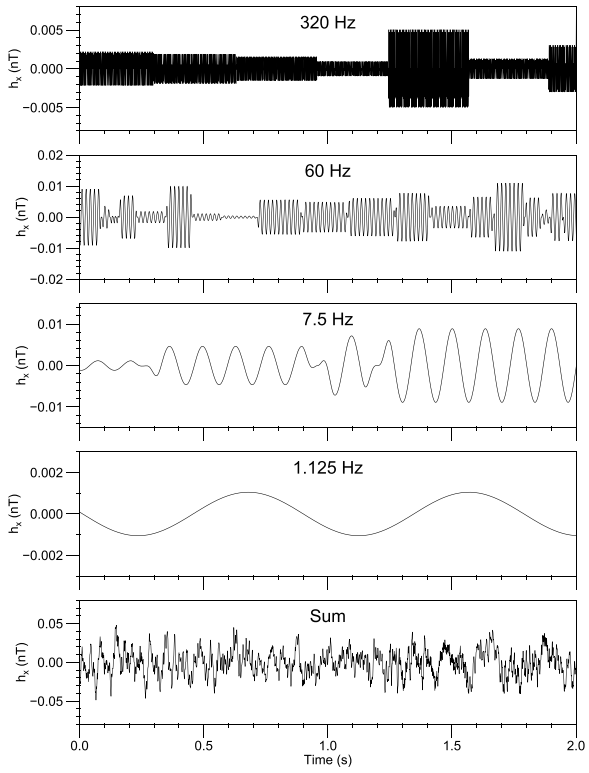

FIGURE 3
Synthesis of multi-frequency time series. The frequency ranges from 320 to 1.125 Hz, with 18 frequencies, of which only four are plotted in the figure. The sampling rate is 2,400 Hz, and the field component is H_x. The last subplot is a superimposed time series of 18 frequencies.

Any source (denoted as $\mathbf{S}$) can be derived by a linear combination of two orthogonal sources (denoted as $\mathbf{S}^1$ and $\mathbf{S}^2$): $\mathbf{S} = C^1\mathbf{S}^1 + C^2\mathbf{S}^2$. The fields of source $\mathbf{S}$, $\mathbf{S}^1$ and $\mathbf{S}^2$ are $\mathbf{A} = (E_x, E_y, H_x, H_y, H_z)$, $\mathbf{A}^1 = (E_x^1, E_y^1, H_x^1, H_y^1, H_z^1)$ and $\mathbf{A}^2 = (E_x^2, E_y^2, H_x^2, H_y^2, H_z^2)$, respectively. The linear combination consistent with the source also holds in the fields: $\mathbf{A} = C^1\mathbf{A}^1 + C^2\mathbf{A}^2$. For the 1D model, the two field components (E^{1D} and H^{1D}) can be calculated by forward modeling. The fields of the two orthogonal sources are:

$$\begin{cases} \mathbf{A}^1 = \left(E^{1D}, \quad 0, \quad 0, \quad H^{1D}, \quad 0\right) \\ \mathbf{A}^2 = \left(0, \quad E^{1D}, \quad -H^{1D}, \quad 0, \quad 0\right) \end{cases}. \tag{5}$$

For the 2D model, E_x^{TE}, H_y^{TE} and H_z^{TE} can be calculated by the forward modeling of the TE polarization, E_y^{TM} and H_x^{TM} can be calculated by the forward modeling of the TM polarization, and the two polarization sources are orthogonal. The fields are:

$$\begin{cases} \mathbf{A}^1 = \left(E_x^{TE}, \quad 0, \quad 0, \quad H_y^{TE}, \quad H_z^{TE}\right) \\ \mathbf{A}^2 = \left(0, \quad E_y^{TM}, \quad H_x^{TM}, \quad 0, \quad 0\right) \end{cases}. \tag{6}$$

For the 3D model, the full field components can be calculated by forward modeling with two orthogonal polarization sources.

After obtaining the forward modeling fields, we can use them to synthesize the time series. The synthesis procedure is described below by taking an example of a particular site, a particular frequency, and a particular time series slice of polarization 1.

First, the intensities of natural field sources in different frequency ranges is simulated. Loddo et al. (2002) used a smoothed natural source horizontal magnetic field curve to simulate the intensity. In the proposed method, the forward fields of each frequency are scaled by a uniform coefficient to be near the natural field intensity (e.g. $\mathbf{A}_s^1 = S^1\mathbf{A}^1$, S^1 is the scaling coefficient of polarization 1).

Second, we use pseudo-random numbers to simulate the field source intensity and polarization variations. The r_a^1 and r_p^1 are randomly generated amplitude coefficients and phase shift. The electromagnetic field of a random field source is:

$$\mathbf{A}_r^1 = r_a^1 e^{ir_p^1} S^1 \mathbf{A}^1. \tag{7}$$

Finally, by substituting Eq. 7 into Eq. 1, the synthetic time series of polarization 1 at the given frequency at the given site in the given segment can be generated. The time series of other sites in the model can be synthesized with the same coefficient ($r_a^1 e^{ir_p^1} S^1$).

Splicing time series segments

We simulate the time-varying MT signal by splicing a large number of time series segments, each generated following the procedure described above. The segmentation, synthesis, and splicing of each frequency and each polarization are performed independently before the final superposition. The length of each segment is randomly generated and needs to be long enough to preserve valid spectral information to make the transfer functions stable. After many tests, we found that stable transfer functions are obtained only when the segment length exceeds four times the period. In this approach, the segment length is generated randomly and ranges from 0 to 8 times

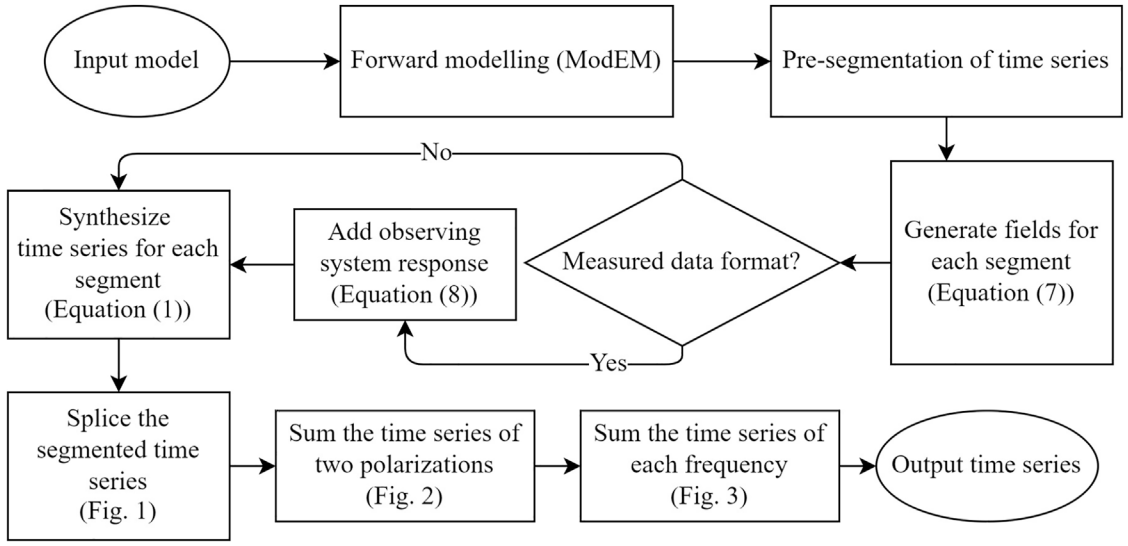

FIGURE 4
Flow chart of synthesis magnetotelluric time series based on forward modeling.

the period by default. It can also be adjusted manually. Excessly short segments are considered noise, which is allowed in this approach.

We randomly generate the amplitude and phase of each segment, and the splice of the two segments is discontinuous. This discontinuity can be ignored as noise or suppressed by windowing at the splice. We design a Hanning window of length half a period and flip the window such that the two endpoints of the window are 1 and the midpoint is 0 (**Figure 1A**).After adding the window, the two segments are smoothly connected. For example, the original time series (**Figure 1B**) is divided into four segments. The time series after windowing (**Figure 1C**) is continuous and smooth.

Figure 2 shows the synthesizing process of the time series of single frequency of H_x channel. The time series of the X-direction source is divided into four segments, whereas that of the Y-direction source is divided into two segments. The amplitude and phase of each segment are randomly generated by Eq. 7. The original time series is calculated by Eq. 1. The original time series is multiplied by the window function to obtain the windowed time series. And the windowed time series of the two sources were superimposed to get the total time series of the single frequency. The time series of multi-frequencies is the sum of all single frequencies, as shown in **Figure 3**.

Synthesizing time series workflow

According to the above theory, the complete workflow of synthesizing magnetotelluric time series based on forward modeling is shown in **Figure 4**.

All the processes except forward modeling in **Figure 4** have been implemented using Delphi language programming. The 3D forward modeling was performed using the modified ModEM code described above.

In addition, synthesizing time series in a measured data format requires the addition of the response of the observed system. In fieldwork, the measured electromagnetic field signal is recorded in a specific format according to the equipment used (e.g. Phoenix Geophysics, MTU-5A). The natural electromagnetic field signal measured by the sensor is transmitted to the instrument in the form of the electrical signals. To facilitate recording, the instrument takes an analog-to-digital conversion of this electrical signal before saving. During the conversion process, the analog-to-digital conversion coefficient (2^{23} in MTU-5A) is multiplied and then rounded and stored (three-byte integer in MTU-5A). The relationship between the recorded data and the real signal is stable in the frequency domain, termed the instrument response (obtained from calibration). The instrument response is added as:

$$A^o(\omega) = CA^r(\omega)R(\omega), \tag{8}$$

where A^r is the real signal, A^o is the output record, and R is the instrument response, C is the analog-to-digital conversion coefficient. Based on this principle, we implemented the synthesized time series with MTU-5A format as output.

Numerical experiments

1D model

To validate this approach, we first synthesized a time series of a 1D model for testing. We designed a three-layer model with resistivity of $10\Omega m$, $100\Omega m$, and $1\Omega m$ from top to bottom, with the top two layers having thicknesses of 1 km and 10 km, respectively. We obtained the electromagnetic fields of the model through forward modeling, and the frequencies we used are approximately log-uniformly distributed, see the vertical grid in **Figure 5D**.

To avoid excessive data due to a single high sampling rate, the synthetic time series is divided into high, medium and low sampling rates of 2,400, 150, and 15 Hz using the parameters of MTU-5A. The length of the synthetic time series is 48 h, where the low sampling rate records are continuous while the high and medium sampling rate records are discontinuous. Each 300 s, a 16 s medium sampling rate record or a 2 s low sampling rate record is

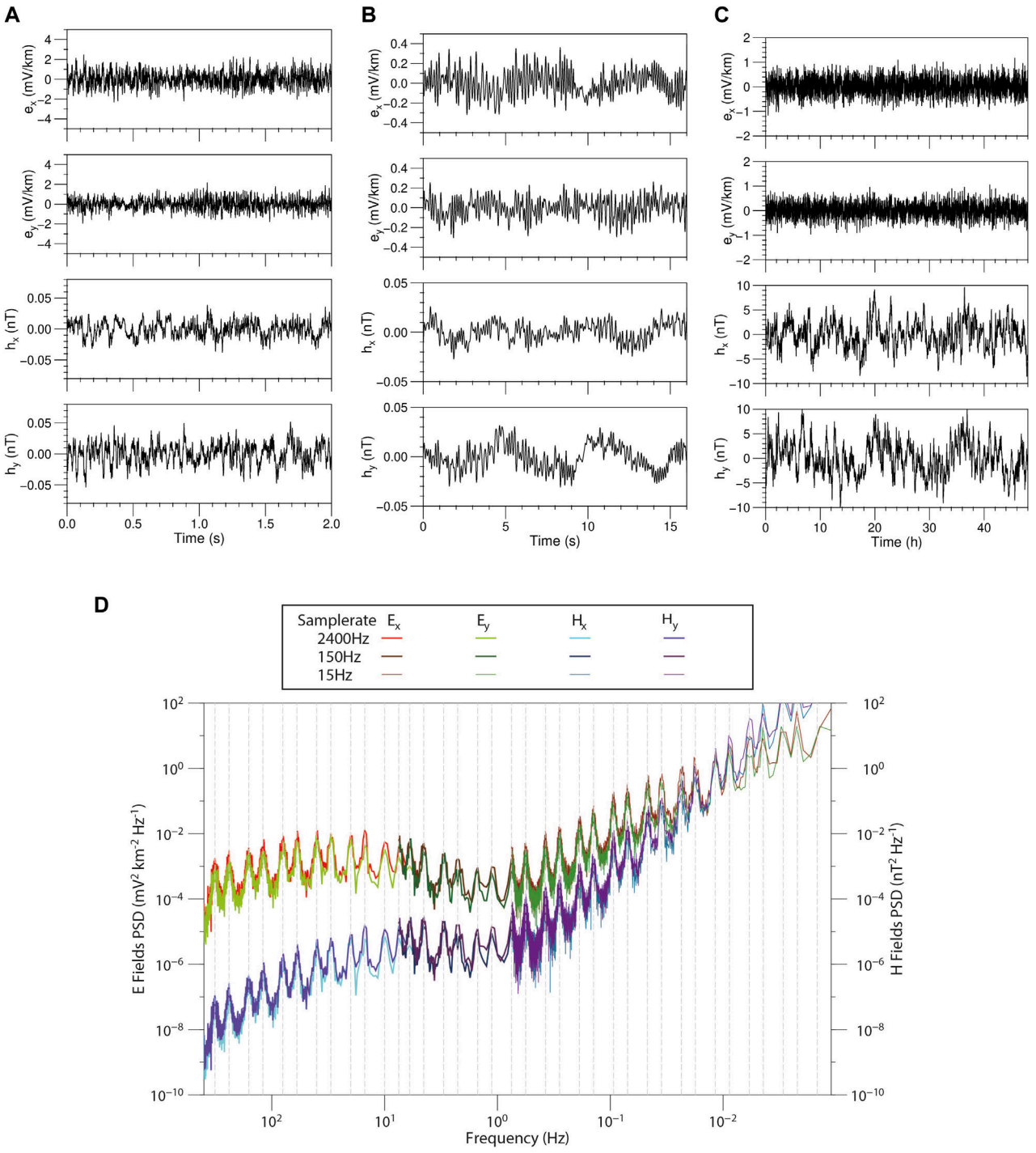

FIGURE 5
The synthetic time series and power spectrum density of the 1D model. **(A)** Time series with 2400Hz sampling rate, **(B)** Time series with 150Hz sampling rate, **(C)** Time series with 15Hz sampling rate, **(D)** power spectrum of the time series.

synthesized alternately. The synthesizing frequency ranges for high, medium, and low sampling rates are 320 Hz–1.125 Hz (a total of 18 frequencies), 10 Hz–0.140625 Hz (a total of 14 frequencies), and 0.75 Hz to 0.00001.72 Hz (a total of 32 frequencies), respectively.

Figure 5 shows the synthetic time series and its power spectral density (PSD). The time series is irregular, random, and resembles a non-stationary signal. The PSD at the given frequencies is approximately one order of magnitude higher than at the frequencies not given, implying that the synthetic time series contains the signal exactly at the target frequencies. Further, we use the least-squares method to estimate the impedance. As shown in Figure 6, the apparent resistivity and phase closely match the theoretical response, indicating that the time series of the 1D model constructed by this method is quite accurate.

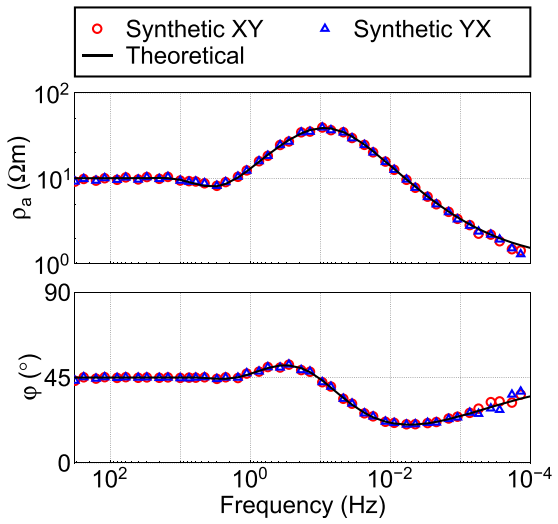

FIGURE 6
The apparent resistivity (ρ_a) and phase (φ) of the synthetic time series of the 1D model obtained by least square method processing.

3D model

The 3D model is closer to the actual situation. To further verify our method, we use the 3D model COMMEMI 3D-2A from (Zhdanov et al., 1997) for the following study. The model background is a three-layer medium (resistivity of 10, 100, and 0.1 Ωm) with two anomalous rectangular bodies (resistivity of 1Ωm and 100Ωm) on the top layer. Eight sites on the model surface were selected to synthesize time series, as shown in **Figure 7**.

The synthetic time series using the same sampling rates as above is shown in **Figure 8**. For clarity, only a portion of the time series is plotted for each sampling rate. The time series of the horizontal magnetic fields (H_x and H_y) at each site are quite similar, which is similar to the slow spatial variation of the natural horizontal magnetic field. The horizontal electric fields (E_x and E_y) at each site are quite similar in morphology but differ in amplitude and phase. This is because the electric field signal is more easily affected by the electrical structure under the same natural field source. The resistivity below site F is much lower than that at site G, so the horizontal electric field amplitude at site F is always smaller than that at site G with the same source. Consequently, the morphology of the synthetic time series is consistent with the given model.

To facilitate processing with existing software, we add the observed system responses to the synthetic time series and output them in MTU-5A format. We processed the time series using the least-squares method, the commercial software SSMT2000 and the open-source software EMTF (Egbert, 1997). **Figure 9** shows the processing results. All the results are consistent with the theoretical response, indicating that the synthetic time series of the 3D model are accurate and can be processed by existing methods.

To further analyze the synthetic time series, we divided the time series into sections (to distinguish the "segment" in synthesizing time series, "section" is used here). Every two adjacent sections overlap by 50%. We preform the Fourier transform on each section, and calculate the frequency domain parameters such as the PSD of the electromagnetic field, the impedance tensor, the tipper vector, the ordinary coherence, and the polarization direction. These parameters were usually used in frequency domain selection techniques for MT noise separation (Weckmann et al., 2005). The PSD is defined as:

$$PSD(A) = \frac{\sqrt{[AA^*]^2}}{\Delta T}, \tag{9}$$

where $A = E_x(\omega)$, $E_y(\omega)$, $H_x(\omega)$, $H_y(\omega)$ or $H_z(\omega)$, ΔT is the length of the section, A^* is the complex conjugate of A.

The ordinary coherence is defined as:

$$coh(AB) = \frac{|[AB^*]|^2}{[AA^*][BB^*]}, \tag{10}$$

where B is the same as A, but can be different field components.

The polarization direction α_E and α_H of electric and magnetic field are:

$$\begin{cases} \alpha_E = \arctan \dfrac{2 * \Re([E_x E_y^*])}{[E_x E_x^*] - [E_y E_y^*]} \\ \alpha_H = \arctan \dfrac{2 * \Re([H_x H_y^*])}{[H_x H_x^*] - [H_y H_y^*]} \end{cases}. \tag{11}$$

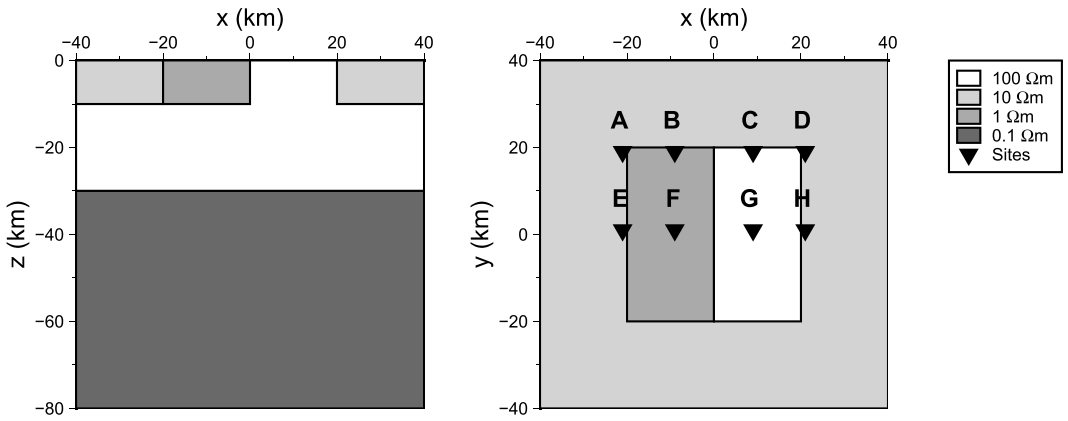

FIGURE 7
Model diagram of COMMEMI 3D-2A, the triangles are the locations of the sites.

10.3389/feart.2023.1086749

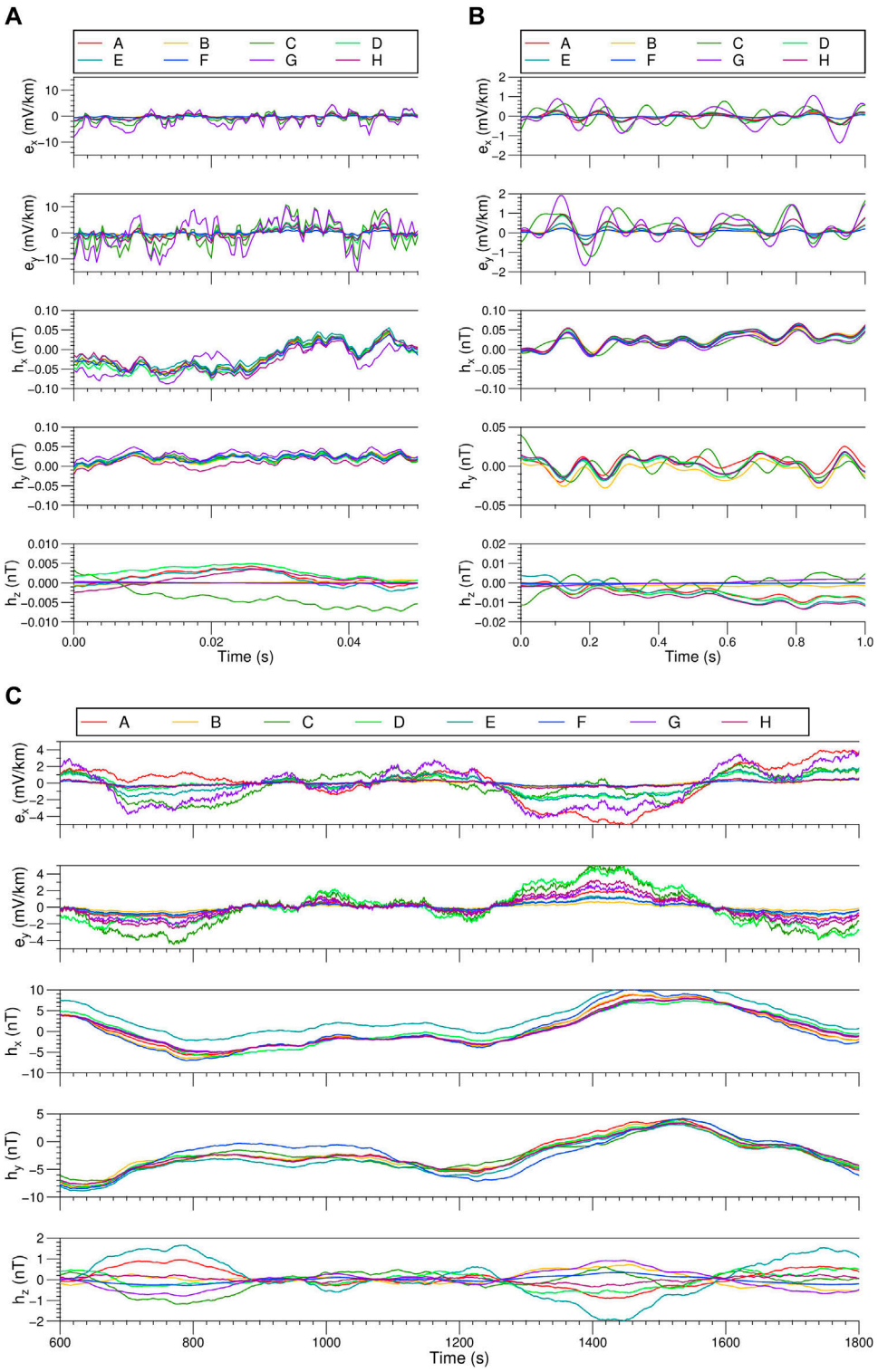

FIGURE 8
Synthetic time series of 8 sites in the 3D model. **(A)** Time series with 2400Hz sampling rate, **(B)** Time series with 150Hz sampling rate, **(C)** Time series with 15Hz sampling rate.

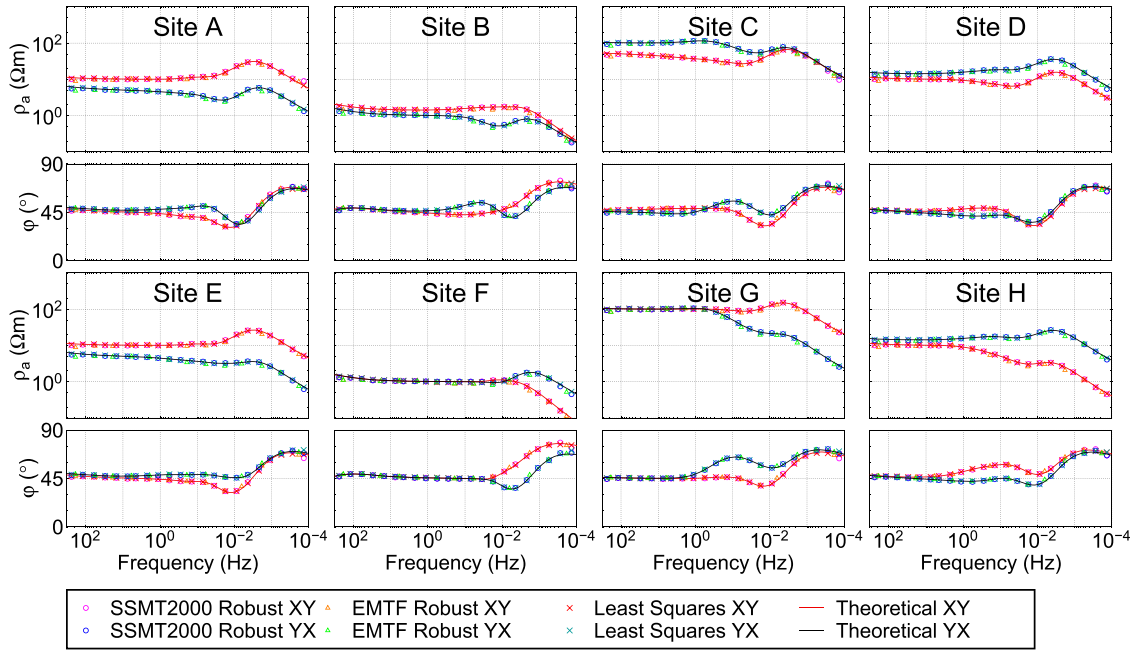

FIGURE 9
The processing results of the synthetic time series of 8 stations in the 3D model.

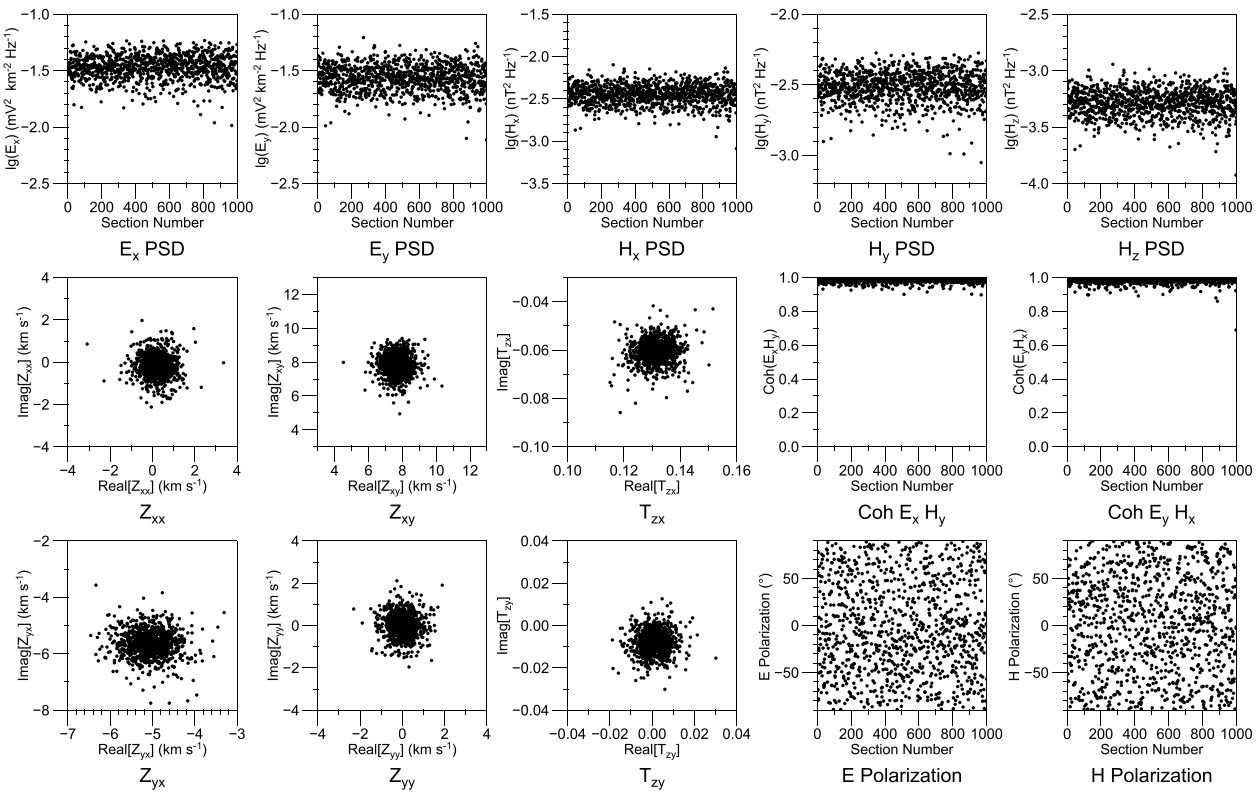

FIGURE 10
The distribution of parameters at 2.25 Hz of synthetic time series of site A. The *x*-axis of most graphs shows the section numbers. The six response function plots are displayed in the complex plane.

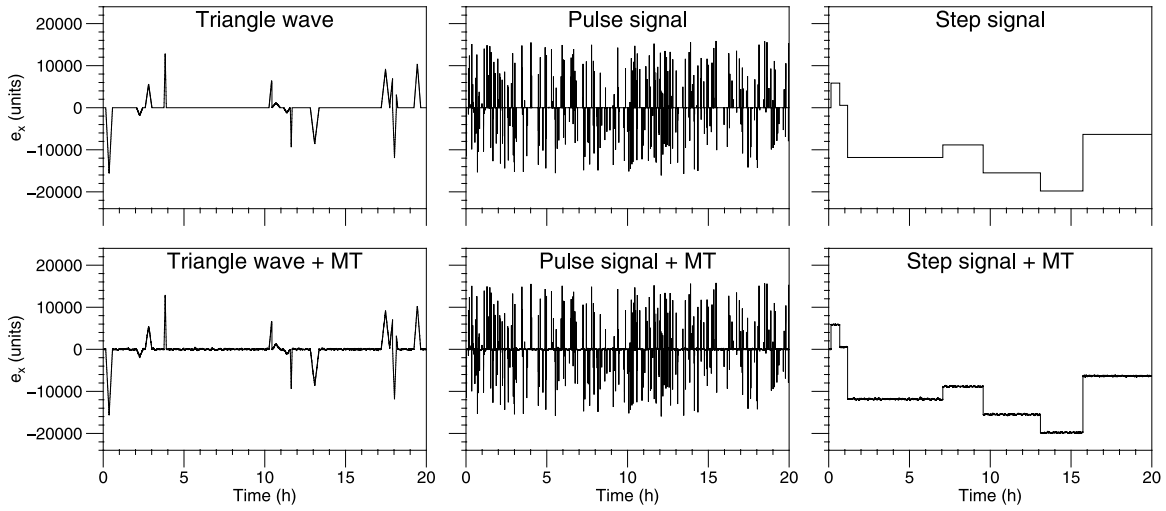

FIGURE 11
Synthetic time series with noise. The duration of the time series is 20 h.

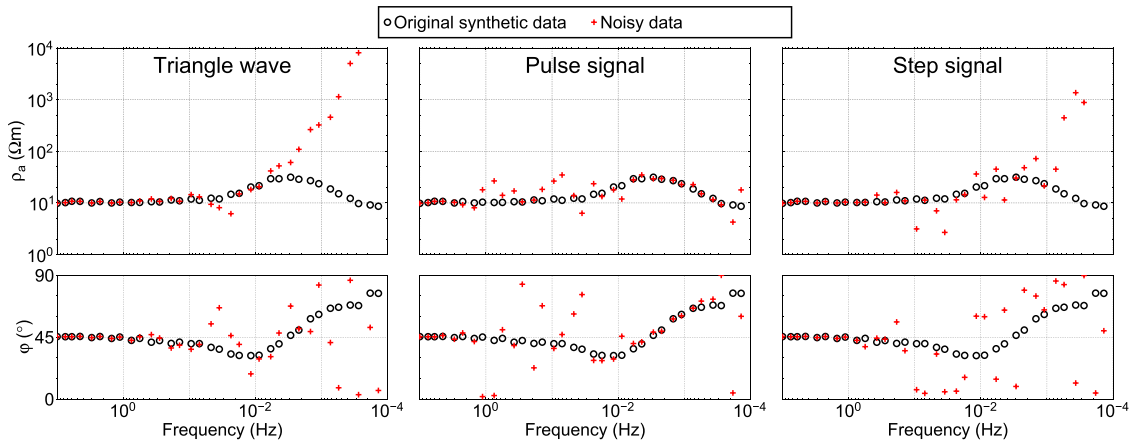

FIGURE 12
Response of time series with noise. Processed by the least-square method.

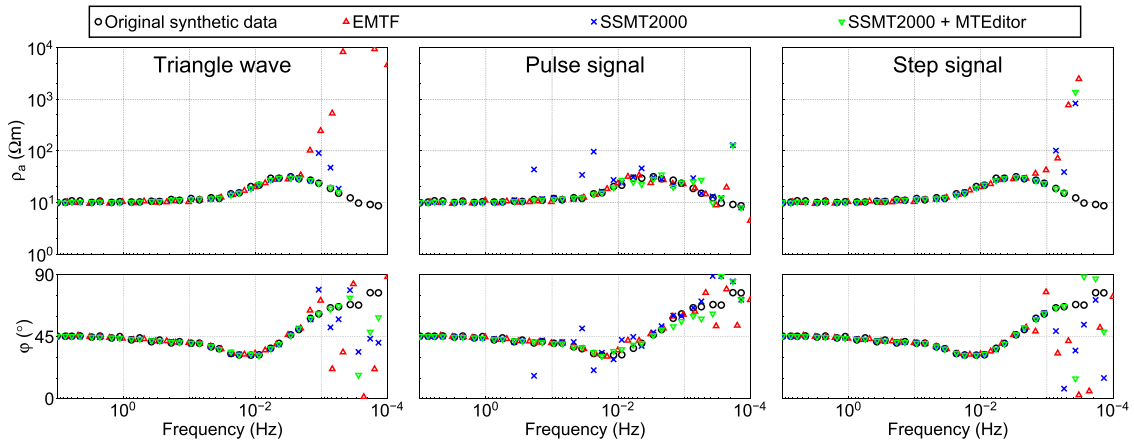

FIGURE 13
Comparison of processing results between EMTF and SSMT 2000. SSMT2000+MTEditor is the result processed by SSMT2000 and by MTEditor.

where $\Re$ stands for the real part.

Figure 10 shows the MT parameters at 2.25 Hz. The PSD distribution of electromagnetic field shows a random variation of signal intensity similar to natural fields. The distribution of the transfer function estimates exhibit one cluster around the actual value. The coherence of the orthogonal electromagnetic field is concentrated near 1. The polarization direction of electric and magnetic fields are disordered with time. The distributions of all these parameters follow those of a low-noise natural-field MT signal, suggesting that the synthetic time series can simulate natural MT signal with a high signal-to-noise.

Noise test

By adding noise to the synthetic time series, we can test the effects of various noises on the MT response and verify the denoising ability, estimation results, and robustness of the data processing methods. For example, square-wave, triangular-wave, and impulsive noise are three common types of noise in MT exploration. We generated the three types of noise by pseudo-random, and added them to the E_x channel at site A (Figure 11).

We investigated the effect of different noises on the MT response by processing raw synthetic and noisy time series using the least-squares method. Figure 12 shows the apparent resistivity and phase curves. Different noises affect different frequency ranges. Triangular waves and step noise with large timescales affect low frequencies below 1 Hz. Impulsive noise has no effect on frequencies below 0.01 Hz, but only affects frequencies between 2 Hz and 0.01 Hz in a range similar to the dead band. Different noise has different effects on apparent resistivity and phase curve morphology. The apparent resistivity and phase, the apparent resistivity and phase are irregular in all but the case of triangular wave noise, which causes the apparent resistivity to increase steadily with decreasing frequency.

EMTF and SSMT2000 are the two most commonly used MT time series processing software. SSMT2000 is commonly used in conjunction with the frequency domain data selection software MTEditor to improve estimation quality. We used EMTF and SSMT2000 to process the noisy time series, and use MTEditor to select the spectral data processed by SSMT 2000. The final results are shown in Figure 13. Both EMTF and SSMT2000 provided accurate impedance estimation for synthetic time series with triangular and step noise at frequencies above 0.002 Hz. For low frequencies below 0.002 Hz, accurate impedance estimates were not obtained by either method due to insufficient stacking. For time series with impulsive noise, EMTF was able to accurately estimate the impedance in the frequency band affected by the noise, while SSMT2000 was unable to accurately estimate the impedance in a few frequencies. However, careful selection of spectral data using MTEditor improved the estimation of these frequencies. Moreover, in the low-frequency, the MTEditor result had three or four more effective frequencies than the other two results, so that SSMT2000 combined with MTEditor achieves the best performance in this test.

The above test results show that the synthesized time series of the proposed method can be used not only as the carrier of noise signals to study the influence of different noises on MT response, but also as a test standard to study the processing performance of different data processing methods to specific noises.

Conclusion

We propose a synthetic MT time series method based on forward modeling. First, the electromagnetic response of two orthogonal polarization sources for a given model is calculated using MT forward modeling. Then, the electromagnetic responses of the two polarization sources are randomly combined to simulate the random polarization properties of the natural field sources. Next, the electromagnetic fields are transformed from the frequency domain to the time domain according to the correspondence between the time and frequency domains. Finally, the time-varying source polarization is simulated by segmentation and concatenation to generate time series. We use this method to synthesize time series of 1D and 3D models. The spectral analysis of the synthetic time series shows that the distribution of the parameters in the frequency domain is similar to that of the measured low-noise natural field data. Commercial software and open-source software were used to process the synthetic time series, and the apparent resistivity and phase closely match the forward modeling response of the given model, confirming the correctness of the proposed method. By adding different types of noise into the synthetic time series, the effect of noise on MT response is analyzed, and the performance of different time series processing methods is tested and compared, which proves that the synthetic time series can be used as the evaluation criterion of time series processing methods.

The time series of all channels synthesized by the proposed method are directly derived from MT forward modeling, which is more reasonable than previous techniques that require a pre-determined time series of the magnetic fields. As shown in the 3D model example, time series of complex models can be synthesized to provide an effective study sample for analyzing the spatial distribution and temporal variability of MT time series of specific models. Synthetic time series can be used for single- and multi-site data processing studies. This method can be used to synthesize not only MT time series, but also time series of other frequency-domain electromagnetic methods. Therefore, various artificial source noises can be synthesized and added to the synthetic MT time series to investigate the signal-to-noise separation method, which is also the focus of our future study. Synthetic time series can provide rich and diverse learning samples for deep learning techniques, which can help apply artificial intelligence techniques in MT time series processing.

In summary, the method presented in this paper provides a technical basis to transform the forward modeling of electromagnetic responses from the frequency domain to the time domain. We can obtain time series for any model, which amounts to providing a standard signal generator for the study of time series processing techniques. In addition to testing the effectiveness of the time series processing method, it can be applied to other aspects. For example, to analyze the effect of different types of noise on the MT response, we can synthesize time series containing different noises, and then compare the processing results of noisy time series with the forward modeling response. In a practical MT application, after obtaining the inversion model of the studied region, we can attempt to extract the

actual natural source information through time series of low-noise sites. We may then be able to construct random sources that are highly correlated with the true natural sources and synthesize time series for the inversion model. Moreover, time series not derived from the inversion model can be separated to study the distribution of noise. In this way, we can extract the source of the remote reference station and synthesize the time series highly correlated with the observation station, which can be used as the reference channels to improve the quality of the measured data. In other words, many new and interesting studies can be carried out based on the synthetic time series method proposed in this paper.

Data availability statement

The open-source code for the method and the data in the paper are available on Github: https://github.com/EMWPJ/SyntheticMTTimeSeries and https://github.com/EMWPJ/MT-synthetic-time-series-Data.

Author contributions

PW implemented the algorithms and wrote the manuscript. XC came up with the idea of the algorithm, supervised the study, performed the analyses, and edited the manuscript. YZ helped in processing the data and drew the figures.

Funding

This work is supported by the National Natural Science Foundation of China (41941016), the 2nd comprehensive scientific investigation into the Tibetan Plateau (2019QZKK0708), and the National Natural Science Foundation of China (42174093).

Acknowledgments

We are grateful to Anna Kelbert, Naser Meqbel, Gary D. Egbert, and Kush Tandon for providing the ModEM code (Kelbert et al., 2014). Generic Mapping Tools software (Wessel et al., 2019) was used to produce the figures in this manuscript.

Conflict of interest

The authors declare that the research was conducted in the absence of any commercial or financial relationships that could be construed as a potential conflict of interest.

Publisher's note

All claims expressed in this article are solely those of the authors and do not necessarily represent those of their affiliated organizations, or those of the publisher, the editors and the reviewers. Any product that may be evaluated in this article, or claim that may be made by its manufacturer, is not guaranteed or endorsed by the publisher.

Supplementary material

The Supplementary Material for this article can be found online at: https://www.frontiersin.org/articles/10.3389/feart.2023.1086749/full#supplementary-material

References

Banks, R. J. (1998). The effects of non-stationary noise on electromagnetic response estimates. *Geophys. J. Int.* 135, 553–563. doi:10.1046/j.1365-246X.1998.00661.x

Cai, J., and Chen, Q. (2015). Spectrum analysis of magnetotelluric data series based on EMD-teager transform. *Pure Appl. Geophys.* 172, 2901–2915. doi:10.1007/s00024-015-1083-0

Cai, J., Chen, X., Xu, X., Tang, J., Wang, L., Guo, C., et al. (2017). Rupture mechanism and seismotectonics of the M_S 6.5 Ludian earthquake inferred from three?dimensional magnetotelluric imaging. *Geophys. Res. Lett.* 44, 1275–1285. doi:10.1002/2016GL071855

Cai, J. (2014). A combinatorial filtering method for magnetotelluric time-series based on Hilbert–Huang transform. *Explor. Geophys.* 45, 63–73. doi:10.1071/EG13012

Campanya, J., Ledo, J., Queralt, P., Marcuello, A., and Jones, A. G. (2014). A new methodology to estimate magnetotelluric (mt) tensor relationships: Estimation of local transfer-functions by combining interstation transfer-functions (elicit). *Geophys. J. Int.* 198, 484–494. doi:10.1093/gji/ggu147

Carbonari, R., D'Auria, L., Di Maio, R., and Petrillo, Z. (2017). Denoising of magnetotelluric signals by polarization analysis in the discrete wavelet domain. *Comput. Geosciences* 100, 135–141. doi:10.1016/j.cageo.2016.12.011

Chave, A. D., and Thomson, D. J. (2004). Bounded influence magnetotelluric response function estimation. *Geophys. J. Int.* 157, 988–1006. doi:10.1111/j.1365-246X.2004.02203.x

Chave, A. D., Thomson, D. J., and Ander, M. E. (1987). On the robust estimation of power spectra, coherences, and transfer functions. *J. Geophys. Res.* 92, 633. doi:10.1029/JB092iB01p00633

Chave, A. D. (2014). Magnetotelluric data, stable distributions and impropriety: An existential combination. *Geophys. J. Int.* 198, 622–636. doi:10.1093/gji/ggu121

Chave, A. D. (2017). Estimation of the magnetotelluric response function: The path from robust estimation to a stable maximum likelihood estimator. *Surv. Geophys.* 38, 837–867. doi:10.1007/s10712-017-9422-6

Egbert, G. D., and Booker, J. R. (1986). Robust estimation of geomagnetic transfer functions. *Geophys. J. Int.* 87, 173–194. doi:10.1111/j.1365-246X.1986.tb04552.x

Egbert, G. D. (1997). Robust multiple-station magnetotelluric data processing. *Geophys. J. Int.* 130, 475–496. doi:10.1111/j.1365-246X.1997.tb05663.x

Escalas, M., Queralt, P., Ledo, J., and Marcuello, A. (2013). Polarisation analysis of magnetotelluric time series using a wavelet-based scheme: A method for detection and characterisation of cultural noise sources. *Phys. Earth Planet. Interiors* 218, 31–50. doi:10.1016/j.pepi.2013.02.006

Gamble, T. D., Goubau, W. M., and Clarke, J. (1979a). Error analysis for remote reference magnetotellurics. *Geophysics* 44, 959–968. doi:10.1190/1.1440988

Gamble, T. D., Goubau, W. M., and Clarke, J. (1979b). Magnetotellurics with a remote magnetic reference. *Geophysics* 44, 53–68. doi:10.1190/1.1440923

Goubau, W. M., Gamble, T. D., and Clarke, J. (1978). Magnetotelluric data analysis: Removal of bias. *Geophysics* 43, 1157–1166. doi:10.1190/1.1440885

Guo, Z., Han, J., Gong, X., Liu, L., Zhou, R., and Wu, Y. (2022). ADMM-based method for estimating magnetotelluric impedance in the time domain. *IEEE Trans. Geoscience Remote Sens.* 60, 1–16. doi:10.1109/TGRS.2022.3171768

Jiang, F., Chen, X., Unsworth, M. J., Cai, J., Han, B., Wang, L., et al. (2022). Mechanism for the uplift of gongga Shan in the southeastern Tibetan plateau constrained by 3d magnetotelluric data. *Geophys. Res. Lett.* 49, e2021GL097394. doi:10.1029/2021GL097394

Junge, A. (1996). Characterization of and correction for cultural noise. *Surv. Geophys.* 17, 361–391. doi:10.1007/BF01901639

Kappler, K. N. (2012). A data variance technique for automated despiking of magnetotelluric data with a remote reference: MT data despiking. *Geophys. Prospect.* 60, 179–191. doi:10.1111/j.1365-2478.2011.00965.x

Kelbert, A., Meqbel, N., Egbert, G. D., and Tandon, K. (2014). ModEM: A modular system for inversion of electromagnetic geophysical data. *Comput. Geosciences* 66, 40–53. doi:10.1016/j.cageo.2014.01.010

Kelbert, A., Balch, C. C., Pulkkinen, A., Egbert, G. D., Love, J. J., Rigler, E. J., et al. (2017). Methodology for time-domain estimation of storm time geoelectric fields using the 3-d magnetotelluric response tensors. *Space weather.* 15, 874–894. doi:10.1002/2017SW001594

Larsen, J. C., Mackie, R. L., Manzella, A., Fiordelisi, A., and Rieven, S. (1996). Robust smooth magnetotelluric transfer functions. *Geophys. J. Int.* 124, 801–819. doi:10.1111/j.1365-246X.1996.tb05639.x

Li, G., Liu, X., Tang, J., Deng, J., Hu, S., Zhou, C., et al. (2020a). Improved shift-invariant sparse coding for noise attenuation of magnetotelluric data. *Earth, Planets Space* 72, 45. doi:10.1186/s40623-020-01173-7

Li, G., Liu, X., Tang, J., Li, J., Ren, Z., and Chen, C. (2020b). De-noising low-frequency magnetotelluric data using mathematical morphology filtering and sparse representation. *J. Appl. Geophys.* 172, 103919. doi:10.1016/j.jappgeo.2019.103919

Li, G., Li, J., Liu, X., and Tang, J. (2020c). Magnetotelluric noise suppression based on impulsive atoms and NPSO-omp algorithm. *Pure Appl. Geophys.* 177, 5275–5297. doi:10.1007/s00024-020-02592-z

Loddo, M., Schiavone, D., and Siniscalchi, A. (2002). Generation of synthetic wide-band electromagnetic time series. *Ann. Geophys.* 45, 289–301. doi:10.4401/ag-3506

Pomposiello, M. C., Booker, J. R., and Favetto, A. (2009). A discussion of bias in magnetotelluric responses. *Geophysics* 74, F59–F65. doi:10.1190/1.3147132

Shalivahan, and Bhattacharya, B. B. (2002). How remote can the far remote reference site for magnetotelluric measurements be? *J. Geophys. Res. Solid Earth* 107, 2105. doi:10.1029/2000JB000119

Sims, W. E., Bostick, F. X., and Smith, H. W. (1971). The estimation of magnetotelluric impedance tensor elements from measured data. *Geophysics* 36, 938–942. doi:10.1190/1.1440225

Smirnov, M. Y. (2003). Magnetotelluric data processing with a robust statistical procedure having a high breakdown point. *Geophys. J. Int.* 152, 1–7. doi:10.1046/j.1365-246X.2003.01733.x

Sutarno, D. (2005). Development of robust magnetotelluric impedance estimation: A riview. *Indonesian J. Phys.* 16, 79–89.

Szarka, L. (1988). Geophysical aspects of man-made electromagnetic noise in the Earth—a review. *Surv. Geophys.* 9, 287–318. doi:10.1007/BF01901627

Varentsov, I., and Sokolova, E. Y. (1995). Generation of synthetic magnetotelluric data. *Izvestiya Phys. Solid Earth* 30, 554–562.

Wang, H., Campanyà, J., Cheng, J., Zhu, G., Wei, W., Jin, S., et al. (2017). Synthesis of natural electric and magnetic time-series using inter-station transfer functions and time-series from a neighboring site (stin): Applications for processing mt data. *J. Geophys. Res. Solid Earth* 122, 5835–5851. doi:10.1002/2017JB014190

Wang, B., Liu, J., Hu, X., Liu, J., Guo, Z., and Xiao, J. (2021). Geophysical electromagnetic modeling and evaluation: A review. *J. Appl. Geophys.* 194, 104438. doi:10.1016/j.jappgeo.2021.104438

Weckmann, U., Magunia, A., and Ritter, O. (2005). Effective noise separation for magnetotelluric single site data processing using a frequency domain selection scheme. *Geophys. J. Int.* 161, 635–652. doi:10.1111/j.1365-246X.2005.02621.x

Wessel, P., Luis, J. F., Uieda, L., Scharroo, R., Wobbe, F., Smith, W. H. F., et al. (2019). The generic mapping Tools version 6. *Geochem. Geophys. Geosystems* 20, 5556–5564. doi:10.1029/2019GC008515

Zhang, Y., Wang, P., Chen, X., Zhan, Y., Han, B., Wang, L., et al. (2022). Magnetotelluric time series processing in strong inferference environment. *Seismol. Geol.* 44, 786. doi:10.3969/j.issn.0253-4967.2022.03.014

Zhdanov, M., Varentsov, I., Weaver, J., Golubev, N., and Krylov, V. (1997). Methods for modelling electromagnetic fields results from COMMEMI—The international project on the comparison of modelling methods for electromagnetic induction. *J. Appl. Geophys.* 37, 133–271. doi:10.1016/S0926-9851(97)00013-X

Zhou, R., Han, J., Li, T., and Guo, Z. (2022). Fast independent component analysis denoising for magnetotelluric data based on a correlation coefficient and fast iterative shrinkage threshold algorithm. *IEEE Trans. Geoscience Remote Sens.* 60, 1–15. doi:10.1109/TGRS.2022.3182504

frontiers | Frontiers in Earth Science

TYPE Original Research
PUBLISHED 26 April 2023
DOI 10.3389/feart.2023.1139523

OPEN ACCESS

EDITED BY
Jin Li,
Hunan Normal University, China

REVIEWED BY
Nian Yu,
Chongqing University, China
Benyu Su,
China University of Mining and Technology, China
Arkoprovo Biswas,
Banaras Hindu University, India

*CORRESPONDENCE
Bo Zhang,
em_zhangbo@163.com

RECEIVED 09 January 2023
ACCEPTED 03 April 2023
PUBLISHED 26 April 2023

CITATION
Su C, Ma G, Liu C, Liu Y and Zhang B (2023), High-resolution imaging of a coal seam based on quasi-2D TEM inversion. *Front. Earth Sci.* 11:1139523. doi: 10.3389/feart.2023.1139523

High-resolution imaging of a coal seam based on quasi-2D TEM inversion

Chao Su, Guoqing Ma, Cai Liu, Yunhe Liu and Bo Zhang*

College of Geoexploration Science and Technology, Jilin University, Changchun, China

In a sedimentary environment, the conventional one-dimensional (1D) inversion based on the horizontal layered model has difficulty restoring the resistivity distribution of the inclined strata when a coal seam has some dip angle or a small interval between layers. In such cases, the inversion resistivity exhibits horizontal discontinuities, which cannot accurately represent actual geological conditions. Therefore, in view of the good horizontal continuity of the underground electrical structure of sedimentary strata, we propose a high-resolution inversion method based on weighted horizontal and vertical constraints. As a quasi-two-dimensional (2D) inversion, this not only ensures the horizontal continuity of resistivity and recovers the inclined strata, but also improves the vertical resolution. Because the constrained factor has a significant influence on the inversion result, different constrained factors are applied in the horizontal and vertical directions to adjust the constraint strength on the model parameters of each layer and the continuity of the layer interface. In the numerical experiments, we design synthetic models with different tilt angles and layer spacings to test the inversion method and optimize the constrained factors used for coal seam detection. Finally, the transient electromagnetic (TEM) field data processing results in Inner Mongolia show that the resistivity distributions of sedimentary strata can be accurately restored by the new method, and the inversion results are consistent with known geological information.

KEYWORDS

sedimentary strata, transient electromagnetic, weighted laterally constrained, quasi-2D inversion, high-resolution imaging

1 Introduction

The transient electromagnetic (TEM) method is a geophysical exploration tool based on electromagnetic induction theory (Stacey, 1976). The electromagnetic pulse signals from a loop source diffuse into the earth to underground anomalies and eventually induce a secondary electromagnetic field that can be observed by a receiver. Secondary field signal processing is employed for the discovery of subsurface minerals or to address geological problems (Fitterman and Stewart, 1986; Fountain et al., 2005; Jiang et al., 2019). This method has been widely used in coal mine water damage detection (Si et al., 2020), hydrogeological surveys (Danielsen et al., 2003), engineering investigations (Hui et al., 2021), and mineral exploration (Yang and Oldenburg, 2012) owing to its flexible working device, high efficiency, and high resolution.

The TEM data must be interpreted to obtain the underground electrical structure. Early TEM data interpretation methods were approximations based on the smoke-ring theory (Nabighian, 1979; Yang et al., 2016). By defining the apparent resistivity and calculating the

diffusion depth (apparent depth) of the smoke ring, a relatively approximate pseudosection map of the apparent resistivity is obtained. These results are inaccurate and are suitable only for preliminary interpretation. Different definitions of the apparent resistivity will lead to large differences in the inversion results. To obtain a more accurate geoelectric model, it is necessary to carry out inversion calculations for TEM data. At present, the mainstream inversion methods are the damped least-squares method (Huang and Palacky, 2010) and the Occam inversion method (Constable et al., 1987), which introduces the regularization of model constraints. By adding a penalty function term to the objective function, different optimizers are used to minimize the difference between the observation data and the model response, and a stable and unique solution can be obtained. Regularization increases the constraint information or prior information of the inversion parameter model, reduces the multiplicity of inversion solutions, and enhances the stability of the inversion. The least squares inversion method requires a good initial guess, and the inversion results easily fall into local minima. The Occam inversion method adds model smoothing constraints to the objective function, which make the stratigraphic interface unclear in the inversion results. These 1D inversion methods are all based on the single-point horizontal layered model, and the inversion resistivity is prone to lateral discontinuity (Farquharson and Oldenburg, 1993; Christensen et al., 2009). In the past decades, the demand of accurate three-dimensional (3D) interpretation of TEM data and the rapid development of computation devices promotes researches on the development of 3D forward modeling and inversion (Liu et al., 2019; Ren et al., 2018; Zhang et al., 2021). Due to the time-consuming inversion of 3D TEM data, their practical applications are limited. Considering the relatively continuous distribution of underground electrical properties in sedimentary strata, it is natural to adopt the laterally constrained inversion method (LCI). The LCI method is a quasi-2D inversion method, which integrates the data of a single profile and multiple measuring points and applies lateral constraints to achieve a relatively continuous resistivity profile.

LCI was first proposed by Auken, Thomsen, and Sorenson (2000) and applied to direct current (DC) data inversion. The main idea is to use a transversely constrained sparse matrix to transform a single-point inversion into a collective inversion of multiple measuring points, to ensure the transverse continuity of the inversion profile. Santos (2004) used this method to obtain the high-quality EM34 inversion profile; Auken and Christiansen (2004) optimized the 2D LCI inversion and segmented the inversion of resistivity data by calculating the Jacobi matrix through the Broyden approximation; Siemon et al. (2009) used the LCI inversion method to process helicopter survey data, which effectively improved the transverse continuity of the profile. Auken et al. (2008) processed TEM data in a paleochannel survey using the LCI technique; Cai et al. (2014) proposed the weighted laterally constrained inversion (WLCI), which was used for inversion calculation of frequency-domain airborne EM data. The effectiveness of the WLCI was verified through inversion processing of theoretical and measured data and comparison with conventional 1D inversion results. Yin et al. (2016) used the WLCI method to invert airborne TEM data. Zhang et al. (2022) used WLCI on time-domain electromagnetic data. To increase the speed of the inversion computation, Lu et al. (2022) developed an analytical technique based on the chain rule to calculate the Jacobi matrix. They then used the WLCI approach to invert four induced polarization parameters from airborne TEM data.

In view of the relatively continuous underground electrical structure of adjacent measuring points in sedimentary strata, we adopt different lateral resistivity constraints and layer interface depth constraints based on the idea of horizontal constraints. Compared with conventional inversion methods, this method effectively improves the vertical resolution of the inversion layer interface. Finally, field data from Inner Mongolia are inverted to test the practicality of the method.

2 Methodology

2.1 Forward modeling theory

To generate 1D TEM forward responses, we first must calculate the frequency domain responses and then translate them to the time domain via Fourier transform (Johansen and Sorensen, 1979). Suppose there are n levels in the strata, and each layer has a conductivity (σ) and thickness (h), as $\sigma_1, h_1; \sigma_2, h_2; \cdots; \sigma_n, h_n; h_n \to \infty$. When calculating the TEM responses in the frequency domain, we simulate a transmitting loop by dividing the loop into a series of current segments, with each segment being treated as an electric dipole. Using the Dirac function integration, the analytical expression in the frequency domain for the vertical component $\mathbf{B}_z$ of the electromagnetic field at any point on the surface is

$$\mathbf{B}_z(x, y, \omega) = \sum_{j=1}^{L} \frac{\mathbf{P}_{E_j}}{2\pi} \mu_0 \sin\varphi_j \int_0^{\infty} \frac{\lambda^2}{\lambda + u_1/R_1} J_1(\lambda r_j) \mathrm{d}\lambda \qquad (1)$$

where L is the number of electric dipoles, $\mathbf{P}_{E_j}$ is the magnetic moment of the jth electric dipole, μ_0 is the magnetic conductivity of vacuum, φ_j is the angle between the jth electric dipole and the measuring point, $J_1(\lambda r_j)$ is the first-order Bessel function, and r_j is the distance between the jth electric dipole and the measuring point, where $R_1 = \mathrm{cth}[u_1 h_1 + \mathrm{arcth}(u_1/u_2)\mathrm{cth}(u_2 h_2 + \cdots + \mathrm{arcth}u_{n-1}/u_n)]$ and $u_j = \sqrt{\lambda^2 + k_j^2}, k_j^2 = -\mathrm{i}\omega\mu_0\sigma_j$, ω is angular frequency. Finally, the time-domain response of any measurement point on the surface of the loop source can be obtained by cosine transformation (Guptasarma, 1982) of Eq. (1).

2.2 1D inversion theory

We use regularization to address the ill-posed nature of the TEM inversion by minimizing the l_2-norm-based objective function, i.e.,

$$\mathbf{U}_m = R + \mu^{-1}\{\|\mathbf{W}\mathbf{d}_{obs} - \mathbf{W}\mathbf{F}[\mathbf{m}]\|^2 - \mathbf{X}_{\infty}^2\} \qquad (2)$$

where μ is the trade-off parameter, $\mathbf{d}_{obs}$ is the observed data, $\mathbf{F}$ is the 1D forward operator, and $\mathbf{m}$ represents the inversion parameters of the model. $\mathbf{X}_{\infty}^2$ is the expected misfit. Here, we adopt the covariance matrix to obtain the misfit between the forward response and observed data, which is represented as

$$\mathbf{W} = \mathrm{diag}\left\{\frac{1}{\varepsilon_1}, \frac{1}{\varepsilon_2}, \cdots, \frac{1}{\varepsilon_j}, \frac{1}{\varepsilon_M}\right\} \tag{3}$$

where ε_j is the standard deviation of the jth observed data, and M is the number of observed data. The roughness function represents the roughness of the inverse model, for which the matrix expression is

$$R = \|\mathbf{P} \cdot \mathbf{m}\|^2 \tag{4}$$

where $\mathbf{P}$ is the unit matrix consisting of 1 and −1, which can be expressed as

$$\mathbf{P} = \begin{bmatrix} 0 & & & & 0 \\ -1 & 1 & & & \\ & -1 & 1 & & \\ & & \cdots & \cdots & \\ & 0 & & -1 & 1 \end{bmatrix} \tag{5}$$

To minimize $\mathbf{U}_m$, we can set $\nabla \mathbf{U}_m$ equal to zero; then we have the iterative equation,

$$\left[(\mathbf{WG})^{\mathrm{T}}\mathbf{WG} + \mu\mathbf{P}^{\mathrm{T}}\mathbf{P}\right]\Delta\mathbf{m}_q = (\mathbf{WG})^{\mathrm{T}}\mathbf{W}\Delta\boldsymbol{d}_q \tag{6}$$

where $\mathbf{G}$ is the Jacobian matrix of sensitivities. Its elements can be expressed as

$$\mathbf{G}_{ij} = \frac{\partial F_i[\mathbf{m}]}{\partial \mathbf{m}_j} \tag{7}$$

By solving Eq. 6 and minimizing the misfit between the predicted data and the observed data Δd_q, we obtain the inversion model update $\Delta\mathbf{m}_q$ of the qth iteration; then we can update the model via $\mathbf{m}^q = \mathbf{m}^{q-1} + s\delta\mathbf{m}$. The value of s is set initially to one. We adopt a cooling approach (Haber and Schwarzbach, 2014) for selecting μ in our inversions.

2.3 WLCI inversion theory

2.3.1 Resistivity lateral constraint

To improve the lateral continuity of the resistivity inversion of adjacent measurement points, we begin with the LCI inversion proposed by Auken and Christiansen (2004) and include the differences between geoelectric parameters of adjacent measurement points as constraint terms to the objective function. Assuming that

$$\mathbf{R}_p\mathbf{m} - \mathbf{e}_{rp} = 0 \tag{8}$$

Where $\mathbf{e}_{rp}$ represents the different model parameters of adjacent points, and $\mathbf{R}_p$ is the horizontal constraint matrix, which is a sparse matrix with the values 1 and −1, i.e.,

$$\mathbf{R}_p = \begin{bmatrix} 1 & 0 & \cdots & 0 & -1 & 0 & \cdots & 0 & 0 & 0 \\ 0 & 1 & 0 & \cdots & 0 & -1 & 0 & \cdots & 0 & 0 \\ \vdots & & & & & \vdots & & & & \vdots \\ 0 & 0 & 0 & \cdots & 0 & 1 & 0 & \cdots & 0 & -1 \end{bmatrix}_{\mathrm{S\times T}} \tag{9}$$

where $\mathrm{S} = (M-1)\times(2N-1), \mathrm{T} = M\times(2N-1)$, M is the number of the data receiver, and N is the number of layers. Subtracting $\mathbf{R}_p\mathbf{m}_0$ from both sides of Eq. (8), we have

$$\mathbf{R}_p\Delta\mathbf{m} = \Delta\mathbf{r}_p + \mathbf{e}_{rp} \tag{10}$$

where $\Delta\boldsymbol{r_p} = -\mathbf{R}_p\mathbf{m}_0, \Delta\mathbf{m}_0 = \mathbf{m} - \mathbf{m}_0$.

We adopt the horizontal constrained factor to accomplish WLCI and adjust the horizontal smoothness of each layer. Thus, Eq. (8) can be written as

$$\mathbf{R}_p^{'}\Delta\mathbf{m} = \Delta\mathbf{r}_p^{'} + \mathbf{e}_{rp}^{'} \tag{11}$$

Where $\mathbf{R}_p^{'} = \mathbf{W}_p\mathbf{R}_p, \Delta r_{\mathrm{p}}^{'} = -\mathbf{R}_p^{'}\mathbf{m}_0, \mathbf{e}_{rp}^{'} = \mathbf{W}_p\mathbf{e}_{rp}$. $\mathbf{W}_p$ is the horizontal constraint weighting matrix, which equals to the horizontal constrained factor multiplied by the matrix $\mathbf{R}_p$. The inversion's smoothness is determined by the constrained factor's value, which is dependent on the smoothness of the parameters and the actual requirements.

2.3.2 Depth and layer interface constraints

The depth of the layer interfaces must be constrained to ensure the smoothness and continuity between the layer interfaces of the multilayer model (Auken and Christiansen, 2004). We have

$$\mathbf{R}_t\mathbf{m} - \mathbf{e}_{rt} = 0 \tag{12}$$

Where $\mathbf{e}_{rt}$ is the depth difference between each layer of adjacent points, and $\mathbf{R}_t$ is the depth constraint matrix, written as

$$\mathbf{R}_t = \begin{bmatrix} \cdots & 0 & \cdots & 0 & 1 & 0 & 0 & \cdots & 0 & \cdots \\ \cdots & 0 & \cdots & 0 & \frac{h_{k,1}}{t_{k,2}} & \frac{h_{k,2}}{t_{k,2}} & 0 & \cdots & 0 & \cdots \\ & \vdots & \vdots & \vdots & \vdots & & & & & \\ \cdots & 0 & \cdots & 0 & \frac{h_{k,1}}{t_{k,N-1}} & \frac{h_{k,2}}{t_{k,N-1}} & \frac{h_{k,3}}{t_{k,N-1}} & \cdots & \frac{h_{k,N-1}}{t_{k,N-1}} & \cdots \\ \cdots & 0 & \cdots & 0 & -1 & 0 & 0 & \cdots & 0 & \cdots \cdots \\ \cdots & 0 & \cdots & 0 & -\frac{h_{k+1,1}}{t_{k+1,2}} & -\frac{h_{k+1,2}}{t_{k+1,2}} & 0 & & \cdots & 0 \cdots \\ & \vdots & \vdots & \vdots & \vdots & & & & & \\ \cdots & 0 & \cdots & 0 & -\frac{h_{k+1,1}}{t_{k+1,N-1}} & -\frac{h_{k+1,2}}{t_{k+1,N-1}} & -\frac{h_{k+1,3}}{t_{k+1,N-1}} & \cdots & -\frac{h_{k+1,N-1}}{t_{k+1,N-1}} & \cdots \end{bmatrix}_{\mathrm{S\times T}} \tag{13}$$

This is a sparse matrix composed of depth t and thickness h, where $h_{i,j}$ and $t_{i,j}$ are the thickness and the depth, respectively, of the lower interface of the ith point at the jth layer, and $S = (M-1)\times(N-1), T = M\times(2N-1)$.

As mentioned in Section 2.3.1, we use a vertically constrained factor to adjust the continuity between the interfaces of each layer. Thus, Eq. (12) can be written as

$$\mathbf{R}_t^{'}\Delta\mathbf{m} = \Delta\mathbf{r}_t^{'} + \mathbf{e}_{rt}^{'} \tag{14}$$

Correspondingly, $\mathbf{R}_t^{'} = \mathbf{W}_t\mathbf{R}_t, \Delta r_{\mathrm{t}}^{'} = -\mathbf{R}_t^{'}\mathbf{m}_0, \mathbf{e}_{rt}^{'} = \mathbf{W}_t\mathbf{e}_{rt}$, where $\mathbf{W}_t$ is the vertically constrained weighting matrix.

2.4 WLCI inversion equation and least-squares solution

Combined with the 1D inversion theory described in Section 2.2, we obtain the WLCI inversion equation,

$$\begin{bmatrix} \boldsymbol{G} \\ \boldsymbol{R}_p^{'} \\ \boldsymbol{R}_t^{'} \end{bmatrix}\Delta\mathbf{m} = \begin{bmatrix} \Delta\boldsymbol{d}_{obs} \\ \Delta\boldsymbol{r}_p^{'} \\ \Delta\boldsymbol{r}_t^{'} \end{bmatrix} + \begin{bmatrix} \boldsymbol{e}_{obs} \\ \boldsymbol{e}_{rp}^{'} \\ \boldsymbol{e}_{rt}^{'} \end{bmatrix} \tag{15}$$

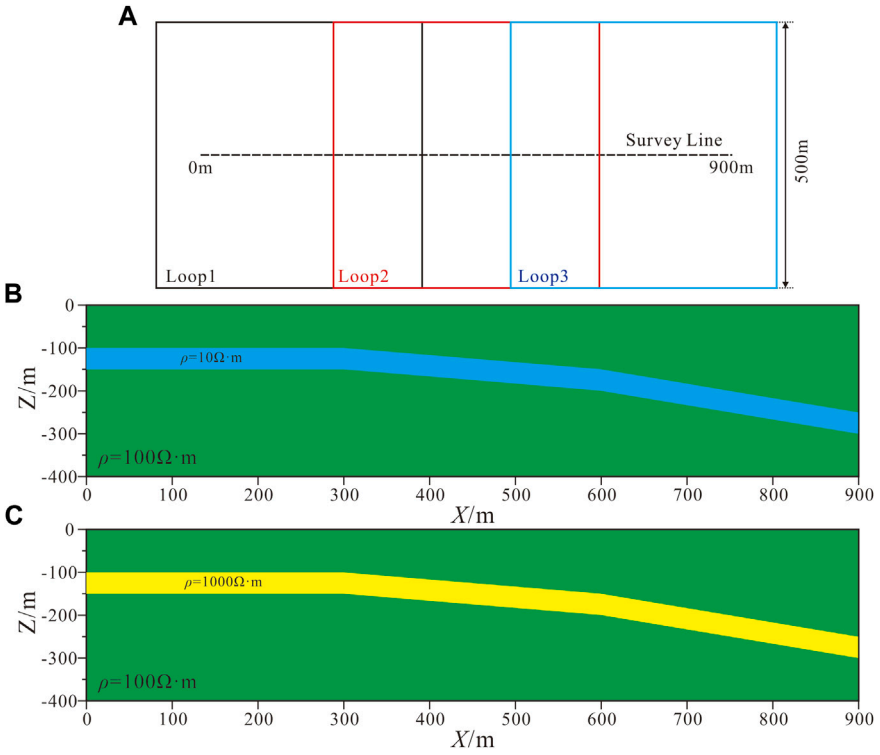

FIGURE 1
Synthetic model of inclined strata **(A)**: Receiving and transmitting schematic. **(B)**: H-type model. **(C)**: K-type model.

Simplifying Eq. (15), we have

$$\mathbf{W}'\Delta\mathbf{m}_q = \Delta\boldsymbol{d}_q + \boldsymbol{e} \tag{16}$$

where $\mathbf{W}'$ is the coefficient matrix. Based on the 1D inversion theory, we obtain the following inversion equation:

$$\left(\mathbf{W}'^{\mathrm{T}}\mathbf{W}' + \mu\mathbf{P}\right)\Delta\mathbf{m}_q = \mathbf{W}'^{\mathrm{T}}\Delta\boldsymbol{d}_q \tag{17}$$

To solve Eq. (17), in this study, we use singular value decomposition (**SVD**) for the coefficient matrix $\mathbf{W}'$, such that we have

$$\mathbf{W}' = \mathbf{D}\Lambda\mathbf{V}^{\mathrm{T}} \tag{18}$$

Where $\mathbf{D}$ and $\mathbf{V}$ are the data matrix and parameters matrix, respectively, and Λ is the singular value matrix. Substituting Eq. (18) into Eq. (17), we have

$$\Delta\mathbf{m}_q = \mathbf{V}\left(\Lambda^2 + \mu\mathbf{P}\right)^{-1}\Lambda\mathbf{D}^{\mathrm{T}}\Delta\mathbf{d}_q \tag{19}$$

The initial resistivity model for inversion is provided first in the actual inversion calculation, and then Eq. (19) is used to perform iterative calculations until the objective function satisfies the specifications.

3 Synthetic examples

We first established a tilted layered stratum model to verify the effectiveness of the inversion strategy. As shown in Figure 1, we designed two groups of typical three-layer models with low-resistivity (H-model) and high-resistivity (K-model) layers in the middle with different dip angles. The background resistivity is 100 Ω·m, of which the resistivity of the low-resistivity layer in the H-type model is 10 Ω·m, and the resistivity of the high-resistivity layer in the K-type model is 1,000 Ω·m. A rectangular loop is used for transmission, and the receiving points are located inside the loop with 20 m point spacing. The transmission current is 1 A, and the maximum sampling time is 10 ms. The dB/dt response data of each measuring point is obtained by forward modeling of the 1D model (Figure 2). In the inversion, we add 3% Gaussian white noise to the dB/dt of each time channel.

Figure 2 shows the TEM decay curves at different measuring points of the H and K models with different dip angles. When X = 260 m, the target layer is shallow, while when X = 860 m, the target layer is deep. In Figure 2A, the large amplitude of the low-resistivity layer at middle and late times indicates low-resistivity characteristics. With the increase in burial depth, the early amplitude tends to be consistent with the uniform half space, and the low-resistivity response is significantly delayed. Compared with the uniform half space in Figure 2B, when the high-resistivity layer is buried shallowly, the early time amplitude is small, reflecting the high resistivity. The late time amplitude tends to be consistent, exhibiting the characteristics of the background strata. With the increase in burial depth, the larger amplitude in the early time is the response of the background strata, the smaller amplitude in the middle stage is the response of the high-resistivity stratum,

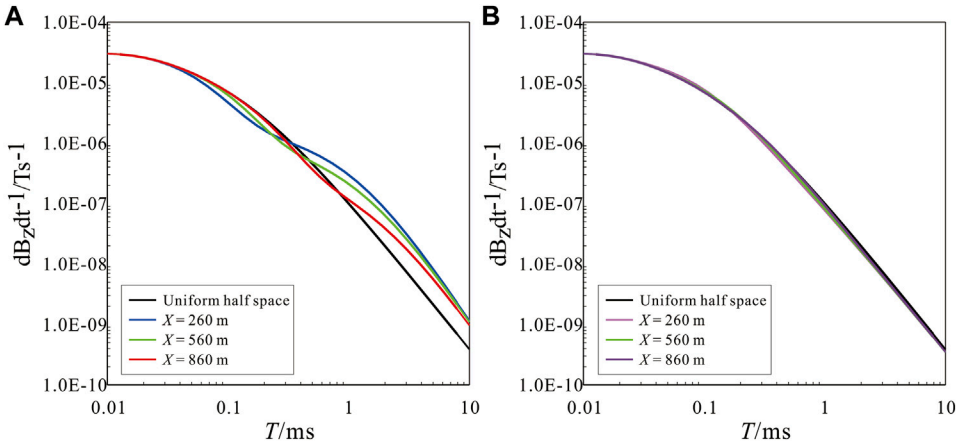

FIGURE 2
Single point decay curves of inclined strata models. **(A)**: H-type model and corresponding uniform half space. **(B)**: K-type model and corresponding uniform half space.

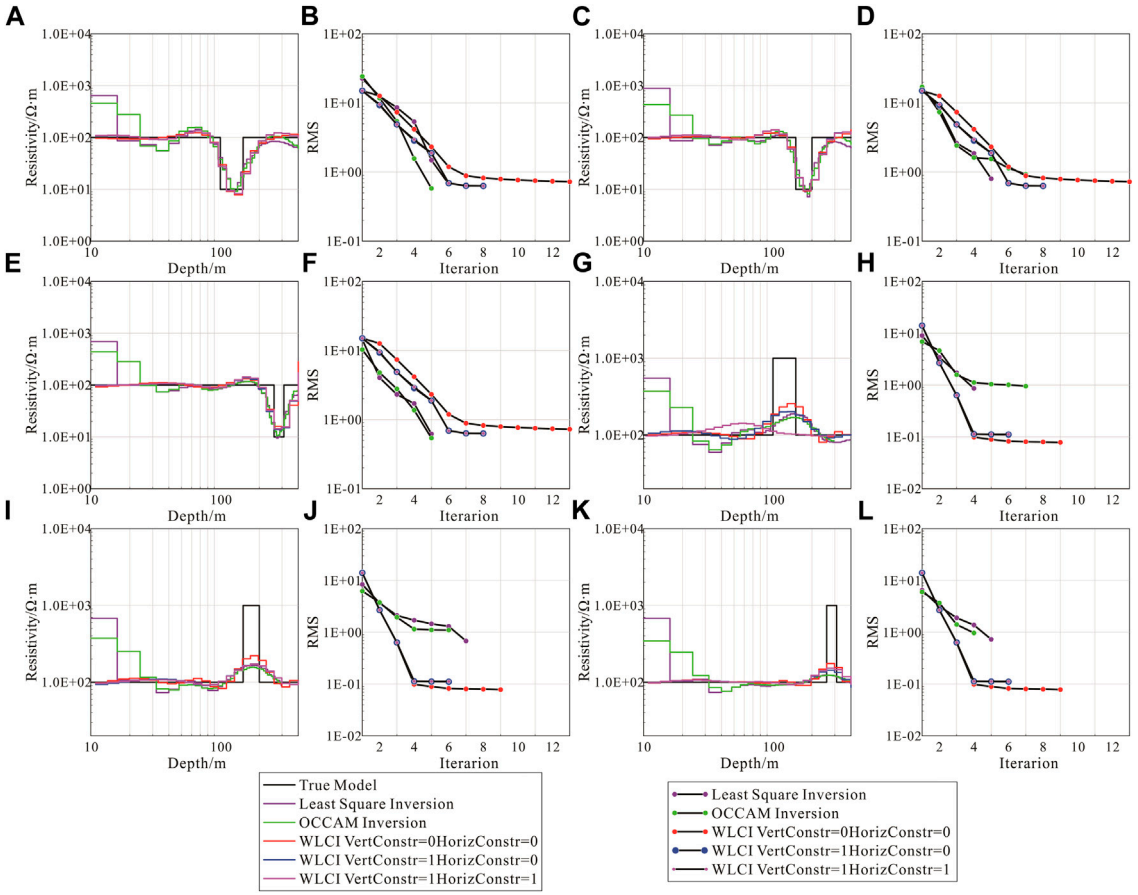

FIGURE 3
Single-point inversion results for different points. **(A)**: Single-point inversion results at X = 260 m of H-type model. **(B)**: The Root Mean Square (RMS) at X = 260 m of H-type model. **(C)**: Single-point inversion results at X = 600 m of H-type model. **(D)**: The RMS at X = 600 m of H-type model. **(E)**: Single-point inversion results at X = 900 m of H-type model. **(F)**: The RMS at X = 900 m of H-type model. **(G)**: Single-point inversion results at X = 260 m of K-type model. **(H)**: The RMS at X = 260 m of K-type model. **(I)**: Single-point inversion results at X = 600 m of K-type model. **(J)**: The RMS at X = 600 m of K-type model. **(K)**: Single-point inversion results at X = 900 m of K-type model. **(L)**: The RMS at X=900 m of K-type model.

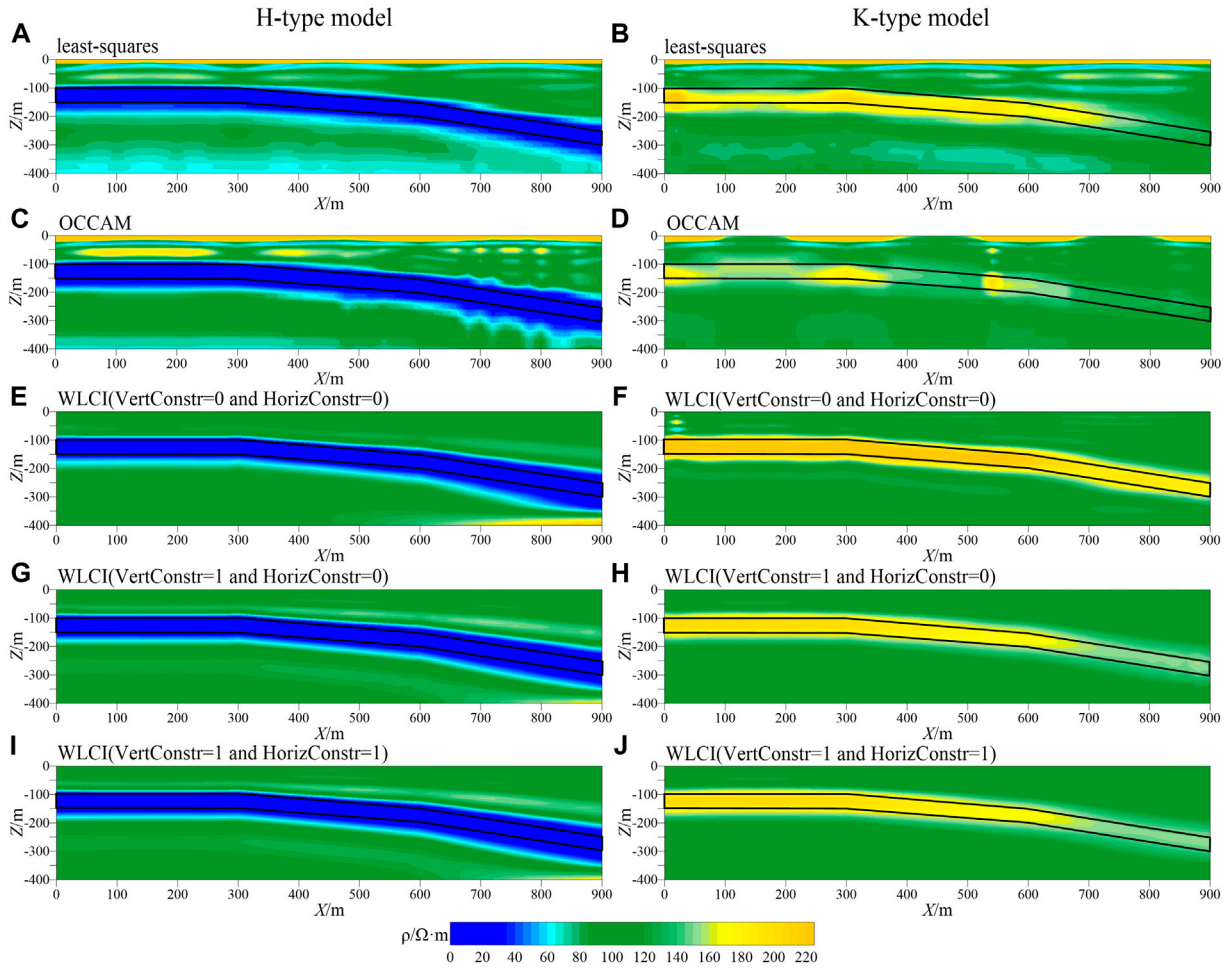

FIGURE 4
Inversion results of H-type and K-type models. **(A)**: least-squares inversion result of H-type model. **(B)**: least-squares inversion result of K-type model. **(C)**: OCCAM inversion result of H-type model. **(D)**: OCCAM inversion result of K-type model. **(E)**: WLCI inversion result of H-type model while vertical constrained factor is 0 and horizontal constrained factor is 0. **(F)**: WLCI inversion result of K-type model while vertical constrained factor is 0 and horizontal constrained factor is 0. **(G)**: WLCI inversion result of H-type model while vertical constrained factor is 1 and horizontal constrained factor is 0. **(H)**: WLCI inversion result of K-type model while vertical constrained factor is 1 and horizontal constrained factor is 0. **(I)**: WLCI inversion result of H-type model while vertical constrained factor is 1 and horizontal constrained factor is 1. **(J)**: WLCI inversion result of K-type model while vertical constrained factor is 1 and horizontal constrained factor is 1.

and the gradual increase in the late stage is close to the response of the background stratum, whereas the amplitude change is not evident.

Figure 3 shows the single-point inversion results of different inversion methods. The initial inversion models are all uniform half space models, and the initial resistivity of the model is 100 Ω·m. In the Occam inversion, the golden section method is used to select the damping factor. For the H-type tilt model, when the local stratum dip is small, the methods shown in Figure 3 better reflect the strata resistivity. When the strata dip is large, there is a significant difference between the resistivity of the shallow part and that of the real model. However, the head end and tail end of the WLCI single-point inversion curve are close to the real resistivity of the first and last layers, which is highly consistent with the actual low-resistivity layer. For the K-type tilt model, the conventional 1D inversion results are poor, the inversion depth of the high-resistivity layer has a large deviation from the given model, and the shallow resistivity is not consistent with the model resistivity. The amplitude characteristics of the high-resistivity layer in the single-point decay curve of the K-type model are not evident, and the horizontal continuity of the data is not considered in the conventional single-point 1D inversion, which is the main reason behind poor inversion results. As a quasi-2D inversion, the WLCI inversion better restores the resistivity distribution of inclined formations by considering the horizontal and vertical continuity of the data.

Comparing the inversion results of different inversion methods in Figure 4, the conventional 1D and WLCI inversions reflect the electrical structure of the three underground layers. When the dip angle of the local layer is small, the conventional 1D inversion results efficiently reflect the low-resistivity layer in the H-type model relatively; however, the layer interface is rough, and the horizontal continuity is poor. In comparison to the least-squares inversion (Figure 4A), the resistivity continuity of the Occam inversion (Figure 4C) is slightly improved. The conventional 1D

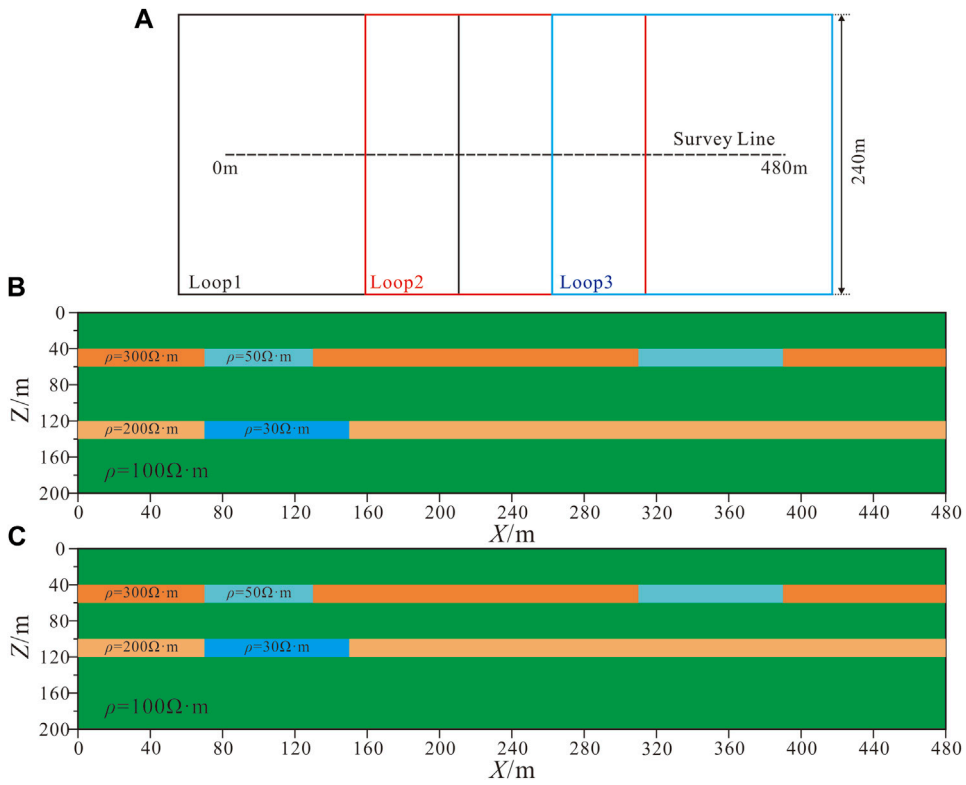

FIGURE 5
Synthetic multilayer models (various colors mean different resistivity in parts B and C). **(A)**: Receiving and transmitting schematic. **(B)**: Model 1 with large layer interval. **(C)**: Model 2 with small layer interval.

inversion has been unable to obtain a continuous high-resistivity layer for the K-type model. The inversion high-resistivity layer becomes thinner, and the resistivity decreases where the burial depth is large. When the dip angle of the local layer is large, the conventional 1D inversion results deviate significantly from the actual model. False anomalies appear in the shallow part of the H-type model (Figure 4A; Figure 4C), the resistivity of the inversion increases, and the layer becomes thicker where the low-resistivity layer is buried deeply. The high-resistivity layer is discontinuous and inconspicuous for the K-type model, and the inversion results can no longer represent the electrical characteristics of the actual formation. The resistivity obtained by the WLCI method is uniformly distributed laterally, and the layer interface is evident and continuous, which better reflects the electrical distribution characteristics of inclined strata. The inversion of the target layer is only slightly thicker than that of the actual model. For the strata with a small dip angle, the size of the constrained factor has little influence on the inversion result. When the size of the constrained factor is increased, the stratum is laterally more continuous. For the strata with a large dip angle, when the size of the constrained factor is increased, there is a certain deviation between the inversion high-resistivity layer and the actual model, although the inversion resistivity is continuous and laterally smooth (Figure 4H; Figure 4J).

We establish multilayered models to verify the effectiveness of the inversion strategy. The models are shown in Figure 5. Two five-layer models with different layer spacings were designed. The background resistivity of the model is 100 Ω·m, the thickness of the high-resistivity layers is 20 m, the resistivity of the upper high-resistivity layer is 300 Ω·m, and the resistivity of the lower high-resistivity layer is 200 Ω·m. The resistivity in the upper high-resistivity layer from 70 to 130 m and 310–390 m along X is 50 Ω·m, and the resistivity in the lower high resistivity layer from 90 to 150 m along X is 30 Ω·m. The burial depth of the upper high-resistivity layer of model 1 is 40 m, the burial depth of the lower interface is 60 m, the burial depth of the upper interface of the lower high-resistivity layer is 120 m, and the burial depth of the lower interface is 140 m. The burial depth of the upper high-resistivity layer of model 2 is 40 m, the burial depth of the lower interface is 60 m, the burial depth of the upper interface of the lower high-resistivity layer is 100 m, and the burial depth of the lower interface is 120 m. The receiving points are located inside the rectangular transmission loop; the distance between the points is 20 m, the transmission current is 1 A, and the maximum sampling time is 10 ms. The dB/dt response data of each measuring point is obtained by forward modeling of the 1D model. In the inversion calculation, 3% Gaussian white noise is added to the dB/dt response at each time.

Figure 6 shows the TEM decay curves at different points. A comparison of Figures 6A–C shows that at X = 40 m, the early and late time amplitudes of Model 1 and 2 are basically consistent with the uniform half space, showing the characteristics of the background strata. The middle time amplitude is small, reflecting the high resistivity. The difference between Model 1 and 2 is not

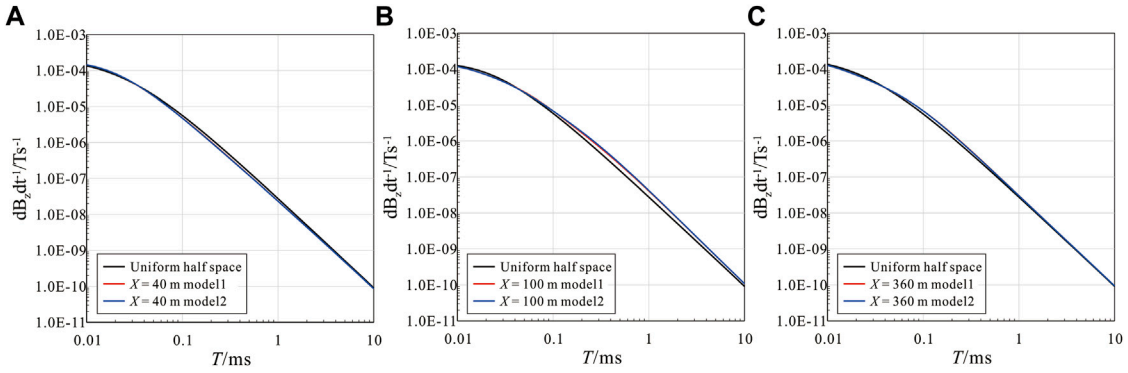

FIGURE 6
Single-point decay curves of synthetic multilayer models and corresponding uniform half space. **(A)**: X = 40 m. **(B)**: X = 100 m. **(C)**: X = 360 m.

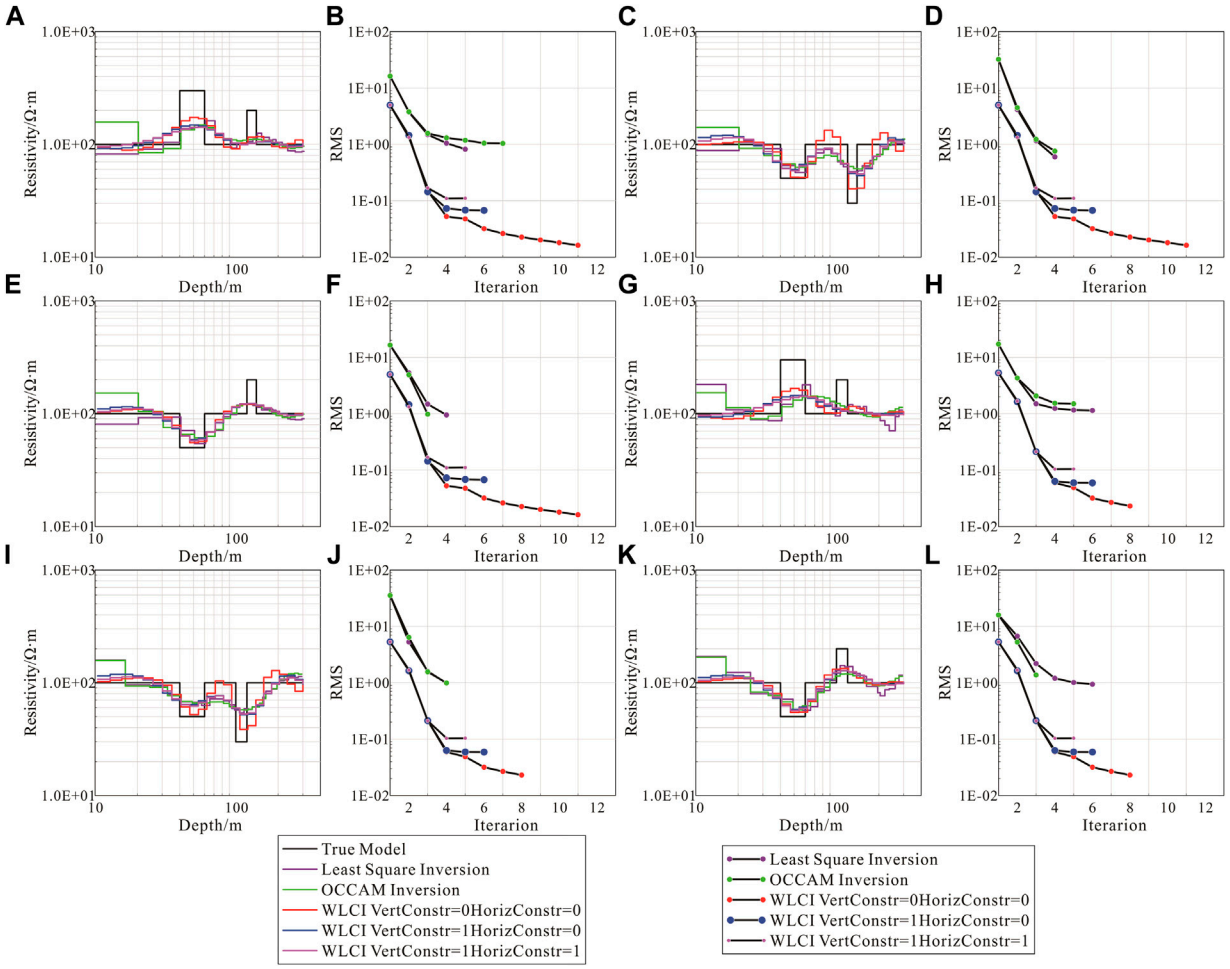

FIGURE 7
Single-point inversion results for different points. **(A)**: Single-point inversion results at X = 40 m of model 1. **(B)**: The Root Mean Square (RMS) at X = 40 m of Model 1. **(C)**: Single-point inversion results at X = 100 m of model 1. **(D)**: The RMS at X = 100 m of model 1. **(E)**: Single-point inversion results at X = 360 m of model 1. **(F)**: The RMS at X = 360 m of model 1. **(G)**: Single-point inversion results at X = 40 m of model 2. **(H)**: The RMS at X = 40 m of model 2. **(I)**: Single-point inversion results at X = 100 m of model 2. **(J)**: The RMS at X = 100 m of model 2. **(K)**: Single-point inversion results at X = 360 m of model 2. **(L)**: The RMS at X = 360 m of model 2.

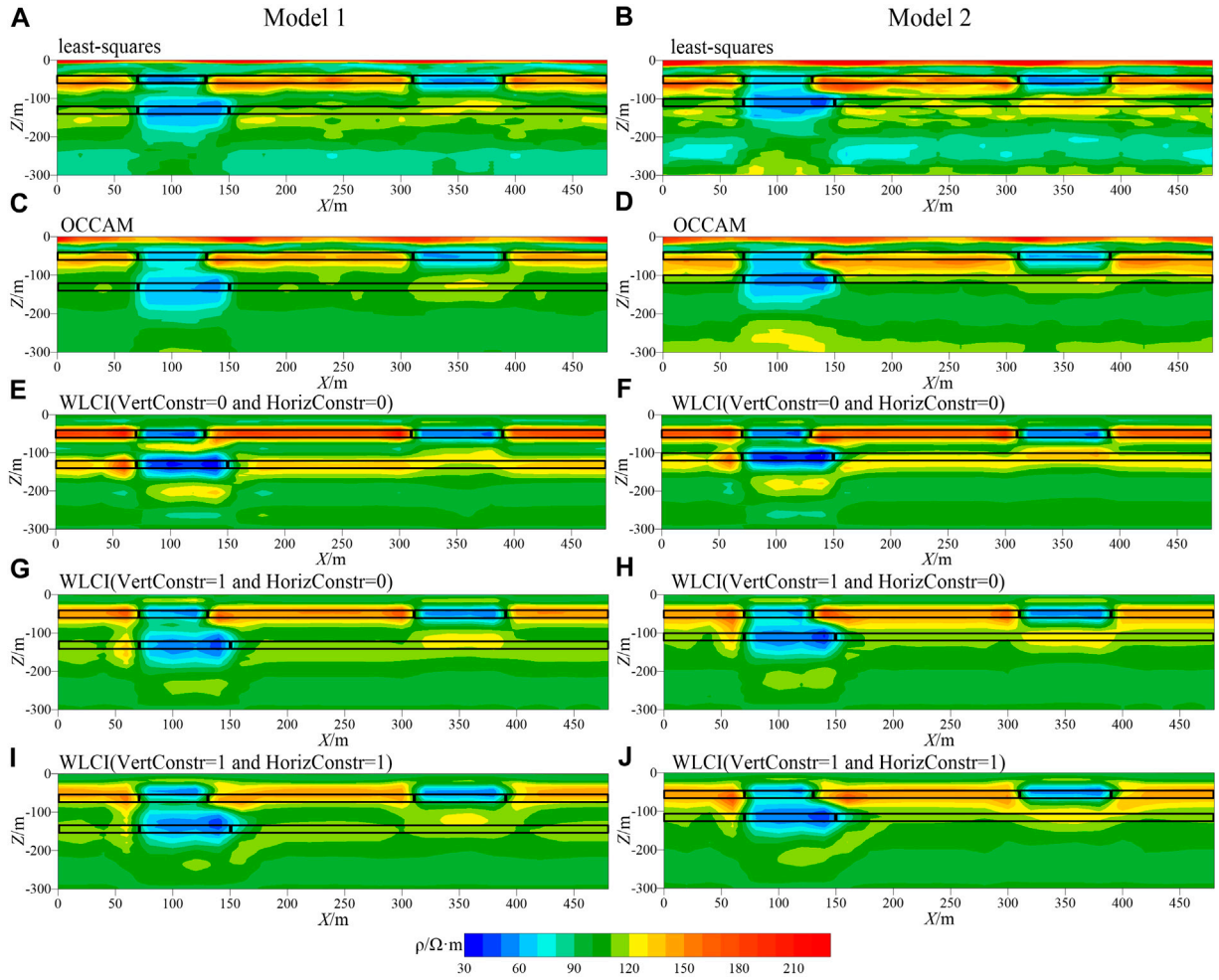

FIGURE 8
Inversion results of Model 1 and Model 2. **(A)**: least-squares inversion result of model 1. **(B)**: least-squares inversion result of model 2. **(C)**: OCCAM inversion result of model 1. **(D)**: Occam inversion result of model 2. **(E)**: WLCI inversion result of model 1 while vertical constrained factor is 0 and horizontal constrained factor is 0. **(F)**: WLCI inversion result of model 2 while vertical constrained factor is 0 and horizontal constrained factor is 0. **(G)**: WLCI inversion result of model 1 while vertical constrained factor is 1 and horizontal constrained factor is 0. **(H)**: WLCI inversion result of model 2 while vertical constrained factor is 1 and horizontal constrained factor is 0. **(I)**: WLCI inversion result of model 1 while vertical constrained factor is 1 and horizontal constrained factor is 1. **(J)**: WLCI inversion result of model 2 while vertical constrained factor is 1 and horizontal constrained factor is 1.

evident; at X = 100 m, the early time amplitudes of Model 1 and 2 is basically consistent with that of the uniform half space, showing the characteristics of the background strata. The middle time amplitude is relatively strong, reflecting the low resistivity. Because the lower low-resistivity layer is shallower in Model 2, the low-resistivity response is more evident than that of Model 1 and appears at an earlier time. The late time response gradually increases, approaching the response of the background strata. At X = 360 m, the early and late time amplitudes of Model 1 and 2 are basically consistent with the uniform half space, showing the characteristics of the background strata. The middle time amplitude is strong, reflecting the low resistivity. There is little difference between Model 1 and 2. The single-point least-squares method, Occam method, and different horizontal and vertical constraints are used for inversion calculation. The single-point inversion results of different models and different measuring points are shown in Figure 7.

The initial inversion models are all uniform half space models, and the initial resistivity of the models is 100 Ω·m while using different methods to inverse the synthetic multilayer models in Figure 7. We also use the golden section method to select the damping factor with the Occam inversion. When the layer spacing is large, all the inversion methods labeled in Figure 7 can better reflect the low-resistivity layer in the model, and the layer interface is relatively clear. When there are two high-resistivity layers (Figure 7A), the conventional 1D inversion effect is poor, and the interface of the high-resistivity layer is unclear. By reducing the layer spacing, each method can still restore the low-resistivity layer, whereas the layered interface is difficult to distinguish. The Occam method can only inverse the

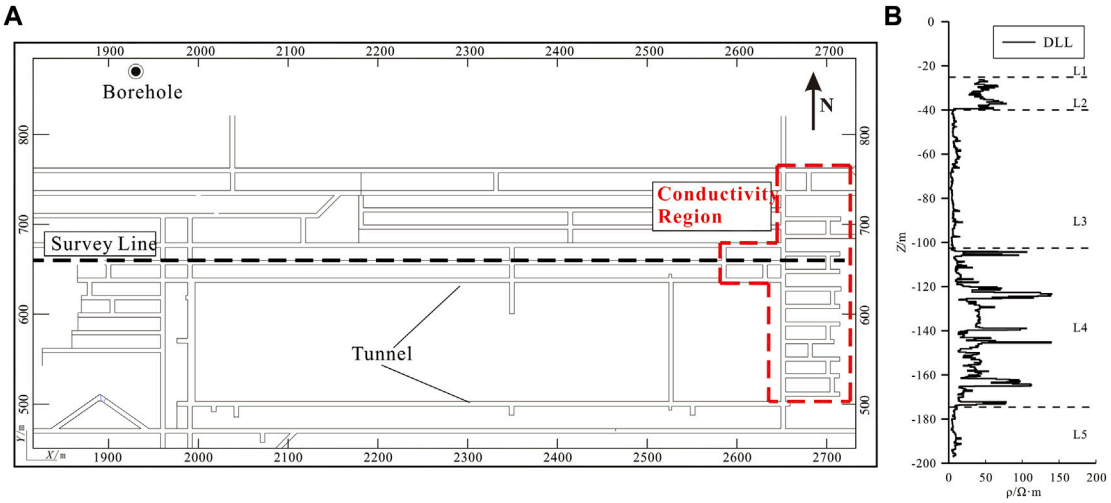

FIGURE 9
Priori information. **(A)**: Extraction engineering diagram. **(B)**: Borehole Dual Lateral Logging (DLL) data of resistivity.

upper high-resistivity layer when there are two high-resistivity layers (Figure 7G). With the WLCI inversion strategy, the inversion effect of the five-layer model is good, and the low-resistivity layer interface is clear. However, after the horizontal and vertical constrained factors are applied, the inversion effect of the two high-resistivity layers is poor, and it is difficult to distinguish the lower high-resistivity layer.

A comparison of the results of different inversion methods (Figures 8A–J) shows that when the layer spacing is large, all methods better restore the low-resistivity segments in each high-resistivity layer; however, the lower high-resistivity layer inverted by the least-squares and Occam methods is transversely discontinuous. The resistivity inverted by the Occam method is smooth, but it cannot restore the lower high-resistivity layer. When the layer spacing is reduced, the continuity of the lower high-resistivity layer is poor (Occam cannot inverse the lower high-resistivity layer), and two layers of low resistivity cannot be distinguished vertically. Using the WLCI strategy, when the applied horizontal and vertical constrained factors are zero, the multilayer model can be better restored. The resistivity is more continuous in the horizontal direction, and the layer interface is clear. Increasing the constraint factor makes the resistivity more continuous in the horizontal and vertical directions. Reducing the layer spacing while increasing the constraint factors makes the inversion resistivity more continuous, but the vertical resolution decreases and cannot clearly restore the lower high-resistivity layer.

According to the synthetic model inversion results in this work, the WLCI strategy with different horizontal and vertical constrained factors is verified as effective for inversion, producing results that are laterally continuous with high vertical resolution. For sedimentary strata inversion, we must select smaller constrained factors.

4 Field data inversion

To further verify the effectiveness of the inversion strategy and the selection of weighting factors for field data inversion processing, we selected measured data collected in a region of Inner Mongolia. The data of 101 measuring points from 720 to 2,720 m of Line 35 were used for inversion calculation (Figure 9A); the distance between measuring points is 20 m. The tunnels of the #2 coal seam on the east side of the survey line have been closed and filled with mine water and soil. This is a known low-resistivity area (the range delineated by the red dotted line in Figure 9A).

The electrical distributions of the strata in this area are clearly shown in Figure 9B. With the exception of the shallow part above 30 m, the electrical distribution of the remaining strata from shallow to deep alternates from high-to low-resistivity in two cycles, as the L2 to L5 formations show in Figure 9B. According to the relevant geological information, the shallow part of the strata (L1) is approximately 30 m, including the Quaternary, Neogene and Upper Cretaceous Zhidan Group. The rocks of L1 include grayish-yellow and brownish-yellow alluvial and proluvial sand and gravel with low resistivity, dark red mudstone, and sandy mudstone mixed with fine sandstone, such that the L1 formation has low resistivity. According to logging and geological data, the resistivity characteristics of formations L2 to L5 are as follows. L2: Composed of the bottom part of the Cretaceous Zhidan Group, the formations are grayish-green and light-red conglomerates characterized by high resistivity; L3: Zhiluo Formation of the Upper Jurassic strata is grayish-white and grayish-green, medium-to coarse-grained sandstone and pebbly coarse-grained sandstone mixed with siltstone and sandy mudstone presenting low resistivity; L4: The top of the Jurassic Yan'an Formation with coal seams (the #2 coal seam is located in its upper part) and nearby rock that are characterized with high resistivity; L5: The bottom of the Jurassic Yan'an Formation, with coarse sandstone and sandy

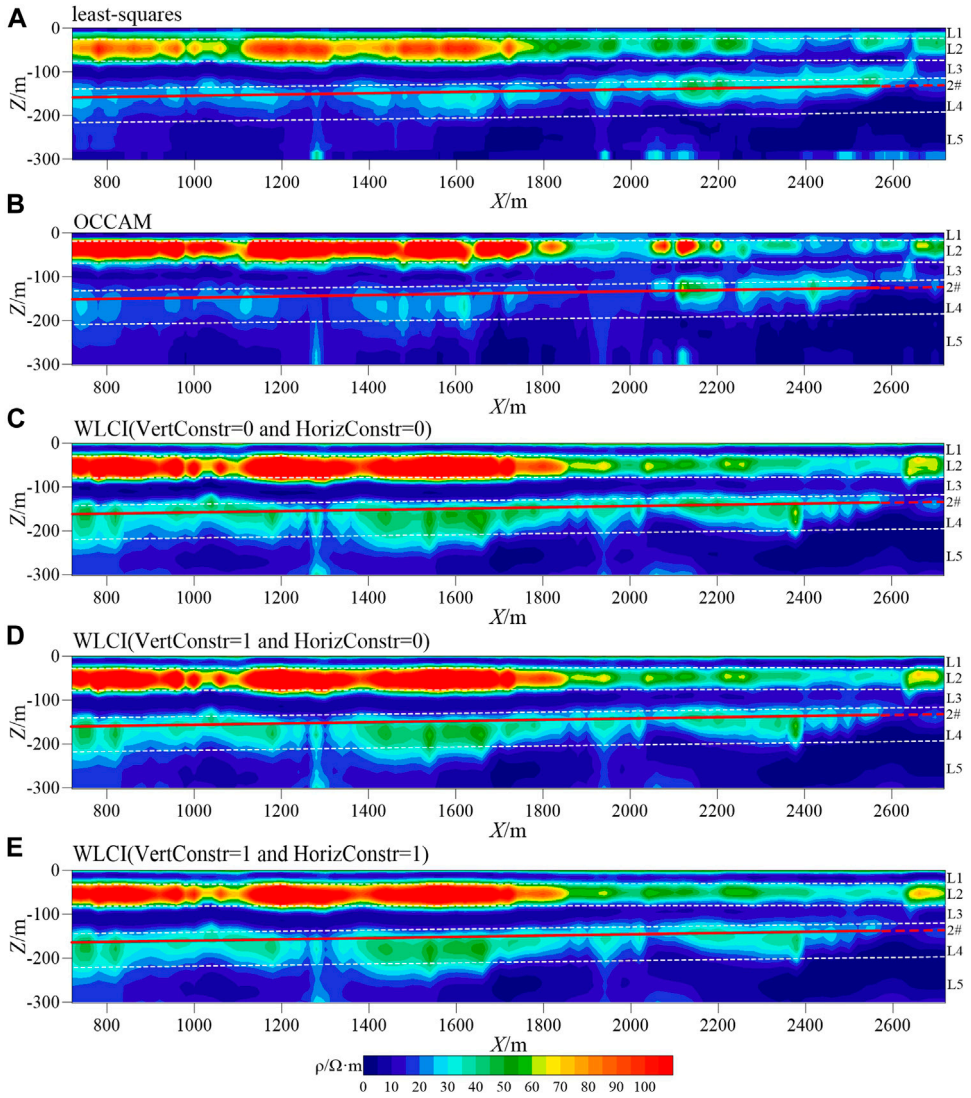

FIGURE 10
Field data inversion results. **(A)**: least-squares inversion result. **(B)**: Occam inversion result. **(C)**: WLCI inversion result while vertical constrained factor is 0 and horizontal constrained factor is 0. **(D)**: WLCI inversion result while vertical constrained factor is 1 and horizontal constrained factor is 0. **(E)**: WLCI inversion result while vertical constrained factor is 1 and horizontal constrained factor is 1.

mudstone and good conductivity. In summary, the strata in this area are characterized by five layers.

We use the least-squares, Occam, and WLCI methods to perform inversion calculations on the measured data. The calculation results are shown in Figure 10. The solid red lines in the figure represent the #2 coal seam. The initial model for the inversion calculation is 31 layers. The resistivity of the initial model for least-squares and Occam inversion is 30 Ω·m, and the resistivity of the initial model for WLCI inversion is 100 Ω·m. Figure 10A shows the single-point least squares inversion results, Figure 10B shows the Occam one-dimensional inversion results, and Figures 10C–E show the inversion results using different horizontal and vertical constrained factors. Figure 10 shows that the single-point least squares inversion, Occam 1D inversion, and WLCI inversion all reflect the resistivity structure of the five underground layers (L1 to L5) with good stratification that reflects the characteristics of the sedimentary strata, and the inversion of the electrical distribution characteristics is consistent with the borehole resistivity logging results. The inversion results in Figures 10A,B are basically consistent. The resistivity distribution of the Occam 1D inversion is more continuous than the least-squares inversion result, but the lower high-resistivity layer (L3) of the Occam inversion is discontinuous, and the layer interface is not clear. Figures 10C–E adopt the WLCI method, and the inversion results are basically consistent. The lateral continuity of the inversion results has been significantly improved. The lower high-resistivity layer is continuous, and the interface is clear. After increasing the constrained factor, the inversion resistivity is more continuous and smoother, but the difference between the WLCI inversion results for each layer is small. The red dotted line (2,600–2,720 m) on the east side of Figure 9B shows the characteristics of low resistivity, which is consistent with the known low-resistivity area.

Therefore, for sedimentary strata, we conclude that the laterally constrained inversion strategy with different constrained factors in the horizontal and vertical directions can improve the continuity of the inversion profile and improve the vertical resolution simultaneously, making it possible to identify the layer interface. In the actual inversion, smaller constrained factors must be selected.

5 Conclusion

We successfully implemented the WLCI inversion, optimized the constrained factors, and tested it with synthetic and field data sets. Numerical experiments show that compared with the conventional 1D inversion, this new method can improve the vertical resolution by ensuring the continuity of the lateral resistivity distribution, and the inversion layer interface becomes more clear. The underground electrical structure of adjacent measuring points in the sedimentary strata is relatively continuous. Notably, the constrained factors have evident impacts on the inversion results. Small constrained factors will make the constraint less effective. On the contrary, large constrained factors may lead to serious horizontal resistivity averaging, which may eliminate real anomalies. For quasi-horizontally layered sedimentary strata, the selection of constrained factors must not be excessively large. In actual inversion, appropriate constrained factors can be determined by referring to borehole or other relevant geological data. These numerical results prove that as a quasi-2D inversion method, WLCI is effective in imaging a thin and continuous coal seam and provides a more reasonable initial model for 3D inversion.

Data availability statement

The raw data supporting the conclusion of this article will be made available by the authors, without undue reservation.

Author contributions

CS, BZ, and YL contributed to conception and design of the study. CS contributed to build the synthetic model and inversion. YL contributed to the synthetic and field data analysis. CL and GM contributed to the discussion of the results. CS wrote the first draft of the manuscript. All authors read and approved the final manuscript.

Funding

This research is funded by the National Natural Science Foundation of China (42174167, 42074120).

Acknowledgments

We thank Yang Su and Laonao Wei for their useful advice through the research.

Conflict of interest

The authors declare that the research was conducted in the absence of any commercial or financial relationships that could be construed as a potential conflict of interest.

Publisher's note

References

Auken, E., Christiansen, A. V., Jacobsen, L. H., and Sørensen, K. I. (2008). A resolution study of buried valleys using laterally constrained inversion of TEM data. *J. Appl. Geophys.* 65 (1), 10–20. doi:10.1016/j.jappgeo.2008.03.003

Auken, E., and Christiansen, A. V. (2004). Layered and laterally constrained 2D inversion of resistivity data. *Geophysics* 69 (3), 752–761. doi:10.1190/1.1759461

Auken, E., Thomsen, P., and Sorensen, K. (2000). "Lateral constrained inversion (LCI) of profile-oriented data—the resistivity case," in Proceedings of the 6th EAGE/EEGS Meeting, Bochum, Germany, September 2000, EL06.

Cai, J., Qi, Y., and Yin, C. (2014). Weighted laterally-constrained inversion of frequency-domain airborne EM data. *Chin. J. Geophys.* 57 (3), 953–960.

Christensen, N. B., Reid, J. E., and Halkjær, M. (2009). Fast, laterally smooth inversion of airborne time-domain electromagnetic data. *Near Surf. Geophys* 7 (5–6), 599–612. doi:10.3997/1873-0604.2009047

Constable, S. C., Parker, R. L., and Constable, C. G. (1987). Occam's inversion; a practical algorithm for generating smooth models from electromagnetic sounding data. *Geophysics* 52 (3), 289–300. doi:10.1190/1.1442303

Danielsen, J. E., Auken, E., Jørgensen, F., Søndergaard, V., and Sørensen, K. I. (2003). The application of the transient electromagnetic method in hydrogeophysical surveys. *J. Appl. Geophys.* 53, 181–198. doi:10.1016/j.jappgeo.2003.08.004

Farquharson, C., and Oldenburg, D. (1993). Inversion of time-domain electromagnetic data for a horizontally layered Earth. *Geophys. J. Int.* 114, 433–442. doi:10.1111/j.1365-246x.1993.tb06977.x

Fitterman, D. V., and Stewart, M. T. (1986). Transient electromagnetic sounding for groundwater. *Geophysics* 51, 995–1005. doi:10.1190/1.1442158

Fountain, D., Smith, R., Payne, T., and Limieux, J. (2005). *A helicopter time domain EM system applied to mineral exploration: System and data*, 23. doi:10.3997/1365-2397.23.1089.26741*First Break*

Guptasarma, D. (1982). Computation of the time-domain response of a polarizable ground. *Geophysics* 47 (11), 1574–1576. doi:10.1190/1.1441307

Haber, E., and Schwarzbach, C. (2014). Parallel inversion of large-scale airborne time-domain electromagnetic data with multiple OcTree meshes. *Inverse Probl.* 30 (5), 55011. doi:10.1088/0266-5611/30/5/055011

Huang, H., and Palacky, G. J. (2010). Damped least-squares inversion of time-domain airborne EM data based on singular value decomposition. *Geophys. Prospect.* 39 (6), 827–844. doi:10.1111/j.1365-2478.1991.tb00346.x

Hui, Z., Liu, Y., Yin, C., Su, Y., Ren, X., Zhang, B., et al. (2021). Detection of coal spontaneous combustion using the TEM method: A synthetic study. *Pure Appl. Geophys.* 178 (4), 3987–4000. doi:10.1007/s00024-021-02829-5

Jiang, Z., Liu, L., Liu, S., and Yue, J. (2019). Surface-to-underground transient electromagnetic detection of water-bearing goaves. *IEEE Trans. Geosci. Remote Sens.* 57 (8), 5303–5318. doi:10.1109/tgrs.2019.2898904

Johansen, H. K., and Sorensen, K. (1979). Quasi fast Hankel transform. *Geophys. Prospect.* 27, 876–901. doi:10.1111/j.1365-2478.1979.tb01005.x

Liu, Y., Yin, C., Qiu, C., Hui, Z., Zhang, B., Ren, X., et al. (2019). 3D inversion of transient EM data with topography using unstructured tetrahedral grids. *Geophys. J. Int.* 217 (1), 301–318. doi:10.1093/gji/ggz014

Lu, J., Lei, D., and Ren, H. (2022). Laterally constrained inversion of airborne transient electromagnetic data with induced-polarization effects. *Prog. Geophys. (in Chinese)* 37 (1), 0220–0229. doi:10.6038/pg2022FF0045

Nabighian, M. N. (1979). Quasi-static transient response of a conducting half-space - an approximate representation. *Geophysics* 44, 1700–1705. doi:10.1190/1.1440931

Ren, X. Y., Yin, C. C., Macnae, J., Liu, Y. H., and Zhang, B. (2018). 3D time-domain airborne electromagnetic inversion based on secondary field finite-volume method. *Geophysics* 83, E219–E228. doi:10.1190/geo2017-0585.1

Santos, F. A. M. (2004). 1-D laterally constrained inversion of EM34 profiling data. *J. Appl. Geophys.* 56 (2), 123–134. doi:10.1016/j.jappgeo.2004.04.005

Si, Y., Li, M., Liu, Y., and Guo, W. (2020). One-dimensional constrained inversion study of TEM and application in coal goafs' detection. *Open Geosci* 12 (1), 1533–1540. doi:10.1515/geo-2020-0148

Siemon, B., Auken, E., and Christiansen, A. V. (2009). Laterally constrained inversion of helicopter-borne frequency-domain electromagnetic data. *J. Appl. Geophys.* 67 (3), 259–268. doi:10.1016/j.jappgeo.2007.11.003

Stacey, W. M. (1976). "Transient electromagnetic fields," in *Section 1.2: Field equations and boundary conditions* (Berlin, Germany: Springer-Verlag), 5–6.

Yang, D., and Oldenburg, D. W. (2012). Three-dimensional inversion of airborne time-domain electromagnetic data with applications to a porphyry deposit. *Geophysics* 77, B23–B34. doi:10.1190/geo2011-0194.1

Yang, H., Li, F., Yue, J., Liu, X., Zhao, H., Zhan, J., et al. (2016). Molecular cloning, expression, and functional analysis of the copper amine oxidase gene in the endophytic fungus Shiraia sp. Slf14 from Huperzia serrata. *J. China Univ. Mining Technol.* 45 (6), 8–13. doi:10.1016/j.pep.2016.07.013

Yin, C., Qiu, C., Liu, Y., and Cai, J. (2016). Weighted laterally-constrained inversion of time-domain airborne electromagnetic data. *J. Jilin Univ. (Earth Sci. Ed.)* 46 (1), 254–261.

Zhang, B., Engebretsen, K. W., Fiandaca, G., Cai, H., and Auken, E. (2021). 3D inversion of time-domain electromagnetic data using finite elements and a triple mesh formulation. *Geophysics* 86 (3), E257–E267. doi:10.1190/geo2020-0079.1

Zhang, J., Zhou, G., Liu, Z., Sun, N., Zhang, F., and Wang, Z. (2022). Lateral constrained inversion of E-Ex wide field data. *J. China Coal Soc.* 47 (7), 2698–2707.

frontiers | Frontiers in Earth Science

TYPE Methods
PUBLISHED 06 June 2023
DOI 10.3389/feart.2023.1158702

OPEN ACCESS

EDITED BY
Cong Zhou,
East China University of Technology, China

REVIEWED BY
Ruiheng Li,
Chongqing University, China
Linjiang Qin,
Ministry of Natural Resources, China

*CORRESPONDENCE
Jianke Qiang,
qiangjianke@163.com

RECEIVED 08 February 2023
ACCEPTED 22 May 2023
PUBLISHED 06 June 2023

CITATION
Tian H, Qiang J, Li K, Tan Z, Zhang Y and Zhu D (2023), Wide field electromagnetic method calculation in arbitrary orientation and its effectiveness analysis. *Front. Earth Sci.* 11:1158702. doi: 10.3389/feart.2023.1158702

Wide field electromagnetic method calculation in arbitrary orientation and its effectiveness analysis

Hongjun Tian[1,2], Jianke Qiang[1,2]*, Kun Li[3], Zhangkun Tan[4], Ying Zhang[1,2] and Dexiang Zhu[1,2]

[1]Key Laboratory of Metallogenic Prediction of Non-ferrous Metals and Geological Environment Monitoring, Ministry of Education, Central South University, Changsha, China, [2]School of Geosciences and Info-Physics, Central South University, Changsha, China, [3]School of Geosciences and Technology, Southwest Petroleum University, Chengdu, China, [4]Sichuan Zhongcheng Coal Field Geophysical Engineering, Research Institute Co., Ltd., Chengdu, China

The wide field electromagnetic method E_E_x observation method requires the horizontal electrical field source (AB) to be parallel to the measure station (MN), but the complex terrain conditions make it difficult to meet the AB parallel MN in field construction, and there is always an azimuthal difference α between them, which will bring a large calculation error and cause distortion of the interpretation parameters if the calculation method E_E_x continues to be used. In order to tackle this problem, we analyse and study the E_E_x method and derive the new calculation method of E_E_{MN} for the wide field electromagnetic method along the MN (E_E_{MN}). The method is based on the intrinsic relationship between the electric field components E_x, E_y and the azimuthal difference α and derives the expression for the electric field E_E_{MN} along the MN direction, and then uses the E_E_{MN} to calculate the wide field apparent resistivity. In this paper, we design a three-layer geoelectric model and calculate the azimuthal angle difference α = 0° and α = 15°wide field apparent resistivity parameters, respectively. The results show that the relative error between the calculated apparent resistivity and the theoretical value is less than 1%, which verifies the correctness and validity of the method. To further verify the accuracy of the method, experimental work on azimuthal difference α was carried out next to a known well in Sichuan. The results show that: firstly, when α is 1°, 3°, 5°, 10°, and 15°, respectively, the relative error of each frequency point increases with α increasing. Secondly, when α is 1°, 3°, 5°, 10°, and 15°, respectively, the relative error of each frequency point is less than 10% when the E_{MN} method is used to calculate the wide field apparent resistivity value; thirdly, taking α = 15° as an example, single-station inversions are performed with E_x and E_{MN} apparent resistivity parameters, in which the E_x inversion results are more different from the trend of the logging curve, while the E_{MN} inversion results are relatively more consistent with the trend of the logging curve. The arbitrary orientation E_{MN} calculation method proposed in this paper can effectively reduce the influence of α on the interpretation parameters and improve the accuracy of interpretation, and also greatly expand the applicability and flexibility of E_x wide field electromagnetic method in the observation of complex terrain areas, which has important theoretical research and practical production significance.

KEYWORDS

electromagnetic prospecting, controlled source electromagnetic, wide field electromagnetic method, azimuth angle correction, accuracy and validity

1 Introduction

The electromagnetic induction method is an important branch of geophysical-electrical exploration, which mainly uses the differences in electrical conductivity, permeability and dielectricity of the subsurface medium and applies the principle of electromagnetic induction to observe and study the distribution patterns (frequency characteristics and temporal characteristics) of artificial or naturally occurring electromagnetic fields and thus solve relevant geological problems (Tikhonov, 1950; Cagniard, 1953; He, 2010a; He, 2019; Chen et al, 2014a). Therefore, studying the frequency response of the earth to electromagnetic fields can obtain the distribution pattern of the resistivity of the subsurface medium at different depths (Zonge, 1991; He, 2019; He, 2020; Liu et al, 2019; Liu et al, 2022; Li et al, 2023). In electrical exploration, the electromagnetic field itself has interference and resonance phenomena, which complicates the characteristics of the field. By introducing an appropriate definition of apparent resistivity, highlighting the useful information and suppressing the interference information can help us make good analysis and judgment of the observation results, which is beneficial to the inverse interpretation, so the study of the definition of apparent resistivity is meaningful (Yin et al, 1991a; Liu et al, 2013; Chen, 2014b).

There are several resistivity definition methods in the frequency domain EM method, which are mostly based on the uniform half-space model (Spies, 1986; Yin et al, 1991b; Tang et al, 2005). ТИхонов (1950) and Cagniard (1953) separately and independently proposed the Magnetotelluric (MT), which defined the apparent resistivity by a pair of orthogonal component electric field to magnetic field ratios, and established the apparent resistivity as the interpretation parameter. Goldstein (1971) proposed controlled source audio Magnetotelluric method (CSAMT), which replaced natural source with a controlled source. However, there is a complex implicit function relationship between the uniform half-space surface electromagnetic field values and resistivity in the controlled source frequency domain electromagnetic method, and it is difficult to find the explicit inverse function between resistivity and field by analytical methods (He, 2010a; Li et al, 2013), Therefore, the complex high-order function in the field is abandoned, and the MT method is used to define the apparent resistivity parameter. Therefore, the near zone, mid-zone, and wave zone were divided according to the variation properties of the electromagnetic field (Yin et al, 1991a; Liu et al, 2013), and the approximate definition of the apparent resistivity in the wave zone was adopted, resulting in serious distortion of the apparent resistivity in the mid-zone and near zone, which affects the interpretation of the sounding curve (Yin et al, 1991b; Liu et al, 2013; Cheng et al, 2014b; Tang et al, 1994; Tang, 1993).

In order to unify the wave zone, mid-zone and near zone, a full-zone apparent resistivity is defined, which can reflect the vertical electrical variation of the geoelectric section directly and also expand the controlled source observation zone (Cao, 1978; Huang et al, 1992; Tang et al, 1993; Tang et al, 1994). Yin et al (1991a) pointed out that the definition of full-zone apparent resistivity can reflect information of the geoelectric section more realistically than other approximate definitions and is less influenced by the pole distance. Fang et al (1992) compared the exact formula of uniform half-space field with the formula of the wave zone to obtain a correction coefficient K, and multiplied the apparent resistivity defined in the wave zone by the correction coefficient K to obtain the apparent resistivity value defined in the full zone. This method is simple and easy to implement. Mao and Bao (1996) proposed a direct algorithm for the full-zone apparent resistivity, which is a concise and accurate method. Tang and He (2005) analyzed and compared in detail the differences and similarities of apparent resistivity defined by wave zone and full zone. He (2010b) proposed the wide field electromagnetic sounding method based on the analytic expressions of electromagnetic fields of horizontal current sources and vertical magnetic sources at the ground in semi-uniform space, and proposed the use of computers to realize the calculation of wide field apparent resistivity using the iterative method or the inverse interpolation method. The wide field apparent resistivity calculated by the inverse interpolation method and the iterative method both correctly reflect the electrical variation properties of the subsurface medium, whice completely reflects the opposition and unity of the controlled source frequency electromagnetic field, and more intuitively reflect the objective variation of the geoelectric section with depth (Yu, 2010; Wang et al, 2012, 2013; Yuan et al, 2020). The direct integration method proposed by Dai (2020) can be widely applied to the calculation of electromagnetic fields at different frequencies and different transceiver distances, which has a strong universality. Li (2017) pointed out that the distribution and variation pattern of E_E_x and E_E_φ wide field apparent resistivity with azimuth was determined by the propagation and distribution characteristics of E_E_x and E_E_φ and did not change depending on the definition of apparent resistivity. Yin (1991a) found that the apparent resistivity response was affected by the radial angle, and the effect occured mainly in the mid and near zone, with the mostly serious effect in the near zone, but it was not affected in the wave zone. Liu et al (2013) eliminated the influence of observation orientation by the improved method of E_E_φ wide field apparent resistivity definition, which could intuitively and truly reflect the objective variation of geoelectric section with depth. Wang et al (2021) derived the resistivity expression for the ground-well frequency-domain wide field electromagnetic method from the theory of frequency domain electromagnetic method, and the technique was successfully applied in a super-large metal mine. The above literature is based on the assumption that the AB is parallel to the MN, and discusses how to define the apparent resistivity or discuss the radial angle affects the apparent resistivity parameter, but the effect of the azimuth angle difference α between the AB and MN to the observed data is rarely studied. Due to the influence of terrain conditions, it is often difficult to make the current source AB parallel to the observation dipole MN, and there is always a certain azimuth angle difference α between them. How to define the apparent resistivity expression accurately and effectively so that the interpreted parameters can reflect the geoelectric cross-section information more truly? This paper takes E_E_x wide field electromagnetic method as an example, combining the theoretical model and field measurement data to analyze and study the impact of azimuth angle difference on the observation results, so as to put

forward the calculation method of arbitrary azimuth wide field electromagnetic method E_E_{MN}. Firstly, based on the intrinsic relationship between the electric field components E_x, E_y and the azimuthal difference α, we derive the expression of electric field E_{MN} along the MN direction. Secondly, a three-layer geoelectric model is designed to compare and analyze the E_E_x and E_E_{MN} apparent resistivity parameters corresponding to the azimuthal difference α, so as to verify the algorithm in this paper; Finally, in order to further analyze and study the influence of α on the observation data and interpretation results, the field experiments are carried out next to a known well in Sichuan Province, China. The results show that the relative error of the apparent resistivity of E_E_x increases with the increase of α, and when the α reaches 10° and 15°, the relative error is more than 100%, and the geoelectric information reflected by the same measurement point is seriously distorted, and the inversion results are different from the change trend of the logging curve; the E_E_{MN} method effectively reduces the influence of α on the apparent resistivity parameters, and more effectively reflects the real geoelectric structure information of the subsurface. The E_E_{MN} calculation method effectively reduces the influence of α on the apparent resistivity parameter, and more effectively reflects the real geoelectric structure information in the subsurface. Using the method of arbitrary azimuth E_E_{MN} can effectively weaken the influence of azimuth difference α on the interpreted parameters, which is convenient to reduce the requirement of electric couple source azimuth layout in practical work in the future, and has important theoretical research and practical application significance.

2 Basic theory

2.1 Wide field electromagnetic method E_E_x

Under quasi-static conditions, the receiver MN remains parallel to the current source AB, i.e., the angular difference between AB and MN is $\alpha = 0°$. Set the harmonic factor $e^{i\omega t}$, where $i = \sqrt{-1}$, $\omega = 2\pi f$ is the angular frequency, and t is time. The analytical expressions for the horizontal components E_x and E_y in the laminar medium are written as (He, 2010b)

$$\begin{cases} E_x = \dfrac{IdL}{2\pi}\left(2\cos^2\varphi - 1\right)\int_0^\infty \dfrac{i\omega\mu}{r}\dfrac{R_N}{mR_N + m_1}J_1(mr)dm - \dfrac{IdL\rho_1\cos^2\varphi}{2\pi} \\ \qquad \int_0^\infty \dfrac{mm_1}{R_N^*}J_0(mr)dm \\ \quad + \dfrac{IdL}{2\pi}\left(2\cos^2\varphi - 1\right)\int_0^\infty \dfrac{\rho_1}{r}\dfrac{m_1}{R_N^*}J_1(mr)dm + \dfrac{IdL\sin^2\varphi}{2\pi} \\ \qquad \int_0^\infty i\omega\mu\dfrac{R_N}{mR_N + m_1}J_0(mr)dm \\ E_y = \dfrac{IdL\sin 2\varphi}{2\pi}\int_0^\infty \dfrac{i\omega\mu}{r}\dfrac{R_N}{mR_N + m_1}J_1(mr)dm + \dfrac{IdL\sin 2\varphi}{2\pi} \\ \qquad \int_0^\infty \dfrac{\rho_1}{r}\dfrac{m_1}{R_N^*}J_1(mr)dm \\ \quad - \dfrac{IdL\rho_1\sin 2\varphi}{2\pi}\int_0^\infty \dfrac{mm_1}{R_N^*}J_0(mr)dm - \dfrac{IdL\sin 2\varphi}{2\pi} \\ \qquad \int_0^\infty i\omega\mu\dfrac{R_N}{mR_N + m_1}J_0(mr)dm \end{cases} \tag{1}$$

Where I is Current; dL is electric dipole; r is distance between the receiving point and the center point of the electric dipole; J_1 and J_0 are 1st and 0th order Bessel functions respectively; R_N is the first layer factor; R_N^* is the second layer factor.

$$\begin{aligned} R_N &= \mathrm{cth}\left|m_1h_1 + \mathrm{cth}^{-1}\left|\frac{m_1}{m_2}\mathrm{cth}\left\{\left[m_2h_2\right.\right.\right.\right. \\ &\quad \left.\left.\left.\left. + \mathrm{cth}^{-1}\left[\frac{m_2}{m_3}\mathrm{cth}\left[m_3h_3 + \cdots + \mathrm{cth}^{-1}\left(\frac{m_{N-1}}{m_N}\right)\right]\right]\right\}\right|\right| \\ R_N^* &= \mathrm{cth}\left|m_1h_1 + \mathrm{cth}^{-1}\left\{\frac{\sigma_2m_1}{\sigma_1m_2}\mathrm{cth}\left[m_2h_2 + \cdots + \mathrm{cth}^{-1}\left(\frac{\sigma_Nm_{N-1}}{\sigma_{N-1}m_N}\right)\right]\right\}\right| \end{aligned} \tag{2}$$

If the number of layers $N = 1$, then the layer factors R_N and R_N^* of Eq. 2 are both equal to 1, and Eq. 1 will be transformed into an expression for the field on the surface of a uniform earth (He, 2010a).

$$\begin{cases} E_x = \dfrac{I\rho dL\rho}{2\pi r^3}\left[3\cos^2\varphi - 2 + e^{-ikr}(1 + ikr)\right] \\ E_y = \dfrac{I\rho dL\rho}{2\pi r^3}3\cos\varphi\sin\varphi \end{cases} \tag{3}$$

The expressions of E_E_x wide field apparent resistivity ρ_a (He, 2010b; He, 2019) are

$$\begin{cases} \rho_a = K_{E-E_x}\dfrac{\Delta V_{MN}}{I}\dfrac{1}{F_{E-E_x}(ikr)} \\ \Delta V_{MN} = MN\cdot E_x \\ E_x = \dfrac{I\rho dL\rho}{2\pi r^3}\left[3\cos^2\varphi - 2 + e^{-ikr}(1 + ikr)\right] \\ K_{E-E_x} = 2\pi r^3/(dL\cdot MN) \end{cases} \tag{4}$$

Eq. 4, K_{E-E_x} is the device coefficient of the observation system; $\Delta V_{MN} = MN\cdot E_x$ is the potential difference between the MN at the measurement end, the unit is V; MN is the distance between the MN at the measurement end, the unit is m; I is the intensity of the emission current, the unit is A; dL is the dipole moment length, in m; E_x is the component of the uniform half-space electric field along the x-axis; k is the wave number; $F_{E-E_x}(ikr)$ is the electromagnetic response function, and the specific expressions are:

$$\begin{aligned} F_{E-E_x}(ikr) &= 3\cos^2\varphi - 2 + e^{-ikr}(1 + ikr) \\ k &= \sqrt{\omega^2\mu\varepsilon - i\mu\omega/\rho} \end{aligned} \tag{5}$$

In Eq. 5, φ is the angle between x-axis and radial vector $\boldsymbol{r}$, μ is the magnetic permeability, ρ is the model resistivity of uniform half-space, ε is the dielectric constant. When the detection object is a non-uniform half-space, the wide field apparent resistivity at different measurement points and different frequencies can be obtained according to Eq. 4, which reflects the overall resistivity response caused by the entire subsurface medium.

The observation system is designed according to Eq. 4 in the field, and the electrical information of the observation point location is finally obtained. However, the field construction deployment is restricted by the terrain conditions, and it is difficult to keep the current source AB parallel to the receiving dipole MN, and there is always an azimuthal difference α between them, which will cause the wide field apparent resistivity calculation error and distortion of the geoelectric parameters if we continue to calculate the wide field apparent resistivity along the E_E_x direction.

2.2 Wide field electromagnetic method E_E_{MN}

In order to eliminate the effect caused by the difference α in azimuth between AB and MN. In this paper, the formula for calculating E_E_{MN} wide field apparent resistivity at any azimuth is derived. Instead of calculating the apparent resistivity along the E_E_x direction, this method calculates the apparent resistivity along the MN direction at the measurement end. The advantage of this method is that the field measurement does not require the current source AB to be strictly parallel to the lateral or tangential direction to obtain the true resistivity parameters.

Let the electromagnetic field excited by the electric dipole source be located in the coordinate system *xyz*, the electric dipole source AB is parallel to the *x*-axis, and the angle between the receiving dipole MN and AB is α (Figure 1).

The relationship between E_{MN} and E_x, E_y is obtained as follows.

$$E_{MN} = E_x \cos\alpha + E_y \sin\alpha \tag{6}$$

According to Eq. 6, the expression for the electric field of E_{MN} is as follows.

$$E_{MN} = \cos\alpha \left\{ \begin{array}{c} \frac{IdL}{2\pi}\left(2\cos^2\varphi - 1\right)\int_0^\infty \frac{i\omega\mu}{r}\frac{R_N}{mR_N + m_1}J_1(mr)dm + \\ \frac{2\cos^2\varphi IdL}{2\pi}\int_0^\infty \frac{\rho_1}{r}\frac{m_1}{R_N^*}J_1(mr)dm - \frac{2IdL}{2\pi}\int_0^\infty \frac{\rho_1}{r}\frac{m_1}{R_N^*}J_1(mr)dm - \\ \frac{IdL\rho_1\cos^2\varphi}{2\pi}\int_0^\infty \frac{mm_1}{R_N^*}J_0(mr)dm \end{array} \right\} +$$

$$\sin\alpha \left\{ \begin{array}{l} \frac{IdL\sin 2\varphi}{2\pi}\int_0^\infty \frac{i\omega\mu}{r}\frac{R_N}{mR_N + m_1}J_1(mr)dm + \frac{IdL\sin 2\varphi}{2\pi}\int_0^\infty \frac{\rho_1}{r}\frac{m_1}{R_N^*}J_1(mr)dm \\ -\frac{IdL\rho_1\sin 2\varphi}{2\pi}\int_0^\infty \frac{mm_1}{R_N^*}J_0(mr)dm - \frac{IdL\sin 2\varphi}{2\pi}\int_0^\infty i\omega\mu\frac{R_N}{mR_N + m_1}J_0(mr)dm \end{array} \right\} \tag{7}$$

The E_E_{MN} electric field expression is defined by Eq. 7.

If the number of layers $N = 1$, both R_N and R_N^* are equal to 1. The above equations will be transformed into the expressions for the field on a uniform earth obtained in the previous section.

$$E_{MN} = \frac{I\rho dL}{2\pi r^3}\left\{\cos\alpha\left[1 + e^{-ikr}\left(1 + ikr\right)\right] + 3\sin\varphi\sin\left(\alpha - \varphi\right)\right\} \tag{8}$$

Substituting Eq. 8 into Eq. 4, the accurate expression of the wide field apparent resistivity at the measurement of MN can be obtained

$$\left\{ \begin{array}{l} \rho_a = K_{E-E_x}\frac{\Delta V_{MN}}{I}\frac{1}{F_{E-E_x}(ikr)} \\ \Delta V_{MN} = MN \cdot E_{MN} \\ E_{MN} = \frac{I\rho dL}{2\pi r^3}\left\{\cos\alpha\left[1 + e^{-ikr}\left(1 + ikr\right)\right] + 3\sin\varphi\sin\left(\alpha - \varphi\right)\right\} \\ F_{E-E_x}(ikr) = \left\{\cos\alpha\left[1 + e^{-ikr}\left(1 + ikr\right)\right] + 3\sin\varphi\sin\left(\alpha - \varphi\right)\right\} \end{array} \right. \tag{9}$$

In Eq. 9: when $\alpha = 0°$, $E_x = E_{MN}$, the correct geoelectric parameters under the observation station can be obtained either by using Eq. 9 or Eq. 4; when $\alpha \neq 0°$, $E_x \neq E_{MN}$, the correct geoelectric parameters under the MN at the measurement end can be obtained by iterative calculation of Eq. 9. The wide field apparent resistivity parameters along the MN direction of the receiving dipole can be obtained by iteration or inverse spline difference.

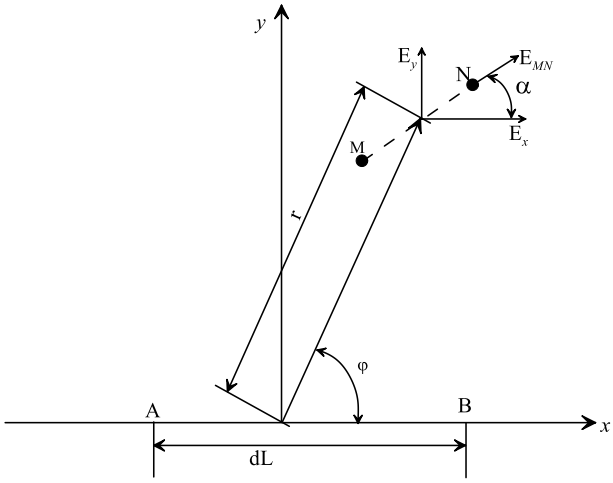

FIGURE 1
Schematic diagram of the arbitrary observation direction MN.

2.3 Evaluation basis

When discussing the evaluation of the error caused by the azimuthal angle difference α between the current source dipole AB and the receiving dipole MN, the degree of separation between the observed change value caused by α and the background must be determined as a criterion, and the relative error between the apparent resistivity value of $\alpha \neq 0°$, and the apparent resistance value of $\alpha = 0°$, under the condition of the same frequency point is taken as a criterion in the paper.

$$error = \frac{\left|\rho_a^j - \rho_0^j\right|}{\rho_0^j} \times 100\%;\ \left(j = 1, 2, \cdots, n\right) \tag{10}$$

In Eq. 10: j is the frequency number, n is the number of frequencies, ρ_a^j is the wide field apparent resistivity value corresponding to the jth frequency at $\alpha \neq 0°$, and ρ_0^j is the wide field apparent resistivity value corresponding to the jth frequency at $\alpha = 0°$.

3 Method verification

In order to verify the correctness of the calculation of the arbitrary directional wide field electromagnetic method E_E_{MN} proposed in this paper, a three-layer geoelectric model is designed: the first layer has a conductivity of $0.01S/m$ and a thickness of 100 m; the second layer has a conductivity of $0.1S/m$ and a thickness of 100 m; the third layer has a conductivity of $0.01S/m$; the horizontal long wire source is laid along the *x*-direction with a length of 200 m and the coordinates of the center point are (0, 0, 0); the transmitting frequency range is 0.01~10,000 Hz, the current amplitude is 1 A; the measurement line offset distance is

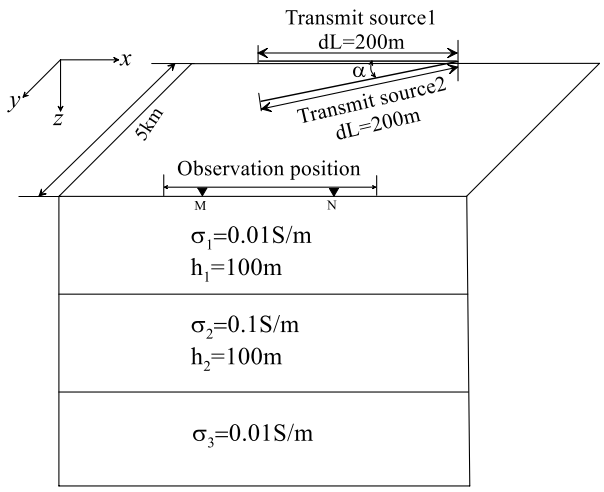

FIGURE 2
Three-layer ground power model and layout scheme.

5 km, and the observation position (MN) laid along the *x*-direction (Figure 2).

Option 1: Assuming that the measurement end MN is parallel to transmit source1, i.e., $\alpha = 0°$, the wide field apparent resistivity is calculated by using the wide field electromagnetic method E_E_x theoretical Eq. 4.

Option 2: The observation end MN is not parallel to transmit source2, and the angle between MN and dL is designed $\alpha = 15°$, and the wide field apparent resistivity is calculated using Eq. 4 and Eq. 9, respectively, and the relative mean square error is analyzed based on Eq. 10.

Analysis of Figure 3 shows that: ① when = 0° , the black curve in the figure relatively accurately reflects the H-type geoelectric information, in which the high-frequency resistivity value varies at 100 Ω·m and the wide field apparent resistivity value of 100~10 Hz is 23 Ω·m; the low-frequency wide field apparent resistivity value fluctuates around 90 Ω·m.

② When $\alpha = 15°$, the theoretical wide field apparent resistivity Eq. 4 is still used to obtain the frequency-wide field apparent resistivity graph (see Figure 3A). (b) Comparing with the theoretical curve of E_E_x curve $\alpha = 0°$, the two curves separate clearly, and the error curve in Figure 3B reveals that the observation error caused by the azimuthal angle difference $\alpha = 15°$ is >10%.

③ When the azimuth angle $\alpha = 15°$, the wide area apparent resistivity is calculated by using the Formula 10 proposed in this paper for any orientation, and the frequency-wide field apparent resistivity curve is obtained (see Figure 3A). Comparing the theoretical curve in Figure 3A with the 3a E_E_{MN} curve line, the two curves almost overlap together, and the error curve in Figure 3B reflects that the error at each frequency point is <1%.

By designing the 3-layer theoretical model, the validity of the E_E_{MN} calculation formula of the arbitrary azimuthal wide area E_E_{MN} method is verified. The use of the arbitrary azimuthal wide field E_E_{MN} method to calculate the wide field apparent resistivity parameters can effectively reduce the influence of the observed parameters by the azimuthal angle difference and make the observed apparent resistivity parameter values closer to the theoretical calculated values. In order to further illustrate the effectiveness and correctness of the proposed method, experimental work was carried out next to a known well in Sichuan.

4 Experimental analysis

4.1 Field construction layout

In order to analyze the effect of α on the observed parameters and further verify the correctness of E_E_{MN} method in this paper. Different experimental work were carried out without obvious electromagnetic humanistic interference, in which α was 0°, 1°, 3°, 5°, 10°, and 15° respectively. The field experiment scheme is shown in Figure 4: only the position of pole B is changed, while other experimental parameters remain unchanged. When $\alpha = 0°$, it indicates that the parallel observation position of the transmitting source AB is parallel to that of the receiving end MN, and there is no azimuth Angle difference.

This field using pseudo-random 7-frequency wave signal, that is, a simultaneous transmission and reception from the underground 7 frequency signals. The parameters of this experiment: current transmitting source AB = 1 km, receiving end MN = 100 m, transmitting current I = 80 A, keeping the intensity of

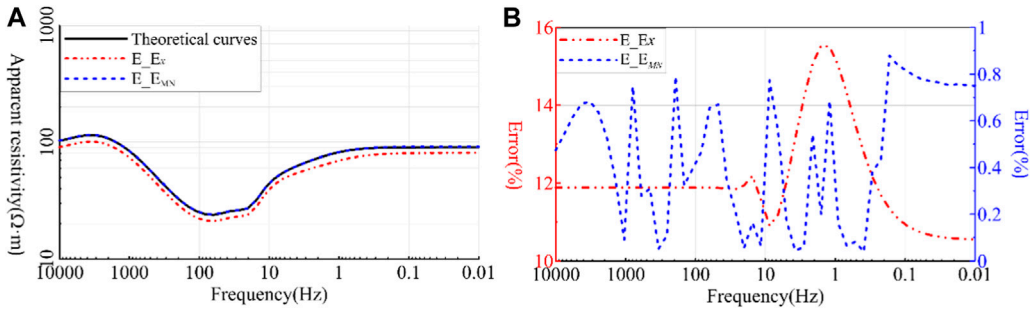

FIGURE 3
Curve diagram of different calculation methods. **(A)**: Frequency-visual resistance sounding graph; **(B)**: Relative error of E_E_x method and E_E_{MN} method.

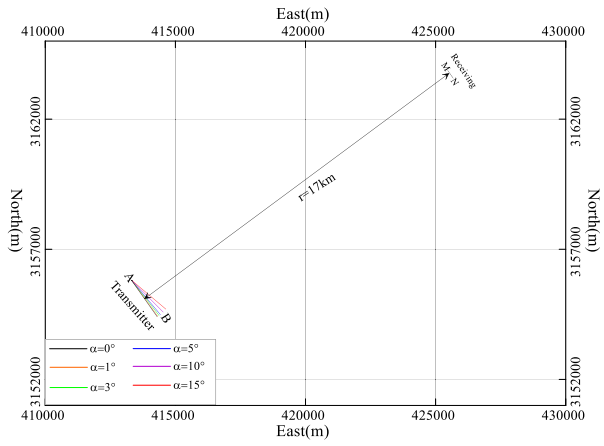

FIGURE 4
Schematic diagram of field test construction.

transmitting current constant, transmitting frequency range 8,192~0.01 Hz, total 54 frequency points.

To eliminate the effect of current, the observed potential difference data were normalized by current and the "frequency-electric field" curves were plotted along the MN direction for different α conditions (Figure 5). From the analysis of Figure 5, the difference of electric field caused by different α is small, and it is difficult to discern the influence of α on the observation results intuitively. In the later analysis, the influence of α on the observation results is analyzed from the apparent resistivity parameter, and the validity and correctness of the calculation formula proposed in this paper are verified.

4.2 Analysis of E_E_x experimental results

Figure 5 shows the "frequency-apparent resistivity" graph and "frequency-relative error" graph for different azimuthal differences without considering the effect of azimuthal difference α, but directly calculated by inverse spline numerically from Eq. 4. The analysis of the "frequency-apparent resistivity" graph and the relative error graph in Figure 6 is shown as follows.

(1) When $\alpha = 1°$, the corresponding "frequency-apparent resistivity" curve is the same as the "frequency-apparent resistivity" curve with $\alpha = 0°$, and there is no obvious separation, and the relative error of the corresponding apparent resistivity is ≤5%, while the relative error of the apparent resistivity of individual frequency points is >5%. The relative error of the apparent resistivity at individual frequency points is >5%. It means that the azimuthal difference between the current source AB and the receiver MN $\alpha \leq 1°$ has a small effect on the wide field apparent resistivity.

(2) When $\alpha = 3°$, the "frequency-apparent resistivity" curve of Figure 6 and the "frequency-apparent resistivity" curve of $\alpha = 0°$ have no obvious separation in the frequency band (8,192~10 Hz), and the relative error of each frequency point is ≤10%; in the middle and low There is a weak separation in the frequency band (10~0.011 Hz), and the relative error at each frequency point varies from 10% to 25%.

(3) When $\alpha = 5°$, the "frequency-apparent resistivity" curve of Figure 6 and the "frequency-apparent resistivity" curve of $\alpha = 0°$ do not show significant separation in the frequency band (8,192~10 Hz), and the relative error of each frequency point is ≤10%; in the middle and low frequency band (10~0.011 Hz), the separation is more obvious, and the relative error of each frequency point is ≤15%. (10~0.011 Hz), with relative error ≤15% at each frequency point.

(4) When $\alpha = 10°$, the "frequency-apparent resistivity" curves of Figure 6 and $\alpha = 0°$ both show a clear separation, and even the shape of the curves changes in the low and middle frequency bands (30~0.01 Hz). In the high-mid frequency band (8,192~10 Hz), the relative error of apparent resistivity at each frequency point varies from 20% to 40%; in the low-mid frequency band (10~0.01 Hz), the relative error ranges from 100% to 170%. It indicates that the azimuthal difference between the current source AB and the MN at the receiver has a large effect on the wide field apparent resistivity of the full frequency band, even causing distortion of the apparent resistivity parameters.

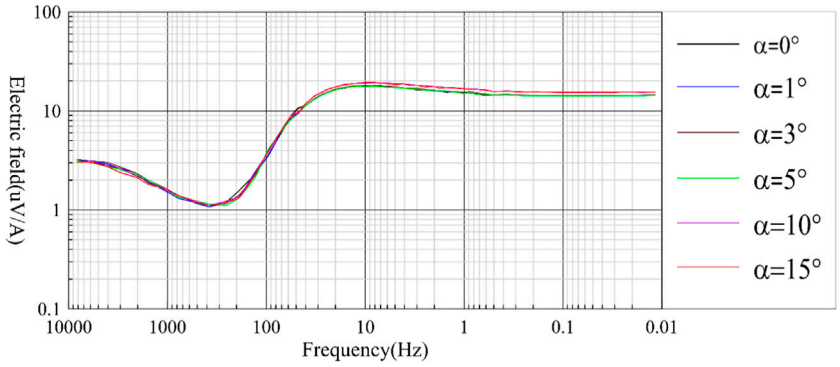

FIGURE 5
Normalized "frequency-field" curves for different α currents.

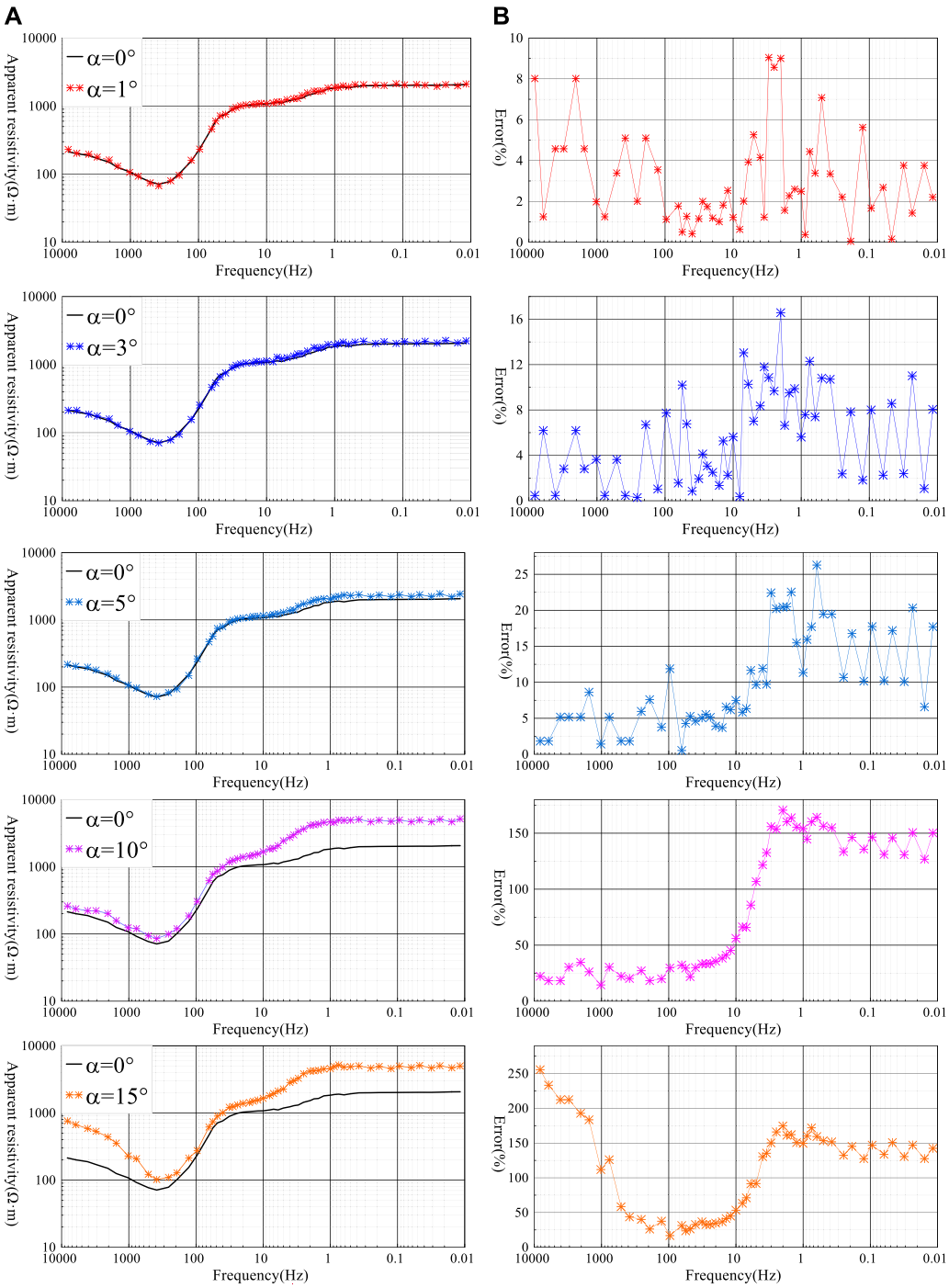

FIGURE 6
Apparent resistivity and error graphs **(A)**: Apparent resistivity graph; **(B)**: Relative error graph.

(5) When α = 15°, the "frequency-apparent resistivity" curve of Figure 7 and the "frequency-apparent resistivity" curve of α = 0° both show significant separation, and the shape of the curves in the high-middle frequency band (8,192~10 Hz) and the low-middle frequency band (30~0.01 Hz The curves in the high-mid frequency band (8,192~10 Hz) and the low-mid frequency band (30~0.01 Hz) have changed or even become distorted. The relative error range of the apparent resistivity at each frequency point in the high-mid frequency band (8,192~10 Hz) varies from 40% to 255%; the relative error range in the mid-low frequency band (10~0.01 Hz) is greater than 100%. This indicates that the azimuthal difference between the current source AB and the receiver MN has a large effect on the wide field apparent resistivity in the full frequency band, causing distortion of the apparent resistivity parameters.

From the above analysis, it can be concluded that: in the range of $\alpha \leq 1°$, the azimuthal difference α has a small effect on the apparent resistivity parameters; when $\alpha \leq 5°$, the azimuthal difference aa mainly affects the apparent resistivity parameters in the middle and low frequency bands; when $\alpha = 10° \sim 15°$, the azimuthal difference aa has a large effect on the apparent resistivity parameters in the whole frequency band, and the more serious the distortion of the high-middle frequency data, the more obvious the false anomaly caused, and even causes the interpretation of the parameter distortion. If the relative error of the apparent resistivity value ≤10% is considered reasonable, it must be ensured that $\alpha \leq 3°$, but the field construction conditions are restricted by the terrain, and it is often difficult to achieve the azimuthal difference $\alpha \leq 3°$ between the current source AB and the receiver MN, so the angle correction must be made to the observed data to eliminate the influence brought by α and improve the interpretation accuracy of the apparent resistivity parameters.

4.3 Analysis of E_E_{MN} experimental results

Figure 7 shows the "frequency-apparent resistivity" curve and the relative error curve calculated and plotted according to the arbitrary orientation E_E_{MN} of Eq. 9. The analysis of the "frequency-apparent resistivity" curve and the relative error graph in Figure 7 is shown as follows.

(1) When $\alpha = 1°$, the "frequency-apparent resistivity" curve of Figure 7 and the "frequency-apparent resistivity" curve of $\alpha = 0°$ do not show significant separation and approximately coincide, and the relative error of the apparent resistivity at each frequency point is ≤1%, which is reduced from 8% to 1% compared with the calculation of Figure 6.
(2) When $\alpha = 3°$, the "frequency-apparent resistivity" curve of Figure 7 and the "frequency-apparent resistivity" curve of $\alpha = 0°$ do not show significant separation and almost coincide, and the relative error of the apparent resistivity at each frequency point corresponds to a range of (−2% ~ 2%), which is reduced from 15% to 2% compared with the calculation of Figure 6 E_E_x.
(3) When $\alpha = 5°$, the "frequency-apparent resistivity" curve of Figure 7 and the "frequency-apparent resistivity" curve of $\alpha = 0°$ do not show any obvious separation, and the shape of the curve changes similarly, and the relative error of the corresponding apparent resistivity at each frequency point changes in the range of (−4% ~ 4%), compared with the relative error of Figure 6 E_E_x calculation method from 25% to 4%.
(4) When $\alpha = 10°$, the "frequency-apparent resistivity" curve of Figure 7 is not significantly separated from the "frequency-apparent resistivity" curve with $\alpha = 0°$. The curve shape changes similarly, and the relative error of the apparent resistivity at each frequency point is (−4% ~ 5%), which is reduced from 150% to 5% compared with the relative error of Figure 6 E_E_x calculation.
(5) When $\alpha = 15°$, there is no obvious separation between the "frequency-apparent resistivity" curve in Figure 7 and the "frequency-apparent resistivity" curve with $\alpha = 0°$. The shape of the curve changes similarly, and the relative error of the apparent resistivity at each frequency point varies in the range of (−7% ~ 10%), which is reduced from 300% to 10% compared with the relative error of the E_E_x calculation in Figure 6.

The analysis results of Figures 6, 7 show that: firstly, the maximum relative error of the wide area apparent resistivity obtained by the arbitrary azimuthal wide area electromagnetic method E_E_{MN} is reduced from 25% to 4% when $\alpha \leq 5°$, which makes the apparent resistivity parameter closer to the real underground geoelectric information; secondly, the relative error of the wide area apparent resistivity obtained by the arbitrary azimuthal wide area electromagnetic method E_E_{MN} is reduced from 270% to less than 10% when $\alpha = 10°$ and 15°. Thirdly, if the azimuth angle difference α is larger, the effect of using E_E_{MN} method of arbitrary azimuth wide field electromagnetic method on eliminating α is more obvious, which reflects the real resistivity value of the subsurface and improves the accuracy of the wide field apparent resistivity effectively.

4.4 Analysis of inversion effect

In this section, we take $\alpha = 15°$ as an example, and perform single-point inversions of E_E_x and E_E_{MN} apparent resistivity respectively, and further analyze the effect of azimuthal difference α on the interpretation parameters by combining the electric logging data of Ning 227 borehole. One-dimensional continuum imaging was performed on the processed data, and the relevant parameters of inversion were as follows: inversion depth was 4.5 km; The number of iterations in the inversion process was 20; The horizontal and depth resolution were 1; The regularization parameter was 5; The fitting error was 0.02. Figure 8 shows the bathymetric curves of "frequency-apparent resistivity" obtained from different calculation methods of E_E_x and E_E_{MN}, and the single-point inversion curves are shown in Figure 9.

(1) From Figure 8 E_E_x and E_E_{MN} "frequency-apparent resistivity" curve analysis, it can be seen that when the azimuth angle difference is 15°, the corresponding "frequency-apparent resistivity" sounding curves of different calculation methods of the same measurement point are different, and the two curves are completely separated, and the curve change pattern is also different, which means that the azimuth angle difference α has a greater influence on the apparent resistivity parameter.
(2) From the comparative analysis of the single-point inversion curve and the drilling electric logging curve in Figure 9, it can be obtained that: Firstly, above elevation 0 km, both E_E_x and E_E_{MN} have less variability and are in basic agreement with the trend of the logging resistivity curve, and the electrical stratification of the single-point inversion curve is obvious. Secondly, the variation patterns of depth-resistivity curves of E_E_x and E_E_{MN} after single-point inversion in the middle and deep parts (0~−3 km) differ greatly, in which the variation trends of E_E_{MN} mode curves are generally more consistent with the variation trends of electric logging curves and the resistivity stratification is also obvious, while the

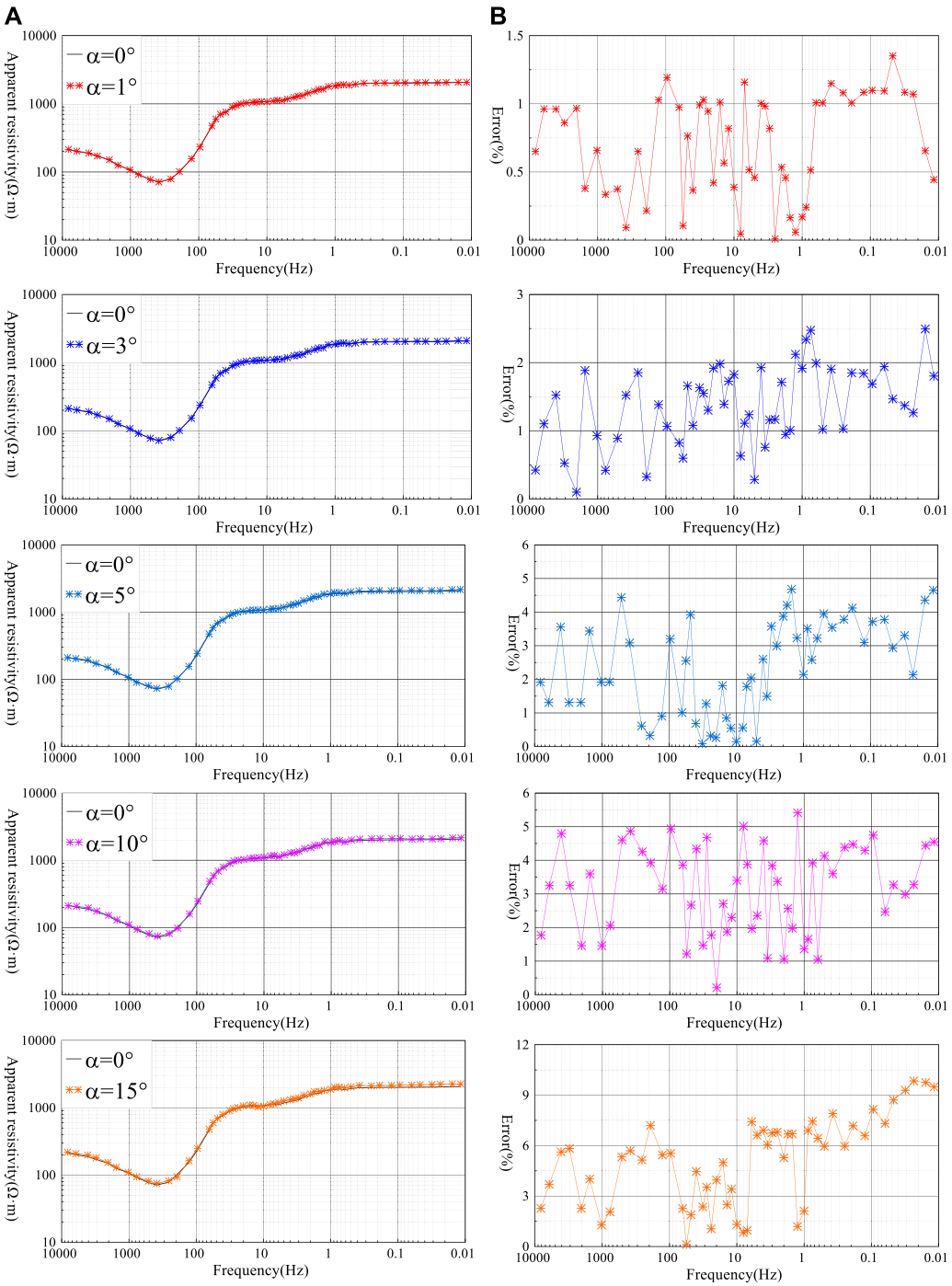

FIGURE 7
Apparent resistivity and error" graphs **(A)**: Apparent resistivity graph; **(B)**: Relative error graph.

variation trends of E_E_x curves are more consistent with the variation trends of electric logging curves and the electrical stratification is weaker. Thirdly, from the analysis of the inversion iteration error curve in Figure 9, it can be seen that the number of iterations of E_E_{MN} apparent resistivity inversion is 6, and the error decreases from 33% to about 2%, and the error almost no longer changes with the increase of the number of iterations; on the contrary, the number of iterations of E_E_x apparent resistivity inversion is 10, and the error decreases from 34% to 3.8%, and the inversion fitting error no longer changes with the increase of the number of iterations. Therefore, the inversion of the E_E_{MN} apparent resistivity parameter can achieve a more satisfactory fitting error with fewer iterations.

(3) The use of arbitrary azimuthal wide area electromagnetic method E_E_{MN} observation method for field observation

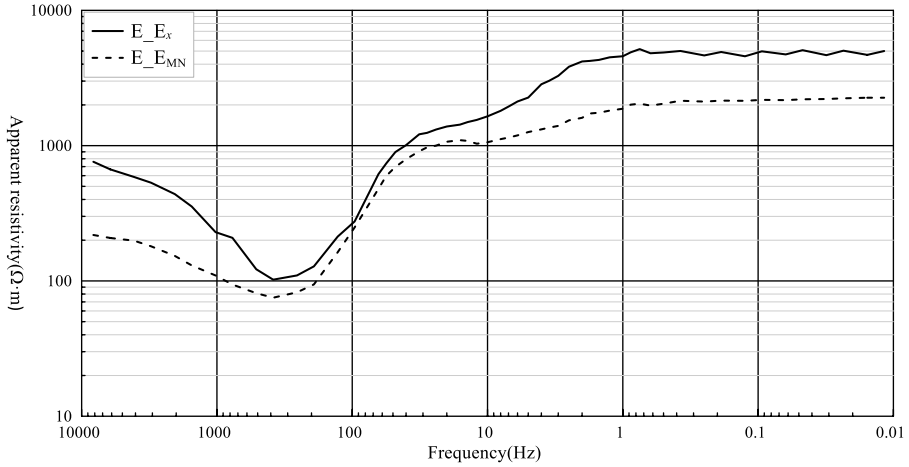

FIGURE 8
E_E_x and E_E_{MN} "frequency-apparent resistivity" curves.

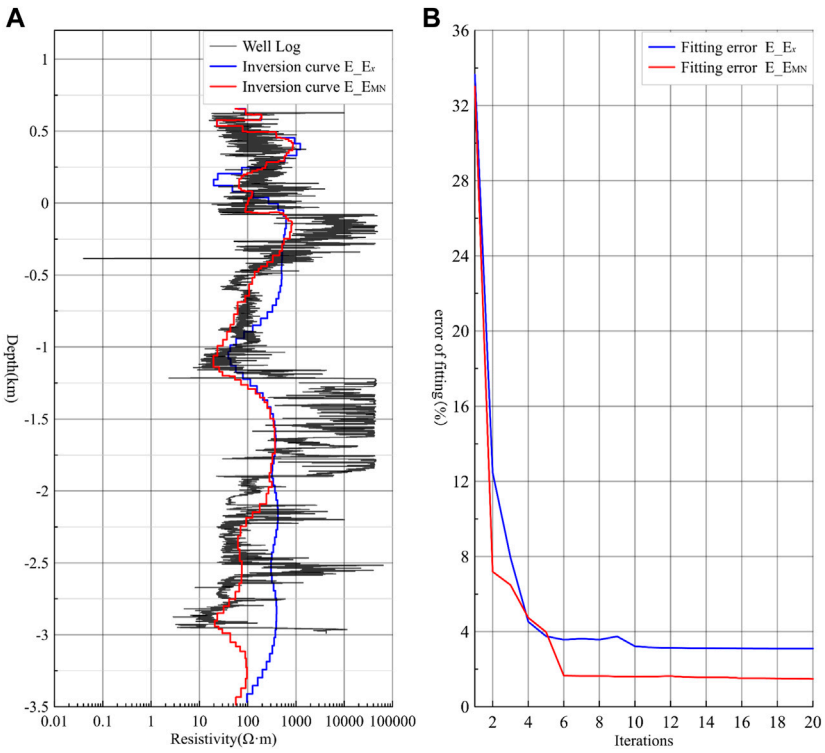

FIGURE 9
E_E_x and E_E_{MN} inversion curves and fitting error curves **(A)**: Black line: electric logging curve of well Ning 227; Blue line: E_E_x inversion curve; Red line: E_E_{MN} inversion curve **(B)**: Blue line: E_E_x error curve; Red line: E_E_{MN} error curve.

data can effectively reduce the observation error caused by azimuthal angle difference, improve the validity and accuracy of the interpretation parameters, and also greatly reduce the construction requirements of E_E_x wide area electromagnetic method field current source AB parallel receiving dipole MN, improve the field production efficiency and save economic costs, which has important research significance and practical production significance.

5 Conclusion

In order to eliminate the influence of azimuthal angle difference α to the observation parameters and improve the validity and accuracy of the interpretation parameters, we proposed an arbitrary observation orientation wide field electromag-netic E_E_{MN} method in this paper, i.e., calculating the wide field apparent resistivity parameters along the MN direction of any measurement end. Based on the results of theoretical model orthorectification and field measurement data, the following conclusions are obtained:

(1) The three-layer geoelectric model and two observation schemes are designed, and by comparing with the theoretical method E_E_x, the method E_E_{MN} calculation method is adopted, which effectively eliminates the influence of azimuthal angle difference α to the apparent resistivity parameters and verifies the effectiveness and correctness of the arbitrary azimuthal wide field electromagnetic method E_E_{MN}.

(2) The experimental work of different azimuth angle difference α was carried out beside the well, and the calculation parameters of wide field electromagnetic method E_E_x and arbitrary azimuth wide field electromagnetic method E_E_{MN} were compared and analyzed. The results show that: Firstly, when $\alpha \leq 5^{\circ}$, at the same frequency of the same measuring station, the maximum relative error of the wide field apparent resistivity value using any azimuth E_E_{MN} method decreases from 30% to 4% compared with the E_E_x method, which effectively improves the accuracy of the apparent resistivity value and makes the qualitative analysis more accurate; Secondly, when $\alpha = 10^{\circ}$ and 15°, the relative error of the whole band apparent resistivity value of E_E_x calculation method is not less than 50%, the maximum is 300%, and the apparent resistivity parameter is seriously distorted. Using any azimuth E_E_{MN} calculation method, the maximum relative error of the all-band apparent resistivity decreases from 300% to less than 10%; Thirdly, the single station inversion results of different methods show that the arbitrary azimuth E_E_{MN} calculation method can achieve a relatively ideal fitting error with fewer iterations, and the interpretation parameters are closer to the actual formation electrical information, improving the accuracy of resistivity parameter. Arbitrary azimuth wide field electromagnetic method E_E_{MN} can effectively reduce the observation error caused by azimuth angle difference α, and can directly and truly reflect the objective change of geoelectric section with depth, which makes the electrical analysis more accurate, and further verifies the validity and reliability of the calculation method in this paper.

(3) The wide field apparent resistivity parameters obtained by the arbitrary orientation E_E_{MN} method can effectively eliminate the observation error caused by α between the current source dipole AB and the receiving dipole MN, which greatly improves the accuracy of the wide field apparent resistivity parameters, and also better expands the applicability and flexibility of the current source E_E_x wide field electromagnetic method in complex terrain areas, with important theoretical research and practical production significance.

Data availability statement

The original contributions presented in the study are included in the article/supplementary material, further inquiries can be directed to the corresponding author.

Author contributions

Author ZT Mainly to assist in field experiments. All authors listed have made a substantial, direct, and intellectual contribution to the work and approved it for publication.

Conflict of interest

Author ZT was employed by Sichuan Zhongcheng Coal Field Geophysical Engineering, Research Institute Co., Ltd.

The remaining authors declare that the research was conducted in the absence of any commercial or financial relationships that could be construed as a potential conflict of interest.

Publisher's note

All claims expressed in this article are solely those of the authors and do not necessarily represent those of their affiliated organizations, or those of the publisher, the editors and the reviewers. Any product that may be evaluated in this article, or claim that may be made by its manufacturer, is not guaranteed or endorsed by the publisher.

References

Cagniard, L. (1953). Basic theory of the magnetotelluric method of geophysical prospecting. *Geophysics* 18 (3), 605–635. doi:10.1190/1.1437915

Cao, C. Q. (1978). The apparent resistivity for layered Earth. *Chin. J. Geophys.* 21 (3), 248–261.

Chen, H., and Li, D. Q. (2014a). A new electromagnetic field division method for horizontal electric dipole. *J. Central South Univ. Sci. Technol.* 45 (7), 2250–2258.

Chen, M, S. (2014b). The electromagnetic field distribution and observation parameters. *Coal Geol. Explor.* 42 (5), 81–86. doi:10.3969/j.issn.1001-1986.2014.05.016

Dai, S. K., Zeng, L., Zhou, Y. M., Li, K., Chen, Q. R., and Ling, J. X. (2020). Research on direct integration algorithm of electromagnetic field in homogeneous layered media for a wide range of frequencies and transceiver distances. *Oil Geophys. Prospect.* 55 (6), 1364–1372.

Fang, W. Z., Li, X., Li, Y. G., and Feng, B. (1992). The whole-zone definition of apparent resistivity used in the frequency domain electromagnetic methods. *J. Xi'an Coll. Geol.* 14 (4), 81–86.

Goldstein, M. A. (1971). *Magnetotelluric experiments employing an artificial dipole source*. Toronto, Canada: University of Toronto.

He, J. S. (2019). Theory and technology of wide field electromagnetic method. *Chin. J. Nonferrous Metals* 29 (9), 1809–1816.

He, J. S. (2020). New research progress in theory and application of wide field electromagnetic method. *Geophys. Geochem. Explor.* 44 (5), 985–990.

He, J. S. (2010a). Wide field electromagnetic sounding methods. *J. Central South Univ. Sci. Technol.* 41 (3), 1065–1072. doi:10.1190/segam2015-5835894.1

He, J. S. (2010b). *Wide field electromagnetic sounding methods and pseudo-random signal coding electrical method*. Beijing, China: Higher Education Press.

Huang, H. P., and Piao, H. R. (1992). Full-wave apparent resistivity from vertical magnetic dipole frequency sounding on a layered Earth. *Chin. J. Geophys.* 35 (5), 389–395. *in Chinese*.

Li, D. Q. (2017). Measurement range of E_E_x and $E_E_\varphi$wide field elegytromagnetic methods. *Oil Geophys. Prospect.* 52 (6), 1315–1323.

Li, G., Wu, S. L., Cai, H. Z., He, Z. S., et al. (2023). A new deep temporal convolutional network combined with dictionary learning for strong cultural noise elimination of controlled-source electromagnetic data. *Geophysics* 88 (4). doi:10.1190/geo2022-0317.1

Liu, J. X., Tong, T. G., Liu, C. M., et al. (2013). Recognition of electromagnetic field asymptotic properties and improved definition of wide field apparent resistivity on $E–E_\varphi$ array. *Chin. J. Nonferrous Metals* 23 (9), 2359–2364.

Liu, J. X., Liu, R., Guo, R. W., Tong, X. Z., and Xie, W. (2022). Research progress of electromagnetic method in nonferrous metal mineral exploration. *Chin. J. Nonferrous Met.* 33 (1), 261–284.

Liu, J. X., Zhao, R., and Guo, Z. W. (2019). Research progress of electromagnetic methods in the exploration of metal deposits. *Prog. Geogr. (in Chinese)* 34 (1), 0151–0160. doi:10.6038/pg2019CC0222

Mao, X. J., and Bao, G. S. (1996). A direct algorithm for full-wave apparent resistivity from horizontal electric dipole frequency sounding. *J. Cent. South Univ. Technol.* 27 (3), 254–257.

Spies, B. R., and Eggers, D. E. (1986). The use and misuse of apparent resistivity in electromagnetic methods. *Geophysics* 51 (7), 1462–1471. doi:10.1190/1.1442194

Tang, J. T., and He, J. S. (1994). A new method to define the full-zone resistivity in horizontal electric dipole frequency sounding on a layerd Earth. *Chin. J. Geophys.* 3 (4), 543–552.

Tang, J. T., and He, J. S. (2005). *Controlled source audio-frequency magnetotelluric method and its application*. Changsha, China: Central South University Press.

Tang, J. T., and He, J. S. (1993). Effective resistivity defined by the electromagnetic fields induced by horizontal electric dipole. *J. Cent. South Univ. Technol.* 24 (2), 137–142.

Tikhonov, A., N. (1950). On determining electrical characteristics of the deep layers of the Earth's crust. *Dokl. Akad. Nauk. SSSR* 73, 295–297.

Wang, H. Y., Guo, W. B., and Liu, Y. A. (2021). "Research and application of ground-well frequency domain electromagnetic method," in Proceedings of the First National Conference on Mineral Exploration, Barcelona, Spain, September 2016, 55–58. Chinese Geophysical Society (Chinese Geophysical Society: Chinese Geophysical Society.

Wang, S. G., Xiong, B., and Dai, S. K. (2013). Analysis of resolution ability to *E-Ex* arrangement wide field electromagnetic method using 1-D modeling and inversion. *J. Central South Univ. Sci. Technol.* 44 (9), 3766–3774.

Wang, S. G., and Xiong, B. (2012). Numerical calculation methods of wide field apparent resistivity. *Comput. Tech. geopaysical Geochem. Explor.* 34 (4), 0380–0383. doi:10.1002/cjg2.419

Yin, C. C. (1991a). Forward calculation and application of frequency domain sounding at any azimuth. *Comput. Tech. Geophys. Geochem. Explor.* 13 (2), 129–138.

Yin, C. C., and Piao, H. R. (1991b). A study of the definition of apparent resistivity in electromagnetic sounding. *Geophys. Geochem. Explor.* 15 (4), 290–299.

Yu, Y. C. (2010). *Wide field electromagnetic method of one-dimensional positive inversion*. Changsha, Hunan: Central South University.

Yuan, B., Li, D. Q., and Hu, Y. F. (2020). New correction method for controlled-source electromagnetics source effects. *Trans. Nonferrous Metals Soc. China* 30 (12), 3356–3366. doi:10.1016/S1003-6326(20)65467-X

Zonge, K. L., and Hughes, L. J. (1991). Controlled source audio-frequency magnetotellurics. *Electromagn. Methods Appl. Geophys.* 2. Application, Parts A and B. doi:10.1190/1.9781560802686.ch9

frontiers | Frontiers in Earth Science

TYPE Original Research
PUBLISHED 15 June 2023
DOI 10.3389/feart.2023.1183150

OPEN ACCESS

EDITED BY
Cong Zhou,
East China University of Technology, China

REVIEWED BY
Xiaoyue Cao,
Yangtze University, China
Ying Liu,
Ocean University of China, China
Bin Xiong,
Guilin University of Technology, China

*CORRESPONDENCE
Ya Sun,
sunya_seis@csu.edu.cn

RECEIVED 09 March 2023
ACCEPTED 19 April 2023
PUBLISHED 15 June 2023

CITATION
Tong X, Sun Y and Zhang B (2023), An efficient spectral element method for two-dimensional magnetotelluric modeling.
Front. Earth Sci. 11:1183150.
doi: 10.3389/feart.2023.1183150

An efficient spectral element method for two-dimensional magnetotelluric modeling

Xiaozhong Tong[1,2], Ya Sun[1,2]* and Boyao Zhang[1]

[1]School of Geosciences and Info-Physics, Central South University, Changsha, China, [2]Key Laboratory of Metallogenic Prediction of Nonferrous Metals of Ministry of Education, Central South University, Changsha, China

We introduce a new efficient spectral element approach to solve the two-dimensional magnetotelluric forward problem based on Gauss–Lobatto–Legendre polynomials. It combines the high accuracy of the spectral technique and the perfect flexibility of the finite element approach, which can significantly improve the calculation accuracy. This method mainly includes two steps: 1) transforming the boundary value problem in the partial differential form into the variational problem in the integral form and 2) solving large symmetric sparse systems based on the combination of incomplete LU factorization and the double conjugate gradient stability algorithm through the spectral element with quadrilateral meshes. We imply the spectral element method on a resistivity half-space model to obtain a simple analytical solution and find that the magnetic field solutions simulated by the spectral element approach matched closely to the exact solutions. The experiment result shows that the spectral element solution has high accuracy with coarse meshes. We further compare the numerical results of the spectral element, finite difference, and finite element approaches on the COMMEMI 2D-1 and smooth models, respectively. The numerical results of the spectral element procedure are highly consistent with the other two techniques. All these comparison results suggest that the spectral element technique can not only give high accuracy for modeling results but also provide more detailed information. In particular, a few nodes are required in this method relative to the finite difference and finite element methods, which can decrease the relative errors. We then deduce that the spectral element method might be an alternative approach to simulate the magnetotelluric responses in two- or three-dimensional structures.

KEYWORDS

magnetotelluric, two-dimensional, forward modeling, spectral element method, numerical experiments

1 Introduction

As a special geo-electromagnetic method, magnetotelluric sounding can identify the resistivity or conductivity distributions in a geological medium based on harmonic and variable electromagnetic fields (Chave and Jones, 2012). Magnetotelluric sounding is based on naturally occurring electromagnetic fields, which can provide a comprehensive and continuous spectrum of the geo-electromagnetic field. This electrical resistivity, measured by comparing the electric field's horizontal component to the magnetic field on the surface, can detect a depth of several tens of kilometers associated with the acquisition frequency. With the rapid advancement in magnetotelluric modeling and inversion, it has become one of the

essential tools for recognizing deep geological structures (Unsworth, 2010; Avdeeva et al., 2012; Azeez et al., 2017; Nagarjuna et al., 2021) and geophysical investigations, such as geothermal exploration (Barcelona et al., 2013; Patro, 2017; Tarek et al., 2023), mineral deposit exploration (Benjamin et al., 2018; Jiang et al., 2022), and gas exploration (Zhang et al., 2014).

There are some numerical approaches for solving two-dimensional magnetotelluric forward problems, such as finite difference and finite element, and they are applied to two-dimensional magnetotelluric inversion (deGroot-Hedlin and Constable, 1990; Rodi and Mackie, 2001; Siripunvaraporn and Egbert, 2007; Lee et al., 2009; Kelbert et al., 2014; Guo et al., 2020; Liao et al., 2022). The finite difference numerical approach can solve partial differential equations for approximating first-order or second-order derivatives with a difference scheme (Pek and Verner, 1997; deGroot-Hedlin, 2006; Rao and Babu, 2006; Kumar et al., 2011). They also investigated the efficiency of computing two-dimensional magnetotelluric responses. This method also has high accuracy on the electric field and magnetic field components (Guo et al., 2018; Kalscheuer et al., 2018; Sarakorn and Vachiratienchai, 2018). Unfortunately, it is not easy to compute the resulting fields' accurate apparent resistivities and phases. As another important numerical approach, finite element can be applied to solve the two-dimensional magnetotelluric forward problem (Wannamaker et al., 1986; Key and Weiss, 2006; Franke et al., 2007; Lee et al., 2009; Sarakorn, 2017; Yao et al., 2021). It involves the hypothetical functional form of the model and the field in a small area of the specified geometry. The finite element method can introduce complex information from the real world to construct the initial model, including surface topography, and can also improve the flexibility of mesh discretization. However, it requires fine meshing to obtain high accuracy, which results in high computational costs. Some other numerical methods are also used to simulate two-dimensional magnetotelluric forward modeling, such as the boundary element (Xu and Zhou, 1997), the finite-volume (Du et al., 2016; Wang et al., 2019), the mesh-free (Wittke and Tezkan, 2014; Wittke and Tezkan, 2021), the domain decomposition (Bihlo et al., 2017), the numerical manifold (Liang et al., 2021), and the pseudo-spectral methods (Tong et al., 2020). These numerical methods provide an essential practical basis for two-dimensional magnetotelluric forward modeling.

Compared to other numerical approaches, the finite element method requires fine grids to obtain higher calculation accuracy. This will bring challenges, especially when computational resources are limited. Moreover, in practical geophysical applications, when the discrete meshes need be refined to a geo-electrical model, the convergence rate will decrease gradually, while the number of meshes and the computational cost can increase largely (Key and Weiss, 2006). The spectral method, as a novel approach, can provide the numerical approximation of partial differential equations (Zou and Cheng, 2018). In this numerical approach, the field in the computational domain can be approximated by polynomials or Fourier expansions. Since high-order orthogonal basis functions are applied in the spectral method, it has exponential convergence. In addition, the spectral interpolation points are densely distributed at the boundary, which can avoid the Runge phenomenon in the traditional high-order interpolation (Tong et al., 2020). The method that combines the finite element and spectral method is called the spectral element method. In the past 20 years, geophysicists have dedicated these numerical methods to developing efficiency and accuracy. Some recent developments found that the spectral element approach can be seen as a high-order finite element method and its high-accuracy is derived from the properties of the spectral method (Patera, 1984). It can combine the high-accuracy of the spectral method and the flexibility of the finite element technique. Compared with the classical finite element method, the Runge phenomenon of isometric interpolation can be avoided using Gaussian orthogonal basis functions and Gaussian points (Xu et al., 2022). There are two types of spectral element methods, one based on Legendre polynomials and another based on Chebyshev polynomials. It is widely used in applications for wave propagation (Komatitsch and Tromp, 1999; Seriani and Oliveria, 2008; Luo et al., 2013; Trinh et al., 2019; Lyu et al., 2020), forward gravity modeling (Ghariti et al., 2018; Martin et al., 2017), and for geo-electromagnetic forward modeling problems (Zhou et al., 2016; Huang et al., 2019; Yin et al., 2019; Zhu et al., 2020; Huang et al., 2021; Weiss et al., 2023). However, it is rarely used in two-dimensional magnetotelluric forward modeling.

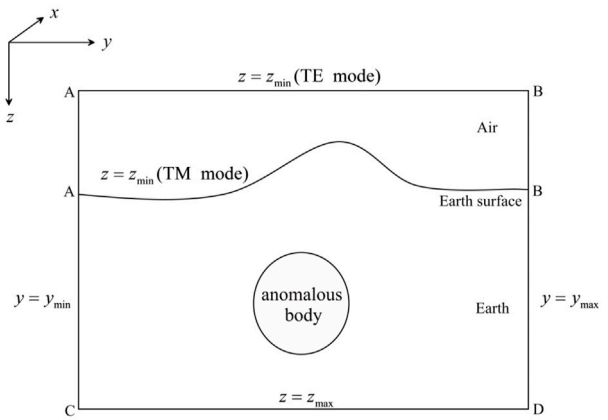

FIGURE 1
Geo-electrical model of the two-dimensional magnetotelluric forward problem.

This paper proposes an efficient and accurate spectral element approach to compute the two-dimensional magnetotelluric responses of the boundary problem without measuring Earth's curvature. To benchmark the accuracy, we compare the numerical results of the spectral element forward algorithm with the analytical solutions and numerical results of the finite difference and finite element schemes. Although our approach can be applied to any two-dimensional geo-electromagnetic forward modeling, in this study, we demonstrate its implementation mainly in numerical experiments.

2 Boundary value problem

2.1 Electromagnetic equations

We define the z-axis at the depth and the x-axis along the geologic strike, as shown in Figure 1. Using a time-harmonic factor

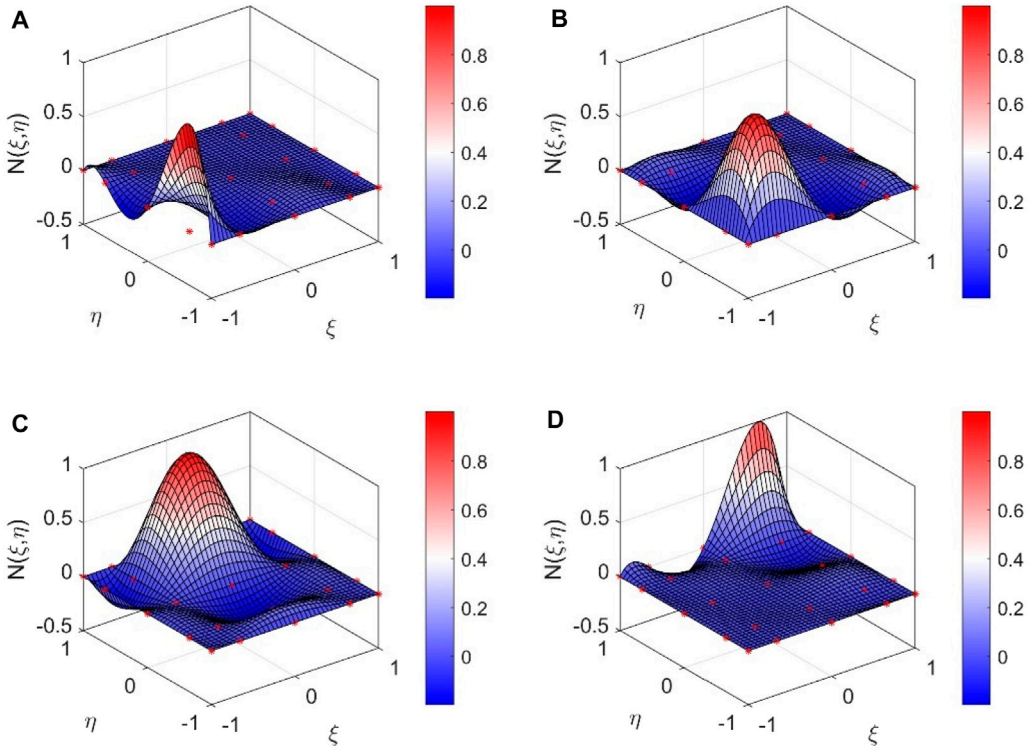

FIGURE 2
Two-dimensional spectral basis functions in part of order p=4. **(A)** $N_{12}(\xi,\eta) = \phi_1(\xi)\phi_2(\eta)$; **(B)** $N_{22}(\xi,\eta) = \phi_2(\xi)\phi_2(\eta)$; **(C)** $N_{34}(\xi,\eta) = \phi_3(\xi)\phi_4(\eta)$; and **(D)** $N_{45}(\xi,\eta) = \phi_4(\xi)\phi_5(\eta)$.

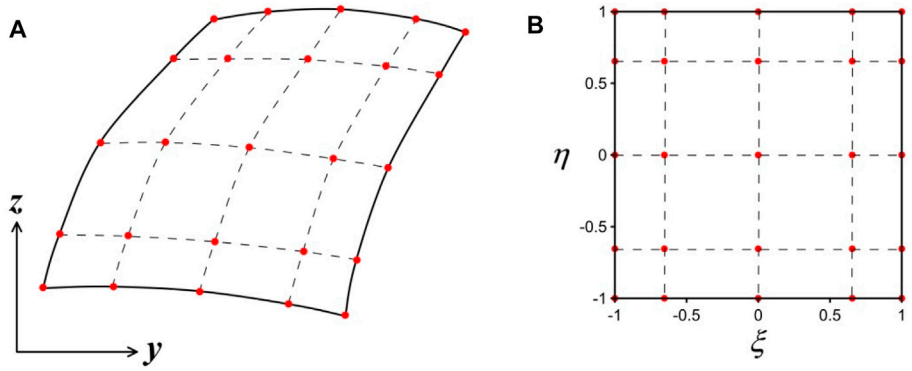

FIGURE 3
Mapping coordinate system of the spectral element of order p = 4. **(A)** Sub-element; **(B)** parent element.

$e^{-i\omega t}$, Maxwell's equations can then be written as (Wannamaker et al., 1987; Yao et al., 2021)

$$\nabla\times \boldsymbol{E} = i\omega\mu\boldsymbol{H} \tag{1}$$

$$\nabla\times \boldsymbol{H} = \sigma\boldsymbol{E} \tag{2}$$

where $\boldsymbol{E}$ means the electric field, $\boldsymbol{H}$ represents the magnetic field, ω denotes the angular frequency, $\mu = 4\pi \times 10^{-7}$H/m is the magnetic permeability, and σ is the conductivity.

For a two-dimensional structure, due to $\partial\boldsymbol{E}/\partial x \equiv 0$ and $\partial\boldsymbol{H}/\partial x \equiv 0$, we can expand the curl operators in Eqs 1, 2as follows:

$$\frac{\partial E_z}{\partial y} - \frac{\partial E_y}{\partial z} = i\omega\mu H_x \tag{3}$$

$$\frac{\partial E_x}{\partial z} = i\omega\mu H_y \tag{4}$$

$$\frac{\partial E_x}{\partial y} = -i\omega\mu H_z \tag{5}$$

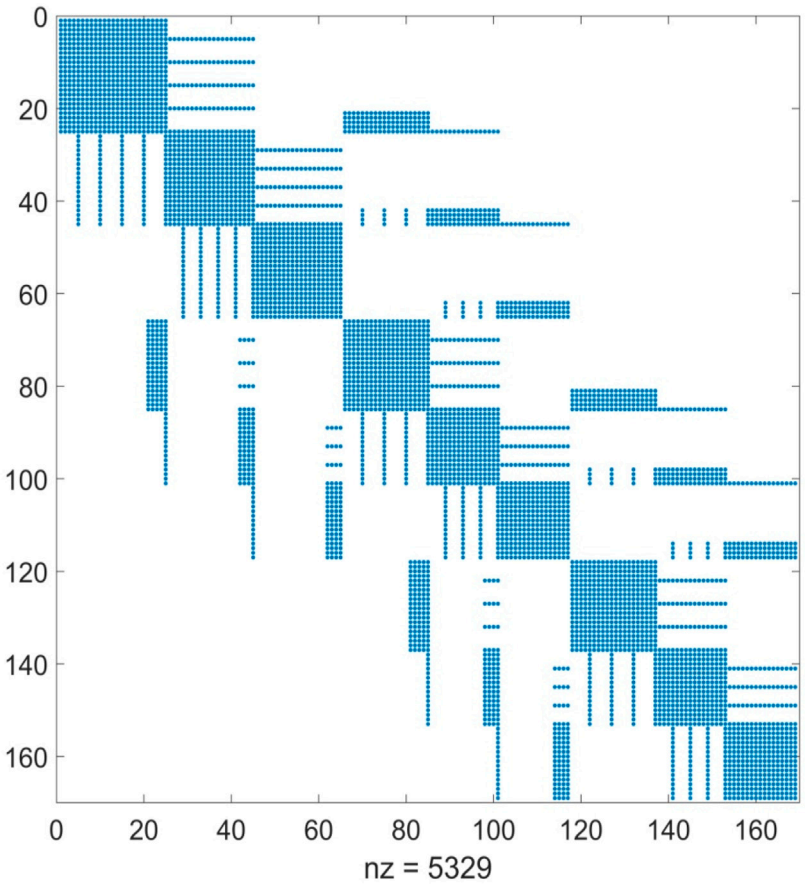

FIGURE 4
Non-zero sparse elements of the discretization coefficient matrix obtained a 3 × 3 grid with a fourth-order polynomial spectral element approach.

and

$$\frac{\partial H_z}{\partial y} - \frac{\partial H_y}{\partial z} = \sigma E_x \tag{6}$$

$$\frac{\partial H_x}{\partial z} = \sigma E_y \tag{7}$$

$$\frac{\partial H_x}{\partial y} = -\sigma E_z \tag{8}$$

The electromagnetic equations are more complex than homogeneous media for two-dimensional modeling, where resistivity changes occur in the y-axis and z-axis. According to Eqs 4–6, E_x the TE mode can yield a second-order Helmholtz equation:

$$\frac{\partial^2 E_x}{\partial y^2} + \frac{\partial^2 E_x}{\partial z^2} + i\omega\mu\sigma E_x = 0 \tag{9}$$

Meanwhile, for the TM mode, H_x yields another second-order Helmholtz equation:

$$\frac{\partial}{\partial y}\left(\frac{1}{\sigma}\frac{\partial H_x}{\partial y}\right) + \frac{\partial}{\partial z}\left(\frac{1}{\sigma}\frac{\partial H_x}{\partial z}\right) + i\omega\mu H_x = 0 \tag{10}$$

Then the electric field E_x or the magnetic field H_x in the Helmholtz-type equation can be rewritten as

$$\nabla \cdot (\tau \nabla u) + \lambda u = 0 \tag{11}$$

where u, τ, and λ represent different meanings relying on the different polarized modes. In the TE mode,

$$u = E_x, \tau = \frac{1}{i\omega\mu}, \lambda = \sigma \tag{12}$$

and in the TM mode,

$$u = H_x, \tau = \frac{1}{\sigma}, \lambda = i\omega\mu \tag{13}$$

2.2 Boundary conditions

We restrict the computational region for Eq. 11 to a two-dimensional bounded domain $\Omega = [y_{\min}, y_{\max}] \times [z_{\min}, z_{\max}]$, as shown in Figure 1. Therefore, the boundary conditions in the computational domain can be expressed as

$$u|_{z=z_{\min}} = 1 \text{ (in AB)} \tag{14a}$$

$$\left.\frac{\partial u}{\partial y}\right|_{y=y_{\min}} = 0 \text{ (in AC)}, \left.\frac{\partial u}{\partial y}\right|_{y=y_{\max}} = 0 \text{ (in BD)} \tag{14b}$$

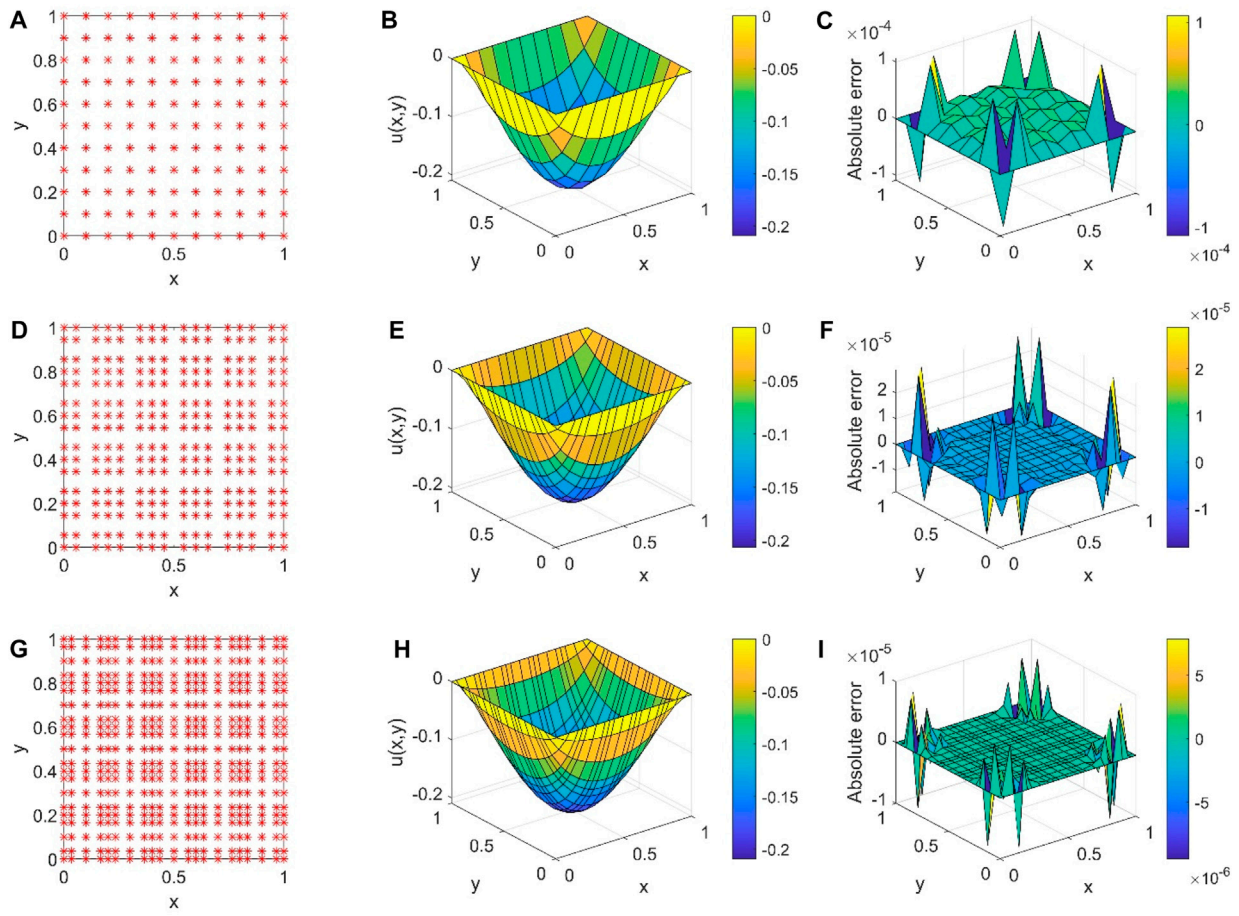

FIGURE 5
Spectral element numerical modeling for the Helmholtz equation with the interpolating polynomial order. **(A)** Two GLL points; **(B)** numerical solution with a second-order polynomial; **(C)** absolute error for a second-order polynomial; **(D)** three GLL points; **(E)** numerical solution with a third-order polynomial; **(F)** absolute error for a third-order polynomial; **(G)** four GLL points; **(H)** numerical solution with a fourth-order polynomial; and **(I)** absolute error for a fourth-order polynomial.

$$\left(\frac{\partial u}{\partial z}+ku\right)\Big|_{z=z_{\max}}=0\ (\text{in CD}) \tag{14c}$$

where $k=\sqrt{-i\omega\mu\sigma}$.

3 Spectral element formulation

3.1 Discretization of a variational problem

The magnetotelluric fields can be simulated by the Helmholtz equation of Eq. 12 under the boundary conditions of Eq. 14. Using the variational principle (Pozrikidis, 2014), the boundary value problem of the partial differential form displayed in Eq. 12 and Eq. 14 can be written as the variational problem of the integral form:

$$\begin{cases} F(u)=\iint\left\{\frac{1}{2}\tau\left[\left(\frac{\partial u}{\partial y}\right)^2+\left(\frac{\partial u}{\partial z}\right)^2\right]-\frac{1}{2}\lambda u^2\right\}\mathrm{d}y\mathrm{d}z+\int_{CD}\frac{1}{2}\tau k u^2\mathrm{d}l=\min \\ u\,|_{y=y_{\min}}=0. \end{cases} \tag{15}$$

Within spectral element approximation, the magnetotelluric field can be expanded with two-dimensional interpolation basis functions:

$$\boldsymbol{u}=\sum_{i=1}^{N_r}N_i(\xi,\eta)u_i \tag{16}$$

where N_r is the number of primary procedures for an element and $N_i(\xi,\eta)$ are the essential functions.

The integral of all elements, Eq. 15, can be rewritten as

$$F(u)=\sum\iint_e\left\{\frac{1}{2}\tau\left[\left(\frac{\partial u}{\partial y}\right)^2+\left(\frac{\partial u}{\partial z}\right)^2\right]-\frac{1}{2}\lambda u^2\right\}\mathrm{d}y\mathrm{d}z+\sum\int_{CD}\frac{1}{2}\tau k u^2\mathrm{d}l=\min \tag{17}$$

This will lead to a discrete linear equation as follows:

$$\boldsymbol{K}\boldsymbol{u}=0 \tag{18}$$

where u represents the values of the unknown magnetic field or electric field.

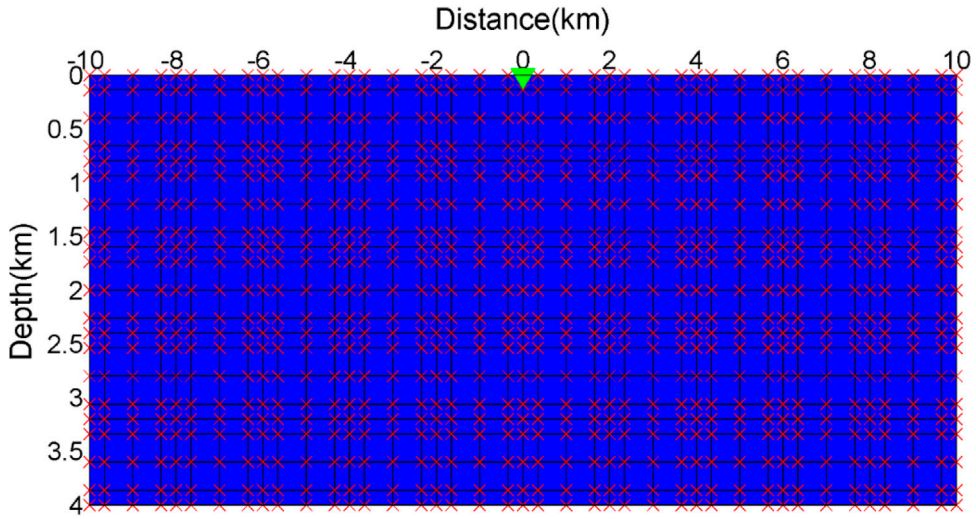

FIGURE 6
Homogeneous half-space model meshed with four GCL points per element.

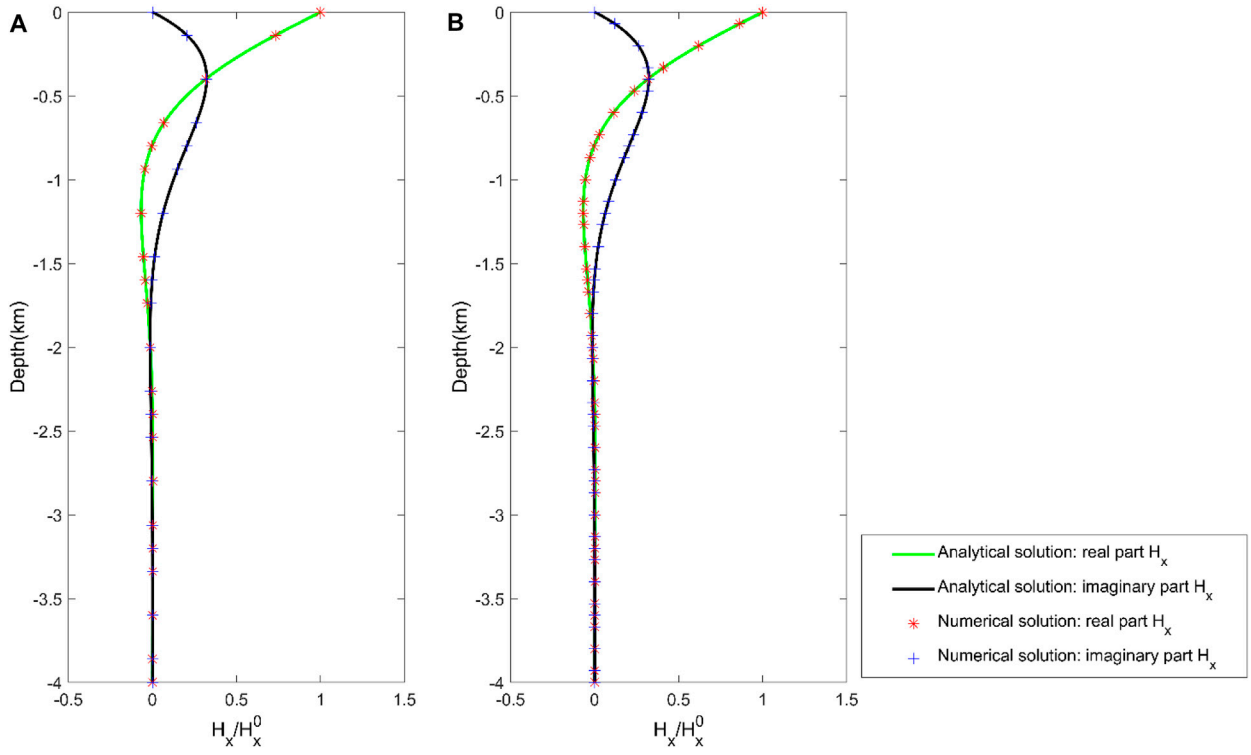

FIGURE 7
Spectral element numerical solution of magnetic field H_x for the frequency f=10 Hz in the half-space resistivity model. The number of elements in the depth direction for **(A)** Nz = 5 and **(B)** Nz = 10.

TABLE 1 RMS errors of the magnetotelluric responses for the half-space resistivity model.

Frequency (Hz)	TM mode		TE mode	
	Apparent resistivity	Phase	Apparent resistivity	Phase
0.01	7.73e-9	3.11e-8	7.71e-9	3.09e-8
0.1	1.83e-6	1.74e-7	1.81e-6	1.72e-7
1	1.69e-4	5.32e-5	1.62e-4	5.24e-5
10	1.26e-2	1.25e-2	1.21e-2	1.22e-2
100	0.39	1.42	0.36	1.39

3.2 Spectral basis functions

Its spectral accuracy characterizes the spectral element, i.e., the numerical error depends on the order of the basis functions (Lee and Liu, 2005). We choose Gauss–Lobatto–Legendre (GLL) element discretization for the magnetotelluric forward problem. The Nth-order GLL basis functions in a one-dimensional reference element $\xi \in [-1, 1]$ can be expressed by

$$\phi_i(\xi) = \frac{1}{N(N+1)L_N(\xi_i)} \frac{\xi^2 - 1}{\xi - \xi_i} L_N^{'}(\xi) \tag{19}$$

for $i = 1, 2, \cdots, N+1$, where $L_N(\xi)$ is the Nth-order Legendre polynomial and $L_N^{'}(\xi)$ is its derivative. On a reference element with $\xi, \eta \in [-1, 1] \times [-1, 1]$, the two-dimensional basis function can be written as

$$N_{ij}(\xi, \eta) = \phi_i(\xi)\phi_j(\eta) \tag{20}$$

For example, if order $p = 4$, there are 25 basis functions to the interpolation nodes. Figure 2 shows two-dimensional basis functions of the 4th order in part, and four of the nodal basis functions corresponding to $N_{12}(\xi, \eta) = \phi_1(\xi)\phi_2(\eta)$, $N_{22}(\xi, \eta) = \phi_2(\xi)\phi_2(\eta)$, $N_{34}(\xi, \eta) = \phi_3(\xi)\phi_4(\eta)$, and $N_{45}(\xi, \eta) = \phi_4(\xi)\phi_5(\eta)$ are represented.

3.3 Spectral element equation

In the spectral element method, a physical sub-element needs to be mapped into a reference parent element and the element coefficient matrix can be achieved in the reference element. Figure 3 shows a mapping example of a two-dimensional spectral element (y, z)-coordinate and the normalized $\xi, \eta \in [-1, 1] \times [-1, 1]$ reference coordinate.

The derivatives and the volume in the (y, z)-coordinate system in Eq. 17 can be transformed to the (ξ, η)-coordinate system as follows:

$$\mathrm{d}y\mathrm{d}z = \begin{vmatrix} \frac{\partial y}{\partial \xi} & \frac{\partial z}{\partial \xi} \\ \frac{\partial y}{\partial \eta} & \frac{\partial z}{\partial \eta} \end{vmatrix} \mathrm{d}\xi\mathrm{d}\eta = |J|\mathrm{d}\xi\mathrm{d}\eta \tag{21}$$

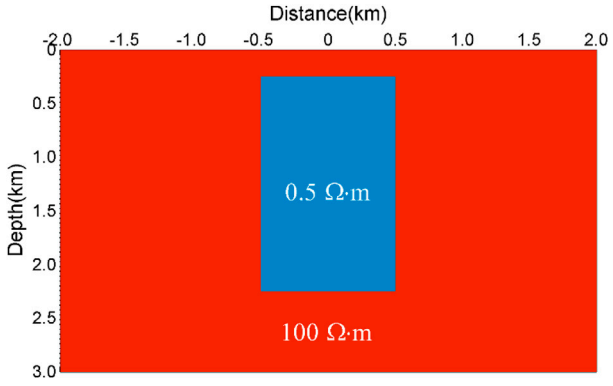

FIGURE 8
Resistivity distribution of the COMMEMI 2D-1 model.

where J is the Jacobian matrix.

The first-term integral in Eq. 17 is

$$\iint_e \frac{1}{2}\tau\left[\left(\frac{\partial u}{\partial y}\right)^2 + \left(\frac{\partial u}{\partial z}\right)^2\right]\mathrm{d}y\mathrm{d}z = \frac{1}{2}\boldsymbol{u}_e^T\boldsymbol{K}_{1e}\boldsymbol{u}_e \tag{22}$$

where

$$\boldsymbol{K}_{1e} = \iint_e \left[\left(\frac{\partial u}{\partial y}\right)^2 + \left(\frac{\partial u}{\partial z}\right)^2\right]\mathrm{d}y\mathrm{d}z$$
$$= \int_{-1}^{1}\int_{-1}^{1}\tau\left(\frac{\partial N_i}{\partial \xi}\frac{\partial \xi}{\partial y}\right)\left(\frac{\partial N_j}{\partial \xi}\frac{\partial \xi}{\partial y}\right)|J|\mathrm{d}\xi\mathrm{d}\eta + \int_{-1}^{1}\int_{-1}^{1}\tau\left(\frac{\partial N_i}{\partial \eta}\frac{\partial \eta}{\partial z}\right)\left(\frac{\partial N_j}{\partial \eta}\frac{\partial \eta}{\partial z}\right)|J|\mathrm{d}\xi\mathrm{d}\eta$$

The second-term integral in Eq. 17 is

$$\iint_e \frac{1}{2}\lambda u^2\mathrm{d}y\mathrm{d}z = \frac{1}{2}\boldsymbol{u}_e^T\boldsymbol{K}_{2e}\boldsymbol{u}_e \tag{23}$$

where $\boldsymbol{K}_{2e} = \iint_e \lambda u^2\mathrm{d}y\mathrm{d}z = \int_{-1}^{1}\int_{-1}^{1}\lambda N_i N_j|J|\mathrm{d}\xi\mathrm{d}\eta$.

The third-term integral in Eq. 17 is

$$\int_{CD}\frac{1}{2}\tau k u^2\mathrm{d}l = \frac{1}{2}\boldsymbol{u}_e^T\boldsymbol{K}_{3e}\boldsymbol{u}_e \tag{24}$$

where $\boldsymbol{K}_{3e}$ can be obtained with a one-dimensional line integral.

Considering the Dirichlet boundary condition at $z = z_{\min}$, we can derive the linear equations with the spectral element approach to build the two-dimensional magnetotelluric forward modeling:

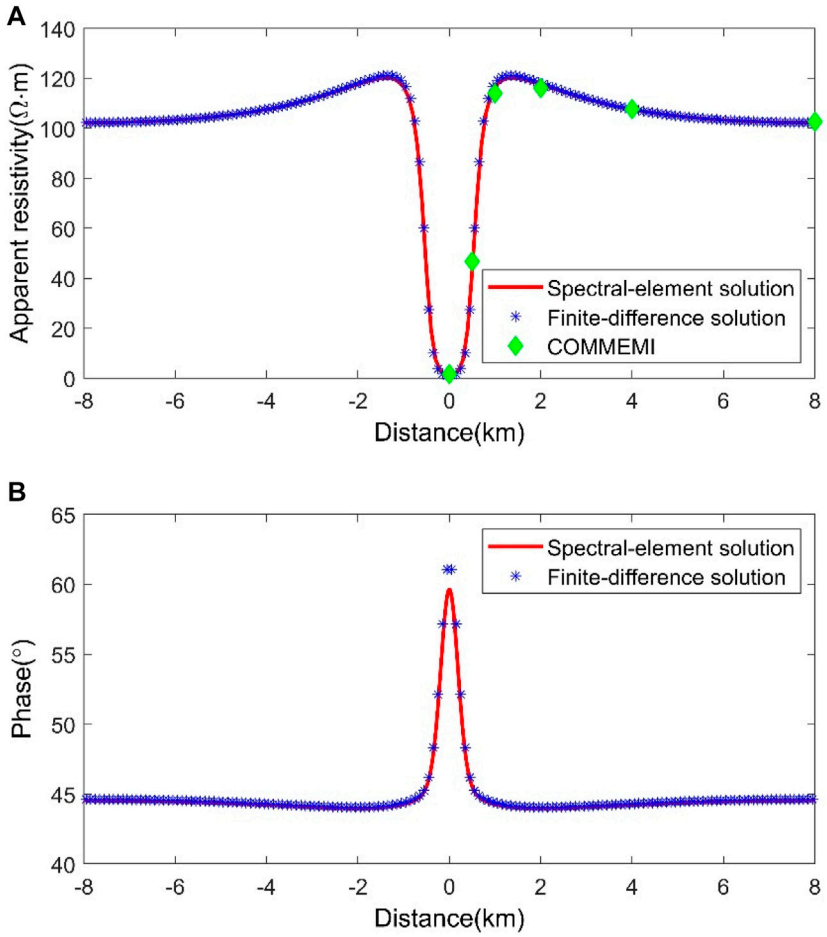

FIGURE 9
Comparison of numerical results for the COMMEMI 2D-1 model in the TM mode. **(A)** Apparent resistivities and **(B)** phases.

$$\boldsymbol{K}\boldsymbol{u} = \boldsymbol{p} \tag{25}$$

where $\boldsymbol{K} = \sum_{i=1}^{N_e} \boldsymbol{K}_{1e} - \sum_{i=1}^{N_e} \boldsymbol{K}_{2e} + \sum_{i=1}^{N_e} \boldsymbol{K}_{3e}$ is the coefficient matrix containing conductivity parameters σ, and N_e is the number of all elements. The right-side vector $\boldsymbol{p}$ is interrelated to the Dirichlet boundary conditions. The coefficient matrix $\boldsymbol{K}$ is a sparse, positive-defined, symmetric matrix. Figure 4 shows the sparse elements' distribution of the coefficient matrix for a 3 × 3 grid with the 4th polynomial order (just for illustration purposes). We use the biconjugate gradient-stabilized algorithm (van der Vorst, 1992; Chen et al., 2002), preconditioned with incomplete LU factorization (Pan et al., 2022), for our forward problem.

After obtaining E_x, the corresponding magnetic field component H_y can be solved by Eq. 4 for the TE mode. Since we acquired H_x, the corresponding electric component E_y can be solved by Eq. 7 for the TM mode. Then, we can obtain the two-dimensional impedance tensor from

$$\begin{bmatrix} E_x \\ E_y \end{bmatrix} = \begin{bmatrix} 0 & Z_{xy} \\ Z_{yx} & 0 \end{bmatrix} \begin{bmatrix} H_x \\ H_y \end{bmatrix} \tag{26}$$

The impedance can be used to calculate apparent resistivities

$$\rho_a^{xy} = \frac{1}{\omega\mu}\left|Z_{xy}\right|^2, \rho_a^{yx} = \frac{1}{\omega\mu}\left|Z_{yx}\right|^2 \tag{27}$$

and impedance phases

$$\phi^{xy} = \arctan\frac{\mathrm{Im}\left[Z_{xy}\right]}{\mathrm{Re}\left[Z_{xy}\right]}, \phi^{yx} = \arctan\frac{\mathrm{Im}\left[Z_{yx}\right]}{\mathrm{Re}\left[Z_{yx}\right]} \tag{28}$$

4 Accuracy of the method

For all the spectral element numerical approaches, the numerical solution of the boundary value problem depends on two parameters: (1) the size of each spectral element and (2) the interpolating polynomial order. To verify our spectral element method numerically, we consider the Dirichlet boundary for a Helmholtz equation

$$\nabla^2 u - u = 3 \tag{29}$$

with the exact solution

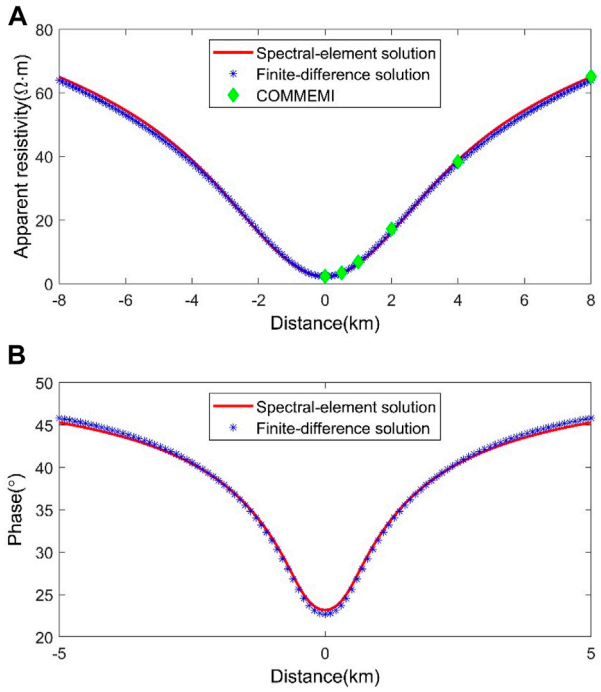

FIGURE 10
Comparison of numerical results for the COMMEMI 2D-1 model in the TE mode. **(A)** Apparent resistivities and **(B)** phases.

$$u_e(x,y) = \sum_{m=1,3,\cdots}^{\infty}\sum_{n=1,3,\cdots}^{\infty} -\frac{48}{(1+\pi^2m^2+\pi^2n^2)}\frac{1}{mn\pi^2}\sin(n\pi x)\sin(m\pi y) \quad (30)$$

The physical domain $\Omega = [0,1] \times [0,1]$ is discretized using a uniform mesh with 5 × 5 elements. Figure 5 shows the spectral element solutions obtained using different interpolating polynomial orders. The maximum absolute errors of spectral element solutions for 2, 3, and 4th polynomial orders are 1.06E-4, 2.89E-5, and 7.84E-6, respectively. The numerical results computed by our spectral element approach are generally consistent with the series solutions.

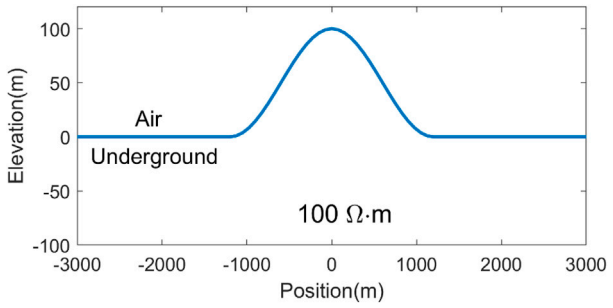

FIGURE 11
Ridge topographical model with background resistivity 100 Ω · m.

5 Model studies and discussion

5.1 Homogeneous half-space

We developed a half-space resistivity model to test the high-accuracy benchmark of our spectral element scheme. The half-space resistivity is designed as 10 Ω · m and the computational domain is set as 20 km × 4 km. During numerical simulation, each spectral element includes 4 GLL points in the y-direction and z-direction, as shown in Figure 6. In addition, we assume that only one measuring point is located on the ground, marked by a green triangle. The numerical magnetic field H_x is simulated at f = 10 Hz.

We set the number of elements in the horizontal direction to 10 (i.e., $N_y = 10$), while the number of elements in the depth direction is designed to 5 and 10, respectively (i.e., N_z = 10 and 5). Figure 7

TABLE 2 Apparent resistivities simulated by the spectral element code compared to the COMMEMI results.

	0 m	500 m	1,000 m	2,000 m	4,000 m
p_c (T M)					
SEM, p=1	1.34	41.49	120.21	117.38	108.20
SEM, p=2	1.44	44.56	114.84	115.57	107.23
SEM, p=3	1.48	45.76	114.64	116.07	107.40
SEM, p=4	1.51	46.02	114.25	116.37	107.81
COMMEMI	1.60 ± 0.27	46.70 ± 3.64	114.01 ± 3.69	116.11 ±2.67	107.62 ± 2.25
p_a (TE)					
SEM, p=1	2.27	3.20	6.33	16.20	37.89
SEM, p=2	2.28	3.29	6.60	16.59	38.83
SEM, p=3	2.30	3.34	6.71	17.06	38.26
SEM, p=4	2.30	3.35	6.76	17.12	38.29
COMMEMI	2.31 ± 0.12	3.39 ± 0.36	6.86 ± 0.30	17.19 ± 1.09	38.35 ± 1.96

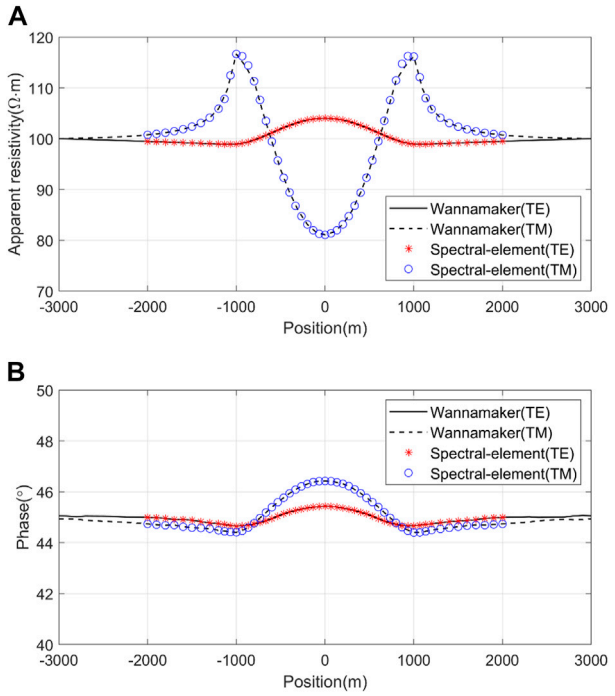

FIGURE 12
Comparison of numerical solutions for the ridge topographical model. **(A)** Apparent resistivities in the TM mode and TE mode; **(B)** phases in the TM mode and TE mode.

shows the numerical solution of the magnetic field H_x for the homogeneous half-space frequency of f = 10 Hz. They also offer that the real part and imaginary part of the magnetic field H_x calculated by the spectral element method agree with the analytical solution. This phenomenon also shows the correlation between the number of discrete elements and computational accuracy. Furthermore, it indicates that the number of discrete components does not affect the computational accuracy under high-polynomial order conditions. These results suggest that the spectral element approach can improve the accuracy for the two-dimensional magnetotelluric forward modeling.

To further verify the applicability of our spectral element approach, we increase the number of elements in horizontal and depth directions to 20. We then calculated the magnetotelluric response, including apparent resistivity and phase, at f = 0.1, 1.1, 10, 10, and 100 Hz frequencies in the TM mode and TE mode. The computing time of our code is about 1.6 s for each frequency. The apparent resistivity for each frequency is identical to the true resistivity 10 $\Omega \cdot$ m, and the phase was equal to 45°. The RMS errors of the magnetotelluric responses are given in Table 1. It is clear that the RMS error is proportional to the frequency, with the minimum error at f = 0.01 Hz and the maximum error at f = 100 Hz. In general, the RMS error value falls within the frequency band that we set, which is also the acceptable error range. The results show that our spectral element approach has high computational accuracy.

5.2 COMMEMI 2D-1 model

We conducted a numerical experiment to compare with the finite difference method. This numerical experiment coincides with the COMMEMI 2D-1 example (Zhdanov et al., 1997), which can test the accuracy and reliability of the spectral element forward algorithm. The COMMEMI 2D-1 model is shown in Figure 8. A symmetrical, rectangular, low-resistivity body is inserted in a homogeneous conductive half-space. The rectangular anomaly body has a width of 1,000 m, a length of 2,000 m, and a burial depth of 250 m from the ground surface. The resistivity of the anomaly is set as = 0.5 $\Omega \cdot$ m, and the half-space resistivity is designed as ρ = 100 $\Omega \cdot$ m. The frequency we applied in the next two experiments was f = 0.1 Hz.

First, we simulated the numerical solutions for the COMMEMI 2D-1 model using the spectral element algorithm and the finite difference method (Tong et al., 2018). In this example, the uniform meshes of the model for the whole calculation area are set to $\Delta y \times \Delta z$ = 100m × 50m. For spectral element numerical modeling, each spectral element includes two GLL points in the y-direction and z-direction, and has nine points for each element. The numerical apparent resistivities and phases in the TM mode are shown in Figure 9. The results show that the numerical results calculated by the spectral element method match well with those of

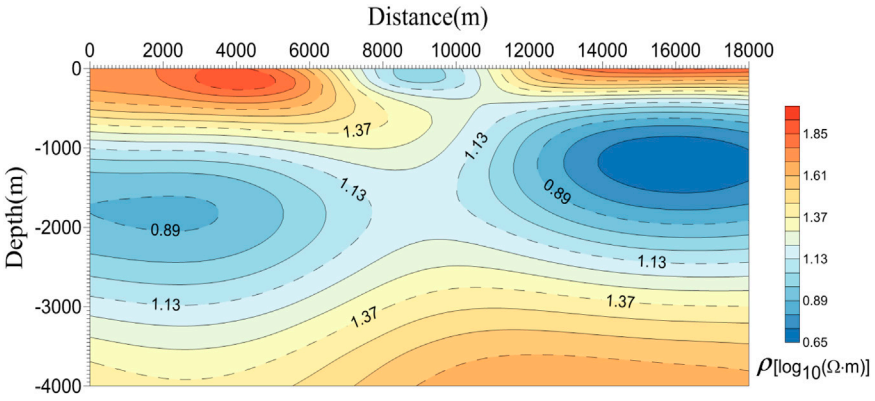

FIGURE 13
Smooth resistivity distribution inverted by the MT2DInvMatlab subroutine (Lee et al., 2009).

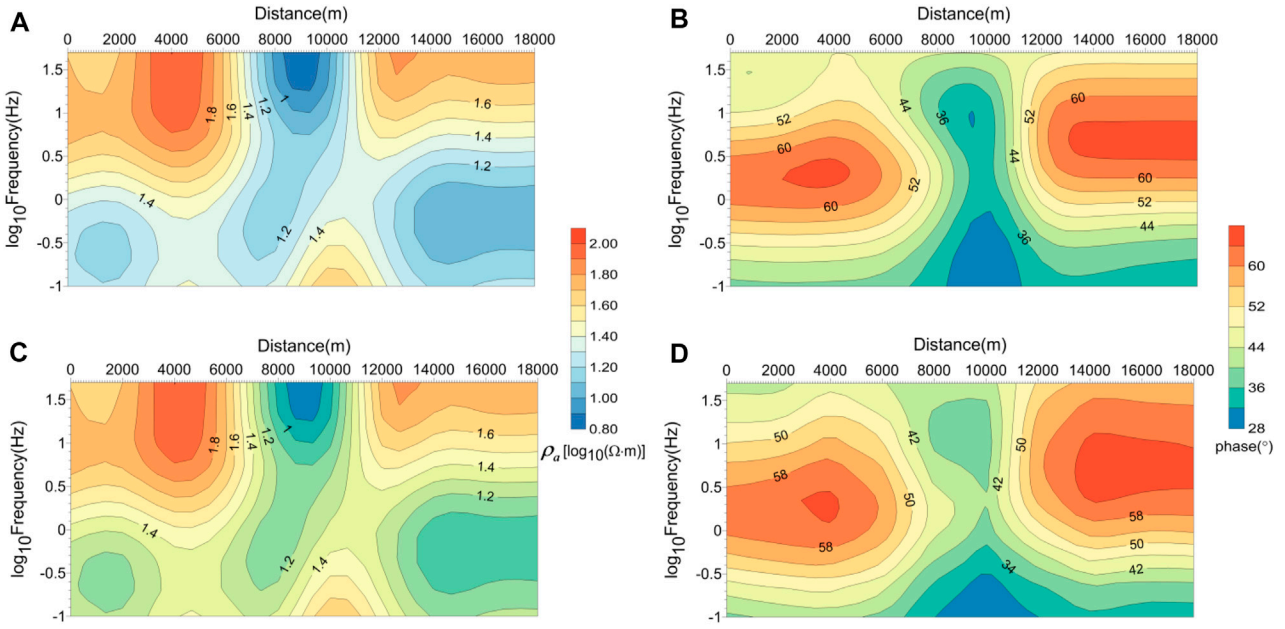

FIGURE 14
Comparison of numerical results for the smooth model. **(A)** TM apparent resistivity pseudo-section and **(B)** TM phase pseudo-section simulated by the spectral element method; **(C)** TM apparent resistivity pseudo-section and **(D)** TM phase pseudo-section simulated by the finite element method (Lee et al., 2009).

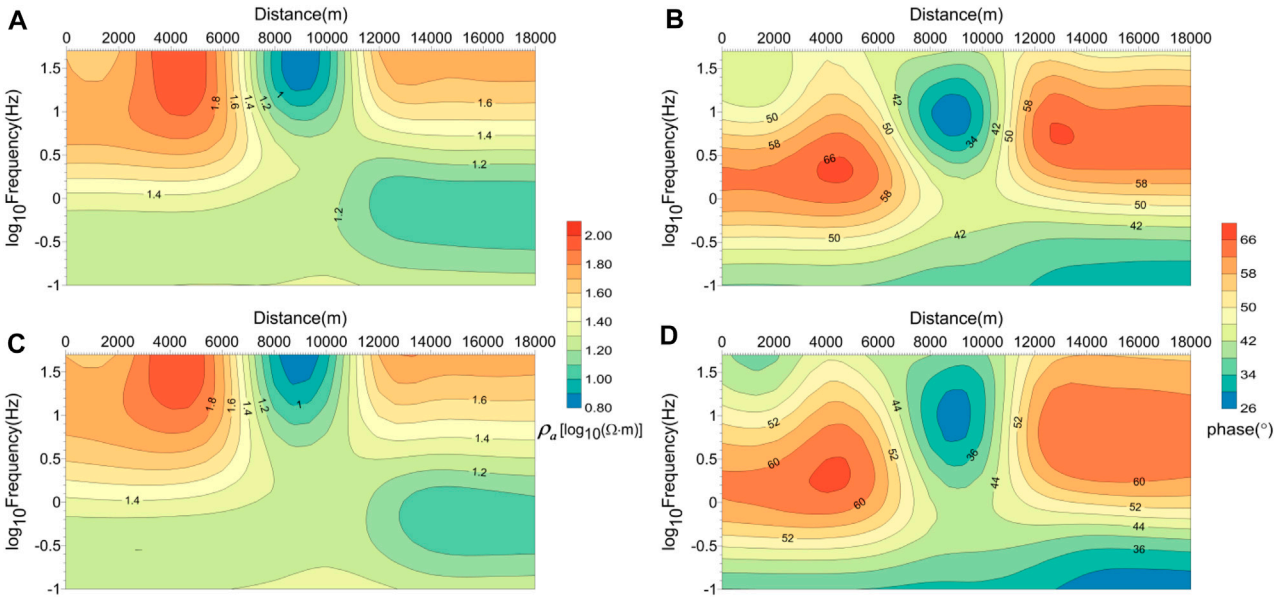

FIGURE 15
Comparison of numerical results for the smooth model. **(A)** TE apparent resistivity pseudo-section and **(B)** TE phase pseudo-section simulated by the spectral element method; **(C)** TE apparent resistivity pseudo-section and **(D)** TE phase pseudo-section simulated by the finite element method (Lee et al., 2009).

the finite difference method. Compared to finite difference results, the spectral element method shows a clear and continuous downward smoothness in TM mode calculations. The numerical results for the TE mode are shown in Figure 10. These results also matched well for the numerical magnetotelluric responses in the TE mode. The computing time of the COMMEMI 2D-1 model is about 0.5 s for the finite difference algorithm and about 1.8 s for the spectral element algorithm.

We also compare the numerical apparent resistivities calculated by the spectral element scheme and the finite difference approach with the

averaged numerical solutions of the COMMEMI project (Zhdanov et al., 1997), showing that the numerical apparent resistivities of the spectral element scheme agree well with the averaged numerical solutions of the COMMEMI project compared to those measured by the finite difference approach (Figure 9 top; Figure 10 top). It means that the modeling precision of the spectral element scheme is higher than that of the finite difference method in calculating the magnetotelluric responses using the same mesh size.

In the second example, we only simulate the spectral element solutions with different polynomial orders in the COMMEMI locations. In this experiment, we designed a non-uniform grid of the model over the entire computational domain. To make a more precise comparison with the resistivity values published by the committee experiments, in Table 2, we list the standard deviation from Table B.11 (Zhdanov et al., 1997) along with the numerical resistivity values simulated by the spectral element approach. From Table 2, the values produced by the spectral element method match well with the numerical results published in the COMMEMI experiments. The accuracy of the apparent resistivity simulated by the spectral element might depend on the polynomial order.

5.3 Topographical model

To compute the magnetotelluric responses of the two-dimensional undulating terrain, we applied our spectral element code to a ridge topographical model, as shown in Figure 11, which is the same as that used by other researchers (Wannamaker et al., 1986; Liang et al., 2021). The ridge model has a width of 2,400 m with a height of 100 m, and its resistivity value of half-space is $= 100\ \Omega \cdot \mathrm{m}$. The calculated magnetotelluric responses obtained by the finite element subroutine (Wannamaker et al., 1986) are the reference for this simulation.

In this study, the non-uniform meshes in the TM mode and TE mode are set as 15×10 and 20×10, respectively (in which 10 km is the air media and its resistivity is equal to $10^{15}\ \Omega \cdot \mathrm{m}$), and each spectral element has four GLL points in the y-direction and z-direction. The measurement profile along the atmospheric grounding interface varies from −2,000 to 2,000 m. The frequency to be tested is only 10 Hz. Figure 12 shows the comparison of the finite element results from Wannamaker et al. (1986) and our spectral element forward code, and the results match well. The maximum relative apparent resistivity error between the two forward schemes is equal to 0.15% in the TM mode and 0.07% in the TE mode, respectively. The maximum relative phase error is equal to 0.04% in the TM mode and 0.05% in the TE mode, respectively. As shown in Figure 12A, the topographic resistivity distortion of the TE mode is smaller than that of the TM mode.

5.4 Smooth resistivity model

In this numerical example, a smooth resistivity model is set to 18 km × 4 km, as shown in Figure 13. We calculate the response of a two-dimensional magnetotelluric model with a smooth resistivity distribution. The least-square iterative algorithm calculated the inversion of the resistivity distribution for this model with the MT2DInvMatlab subroutine (Lee et al., 2009) for a fault model tested by Sasaki (1989).

We chose nine frequencies to test this model, which are 0.1, 0.2, 0.5, 1.0, 2.0, 5.0, 10.0, 20.0, and 50.0 Hz (Lee et al., 2009). The computational domain was set as 200 km × 100 km, and the resistivity value for the extended region was designed as $50\ \Omega \cdot \mathrm{m}$. We chose four GLL points for each element in the y-direction and z-direction, and 25 points per element. Figures 14, 15 show the pseudo-sections of the apparent resistivity and phase for this smooth model in the TM mode and the TE mode. By comparing the spectral element results and the finite element results, we found that the accuracy of the two ways is almost the same, and the results agree well.

6 Conclusion

The spectral element method combined with the GLL point interpolating scheme has been developed for the first time to solve the two-dimensional magnetotelluric forward problem. We presented the spectral element formulas and implemented this algorithm. Compared with the finite difference scheme and the finite element technique, our spectral element approach requires fewer elements and produces accurate results. In the first investigation, we apply the spectral element strategy on a simple half-space geo-electric model to test its high accuracy. We presented the comparison results of the finite difference algorithm and the spectral element algorithm for the COMMEMI 2D-1 model. The accuracy of our spectral element method is better than that of the finite difference approach. We compare the numerical results from Wannamaker et al. (1986) and our spectral element scheme for a ridge topographical model, and they agree well. These results demonstrate the effectiveness and flexibility of the spectral element forward algorithm. We also applied the spectral element method to a model with a smooth resistivity structure and compared the simulation results with those of the finite element code (Lee et al., 2009). This shows that the calculation results of the spectral element algorithm are as smooth and accurate as those of the finite element method. These measurements and comparative results suggest that the spectral element method can provide another effective scheme for the two-dimensional magnetotelluric forward problem.

Data availability statement

The raw data supporting the conclusion of this article will be made available by the authors, without undue reservation.

Author contributions

All authors participated in editing and reviewing the manuscript. XT derived the linear equation system of the spectral element approach and developed the numerical simulation code. YS performed the numerical experiments and result analysis. BZ plotted some of the figures. All authors read and agreed to the submitted version of the manuscript.

Funding

This research work was partly supported by the National Natural Science Foundation of China under grants 42274083 and 41974049, and partly by the Hunan National Natural Science Foundation under Grant 2023JJ30411.

Acknowledgments

The authors would like to thank Syed Muzyan Shahzad, who modified the whole paper for English writing and gave excellent suggestions to improve the writing quality. They would also like to thank Dawei Gao for checking the numerical results of the paper. Last but not least, they thank reviewers and editors for their helpful suggestions and for improving the manuscript.

Conflict of interest

The authors declare that the research was conducted in the absence of any commercial or financial relationships that could be construed as a potential conflict of interest.

Publisher's note

All claims expressed in this article are solely those of the authors and do not necessarily represent those of their affiliated organizations, or those of the publisher, the editors, and the reviewers. Any product that may be evaluated in this article, or claim that may be made by its manufacturer, is not guaranteed or endorsed by the publisher.

References

Avdeeva, A., Avdeev, D., and Jegen, M. (2012). Detecting a salt dome overhang with magnetotellurics: 3D inversion methodology and synthetic model studies. *Geophysics* 77 (4), 251–263. doi:10.1190/geo2011-0167.1

Azeez, K. K., Patro, P. K., Harinarayana, T., and Sarma, S. V. (2017). Magnetotelluric imaging across the tectonic structures in the eastern segment of the Central Indian Tectonic Zone: Preserved imprints of polyphase tectonics and evidence for suture status of the Tan Shear. *Precambrian Res.* 298, 325–340. doi:10.1016/j.precamres.2017.06.018

Barcelona, H., Favetto, A., Peri, V., Pomposiello, C., and Ungarelli, C. (2013). The potential of audio magnetotellurics in the study of geothermal fields: A case study from the northern segment of the La candelaria range, northwestern Argentina. *J. Appl. Geophys.* 88 (1), 83–93. doi:10.1016/j.jappgeo.2012.10.004

Benjamin, M. L., Unsworth, J. H., Jeremy, P. R., Jean, M. L., and Legault, J. M. (2018). 3D joint inversion of magnetotelluric and airborne tipper data: A case study from the morrison porphyry Cu–Au–Mo deposit, British columbia, Canada. *Geophys. Prospect.* 66 (2), 397–421. doi:10.1111/1365-2478.12554

Bihlo, A., Farquharson, C. G., Haynes, R. D., and Loredo-Osti, J. C. (2017). Probabilistic domain decomposition for the solution of the two-dimensional magnetotelluric problem. *Comput. Geosci.* 21 (1), 117–129. doi:10.1007/s10596-016-9598-8

Chave, A. D., and Jones, A. G. (2012). *The magnetotelluric method: Theory and practice*. Cambridge: Cambridge University Press.

Chen, J., Haber, E., and Oldenburg, D. W. (2002). Three-dimensional numerical modeling and inversion of magnetometric resistivity data. *Geophys. J. Int.* 149 (3), 679–697. doi:10.1046/j.1365-246X.2002.01688.x

deGroot-Hedlin, C. (2006). Finite-difference modeling of magnetotelluric fields: Error estimates for uniform and nonuniform grids. *Geophysics* 71 (3), 97–106. doi:10.1190/1.2195991

deGroot-Hedlin, N. C., and Constable, S. (1990). Occam's inversion generates smooth, two-dimensional models from magnetotelluric data. *Geophysics* 55 (12), 1613–1624. doi:10.1190/1.1442813

Du, H. K., Ren, Z. Y., and Tang, J. T. (2016). A finite-volume approach for 2D magnetotellurics modeling with arbitrary topographies. *Studia Geophys. Geod.* 60 (2), 332–347. doi:10.1007/s11200-014-1041-9

Franke, A., Börner, R. U., and Spitzer, K. (2007). Adaptive unstructured grid finite element simulation of two-dimensional magnetotelluric fields for arbitrary surface and seafloor topography. *Geophys. J. Int.* 171 (1), 71–86. doi:10.1111/j.1365-246X.2007.03481.x

Gharti, H. N., Tromp, J., and Zampini, S. (2018). Spectral-infinite-element simulations of gravity anomalies. *Geophys. J. Int.* 215 (2), 1098–1117. doi:10.1093/gji/ggy324

Guo, R., Li, M., Yang, F., Xu, S., and Abubakar, A. (2020). Application of supervised descent method for 2D magnetotelluric data inversion. *Geophysics* 85 (4), 53–65. doi:10.1190/geo2019-0409.1

Guo, Z. Q., Egbert, G. D., and Wei, W. B. (2018). Modular implementation of magnetotelluric 2D forward modeling with general anisotropy. *Comput. Geosciences* 118, 27–38. doi:10.1016/j.cageo.2018.05.004

Huang, X., Farquharson, C. G., Yin, C., Yan, L., Cao, X., and Zhang, B. (2021). A 3D forward-modeling approach for airborne electromagnetic data using a modified spectral-element method. *Geophysics* 86 (5), 343–354. doi:10.1190/geo2020-0004.1

Huang, X., Yin, C., Farquharson, C. G., Cao, X., Zhang, B., Huang, W., et al. (2019). Spectral-element method with arbitrary hexahedron meshes for time-domain 3D airborne electromagnetic forward modeling. *Geophysics* 84 (1), 37–46. doi:10.1190/geo2018-0231.1

Jiang, W., Duan, J., Doublier, M., Clark, A., Schofield, A., Brodie, R., et al. (2022). Application of multiscale magnetotelluric data to mineral exploration: An example from the east tennant region, northern Australia. *Geophys. J. Int.* 229 (2), 1628–1645. doi:10.1093/gji/ggac029

Kalscheuer, T., Juhojuntti, N., and Vaittinen, K. (2018). Two-dimensional magnetotelluric modelling of ore deposits: Improvements in model constraints by inclusion of borehole measurements. *Surv. Geophys.* 39 (3), 467–507. doi:10.1007/s10712-017-9454-y

Kelbert, A., Meqbel, N., Egbert, G. D., and Tandon, K. (2014). ModEM: A modular system for inversion of electromagnetic geophysical data. *Comput. Geosciences* 66, 40–53. doi:10.1016/j.cageo.2014.01.010

Key, K., and Weiss, C. (2006). Adaptive finite-element modeling using unstructured grids: The 2D magnetotelluric example. *Geophysics* 71 (6), 291–299. doi:10.1190/1.2348091

Komatitsch, D., and Tromp, J. (1999). Introduction to the spectral element method for three-dimensional seismic wave propagation. *Geophys. J. Int.* 139 (3), 806–822. doi:10.1046/j.1365-246x.1999.00967.x

Kumar, K., Gupta, P. K., and Niwas, S. (2011). Efficient two-dimensional magnetotellurics modelling using implicitly restarted Lanczos method. *J. Earth Syst. Sci.* 120 (4), 595–604. doi:10.1007/s12040-011-0093-2

Lee, J. H., and Liu, Q. H. (2005). An efficient 3-D spectral-element method for Schrodinger equation in nanodevice simulation. *IEEE Trans. Computer-Aided Des. Integr. Circuits Syst.* 24 (2), 1848–1858. doi:10.1109/TCAD.2005.852675

Lee, S. K., Kim, H. J., Song, Y., and Lee, C. K. (2009). MT2Dinvmatlab—A program in MATLAB and FORTRAN for two-dimensional magnetotelluric inversion. *Comput. Geosciences* 35 (8), 1722–1734. doi:10.1016/j.cageo.2008.10.010

Liang, J. W., Tong, D. F., Tan, F., Jiao, Y. Y., and Yan, C. W. (2021). Two-Dimensional magnetotelluric modelling based on the numerical manifold method. *Eng. Analysis Bound. Elem.* 124 (1), 87–97. doi:10.1016/j.enganabound.2020.12.011

Liao, X., Shi, Z., Zhang, Z., Yan, Q., and Liu, P. (2022). 2D inversion of magnetotelluric data using deep learning technology. *Acta Geophys.* 70, 1047–1060. doi:10.1007/s11600-022-00773-z

Luo, Y., Tromp, J., Denel, B., and Calandra, H. (2013). 3D coupled acoustic-elastic migration with topography and bathymetry based on spectral-element and adjoint methods. *Geophysics* 78 (4), 193–202. doi:10.1190/geo2012-0462.1

Lyu, C., Capdeville, Y., and Zhao, L. (2020). Efficiency of the spectral element method with very high polynomial degree to solve the elastic wave equation. *Geophysics* 85 (1), 33–43. doi:10.1190/geo2019-0087.1

Martin, R., Chevrot, S., Komatitsch, D., Seoane, L., Spangenberg, H., Wang, Y., et al. (2017). A high-order 3D spectral-element method for the forward modelling and inversion of gravimetric data - application to the Western Pyrenees. *Geophys. J. Int.* 209 (1), ggx010–424. doi:10.1093/gji/ggx010

Nagarjuna, D., Rao, C. K., Pavankumar, G., Kumar, A., and Manglik, A. (2021). Magnetotelluric evidence for an Archaean – proterozoic lithospheric assemblage within the Cambay rift basin, Western India, and its role in channeling of plume-derived fluids within the basin. *Tectonophysics* 818, 229064. doi:10.1016/j.tecto.2021.229064

Pan, K., Wang, J., Hu, S., Ren, Z., Cui, T., Guo, R., et al. (2022). An efficient cascadic multigrid solver for 3-D magnetotelluric forward modelling problems using potentials. *Geophys. J. Int.* 230 (3), 1834–1851. doi:10.1093/gji/ggac152

Patera, A. T. (1984). A spectral element method for fluid dynamics: Laminar flow in a channel expansion. *J. Comput. Phys.* 54 (3), 468–488. doi:10.1016/0021-9991(84)90128-1

Patro, P. K. (2017). Magnetotelluric studies for hydrocarbon and geothermal resources: Examples from the asian region. *Surv. Geophys.* 38, 1005–1041. doi:10.1007/s10712-017-9439-x

Pek, J., and Verner, T. (1997). Finite-difference modelling of magnetotelluric fields in two-dimensional anisotropic media. *Geophys. J. Int.* 128 (3), 505–521. doi:10.1111/j.1365-246X.1997.tb05314.x

Pozrikidis, C. (2014). *Introduction to finite and spectral element methods using MATLAB*. New York: Chapman and Hall Press.

Rao, K. P., and Babu, G. A. (2006). EMOD2D—A program in C++ for finite difference modeling of magnetotelluric TM mode responses over 2D Earth. *Comput. Geosciences* 32 (9), 1499–1511. doi:10.1016/j.cageo.2006.02.017

Rodi, W., and Mackie, R. L. (2001). Nonlinear conjugate gradients algorithm for 2-D magnetotelluric inversion. *Geophysics* 66 (1), 174–187. doi:10.1190/1.1444893

Sarakorn, W. (2017). 2-D magnetotelluric modeling using finite element method incorporating unstructured quadrilateral elements. *J. Appl. Geophys.* 139, 16–24. doi:10.1016/j.jappgeo.2017.02.005

Sarakorn, W., and Vachiratienchai, C. (2018). Hybrid finite difference–finite element method to incorporate topography and bathymetry for two-dimensional magnetotelluric modeling. *Earth, Planets Space* 70 (1), 103. doi:10.1186/s40623-018-0876-7

Sasaki, Y. (1989). Two-dimensional joint inversion of magnetotelluric and dipole-dipole resistivity data. *Geophysics* 54 (2), 254–262. doi:10.1190/1.1442649

Seriani, G., and Oliveira, S. P. (2008). Dispersion analysis of spectral element methods for elastic wave propagation. *Wave Motion* 45 (8), 729–744. doi:10.1016/j.wavemoti.2007.11.007

Siripunvaraporn, W., and Egbert, G. D. (2007). Data space conjugate gradient inversion for 2-D magnetotelluric data. *Geophys. J. Int.* 170 (3), 986–994. doi:10.1111/j.1365-246X.2007.03478.x

Tarek, A. H., Mohamed, A. Z., Gad, E. Q., Hossam, M., Samah, E., and Yasuhiro, F. (2023). Deep heat source detection using the magnetotelluric method and geothermal assessment of the Farafra Oasis, Western Desert, Egypt. *Geothermics* 109, 102648. doi:10.1016/j.geothermics.2023.102648

Tong, X., Guo, Y., and Xie, W. (2018). Finite difference algorithm on non-uniform meshes for modeling 2D magnetotelluric responses. *Algorithms* 11 (2), 203–217. doi:10.3390/a11120203

Tong, X., Sun, Y., and Guo, R. (2020). A Chebyshev pseudo-spectral approach for simulating magnetotelluric TM-mode responses on 2D structures. *J. Appl. Geophys.* 179, 104085. doi:10.1016/j.jappgeo.2020.104085

Trinh, R. T., Brossier, R., Metiver, L., Tavard, L., and Virieus, J. (2019). Efficient time-domain 3D elastic and viscoelastic full-waveform inversion using a spectral-element method on flexible Cartesian-based mesh. *Geophysics* 84 (1), 61–83. doi:10.1190/geo2018-0059.1

Unsworth, M. (2010). Magnetotelluric studies of active continent-continent collisions. *Surv. Geophys.* 31 (2), 137–161. doi:10.1007/s10712-009-9086-y

van der Vorst, H. A. (1992). Bi-CGSTAB: A fast and smoothly converging variant of Bi-cg for the solution of nonsymmetric linear systems. *SIAM J. Sci. Comput.* 13 (2), 631–644. doi:10.1137/0913035

Wang, N., Tang, J., Ren, Z., Xiao, X., and Huang, X. (2019). Two-dimensional magnetotelluric anisotropic forward modeling using finite-volume method. *Chin. J. Geophys.* 62 (10), 3912–3922. doi:10.6038/cjg2019M0498

Wannamaker, P. E., Stodt, J. A., and Rijo, L. (1987). A stable finite element solution for two-dimensional magnetotelluric modelling. *Geophys. J. Int.* 88 (1), 277–296. doi:10.1111/j.1365-246X.1987.tb01380.x

Wannamaker, P. E., Stodt, J. A., and Rijo, L. (1986). Two-dimensional topographic responses in magnetotellurics modeled using finite elements. *Geophysics* 51 (11), 2131–2144. doi:10.1190/1.1442065

Weiss, M., Kalscheuer, T., and Ren, Z. (2023). Spectral element method for 3-D controlled-source electromagnetic forward modelling using unstructured hexahedral meshes. *Geophys. J. Int.* 232 (2), 1427–1454. doi:10.1093/gji/ggac358

Wittke, J., and Tezkan, B. (2014). Meshfree magnetotelluric modelling. *Geophys. J. Int.* 198 (2), 1255–1268. doi:10.1093/gji/ggu207

Wittke, J., and Tezkan, B. (2021). Two-dimensional meshless modelling and TE-mode inversion of magnetotelluric data. *Geophys. J. Int.* 226 (2), 1250–1261. doi:10.1093/gji/ggab147

Xu, J., Tang, J., and Xiao, X. (2022). A hybrid spectral element-infinite element approach for 3D controlled-source electromagnetic modeling. *J. Appl. Geophys.* 200, 104619. doi:10.1016/j.jappgeo.2022.104619

Xu, S., and Zhou, H. (1997). Modelling the 2D terrain effect on MT by the boundary-element method. *Geophys. Prospect.* 45 (6), 931–943. doi:10.1046/j.1365-2478.1997.610301.x

Yao, H., Ren, Z., Chen, H., Tang, J., Li, Y., and Liu, X. (2021). Two-dimensional magnetotelluric finite element modeling by a hybrid Helmholtz-curl formulae system. *J. Comput. Phys.* 443, 110533. doi:10.1016/j.jcp.2021.110533

Yin, C., Liu, L., Liu, Y., Zhang, B., Qiu, C., and Huang, X. (2019). 3D frequency-domain airborne EM forward modelling using spectral element method with Gauss-Lobatto-Chebyshev polynomials. *Explor. Geophys.* 50 (5), 461–471. doi:10.1080/08123985.2019.1614162

Zhang, K., Wei, W., Lu, Q., Dong, H., and Li, Y. (2014). Theoretical assessment of 3-D magnetotelluric method for oil and gas exploration: Synthetic examples. *J. Appl. Geophys.* 106, 23–36. doi:10.1016/j.jappgeo.2014.04.003

Zhdanov, M. S., Varentsov, I. M., Weaver, J. T., Golubev, N. G., and Krylov, V. A. (1997). Methods for modelling electromagnetic fields results from COMMEMI—The international project on the comparison of modelling methods for electromagnetic induction. *J. Appl. Geophys.* 37 (3-4), 133–271. doi:10.1016/S0926-9851(97)00013-X

Zhou, Y., Shi, L., Liu, N., Zhu, C., Liu, H., and Liu, Q. (2016). Spectral element method and domain decomposition for low-frequency subsurface EM simulation. *IEEE Geoscience Remote Sens. Lett.* 13 (4), 550–554. doi:10.1109/LGRS.2016.2524558

Zhu, J., Yin, C., Liu, Y., Liu, Y., Liu, L., Yang, Z., et al. (2020). 3-D dc resistivity modelling based on spectral element method with unstructured tetrahedral grids. *Geophys. J. Int.* 220 (3), 1748–1761. doi:10.1093/gji/ggz534

Zou, P., and Cheng, J. (2018). Pseudo-spectral method using rotated staggered grid for elastic wave propagation in 3D arbitrary anisotropic media. *Geophys. Prospect.* 66 (1), 47–61. doi:10.1111/1365-2478.12543

frontiers | Frontiers in Earth Science

TYPE Original Research
PUBLISHED 13 July 2023
DOI 10.3389/feart.2023.1206784

OPEN ACCESS

EDITED BY
Cong Zhou,
East China University of Technology, China

REVIEWED BY
Octavio Castillo Reyes,
Barcelona Supercomputing Center, Spain
Ronghua Peng,
China University of Geosciences Wuhan, China

*CORRESPONDENCE
Dajun Li,
lidajun@jlju.edu.cn

RECEIVED 16 April 2023
ACCEPTED 26 June 2023
PUBLISHED 13 July 2023

CITATION
Li D, Wang Z, Li Y and Jin L (2023), A general forward solver for 3D CSEMs with multitype sources and operating environments.
Front. Earth Sci. 11:1206784.
doi: 10.3389/feart.2023.1206784

A general forward solver for 3D CSEMs with multitype sources and operating environments

Dajun Li[1]*, Zhiqiang Wang[1], Yabin Li[2] and Liubiao Jin[1]

[1]College of Surveying and Prospecting Engineering, Jilin Jianzhu University, Changchun, China, [2]College of GeoExploration Science and Technology, Jilin University, Changchun, China

To determine the electromagnetic (EM) fields of different three-dimensional (3D) controlled-source electromagnetic methods (CSEMs) using the same parameters of the forward solution, by explicitly considering the commonalities, we present a general 3D forward modeling solver for CSEMs with multitype sources and operating environments. The commonality of the solver is reflected in two aspects. First, the solver is based on a frequency-domain (FD) vector Helmholtz equation for determining the scattered electric field. The different types of sources are imposed on the right-hand term of the equation, expressed as background Green's function. Second, sources of any CSEM can be composed of electric dipole (ED) or magnetic dipole (MD) superposition. Thus, the focus of the 3D forward modeling of CSEMs is reduced to determining the EM fields of ED or MD sources for the background medium. The quasi-minimal residual (QMR) method is used to solve the large sparse complex linear system. Once the FD EM fields have been calculated, the time-domain (TD) response can be obtained using the cosine/sine transformation. The numerical results show that the relative error is less than 5% between the 3D numerical and analytical solutions, which verifies the accuracy of the solver. We further study the difference between the real (bent) and theoretical (straight) wires. We suggest that the shape of the source must be considered for TD and FD CSEMs with a wire source during data processing and inversion. The last example investigated the characteristics of FD EM fields from a finite-length wire and TD EM fields from a rectangular fixed loop on the same conductive tilted disk model buried in resistive sediments. According to the numerical results, we recommend FD CSEMs with a wire source for detecting deep anomalies.

KEYWORDS

CSEMs, 3D forward modeling solver, multitype sources, operating environments, frequency/time domain

1 Introduction

Controlled-source electromagnetic methods (CSEMs) are a group of geophysical exploration methods that transmit an electromagnetic (EM) signal using an artificial source (Goldstein and Strangway, 1975; Zonge and Hughes, 1991; Constable and Srnka, 2007; Di et al., 2020). CSEMs exhibit various classifications based on different factors, such as the type of source (e.g., wire, loop, electric, and magnetic dipole) and the operating environment (e.g., land, marine, airborne, and borehole), including marine frequency-/time-domain EM methods (mFD/TDCSEMs) (Edwards, 2005; Um and Alumbaugh, 2007; Connell and Key, 2013), long- and short-offset transient EM methods (L/SOTEMs) (Commer and Newman, 2004; Xue, 2018), controlled-source audio-frequency

magnetotelluric (CSAMT) methods (Weng et al., 2012; Yang and Oldenburg, 2016), and land/airborne transient EM methods (TEMs) (Yin et al., 2016; Li et al., 2018; Zhang et al., 2018). By examining and analyzing the distribution patterns of the EM fields of CSEMs associated with variations in the resistivity of underground media, geophysicists can explore mineral and hydrocarbon resources (Hu et al., 2013; Streich, 2016; Schaller et al., 2018; Castillo-Reyes et al., 2022) and address geological and environmental engineering challenges (Everett, 2009; Chave et al., 2017; Malovichko et al., 2019; Castillo-Reyes et al., 2022).

Forward modeling is an effective way to study the EM field laws of CSEMs, and it is also the premise and basis of inversion methods (Avdeev, 2005; Börner, 2010). Over the past decades, innovations in numerical calculations have driven remarkable progress in the three-dimensional (3D) forward modeling of CSEMs, achieving successful breakthroughs (Constable, 2010; Ansari and Farquharson, 2013; Börner et al., 2015; Oldenburg et al., 2020; Werthmüller et al., 2021). The common methods used for developing the 3D forward modeling of CSEMs include finite element techniques (Tonti, 2002; Um et al., 2012; Cai et al., 2014; Rochlitz et al., 2019; Castillo-Reyes et al., 2022), finite volume methods (Haber and Ascher, 2001; Ren et al., 2017; Peng et al., 2018), finite difference methods (Newman and Alumbaugh, 1995; Weiland, 1996; Li et al., 2022), integral equation techniques (Hursán and Zhdanov, 2002; Tang et al., 2018), and spectral element methods (Huang et al., 2019; Xu and Tang, 2022). Furthermore, numerous scholars have dedicated research efforts to enhance the efficiency of numerical solutions in 3D forward modeling for CSEMs. They have employed parallel programming and numerical computation platforms to accelerate the computation speed (Unno et al., 2012; Koldan et al., 2014; Castillo-Reyes et al., 2018; Castillo-Reyes et al., 2019; Castillo-Reyes et al., 2022; Liu et al., 2023).

By employing forward modeling of different CSEMs, geophysical companies, scientific institutions, and individuals can compare the characteristics of EM responses and determine which CSEM offers the strongest resolution for specific geological targets while optimizing the survey parameter design before conducting field studies. However, the majority of forward modeling codes have been developed by various scientific institutions using different programming languages and focusing on a single CSEM with a specific source type and operating environment. The code of each CSEM is based on different essential mathematical procedures and utilizes different parameters for forward solutions, such as grids, interpolations, stations, numerical solution methods, and staggering schemes. These variations in parameterization can introduce biases during resolution analysis. Meanwhile, the expensive cost of secondary development for those codes poses practical challenges. The application effectiveness of a CSEM is influenced by the complexity and risk associated with the forward modeling theory. Technology implementation is the underlying support for practical applications. Therefore, it is necessary to decouple practical applications and concrete mathematical technology to advance geophysical science.

To simplify the forward theory and analyze the EM characteristics of different CSEMs for the same targets using the same parameters of the forward solution and mathematical procedures, we integrated forward modeling technologies and developed a forward solver for CSEMs with multitype sources and operating environments. In this study, our approach involves decomposing the total EM fields into the primary/background fields and secondary/scattered fields. This decomposition helps eliminate the singularity of the EM fields near the source. The primary field can be calculated by using the frequency-domain (FD) and full-space Green's function of the source in a one-dimensional (1D) layered medium. The secondary field can be obtained by solving an FD vector Helmholtz equation for the scattered electric field, which is the reusable design part of the forward modeling for CSEMs. The procedure is the same regardless of the source type used to generate this field and regardless of operating in land, marine, airborne, or borehole environments.

On the other hand, any source type can be viewed as a combination of electric dipoles (EDs) or magnetic dipoles (MDs), each of which can be further decomposed into two horizontal EDs or MDs along the x and y directions, and one vertical ED or MD along the z direction. Thus, the focus of 3D forward modeling of CSEMs is reduced to solving EM fields for the background medium for ED or MD sources. By employing this approach, we can analyze the EM characteristics of different CSEMs using the same parameters for the forward solution, thus enhancing the comparability and understanding of the results.

The forward solver defines the overall structures and the main responsibilities of each module, thereby reducing the difficulty of solving EM fields of CSEMs and simplifying the implementation process of the theory. By avoiding the need to repeatedly construct the underlying mathematical logic, this approach enables geophysicists to focus on their unique application innovation. This paper first gives a brief overview of the mathematical methodology for 3D FD modeling of CSEMs. Once the FD EM fields have been calculated, the time-domain (TD) response can be obtained using the cosine/sine transformation. Then, the accuracy of the solver is verified by comparing the 3D modeling results with reference results obtained from 1D and 3D numerical solutions. Finally, we present two 3D modeling examples and discuss the effects of source shape and type on the EM fields of CSEMs over a 3D conductive Earth model.

2 Methodology

2.1 Maxwell's equations

Assuming harmonic time dependence $e^{-i\omega t}$, Maxwell's equations for the EM fields in the FD can be written as (Streich, 2009)

$$\nabla\times \mathbf{E} = -i\omega\mu_0\mathbf{H}, \tag{1}$$

$$\nabla\times \mathbf{H} = \mathbf{J} + \sigma^{*}\mathbf{E}, \tag{2}$$

where $i^2 = -1$, $\omega = 2\pi f$ is the angular frequency, f is the frequency, $\mathbf{E}$ and $\mathbf{H}$ denote the total electric and magnetic fields, μ_0 within the Earth is assumed to be constant and set to that of free space, $\mathbf{J}$ is the source current distribution, $\sigma^{*} = \sigma + i\omega\varepsilon$ is the ohmic conduction term, σ is the electric conductivity, ε represents the air dielectric constant, and $\sigma^{*}\mathbf{E}$ describes the induced currents inside the Earth. According to Eqs 1, 2, the expression of the FD vector Helmholtz equation for the scattered electric field is as follows (Alumbaugh et al., 1996):

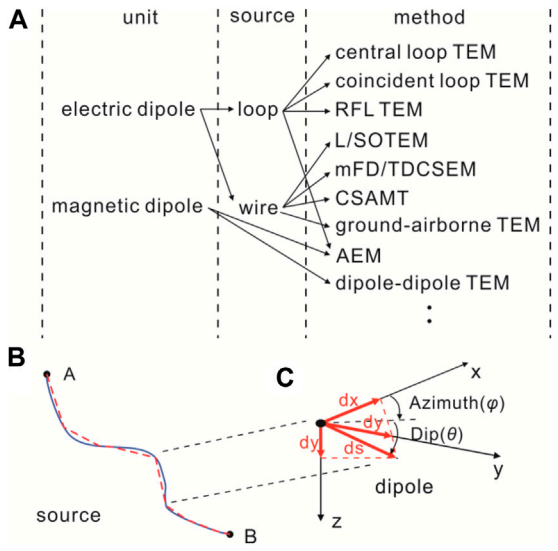

FIGURE 1
The electric or magnetic dipole is used as the unit of any CSEM sources **(A)**. Finite-length wire source of LOTEM **(B)**; A and B are the endpoints of the source, the solid line represents the real layout of the source, and the dotted line represents the source that is discretized by electric dipoles. Vector decomposition of an electric dipole **(C)**.

$$\nabla\times\nabla\times \mathbf{E}^{s} - k^{2}\mathbf{E}^{s} = \left(k^{2} - k_{p}^{2}\right)\mathbf{E}^{p}, \tag{3}$$

where $k^2 = -i\omega\mu_0(\sigma + i\omega\varepsilon)$, the superscripts "p" and "s" represent the primary and scattered fields, respectively, and $\mathbf{E}^s$ and $\mathbf{E}^p$ denote the scattered and primary electrical fields, respectively. Eq. 3 forms the basis of the presented modeling scheme and is well suited for simulations in CSEMs. Eq. 3 can overcome the difficulty of source description and the influence of source singularity on the numerical stability. Regardless of the type of source used to create the field, the procedure for calculating the scattered field remains the same. Then, we obtain the following PDE for the component $\hat{\mathbf{i}}$:

$$\frac{\partial^2 E_y^s}{\partial x\partial y} - \frac{\partial^2 E_x^s}{\partial y^2} - \frac{\partial^2 E_x^s}{\partial z^2} + \frac{\partial^2 E_z^s}{\partial x\partial z} - k^2 E_x = \left(k^2 - k_p^2\right)E_x^p. \tag{4}$$

2.2 The multitype source

In this paper, we adopt the ED or MD as the basic composition unit for any complex geometry source (Figure 1A). For example, the signal emission source of the LOTEM can be decomposed into many EDs (Figure 1B), and vector decomposition is applied to each ED (Figure 1C). The EM fields at any given position can be obtained by superimposing the EM fields generated by the ED component along the *x*, *y*, and *z* directions. Therefore, the primary objective of 3D forward modeling in CSEMs, regardless of the specific source type used, is to solve the electric field of an electric dipole or a magnetic dipole within the background models.

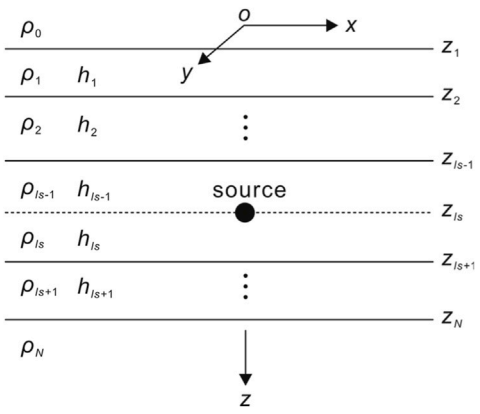

FIGURE 2
Homogeneous stratified medium with an EM transmitting source embedded in an intermediate layer. *N* is the number of layers, $\rho_0, \rho_1, \rho_2, \ldots, \rho_N$ are individual layer resistivities, $h_0, h_1, h_2, \ldots, h_N$ are layer thicknesses, and $z_1, z_2, \ldots, z_N$ denote the depth of the layer. The solid black circle denotes that the source is located at z_{ls} in the ls^{th} layer, and the dashed line denotes that a virtual interface is added at the source location parallel to the layer boundaries.

2.3 Background models for primary fields

The primary field, as described by Weng et al. (2016), employs a virtual interface technique (Das and De Hoop, 1995) to solve the whole-space EM fields in a 1D layer model for different types of sources (Figure 2). These sources include vertical and horizontal electric dipoles (VED and HED) as well as vertical and horizontal magnetic dipoles (VMD and HMD).

By separating the partial wave solutions of the Helmholtz equations into upward and downward waves within certain boundaries, the potentials for Green's function are obtained. Starting from the source level, the amplitudes of the potentials in each layer are derived recursively based on the initial amplitudes. For different types of sources, only the initial terms that are associated with the transmitting sources need to be modified, and the kernel connected to the layered media remains the same. Hence, the aforementioned scheme can be easily applied to EM transmitting sources with slight modifications.

2.4 FD discretization

To calculate the scattered electric field in the medium, the geoelectric model is discretized by the cuboid cell (including the air layer) (Figure 3A), each denoted by a subscript (i, j, and k). The resistivity of each cell is represented by the symbol ρ (i, j, and k). i, j, and k represent the mesh indices in the *x*, *y*, and *z* directions, ranging from 1 to Nx, Ny, and Nz, respectively. Nx, Ny, and Nz denote the numbers of cells in the *x*, *y*, and *z* directions, respectively. Therefore, Eq. 4 can be discretized using the 3D staggered-grid finite-difference method, and the discretized expression is given in Eq. 5. The electric field components are defined on cell edges, while the magnetic field components naturally correspond to the cell faces (Figure 3B). The

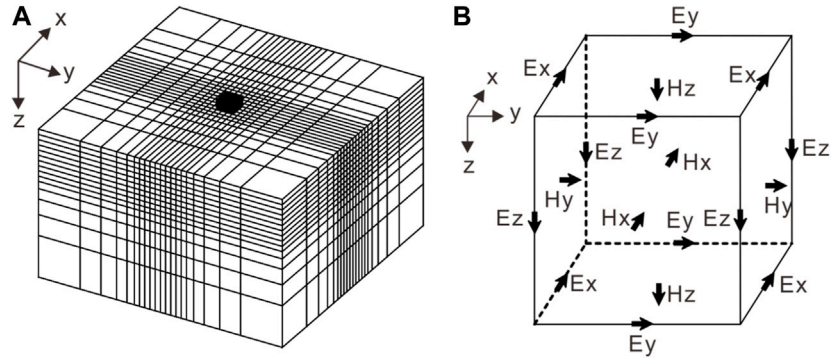

FIGURE 3
Staggered finite-difference grid for 3D CSEM forward modeling **(A)**; the solid black cuboid indicates the survey area. The electric field components are defined on cell edges, and the magnetic field components can be defined naturally on the cell faces **(B)**.

discrete finite difference equations of the $\hat{\mathbf{j}}$ and $\hat{\mathbf{k}}$ components are given in Appendix A.

$$\begin{aligned}
&\left\{\left[\frac{1}{\Delta x_i}\left(E^s_{y_{i+1,j+1/2,k}}-E^s_{y_{i,j+1/2,k}}\right)-\frac{1}{\Delta y_j}\left(E^s_{x_{i+1/2,j+1,k}}-E^s_{x_{i+1/2,j,k}}\right)\right]\right.\\
&\left.-\left[\frac{1}{\Delta x_i}\left(E^s_{y_{i+1,j-1/2,k}}-E^s_{y_{i,j-1/2,k}}\right)-\frac{1}{\Delta y_{j-1}}\left(E^s_{x_{i+1/2,j,k}}-E^s_{x_{i+1/2,j-1,k}}\right)\right]\right\}\cdot\frac{1}{\Delta\bar{y}_j}\\
&+\left\{\left[\frac{1}{\Delta x_i}\left(E^s_{z_{i+1,j,k+1/2}}-E^s_{z_{i,j,k+1/2}}\right)-\frac{1}{\Delta z_k}\left(E^s_{x_{i+1/2,j,k+1}}-E^s_{x_{i+1/2,j,k}}\right)\right]\right.\\
&\left.-\left[\frac{1}{\Delta x_i}\left(E^s_{z_{i+1,j,k-1/2}}-E^s_{z_{i,j,k-1/2}}\right)-\frac{1}{\Delta z_{k-1}}\left(E^s_{x_{i+1/2,j,k}}-E^s_{x_{i+1/2,j,k-1}}\right)\right]\right\}\cdot\frac{1}{\Delta\bar{z}_k}\\
&+i\omega\mu_p\hat{y}_pE^s_{x_{i+1/2,j,k}}\\
&=-i\omega\mu_p\left(\hat{y}_{i+1/2,j,k}-\hat{y}_p\right)E^p_{x_{i+1/2,j,k}},
\end{aligned}\tag{5}$$

where $\hat{y}=\sigma+i\omega\varepsilon$, $w=x, y, z$, and $l=i, j, k$ denote the length of the lth cell in the w direction, and $\Delta\overline{w_l}$ is the distance between the center of the lth and $l1$th cells in the w direction.

2.5 Preconditioning and numerical implementation

Equation 5 can be assembled into the following system:

$$\mathbf{KE}^s=\mathbf{b},\tag{6}$$

where $\mathbf{K}$ is the coefficient matrix, and $\mathbf{b}$ in the right-hand side consists of the dot products between the primary/background field and conductivity abnormalities, as well as the appropriate boundary conditions.

Generally, the coefficient matrix $\mathbf{K}$ for Eq. 6 is a large, sparse, and ill-conditioned matrix that is difficult to solve. To reduce the condition number of the coefficient matrix $\mathbf{K}$, Eq. 6 can be written in the preprocessing form as follows:

$$\left(\mathbf{KM}^{-1}\right)\cdot\mathbf{y}=\mathbf{b}.\tag{7}$$

Here, $\mathbf{y}=\mathbf{ME}^s$ is the modified unknown vector, where the matrix $\mathbf{M}$ is called the (right-hand side) preprocessor, and the matrix $\mathbf{KM}^{-1}$ is considered very close to the identity matrix. Once Eq. 7 is solved approximately, we can obtain $\mathbf{E}^s$ using the relationship between $\mathbf{y}$ and $\mathbf{E}^s$. In this study, an incomplete Cholesky decomposition is used as the precondition to accelerate the convergence and improve the accuracy of the iterative solution. Eq. 7 can be solved by using the quasi-minimal residual method (QMR) (Mackie et al., 1994).

2.6 Boundary conditions and grid generation

Due to the significant difference between the solution region and the anomalous bodies, the secondary field will decay to zero at the boundary far from the anomalous body. As a result, we applied typical homogeneous Dirichlet's boundary conditions. With $\mathbf{n}$ being the normal vector on the domain boundary $\delta\Omega$, it is defined as:

$$\mathbf{n}\times\mathbf{E}^s=\mathbf{0}.\tag{8}$$

The grid generation is centered on the area of interest and is divided into finer grids near the anomaly bodies. As depicted in Figure 3A, the grid size gradually increases as the distance from the area of interest expands. The air layer is set to seven layers, with the uppermost layer having a thickness of 30 km. In our paper, the mini software CSEM mesh is used to generate the mesh, which was developed by teachers and students in our research group. It greatly reduces the cost of generating meshes.

2.7 Divergence correction

The divergence of the secondary electric field $\mathbf{E}^s$ is zero at any point except the source (Shen, 2003; Chen et al., 2011). Due to the accuracy of the numerical calculation, the divergence of $\mathbf{E}^s$ does not disappear during an iteration solution process which can be calculated using $\varphi=\nabla\cdot\mathbf{E}^s$, considering the additional electrical field generated by the source φ. To calculate the additional electrical field, it is necessary to use the Neumann boundary conditions to solve the potential obtained by Poisson's equation as follows:

$$\nabla\cdot\nabla\psi=\varphi.\tag{9}$$

When Eq. 6 is solved, the $\mathbf{E}^s$ values required for divergence correction can be expressed as follows:

$$\mathbf{E}^s_{\text{correct}} = \mathbf{E}^s_{\text{old}} - \nabla\psi, \tag{10}$$

specifically, to satisfy the following equation:

$$\nabla \cdot \mathbf{E}^s_{\text{correct}} = \nabla \cdot \mathbf{E}^s_{\text{old}} - \nabla \cdot \nabla\psi = \varphi - \varphi = 0. \tag{11}$$

The preconditioned conjugate gradient (PCG) algorithm is used to solve the divergence in Eq. 11. The iterative solution's convergence rate is greatly improved, particularly at low frequencies (Smith, 1996a; Smith, 1996b).

2.8 FD EM field interpolation to receiver positions

Once $\mathbf{E}^s$ on the center of the grid edge is obtained by Eq. 6, the total electric field $\mathbf{E}$ can be estimated by adding a primary field $\mathbf{E}^p$, that is,

$$\mathbf{E} = \mathbf{E}^p + \mathbf{E}^s, \tag{12}$$

while the total magnetic field normal to the surface confined by the grid edge at the center can be approximated by Faraday's law:

$$-i\omega\mathbf{B} = \nabla\times \mathbf{E}, \tag{13}$$

from the estimated EM fields. Then, the EM fields at the position of interest can be interpolated by

$$\mathbf{E} = \mathbf{L}_e\mathbf{E} \tag{14}$$

and

$$\mathbf{H} = \mathbf{L}_h\mathbf{H}, \tag{15}$$

where $\mathbf{L}_e$ and $\mathbf{L}_h$ represent bilinear splines from the 3D grid nodes and edges, respectively, to the data sites.

2.9 TD EM responses

According to Weng et al. (2017), the TD EM signal $h(t)$ through

$$h(t) = \frac{1}{2\pi}\int_0^\infty I(\omega)H(\omega)e^{-i\omega t}d\omega \tag{16}$$

is related to the FD response H(ω) from a source excited by current $I(\omega)$ over a conductive model; in the aforementioned equation, $i^2 = -1$, $\omega = 2\pi f$ is the angular frequency, f is the frequency, and t is the time. If a step-off current is assumed, using the Euler formula, Eq. 16 can be further split into a sine transformation as follows:

$$dB/dt = \mu_0 dh/dt = -\mu_0\frac{2}{\pi}\int_0^\infty \text{Im}[H(\omega)]\sin(\omega t)d\omega, \tag{17}$$

where B is the magnetic flux density and Im [·] denotes the imaginary part of the FD EM fields. We sample the exact six points per decade FD data between 10^{-3} Hz and 10^8 Hz and obtain 67 frequencies (Liu et al., 2016). After obtaining the FD results, the TD EM responses for the step wave are calculated using Eq. 17. Based on the aforementioned theory, we have programmed a 3D forward modeling code using Fortran 90 for FD/TD CSEMs with multitype sources.

3 Model verification

To test the correctness and reliability of the aforementioned forward modeling solver for different types of sources, we initially design a 100 Ωm uniform half-space model for the airborne EM method (AEM) with a vertical magnetic dipole (VMD) source and a unit current (Liu and Yin, 2013). The flight altitude is set to 30 m, and the receiver is positioned 2 m away from the transmitter (Figure 4A). The model is divided into 20 × 20 × 25 prisms of dimension 10 m × 10 m × 10 m. The background model with 50 Ωm is used for computing the primary field. Figure 4B illustrates the comparisons between the 3D solution and the 1D results using a step-off current waveform. The results of the 3D solution agree well with the 1D result. The overall relative errors are less than 5%. Figure 4C shows a plot of the error *versus* iteration for the QMR solver for the uniform half-space model for the data with the four frequencies. We can clearly see that the QMR solver is stable and converges quickly to the values of 10^{-7}. We obtained similar results for the other models presented in this paper. The total memory required to solve this model was 73.24 MB. It took approximately 4.3 min per frequency to solve this model on a personal computer with an Intel® Core™ i5-2320 processor and 8 GB memory.

Second, we take the RFLTEM as an example, and a loop source with dimensions of 10 m × 10 m can be decomposed into many EDs. A 3D conductive body (50 m × 50 m × 50 m) of 20 Ωm is embedded in a two-layer Earth model in Ji et al. (2017) (Figure 5A). In the numerical simulation, the origin of the coordinate system is at the surface with the *z*-axis downward through the center of the abnormal body. The model is divided into 51 × 51 × 30 prisms of dimension 10 m × 10 m × 10 m. The FD EM fields are calculated at the measurement points Rx_1 and Rx_2 in Figure 5A. Then, dB_z/dt is obtained using Eq. (17), and it was normalized by the square of the single-turn receiving coil. The solution of the forward modeling solver agrees well with that in the study by Ji et al. (2017) (Figure 5B). These examples serve as strong evidence for the accuracy and reliability of our forward modeling code. Figure 5C shows a plot of the error *versus* iteration for the QMR solver for a two-layer model for the data with four frequencies. The error of the QMR solver converges quickly to the values of 10^{-7}. The total memory required to solve this model was 114.26 MB. It took approximately 6.8 min per frequency.

4 Applications

4.1 The real and theoretical source

In real field surveys, surface obstacles and topography can preclude laying out the source in a theoretical shape such as a straight line, rectangle, or circle. The aforementioned scheme can segment a source with an arbitrarily complex shape into a large number of EDs and MDs. To illustrate this, we conducted a study taking the LOTEM and CSAMT as examples, focusing on the differences between the TD and FD EM fields for both straight and non-straight wire sources. We computed the TD and FD responses for the bent and straight wires. Both wires centered at (0, 0) have the same grounding points; the straight wires of 1 km have a 1 A current on the surface, and the bent wire is the real source consisting of 22 segments (Figure 6A). The 3D model of a 100 Ωm homogeneous half-space is shown in Figure 6B.

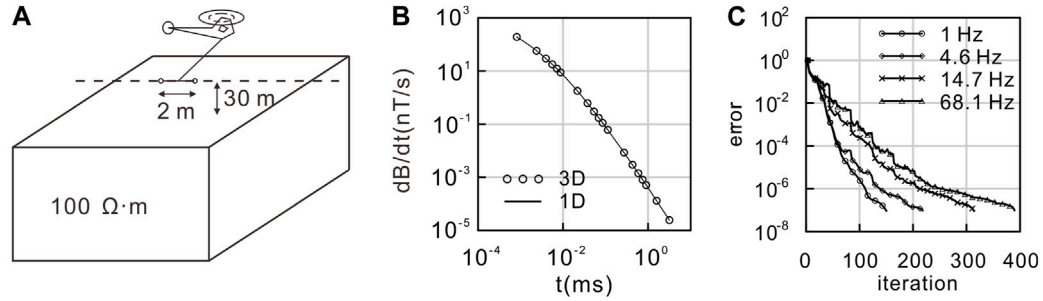

FIGURE 4
A uniform half-space is used to verify the numerical accuracy of 3D modeling for AEM with a VMD source. **(A)** 3D model. **(B)** Comparison of our 3D result against the 1D numerical solution for the TD EM fields (dB/dt). **(C)** Error curve of the QMR solver.

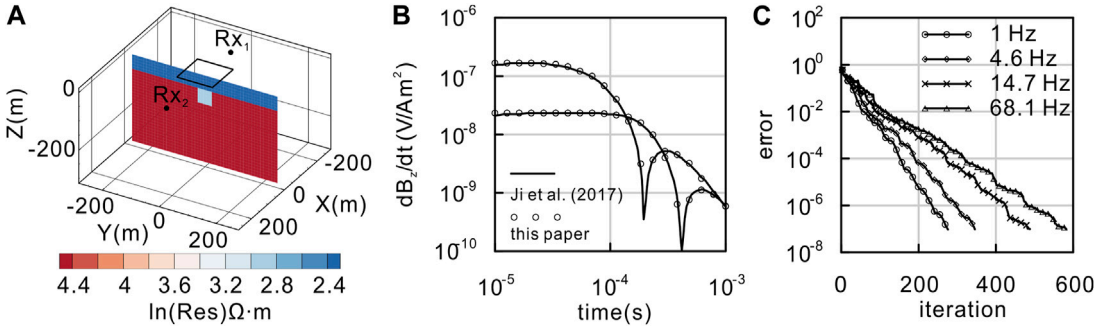

FIGURE 5
A two-layer model is used to verify the numerical accuracy of 3D modeling for the RFLTEM. **(A)** 3D model. **(B)** Comparison between the field solutions obtained in this paper and those of Ji et al. (2017) for the receiver positions denoted by Rx_1 (105, 0, 0) and Rx_2 (−155, 0, 0). **(C)** Error curve of the QMR solver.

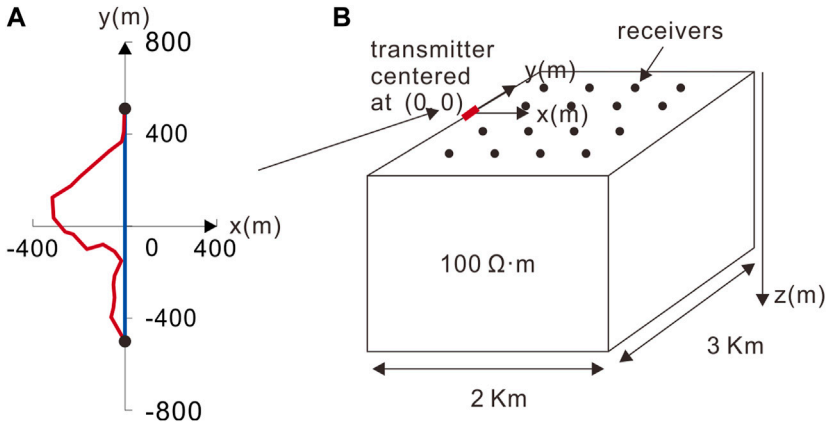

FIGURE 6
The survey geometry **(A)** and 3D model **(B)** are used for modeling a TD and FD CSEM survey. The red and blue lines indicate the real (bent) and theoretical (straight) wires, respectively. The red short line denotes the y-directed 1-km-long wire source.

In Figure 7, we display the TD magnetic field dB/dt for a bent wire compared to dB/dt for a straight wire at different times: 0.065 ms, 0.9 ms, 4 ms, and 10 ms. As time increases, the difference in dB/dt between the bent and straight wires decreases. dB/dt generated by the straight wire exhibits a symmetrical distribution around the source center and is concentrated near the surface (Figure 7A). At the early stage, there is a significant disparity in the dB/dt between the bent and straight wires (Figure 7C). Therefore,

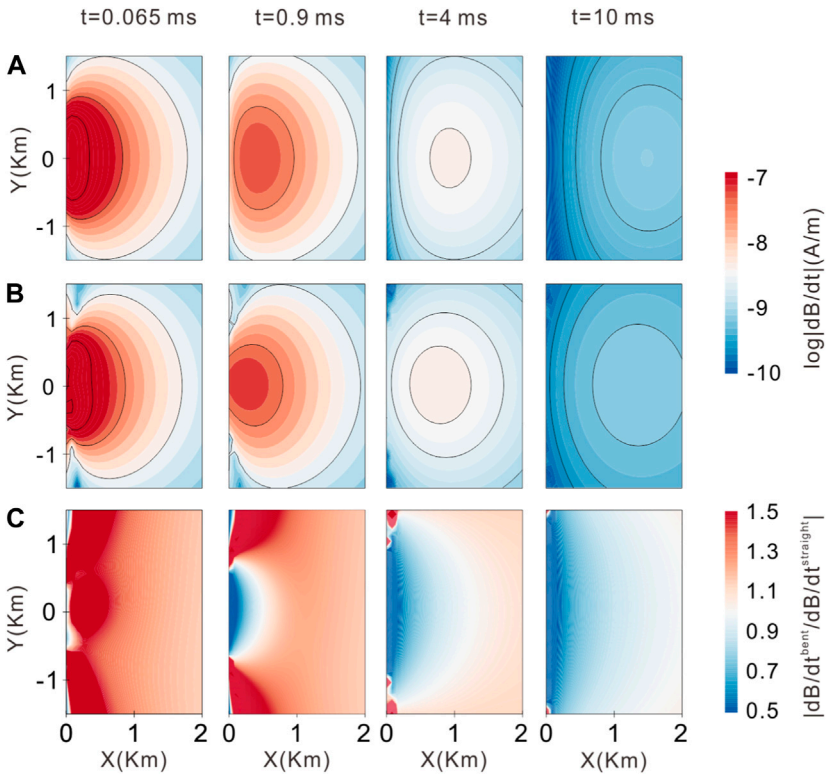

FIGURE 7
TD magnetic field dB/dt for the configuration shown in Figure 7 at different times of 0.065 ms, 0.9 ms, 4 ms, and 10 ms: **(A)** straight wire; **(B)** bent wire; **(C)** ratio difference between bent and straight wire fields.

when analyzing early-time TEM data, it is crucial to consider the shape of the source. With a time delay, the center of dB/dt propagates downward and outward, and the strength of the field gradually decays. At the later stage, dB/dt continues to propagate and becomes more uniform, and the relative differences in dB/dt between the bent and straight wires are minimal (Figure 7C). Spatially, the closer the distance to the source, the greater the difference in dB/dt between the bent and straight wires. Conversely, the farther the distance to the source, the smaller the difference in dB/dt between the bent and straight wires. Therefore, when processing data of TEMs observed close to the source, such as the SOTEM, the source's shape must be taken into account.

Figure 8 shows the FD electric field component Ey for the bent wire relative to Ey for a straight wire at frequencies of 0.1 Hz, 2 Hz, 16 Hz, and 128 Hz. The relative differences in Ey between the bent and straight wires increase with increasing frequency and decrease with increasing distance from the source. At low frequencies, the difference in Ey between the bent and straight wires was very small, and it was mainly concentrated near the source and both sides along the emitting source direction. At high frequencies, the difference in Ey was most pronounced in the survey area. These results highlight the significant influence of the grounding points' locations and the entire wire layout on the EM fields at these frequencies. Therefore, during the inversion of the high-frequency data from a wire source, such as the CSAMT, it is impossible to ignore the impact of the source's shape on the measured data.

The comparison between the TD and FD EM methods shows that the FD CSEM appears to be more significantly influenced by the entire wire layout than the TD CSEM. This difference can be attributed to the nature of the measurements. In the TD CSEMs, observations are made after the current is turned off, capturing the induced eddy field or secondary field. In this case, the shape of the emission source only affects the early data. On the other hand, in FD CSEMs, observations are made under the harmonic excitation of the source, representing the total field. The impact of the source's shape on the field becomes more noticeable, particularly at higher frequencies. At low frequencies, the electric field resembles a potential field that occurs in the static limit. Here, the only factors affecting the electric field are the locations of the grounding points.

According to the aforementioned analysis, we suggest that the shape of the source must be considered for TD and FD CSEMs with a wire source during data processing and inversion. However, in regard to the influence of the source shape, we recommend TD CSEMs when processing data based on the theory of an ideal straight wire or electric dipole source for the same target.

4.2 Wire and loop sources

4.2.1 Model parameters

3D FD forward modeling and TD forward modeling of CSEMs with wire and loop sources were conducted using a conductive

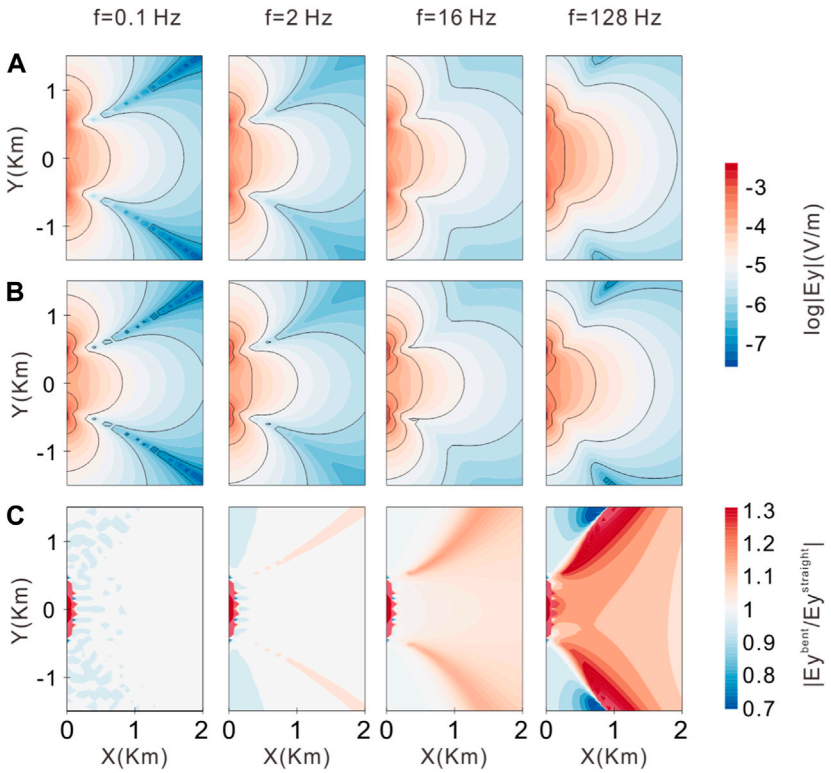

FIGURE 8
FD electric field Ey for the configuration shown in Figure 7 at frequencies of 0.1 Hz, 2 Hz, 16 Hz, and 128 Hz: **(A)** straight wire; **(B)** bent wire; **(C)** ratio of difference between the bent and straight wire fields.

geological model in which a conductive tilted sheet is embedded in a uniform half-space with a strike of 525 m and two high- and low-resistivity bodies on the surface (Figure 9A). In the numerical simulation, the origin of the coordinate system was set at the center of the model at the ground, with the *z*-axis pointing downward. The model space is subdivided into 40 × 40 × 20 prisms of size 25 m × 25 m × 25 m. To ensure that Dirichlet's boundary condition was satisfied, boundary cells in the five layers outside the model were expanded by a factor of 1.5 (Figures 9B–D). In the following solution calculation, all the parameters remained consistent for the 3D forward modeling of CSEMs with both loop and wire sources.

4.2.2 TD CSEM with a loop source

In the TD CSEM, a larger rectangular fixed loop is commonly used as a source, encompassing the target area. The vertical TD magnetic field dB/dt is then measured both inside and outside the loop, simulating the RLFTEM. In this paper, the RLFTEM uses a fixed loop of dimension 300 m × 300 m with a 1 A current on the Earth's surface (Figure 9A). Figure 10 shows the TD scattered field for two specific sections (Y = −270 m and Y = 270 m). According to Faraday's law, the induced eddy currents within the anomalous body are excited when the transmitter switch is abruptly turned off, thus preventing the internal magnetic field of the anomalous body from weakening. At early times, the presence of surface resistive and conductive bodies distorts the induced eddy currents. With a time delay, the induced eddy currents diffuse downward and outward underground, leading to a gradual decay in the strength of the magnetic field. As observed from dB/dt, the RLFTEM has a higher sensitivity to conductive bodies than resistive anomalies.

4.2.3 FD CSEM with a wire source

The wire source is generally used in land and marine CSEMs, such as the CSAMT, LOTEM, and GATEM, and the transmitter is a finite-length wire with complex geometry. In the numerical implementation, we take the CSAMT as an example. A finite-length wire with a length of 1 km and a current of 1 A was laid on the ground along the *x* direction as a signal source. The nearest measuring point is located at a distance of 10 km from the center of the source (Figure 9A). For the CSAMT, the electric field component Ex is generally used as the observed data, as in the wide-field EM method (He, 2010). The proposed forward modeling solver computes Ex in the whole space. The results of the calculation for two sections (Y = −270 m and Y = 270 m) are shown in Figure 11. The FD EM fields from the wire source are similar to those of a plane wave in the measurement area. Among these frequencies, f = 16 Hz is the most sensitive frequency for the tilted target body. The low-frequency data demonstrate a stronger resolution ability to the deep abnormal body. Moreover, high-frequency EM fields have higher energies and stronger abilities to resolve shallow abnormal bodies. However, due to their shorter wavelength and lower penetration, their overall ability to resolve deep anomalous bodies is relatively limited.

The RFLTEM and CSAMT utilize loop and wire sources, representing the magnetic and electric sources, respectively. By comparing the forward results of the RFLTEM and CSAMT, we

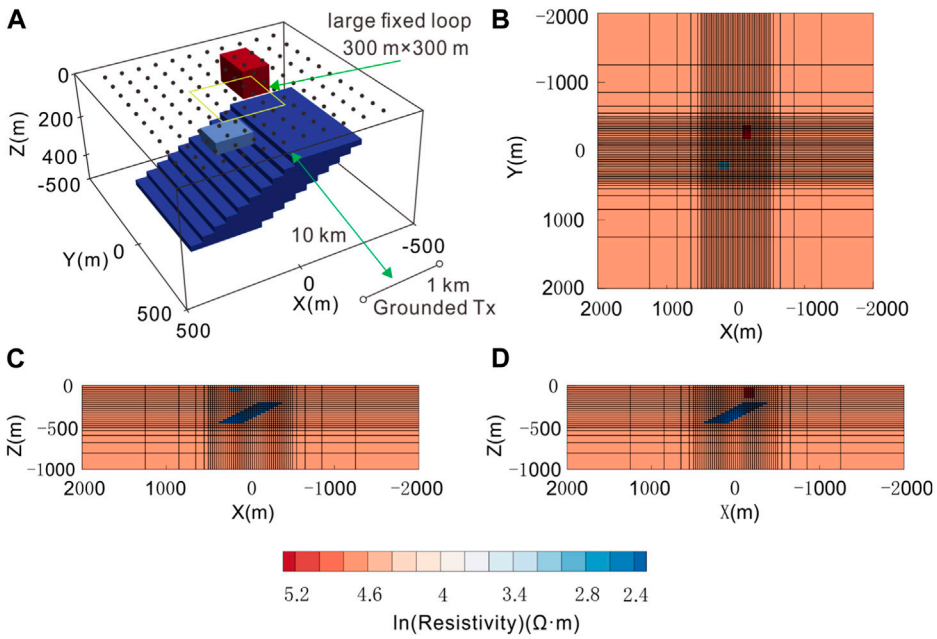

FIGURE 9
3D conductive geological model and the grid used for the model. **(A)** View of the model used for 3D FD and TD forward modeling of CSEMs. The solid circles represent the position of the receivers. The yellow rectangle and the black line indicate the locations of the loop and wire sources, respectively; **(B)** plan view and rectangular mesh with Z = 120 m; **(C)** and **(D)** vertical sections and rectangular mesh with Y = −270 m and Y = 270 m, respectively.

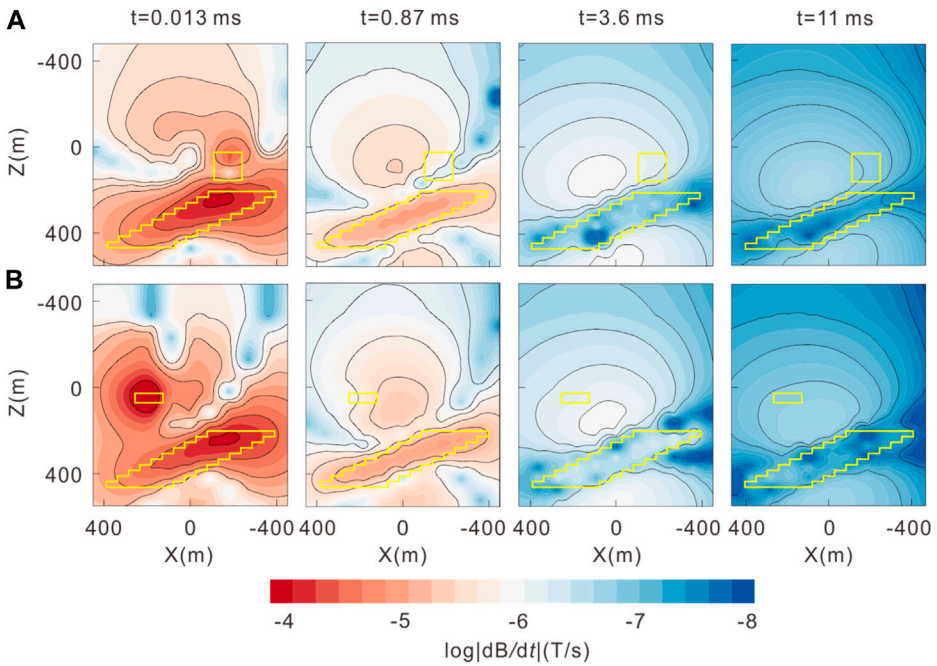

FIGURE 10
TD scattered field at t = 0.013 ms, 0.87 ms, 3.6 ms, and 11 ms: **(A)** Y = −270 m; **(B)** Y = 270 m. The yellow solid lines denote the position of the abnormal bodies. The black solid lines represent the contour line.

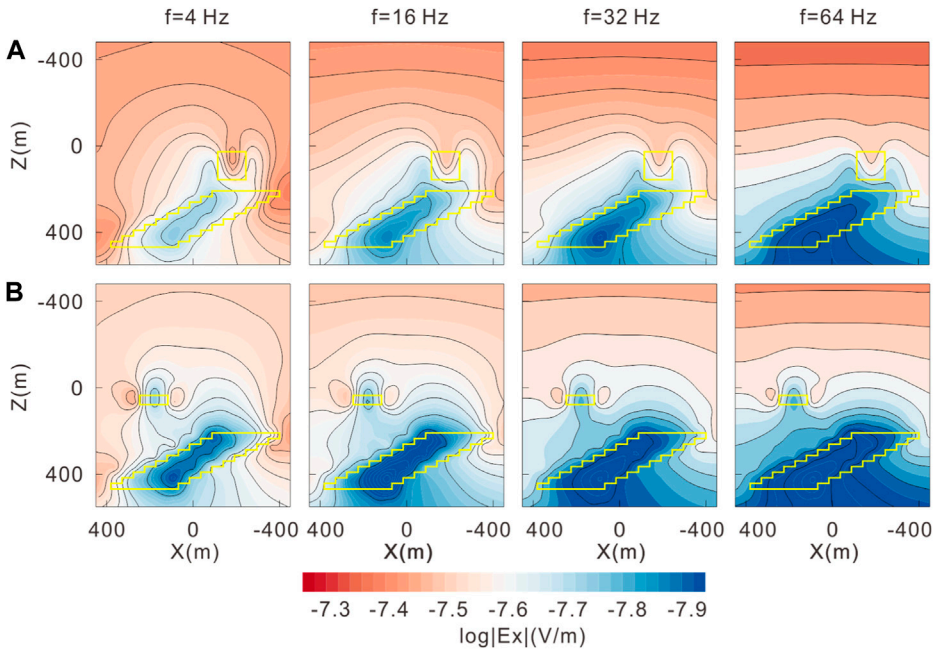

FIGURE 11
FD electric field at f = 4 Hz, 16 Hz, 32 Hz, and 64 Hz. **(A)** Y = −270 m; **(B)** Y = 270 m. The yellow solid lines denote the position of the abnormal bodies. The black solid lines represent the contour line.

can see that both methods are sensitive to shallow conductive anomalies. However, in terms of resolving shallow resistive anomalies, the CSAMT demonstrates a better resolution than the RFLTEM. The observed data distortion, primarily caused by deep conductivity anomalies, is more pronounced in the CSAMT than in the RLFTEM. Furthermore, the resolution of the CSAMT is stronger than that of the RLFTEM for spatial information, such as the occurrence of deep tilted sheets.

Based on the aforementioned analysis, TD CSEMs with loop sources (central loop, coincident loop, and dipole–dipole) are recommended for detecting shallow conductivity anomalies due to their convenience and higher efficiency. On the other hand, for detecting deep anomalies, FD CSEMs with a wire source are sensitive to both resistive and conductive abnormal bodies. The 3D forward modeling solver of CSEMs provides valuable assistance to geophysicists in selecting the most suitable exploration method based on the same forward modeling parameters.

5 Conclusion

In this paper, we have considered the significant commonalities of 3D forward modeling for TD and FD CSEMs with different types of sources and operating environments and developed a general forward solver. Using the same format, the source term of CSEMs is imposed on the right-hand term of an FD vector Helmholtz equation for the scattered electric field. Any complex geometry source can be decomposed into EDs or MDs used as the basic composition unit, each of which can be further decomposed into two horizontal EDs or MDs along the *x* and *y* directions and one vertical ED or MD along the *z* direction. Through this solver, geophysicists can compare the EM field characteristics of different CSEMs for the specific geological targets using the same parameters of the forward solution.

Based on the numerical experimental results of the real and theoretical sources, we suggest that the shape of the source must be considered for TD and FD CSEMs. According to the numerical experiment results of wire and loop sources, we recommend TD CSEMs with the loop source for detecting shallow conductivity abnormal bodies. Moreover, we recommend FD CSEMs with a wire source for detecting deep anomalies.

The solver proposed in this paper leads us to clearly define the basic target objects and methods needed to solve the 3D TD and FD forward problem of the general CSEMs. In the future, we need to further optimize the code computational efficiency, improve the speed of program running, reduce the memory requirements, and lay the foundation for the geophysical interpretation of TD and FD EM data.

Data availability statement

The original contributions presented in the study are included in the article/Supplementary Material; further inquiries can be directed to the corresponding author.

Author contributions

DL implemented the algorithms and wrote the manuscript. YL and ZW conceived the idea of the algorithm, supervised the study, performed the analyses, and edited the manuscript. LJ helped in processing the data and prepared the figures. All authors contributed to the article and approved the submitted version.

Funding

This research was supported by the Natural Science Foundation of Jilin Province, China (Grant Number YDZJ202301ZYTS222) and Jilin Province Education Department Science and Technology Research Project (Grant Number JJKH20230347KJ).

Acknowledgments

Thanks are given to the two reviewers and editors for their helpful suggestions and for improving the manuscript. We would like to thank Prof. Aihua Weng, who modified the whole paper.

Conflict of interest

The authors declare that the research was conducted in the absence of any commercial or financial relationships that could be construed as a potential conflict of interest.

Publisher's note

All claims expressed in this article are solely those of the authors and do not necessarily represent those of their affiliated organizations, or those of the publisher, the editors, and the reviewers. Any product that may be evaluated in this article, or claim that may be made by its manufacturer, is not guaranteed or endorsed by the publisher.

References

Alumbaugh, D. L., Newman, G. A., Prevost, L., and Shadid, J. N. (1996). Three-dimensional wideband electromagnetic modeling on massively parallel computers. *Radio Sci.* 31 (1), 1–23. doi:10.1029/95RS02815

Ansari, S., and Farquharson, C. G. (2013). 3D finite-element forward modeling of electromagnetic data using vector and scalar potentials and unstructured grids. *Geophysics* 79 (4), E149–E165. doi:10.1190/GEO2013-0172.1

Avdeev, D. B. (2005). Three-dimensional electromagnetic modelling and inversion from theory to application. *Surv. Geophys.* 26 (6), 767–799. doi:10.1007/s10712-005-1836-x

Börner, R. U., Ernst, O. G., and Güttel, S. (2015). Three-dimensional transient electromagnetic modelling using Rational Krylov methods. *Geophys. J. Int.* 202 (3), 2025–2043. doi:10.1093/gji/ggv224

Börner, R. U. (2010). Numerical modelling in geo-electromagnetics: Advances and challenges. *Surv. Geophys.* 31 (2), 225–245. doi:10.1007/s10712-009-9087-x

Cai, H., Xiong, B., Han, M., and Zhdanov, M. (2014). 3D controlled-source electromagnetic modeling in anisotropic medium using edge-based finite element method. *Comput. Geosciences* 73, 164–176. doi:10.1016/j.cageo.2014.09.008

Castillo-Reyes, O., Amor-Martin, A., Botella, A., Anquez, P., and García-Castillo, L. E. (2022). Tailored meshing for parallel 3D electromagnetic modeling using high-order edge elements. *J. Comput. Sci.* 63, 101813. doi:10.1016/j.jocs.2022.101813

Castillo-Reyes, O., de la Puente, J., and Cela, J. M. (2022). HPC geophysical electromagnetics: A synthetic vti model with complex bathymetry. *Energies* 15 (4), 1272. doi:10.3390/en15041272

Castillo-Reyes, O., de la Puente, J., and Cela, J. M. (2018). Petgem: A parallel code for 3D CSEM forward modeling using edge finite elements. *Comput. Geosciences* 119, 123–136. doi:10.1016/j.cageo.2018.07.005

Castillo-Reyes, O., de la Puente, J., García-Castillo, L. E., and Cela, J. M. (2019). Parallel 3-D marine controlled-source electromagnetic modelling using high-order tetrahedral Nédélec elements. *Geophys. J. Int.* 219 (219), 39–65. doi:10.1093/gji/ggz285

Castillo-Reyes, O., Modesto, D., Queralt, P., Marcuello, A., Ledo, J., Amor-Martin, A., et al. (2022). 3D magnetotelluric modeling using high-order tetrahedral Nédélec elements on massively parallel computing platforms. *Comput. Geosciences* 160, 105030. doi:10.1016/j.cageo.2021.105030

Castillo-Reyes, O., Queralt, P., Marcuello, A., and Ledo, J. (2022). Land CSEM simulations and experimental test using metallic casing in a geothermal exploration context: Vallès basin (NE Spain) case study. *IEEE Trans. Geoscience Remote Sens.* 60, 1–13. doi:10.1109/TGRS.2021.3069042

Chave, A. D., Everett, M. E., Mattsson, J., Boon, J., and Midgley, J. (2017). On the physics of frequency-domain controlled source electromagnetics in shallow water. 1: Isotropic conductivity. *Geophys. J. Int.* 208 (2), 1026–1042. doi:10.1093/gji/ggw435

Chen, H., Deng, J. Z., Tan, H. D., and Yang, H. Y. (2011). Study on divergence correction method in three-dimensional magnetotelluric modeling with staggered-grid finite difference method. *Chin. J. Geophys. (in Chinese)* 54 (6), 1649–1659. doi:10.3969/j.issn.0001-5733.2011.06.025

Commer, M., and Newman, G. (2004). A parallel finite-difference approach for 3D transient electromagnetic modeling with galvanic sources. *Geophysics* 69 (5), 1192–1202. doi:10.1190/1.1801936

Connell, D., and Key, K. (2013). A numerical comparison of time and frequency-domain marine electromagnetic methods for hydrocarbon exploration in shallow water. *Geophysical Prospecting* 61 (1), 187–199. doi:10.1111/j.1365-2478.2012.01037.x

Constable, S., and Srnka, L. J. (2007). An introduction to marine controlled-source electromagnetic methods for hydrocarbon exploration. *Geophysics* 72 (2), WA3–WA12. doi:10.1190/1.2432483

Constable, S. (2010). Ten years of marine CSEM for hydrocarbon exploration. *Geophysics* 75 (5), 75A67–75A81. doi:10.1190/1.3483451

Das, U. C., and De Hoop, A. T. (1995). Efficient computation of apparent resistivity curves for depth profiling of a layered Earth. *Geophysics* 60 (6), 1691–1697. doi:10.1190/1.1443901

Di, Q., Xue, G., Yin, C., and Li, X. (2020). New methods of controlled-source electromagnetic detection in China. *Science China Earth Sciences* 63 (9), 1268–1277. doi:10.1007/s11430-019-9583-9

Edwards, N. (2005). Marine controlled source electromagnetics: Principles, methodologies, future commercial applications. *Surveys in Geophysics* 26 (6), 675–700. doi:10.1007/s10712-005-1830-3

Everett, M. E. (2009). Transient electromagnetic response of a loop source over a rough geological medium. *Geophysical Journal International* 177 (2), 421–429. doi:10.1111/j.1365-246X.2008.04011.x

Goldstein, M. A., and Strangway, D. W. (1975). Audio-frequency magnetotellurics with a grounded electric dipole source. *Geophysics* 40 (4), 669–683. doi:10.1190/1.1440558

Haber, E., and Ascher, U. M. (2001). Fast finite volume simulation of 3D electromagnetic problems with highly discontinuous coefficients. *SIAM Journal of Scientific Computing* 22 (6), 1943–1961. doi:10.1137/S1064827599360741

He, J. S., Yang, Y., Di-quan, L., and Jing-bo, W. (2010). Wide field electromagnetic sounding methods. *Journal of Central South University (Science and Technology)* 41 (3), 1065–1072. doi:10.4133/sageep.28-047

Hu, X., Peng, R., Wu, G., Wang, W., Huo, G., and Han, B. (2013). Mineral exploration using CSAMT data: Application to Longmen region metallogenic belt, Guangdong Province, China. *Geophysics* 78 (3), B111–B119. doi:10.1190/geo2012-0115.1

Huang, X., Yin, C., Farquharson, C. G., Cao, X., Zhang, B., Huang, W., et al. (2019). Spectral-element method with arbitrary hexahedron meshes for time-domain 3D airborne electromagnetic forward modeling. *Geophysics* 84 (1), E37–E46. doi:10.1190/geo2018-0231.1

Hursán, G., and Zhdanov, M. S. (2002). Contraction integral equation method in three-dimensional electromagnetic modeling. *Radio Science*, 37(6), 1–13. doi:10.1029/2001rs002513

Ji, Y., Hu, Y., and Imamura, N. (2017). Three-dimensional transient electromagnetic modeling based on fictitious wave domain methods. *Pure and Applied Geophysics* 174 (5), 2077–2088. doi:10.1007/s00024-017-1528-8

Koldan, J., Puzyrev, V., De la Puente, J., Houzeaux, G., and Cela, J. M. (2014). Algebraic multigrid preconditioning within parallel finite-element solvers for 3-D electromagnetic modelling problems in geophysics. *Geophysical Journal International* 197 (3), 1442–1458. doi:10.1093/gji/ggu086

Li, D., Shan, X., and Weng, A. (2022). Applying three-dimensional inversion to the frequency-domain response converted from transient electromagnetic data for a rectangular fixed loop. *Journal of Applied Geophysics* 196, 104489. doi:10.1016/j.jappgeo.2021.104489

Li, J., Lu, X., Farquharson, C. G., and Hu, X. (2018). A finite-element time-domain forward solver for electromagnetic methods with complex-shaped loop sources. *Geophysics* 83 (3), E117–E132. doi:10.1190/GEO2017-0216.1

Liu, Y. H., and Yin, C. C. (2013). 3D inversion for frequency-domain HEM data. *Chinese Journal of Geophysics (in Chinese)* 56 (12), 4278–4287. doi:10.6038/cjg20131230

Liu, Y. H., Yin, C. C., Ren, X. Y., and Qiu, C. K. (2016). 3D parallel inversion of time-domain airborne EM data. *Applied Geophysics* 13 (4), 701–711. doi:10.1007/s11770-016-0581-x

Liu, Z., Ren, Z., Yao, H., Tang, J., Lu, X., and Farquharson, C. (2023). A parallel adaptive finite-element approach for 3-D realistic controlled-source electromagnetic problems using hierarchical tetrahedral grids. *Geophysical Journal International* 232 (3), 1866–1885. doi:10.1093/gji/ggac419

Mackie, R. L., Smith, J. T., and Madden, T. R. (1994). Three-dimensional electromagnetic modeling using finite difference equations: The magnetotelluric example. *Radio Science* 29 (4), 923–935. doi:10.1029/94RS00326

Malovichko, M., Tarasov, A. V., Yavich, N., and Zhdanov, M. S. (2019). Mineral exploration with 3-D controlled-source electromagnetic method: A synthetic study of sukhoi log gold deposit. *Geophysical Journal International* 219 (3), 1698–1716. doi:10.1093/gji/ggz390

Newman, G. A., and Alumbaugh, D. L. (1995). Frequency-domain modelling of airborne electromagnetic responses using staggered finite differences. *Geophysical Prospecting* 43 (8), 1021–1042. doi:10.1111/j.1365-2478.1995.tb00294.x

Oldenburg, D. W., Heagy, L. J., Kang, S., and Cockett, R. (2020). 3D electromagnetic modelling and inversion: A case for open source. *Exploration Geophysics* 51 (1), 25–37. doi:10.1080/08123985.2019.1580118

Peng, R., Hu, X., Li, J., Hu, Z., and Yang, H. (2018). 3-D finite-volume forward modeling of wide-field EM using scattered potentials. *Chinese Journal of Geophysics (in Chinese)* 61 (10), 4160–4170. doi:10.6038/cjg2018L0363

Ren, X., Yin, C., Liu, Y., Cai, J., Wang, C., and Ben, F. (2017). Efficient modeling of time-domain AEM using finite-volume method. *Journal of Environmental and Engineering Geophysics* 22 (3), 267–278. doi:10.2113/JEEG22.3.267

Rochlitz, R., Skibbe, N., and Günther, T. (2019). custEM: Customizable finite-element simulation of complex controlled-source electromagnetic data. *Geophysics* 84 (2), F17–F33. doi:10.1190/geo2018-0208.1

Schaller, A., Streich, R., Drijkoningen, G., Ritter, O., and Slob, E. (2018). A land-based controlled-source electromagnetic method for oil field exploration: An example from the Schoonebeek oil field. *Geophysics* 83 (2), WB1–WB17. WB1–WB17. doi:10.1190/geo2017-0022.1

Shen, J. (2003). Modeling of 3-D electromagnetic responses in frequency domain by using the staggeredgrid finite difference method. *Acta Geophysica Sinica* 46 (2), 396–408. doi:10.1002/cjg2.355

Smith, J. T. (1996a). Conservative modeling of 3-D electromagnetic fields, Part I: Properties and error analysis. *Geophysics* 61, 1308–1318. doi:10.1190/1.1444054

Smith, J. T. (1996b). Conservative modeling of 3-D electromagnetic fields, Part II: Biconjugate gradient solution and an accelerator. *Geophysics* 61, 1319–1324. doi:10.1190/1.1444055

Streich, R. (2009). 3D finite-difference frequency-domain modeling of controlled-source electromagnetic data: Direct solution and optimization for high accuracy. *Geophysics* 74 (5), F95–F105. doi:10.1190/1.3196241

Streich, R. (2016). Controlled-source electromagnetic approaches for hydrocarbon exploration and monitoring on land. *Surveys in Geophysics* 37 (1), 47–80. doi:10.1007/s10712-015-9336-0

Tang, J., Zhou, F., Ren, Z., Xiao, X., Qiu, L., Chen, C., et al. (2018). Three-dimensional forward modeling of the controlled-source electromagnetic problem based on the integral equation method with an unstructured grid. *Acta Geophysica Sinica* 61 (4), 1549–1562. doi:10.6038/cjg2018L0121

Tonti, E. (2002). Finite formulation of electromagnetic field. *IEEE Transactions on Magnetics* 38 (2 I), 333–336. doi:10.1109/20.996090

Um, E. S., and Alumbaugh, D. L. (2007). On the physics of the marine controlled-source electromagnetic method. *Geophysics* 72 (2), WA13–WA26. doi:10.1190/1.2432482

Um, E. S., Harris, J. M., and Alumbaugh, D. L. (2012). An iterative finite element time-domain method for simulating three-dimensional electromagnetic diffusion in Earth. *Geophysical Journal International* 190 (2), 871–886. doi:10.1111/j.1365-246X.2012.05540.x

Unno, M., Aono, S., and Asai, H. (2012). GPU-based massively parallel 3-D HIE-FDTD method for high-speed electromagnetic field simulation. *IEEE Transactions on Electromagnetic Compatibility* 54 (4), 912–921. doi:10.1109/TEMC.2011.2173938

Weiland, T. (1996). Time domain electromagnetic field computation with finite difference methods. *International Journal of Numerical Modelling Electronic Networks, Devices and Fields* 9 (4), 295–319. doi:10.1002/(sici)1099-1204(199607)9:4<295::aid-jnm240>3.0.co;2-8

Weng, A. H., Liu, Y. H., Yin, C. C., and Jia, D. Y. (2016). Singularity-free Green's function for EM sources embedded in a stratified medium. *Applied Geophysics* 13 (1), 25–36. doi:10.1007/s11770-016-0549-x

Weng, A., Li, D., Yang, Y., Li, S., Li, J., and Li, S. (2017). Transforming a time-domain electromagnetic signal to a frequency-domain electromagnetic response using regularization inversion. *Geophysics* 82 (5), E287–E295. doi:10.1190/GEO2016-0505.1

Weng, A., Liu, Y., Jia, D., Liao, X., and Yin, C. (2012). Three-dimensional controlled source electromagnetic inversion using non-linear conjugate gradients. *Chinese Journal of Geophysics (in Chinese)* 10, 3506. doi:10.6038/j.issn.0001-5733.2012.10.034

Werthmüller, D., Rochlitz, R., Castillo-Reyes, O., and Heagy, L. (2021). Towards an open-source landscape for 3-D CSEM modelling. *Geophysical Journal International* 227 (1), 644–659. doi:10.1093/gji/ggab238

Xu, J., and Tang, J. (2022). Spectral element method for 3D wide field electromagnetic method forward modeling. *Chinese Journal of Geophysics (in Chinese)* 65 (4), 1461–1471. doi:10.6038/cjg2022P0067

Xue, G. Q. (2018). The development of near-source electromagnetic methods in China. *Journal of Environmental and Engineering Geophysics* 23 (1), 115–124. doi:10.2113/JEEG23.1.115

Yang, D., and Oldenburg, D. W. (2016). Survey decomposition: A scalable framework for 3D controlled-source electromagnetic inversion. *Geophysics* 81 (2), E69–E87. doi:10.1190/GEO2015-0217.1

Yin, C., Qi, Y., and Liu, Y. (2016). 3D time-domain airborne EM modeling for an arbitrarily anisotropic Earth. *Journal of Applied Geophysics* 131, 163–178. doi:10.1016/j.jappgeo.2016.05.013

Zhang, B., Yin, C., Ren, X., Liu, Y., and Qi, Y. (2018). Adaptive finite element for 3D time-domain airborne electromagnetic modeling based on hybrid posterior error estimation. *Geophysics* 83 (2), WB71–WB79. doi:10.1190/geo2017-0544.1

Zonge, K. L., and Hughes, L. J. (1991). "Controlled source audio-frequency magnetotellurics," in *Electromagnetic methods in applied geophysics: Volume 2, application, parts A and B* Editor M. N. Nabighian (United States: Society of Exploration Geophysicists).

Appendix A: Finite difference equations

According to Eq. 5, the expressions of $\hat{\mathbf{j}}$ and $\hat{\mathbf{k}}$ components are, respectively, as follows:

$$\begin{aligned}
&\left\{\left[\frac{1}{\Delta y_j}\left(E^s_{z_{i,j+1,k+1/2}}-E^s_{z_{i,j,k+1/2}}\right)-\frac{1}{\Delta z_k}\left(E^s_{y_{i,j+1/2,k+1}}-E^s_{y_{i,j+1/2,k}}\right)\right]\right.\\
&\left.-\left[\frac{1}{\Delta y_j}\left(E^s_{z_{i,j+1,k-1/2}}-E^s_{z_{i,j,k-1/2}}\right)-\frac{1}{\Delta z_{k-1}}\left(E^s_{y_{i,j+1/2,k}}-E^s_{y_{i,j+1/2,k-1}}\right)\right]\right\}\cdot\frac{1}{\Delta\bar{z}_k}\\
&+\left\{\left[\frac{1}{\Delta y_j}\left(E^s_{x_{i+1/2,j+1,k}}-E^s_{x_{i+1/2,j,k}}\right)-\frac{1}{\Delta x_i}\left(E^s_{y_{i+1,j+1/2,k}}-E^s_{y_{i,j+1/2,k}}\right)\right]\right.\\
&\left.-\left[\frac{1}{\Delta y_j}\left(E^s_{x_{i-1/2,j+1,k}}-E^s_{x_{i-1/2,j,k}}\right)-\frac{1}{\Delta x_{i-1}}\left(E^s_{y_{i,j+1/2,k}}-E^s_{x_{i-1,j+1/2,k}}\right)\right]\right\}\cdot\frac{1}{\Delta\bar{x}_i}\\
&+i\omega\mu_p\hat{y}_pE^s_{y_{i,j+1/2,k}}\\
&=-i\omega\mu_p\left(\hat{y}_{i,j+1/2,k}-\hat{y}_p\right)E^p_{y_{i,j+1/2,k}}
\end{aligned}\tag{A-1}$$

and

$$\begin{aligned}
&\left\{\left[\frac{1}{\Delta z_k}\left(E^s_{x_{i+1/2,j,k+1}}-E^s_{z_{i+1/2,j,k}}\right)-\frac{1}{\Delta x_i}\left(E^s_{z_{i+1,j,k+1/2}}-E^s_{z_{i,j,k+1/2}}\right)\right]\right.\\
&\left.-\left[\frac{1}{\Delta z_k}\left(E^s_{x_{i-1/2,j,k+1}}-E^s_{x_{i-1/2,j,k}}\right)-\frac{1}{\Delta x_{i-1}}\left(E^s_{z_{i,j,k+1/2}}-E^s_{y_{i-1,j,k+1/2}}\right)\right]\right\}\cdot\frac{1}{\Delta\bar{x}_i}\\
&+\left\{\left[\frac{1}{\Delta z_k}\left(E^s_{y_{i,j+1/2,k+1}}-E^s_{y_{i,j+1/2,k}}\right)-\frac{1}{\Delta y_j}\left(E^s_{z_{i,j+1,k+1/2}}-E^s_{z_{i,j,k+1/2}}\right)\right]\right.\\
&\left.-\left[\frac{1}{\Delta z_k}\left(E^s_{y_{i,j-1/2,k+1}}-E^s_{y_{i,j-1/2,k}}\right)-\frac{1}{\Delta y_{j-1}}\left(E^s_{z_{i,j,k+1/2}}-E^s_{z_{i,j-1,k+1/2}}\right)\right]\right\}\cdot\frac{1}{\Delta\bar{y}_j}\\
&+i\omega\mu_p\hat{y}_pE^s_{z_{i,j,k+1/2}}\\
&=-i\omega\mu_p\left(\hat{y}_{i,j,k+1/2}-\hat{y}_p\right)E^p_{z_{i,j,k+1/2}}
\end{aligned}\tag{A-2}$$

frontiers | Frontiers in Earth Science

TYPE Original Research
PUBLISHED 24 July 2023
DOI 10.3389/feart.2023.1194230

OPEN ACCESS

EDITED BY
Jin Li,
Hunan Normal University, China

REVIEWED BY
Ren Zhengyong,
Central South University, China
Benyu Su,
China University of Mining and Technology, China
Nian Yu,
Chongqing University, China
Xiaoyue Cao,
Yangtze University, China

*CORRESPONDENCE
Yuguo Li,
yuguo@ouc.edu.cn

RECEIVED 26 March 2023
ACCEPTED 19 June 2023
PUBLISHED 24 July 2023

CITATION
Ge J and Li Y (2023), Impact of variable seawater conductivity on ocean wave-induced electromagnetic fields simulated with finite difference method.
Front. Earth Sci. 11:1194230.
doi: 10.3389/feart.2023.1194230

Impact of variable seawater conductivity on ocean wave-induced electromagnetic fields simulated with finite difference method

Jiaqi Ge[1] and Yuguo Li[1,2]*

[1]College of Marine Geo-sciences and Key Lab of Submarine Geo-sciences and Prospecting Techniques of Ministry of Education, Ocean University of China, Qingdao, China, [2]National Engineering Research Center of Offshore Oil and Gas Exploration, Beijing, China

Electric fields generated by the motion of ocean waves through the Earth's ambient geomagnetic fields and the induced secondary magnetic field can be observed at the seafloor and at the sea-surface, and even in the air. Most of current studies on ocean wave-induced electromagnetic fields assume that seawater conductivity is constant, and ocean waves are treated as regular waves with a fixed amplitude and frequency. However, these assumptions are inconsistent with actual ocean conditions. In this paper, we present a finite difference algorithm for simulating the ocean wave-induced electromagnetic fields with variable seawater conductivity. We investigate impacts of variable seawater conductivity on the electromagnetic fields induced by the wind waves and swell as well as mixed ocean waves, which are treated as the superposition of a number of regular waves with different frequencies and amplitudes, and analyze the characteristics of the induced electromagnetic fields.

KEYWORDS

electromagnetic fields, variable seawater conductivity, wind waves, swell, mixed ocean waves

Introduction

Oceanic waves can carry charged ions dissolved in seawater, and electromagnetic fields can be induced by the dynamo interaction of ocean waves with the geomagnetic field. The ocean wave-induced electromagnetic fields can be observed at various locations, including the seafloor, sea surface, and, sometimes, even at satellite altitudes (Crews and Futterman, 1962; Cox et al., 1978; Minami, 2017). These electromagnetic fields can provide sufficient information for the inversion of the ocean wave spectrum, which is widely used in ocean engineering and seakeeping considerations in ship design (Cieutat et al., 2003; Techet, 2005; Nielsen and Dietz, 2020). However, they will seriously interfere with natural magnetotelluric (MT) signals and reduce the quality of MT data.

In the past decades, the study of ocean wave-induced electromagnetic fields focused on the plane surface gravity waves with a fixed amplitude and frequency, which are usually considered the approximation of ocean waves. Weaver (1965) and Fraser (1966) calculated and observed the magnetic fields induced by surface gravity waves in the infinite ocean. Larsen (1971) developed a general theory of ocean wave-induced electromagnetic fields, especially long and intermediate surface gravity waves. Miles et al. (1977) established an analog model of magnetic

fields induced by surface gravity waves in the laboratory. Ochadlick (1989) measured the magnetic fields generated by surface gravity waves at an aircraft. Lilley and Weitemeyer (2004a) calculated the apparent aeromagnetic wavelengths of the magnetic signals of the ocean swell. Lilley et al. (2004b) also observed the magnetic fields generated by ocean waves near the sea surface. Semkin and Smagin (2012) investigated the effect of self-induction exhibited by the ocean wave-induced electromagnetic fields. Shimizu and Utada (2015) demonstrated that the ocean wave-induced electromagnetic fields were rarely affected by the conductive subseafloor media.

It is well-known that actual ocean waves are not regular waves with a fixed amplitude and frequency but rather the sum of multiple-frequency amplitudes that exhibit a particular sea state with a significant wave height and peak period (Rasool et al., 2021). Recently, a more realistic and accurate ocean wave-induced electromagnetic field model has been proposed by combining surface gravity waves with the wave spectrum, which provides the distribution of ocean wave energy empirically (Chave, 1983; Ailliot et al., 2013; Ryabkova et al., 2019), and thus, connections between ocean wave-induced electromagnetic fields and the ocean wave spectrum are established. The electromagnetic fields generated by wind waves can be solved efficiently using wind speed and significant wave height, and other parameters (Yaakobi et al., 2011). Meanwhile, many studies focus on the wind-driven electromagnetic fields at different wind speeds (Zhu and Xia, 2014; Zhan and Pan, 2019). To the best of our knowledge, the electromagnetic fields generated by both the swell and mixed ocean waves have not been discussed in the literature.

In the aforementioned studies, seawater conductivity is often assumed to be constant. However, seawater conductivity is variable in the realistic ocean (Zheng et al., 2018). Previous studies have shown that there is an approximately linear relationship between seawater conductivity and temperature, and the salinity of seawater also influences the conductivity of seawater. Both the salinity and temperature of ocean water can exhibit significant spatial and temporal variations, thereby leading to variations in sea water conductivity. The mean conductivity of seawater is approximately 3.3–4 S/m, while it may reach 6 S/m above the main thermocline. Chave and Luther (1990) and Irrgang et al. (2016) investigated the effect of vertically varying seawater conductivity on ocean current-induced electromagnetic fields. As far as we know, the impact of changes in seawater conductivity on the ocean wave-induced electromagnetic fields has not been well-investigated.

In this paper, we simulate the ocean wave-induced electromagnetic fields with variable seawater conductivity using the finite difference method. The impact of variable seawater conductivity will be investigated, especially within the main thermocline at different seasons and latitudes. Then, the wave spectra of wind waves, swell, and mixed waves are presented and the characteristics of the electromagnetic fields are analyzed.

Methodology

FD simulation of surface gravity wave-induced electromagnetic fields

The electromagnetic fields induced by surface gravity waves can be obtained by solving the motional induction equation. Here, we adopt two-dimensional surface waves propagating in the x-direction, with no variation in the y-direction. The z-axis points downward, and the origin of the Cartesian coordinate system is at the averaged sea surface. We assume that seawater is incompressible and flow is irrotational. This means that there exists a velocity potential Φ for the flow. The velocity potential Φ is a harmonic function that obeys the following Laplace equation:

$$\nabla^2\Phi = 0, \tag{1}$$

where Φ can be expressed as follows (Larsen, 1971):

$$\Phi = \frac{ag}{\omega}\frac{\cosh\left[p\left(d-z\right)\right]}{\cosh\left(pd\right)}e^{i\left(\omega t-px\right)}, \tag{2}$$

where a is the height of the ocean wave, the acceleration of gravity g equals to 9.8 m/s^2, and p and ω indicate the wave number and angular frequency of the ocean wave, respectively. The dispersion relation of the ocean wave can be expressed as (Larsen, 1971)

$$\omega^2 = gp\tanh\left(pd\right). \tag{3}$$

The gradient of the velocity potential Φ is the flow velocity $\vec{V}$, i.e., we have

$$\vec{V} = \nabla\Phi. \tag{4}$$

From Eqs. 2 and 4, we get the velocity field of the ocean wave:

$$\begin{aligned}\vec{V} = &-\mathrm{Re}\left[\frac{agpi}{\omega}\frac{\cosh\left[p\left(d-z\right)\right]}{\cosh\left(pd\right)}e^{i\left(\omega t-px\right)}\right]\vec{i}\\ &-\mathrm{Re}\left[\frac{agp}{\omega}\frac{\sinh\left[p\left(d-z\right)\right]}{\cosh\left(pd\right)}e^{i\left(\omega t-px\right)}\right]\vec{k},\end{aligned} \tag{5}$$

where $\vec{i}$ and $\vec{k}$ are the unit vectors in the x- and z-directions, respectively. Re indicates the real part of a complex function.

The frequency domain Maxwell equations in the quasi-stationary state approximation can be written as

$$\begin{cases}\nabla\times\vec{H}-\sigma\vec{E} = \sigma\left(\vec{V}\times\vec{F}\right),\\ \nabla\times\vec{E}+i\omega\mu\vec{H} = 0,\\ \nabla\cdot\vec{H} = 0,\end{cases} \tag{6}$$

where $\vec{E}$ is the *in situ* electric field, $\vec{H}$ is the magnetic field, σ is the conductivity, and μ is the magnetic permeability, which is assumed to be equal to the permeability of free space. $\vec{F}$ is the ambient geomagnetic field given by

$$\vec{F} = F_0\left(\cos I\cos\theta\vec{i}-\cos I\sin\theta\vec{j}+\sin I\vec{k}\right), \tag{7}$$

where $\vec{i}$, $\vec{j}$, and $\vec{k}$ are the unit vectors in the positive directions of x-, y- and z-axes, respectively. F_0 is the intensity of the geomagnetic field, and θ and I are the declination and inclination of the geomagnetic field, respectively.

Taking the curl of first equation of Eq. 6 and eliminating $\vec{E}$ with the use of the second equation of Eq. 6, yields

$$\nabla\times\nabla\times\vec{H}+i\omega\mu\sigma\vec{H} = \sigma\nabla\times\left(\vec{V}\times\vec{F}\right)+\nabla\sigma\times\left(\vec{V}\times\vec{F}+\vec{E}\right). \tag{8}$$

Compared to the spatial variability of ocean waves $\vec{V}$, the variations in the geomagnetic field $\vec{F}$ are small and can be ignored. By using $\nabla\cdot\vec{F} = 0$ and $\nabla\cdot\vec{V} = 0$, Eq. 8 can be rewritten as

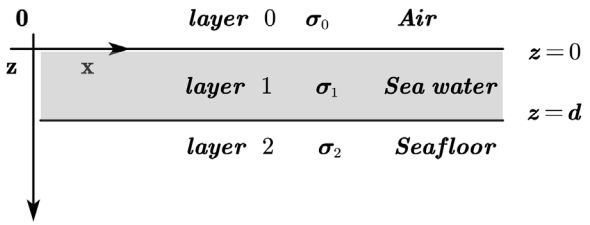

FIGURE 1
Horizontally three-layered conductivity model.

$$\nabla^2\vec{H} - i\omega\mu\sigma\vec{H} = -\sigma\left[\left(\vec{F}\cdot\nabla\right)\vec{V}\right] - \nabla\sigma\times\left(\vec{V}\times\vec{F} + \vec{E}\right). \quad (9)$$

Since the impact of the conductivity of the subseafloor material on the electromagnetic fields within the frequency range of ocean waves at and above the seabed is negligible (Larsen, 1971; Minami and Toh, 2013; Shimizu and Utada, 2015), an air–seawater–seafloor three-layer conductivity model, as shown in Figure 1, is considered here. Assuming that the conductivity of air is σ_0, the conductivity and thickness of seawater are σ_1 and d, respectively, and the conductivity of the seafloor medium is σ_2.

Since the forcing term of $\vec{V}$ is harmonic in time t and x, the electromagnetic fields resulting from $\vec{V}$ have a similar harmonic form as $\vec{H}\propto\exp(i\omega t - ipx)$ and $\vec{E}\propto\exp(i\omega t - ipx)$ (Weaver, 1965; Håland et al., 2012). Hence, Eq. 9 can be rewritten as

$$\frac{\partial^2\vec{H}}{\partial z^2} - m_j^2\vec{H} = -\sigma\left[\left(\vec{F}\cdot\nabla\right)\vec{V}\right] - \nabla\sigma\times\left(\vec{V}\times\vec{F} + \vec{E}\right), \quad (10)$$

where $m_j = \sqrt{p^2 + i\omega\mu\sigma_j}$ is the wave number in the j^{th} layer $(j = 0, 1, 2)$. The first term on the right-hand side of Eq. 10 represents the influence of the source term, and the second term indicates the influence of the change in seawater conductivity.

For the length scale of ocean waves, the horizontal variation in seawater conductivity is negligible compared to its vertical variations (Chave and Luther, 1990; Tyler et al., 2017). Hence, Eq. 10 can be simplified as (Minami et al., 2021)

$$\left(\frac{\partial^2}{\partial z^2} - m_j^2\right)\begin{pmatrix}H_x\\H_z\end{pmatrix} = \begin{pmatrix}-\sigma_j\left(F_x\frac{\partial}{\partial x} + F_z\frac{\partial}{\partial z}\right)V_x - \frac{\partial\sigma_j}{\partial z}\left(V_zF_x - V_xF_z + E_y\right)\\ -\sigma_j\left(F_x\frac{\partial}{\partial x} + F_z\frac{\partial}{\partial z}\right)V_z\end{pmatrix}. \quad (11)$$

The magnetic fields in the air can be expressed as

$$\begin{pmatrix}H_x\\H_z\end{pmatrix} = \begin{pmatrix}P_a\exp(m_0z)\\R_a\exp(m_0z)\end{pmatrix}, \quad (12)$$

where P_a and R_a are the coefficients to be determined.

Similarly, the magnetic fields in the seafloor layer can be expressed as

$$\begin{pmatrix}H_x\\H_z\end{pmatrix} = \begin{pmatrix}P_s\exp(-m_2z)\\R_s\exp(-m_2z)\end{pmatrix}, \quad (13)$$

where P_s and R_s are the coefficients in the seafloor layer to be determined.

At the air–ocean interfaces $(z = 0)$ and the seafloor $(z = d)$, both the tangential (H_x) and normal (H_z) components of the magnetic field are continuous. The induced magnetic field tends to be zero as z approaches ± ∞. Using the third equation of Eqs 6, 12, 13, we have the boundary conditions on both the sea surface and seafloor:

$$\begin{cases}\dfrac{\frac{dH_z(0)}{dz}}{H_z(0)} = m_0,\\ \dfrac{\frac{dH_z(d)}{dz}}{H_z(d)} = -m_2.\end{cases} \quad (14)$$

The boundary value problems (11) and (14) can be solved using the finite difference method. We consider that the one-dimensional grid and the space from the sea surface to the seafloor are spatially discretized into N equally spaced elements. The step size is $h = \frac{d}{N}$, and each spatial point is defined by $z_i = ih, i = 0, 1, \cdots\cdots N$.

Using the Taylor series expansion, the second derivative of the normal (H_z) component of the magnetic field can be approximated by

$$f''(z_i) \approx \frac{f(z_{i+1}) - 2f(z_i) + f(z_{i-1})}{h^2} - \frac{h^2}{12}f^{(4)}(\xi_i), z_{i-1} < \xi_i < z_i, i = 1, 2\cdots, N-1. \quad (15)$$

Eq. 11 can then be approximated using the symmetric difference equation

$$\frac{1}{h^2}\left(f_{i-1} - 2f_i + f_{i+1}\right) + q_if_i \approx g_i, i = 1, 2\cdots, N-1, \quad (16)$$

with

$$q_i = -\left(p^2 + i\omega\mu\sigma_{1,i}\right), g_i = -\sigma_{1,i}\left(F_x\frac{\partial}{\partial x} + F_z\frac{\partial}{\partial z}\right)V_{z,i}. \quad (17)$$

The first derivative of the magnetic field component $f'(z)$ at the sea surface $(z = z_0)$ and seafloor $(z = z_N)$ can be approximated by

$$\begin{cases}f'(z_0) \approx \dfrac{-3f(z_0) + 4f(z_1) - f(z_2)}{2h} + \dfrac{h^2}{3}f'''(\xi_0), z_0 < \xi_0 < z_2,\\ f'(z_N) \approx \dfrac{f(z_{N-2}) - 4f(z_{N-1}) + 3f(z_N)}{2h} + \dfrac{h^2}{3}f^{'''(\xi_N)}, z_{N-2} < \xi_N < z_N.\end{cases} \quad (18)$$

The boundary conditions in Eq. 14 become

$$\begin{cases}-m_0f_0 + \dfrac{-3f_0 + 4f_1 - f_2}{2h} = 0,\\ m_2f_N + \dfrac{f_{N-2} - 4f_{N-1} + 3f_N}{2h} = 0.\end{cases} \quad (19)$$

One obtains a linear system of N-1 equations, which can be written in the following matrix form:

$$\begin{bmatrix} q_1 - \frac{2}{h^2} + \frac{4}{(2hm_0+3)h^2} & \frac{1}{h^2} - \frac{1}{(2hm_0+3)h^2} & 0 & \cdots & 0 \\ \frac{1}{h^2} & q_2 - \frac{2}{h^2} & \frac{1}{h^2} & \cdots & 0 \\ \cdots & \cdots & \cdots & \cdots & \cdots \\ 0 & \cdots & \frac{1}{h^2} & q_{N-2} - \frac{2}{h^2} & \frac{1}{h^2} \\ 0 & \cdots & \frac{1}{2h} & \frac{1}{h^2} - \frac{1}{h^2(3+2hm_2)} & q_{N-1} - \frac{2}{h^2} + \frac{4}{(3+2hm_2)h^2} \end{bmatrix} \times \begin{bmatrix} f_1 \\ f_2 \\ \vdots \\ f_{N-2} \\ f_{N-1} \end{bmatrix} = \begin{bmatrix} g_1 \\ g_2 \\ \vdots \\ g_{N-2} \\ g_{N-1} \end{bmatrix}. \tag{20}$$

The aforementioned equations can be solved by using a direct solver to obtain H_z, and H_x and E_y can be computed from H_z:

$$\begin{cases} H_x = \frac{1}{ip}\frac{\partial}{\partial z}H_z, \\ E_y = \frac{\omega\mu}{p}H_z. \end{cases} \tag{21}$$

It should be noted that the electric fields calculated in this section are *in situ* electric fields. The geomagnetic electro-kinetograph field $\overrightarrow{E'}$, observed by the observer moving with the fluid velocity, can be referred to (Larsen, 1971)

$$\overrightarrow{E'} = \vec{E} + \vec{V}\times\vec{F}. \tag{22}$$

The magnetic induction intensity $\vec{B}$ can be described as

$$\vec{B} = \mu\vec{H}. \tag{23}$$

Validation of FD simulation

In order to validate the accuracy of the finite difference (FD) algorithm described in the previous section, we simulated the wave-induced electromagnetic fields in the model, as shown in Figure 1. The conductivity in the air is set to be $10^{-8}S/m$. The conductivity and depth of seawater are 3.33 S/m and 200 m, respectively, and the seafloor conductivity is supposed to be 1 S/m. The amplitude and frequency of the surface gravity wave are set to be 1 m and 0.1 Hz, respectively. The ambient geomagnetic field is $F_0 = 45000nT$, and the declination $\theta = 30°$ and inclination $I = 60°$. The finite difference grid is a uniform grid with a grid spacing of 0.05 m.

Figure 2 shows the amplitudes of ocean wave-induced electrical and magnetic field components obtained using the FD method. For comparison, the analytic solutions calculated using the formulae used by Shimizu and Utada (2015) are also shown. The FD numerical results agree very well with the analytic solutions. The relative errors of all three components (Ey, Bx, and Bz) are below 0.5%. Figure 2shows that 1) the amplitudes of both B_z and E_y components near the sea surface are much larger and decrease exponentially with increasing$|z|$. The attenuation of both B_z and E_y in seawater is faster than that in the air; 2) the horizontal magnetic component B_x exhibits two peaks, one at the sea surface and the other in the seawater.

Impact of variable seawater conductivity on ocean wave-induced electromagnetic fields

Generally, the conductivity of seawater decreases with the depth of the ocean. It may exhibit either a linear or exponential decrease. In this section, we evaluate how seawater conductivity affects the electromagnetic field generated by ocean waves in both linear and exponential models. Additionally, we utilize empirical formulas to calculate the ocean wave-induced electromagnetic field while also factoring in the effects of the thermocline layer. In the following numerical simulation, the amplitude and frequency of the surface gravity wave are set to be 1 m and 0.1 Hz, respectively.

The effect of the depth-averaged seawater conductivity

To investigate the impacts of seawater conductivity distribution on ocean wave-induced electromagnetic fields, we conducted modeling studies for two cases. In the first case, the seawater conductivity is set to be a constant of 3 S/m, 4 S/m, and 5 S/m. In the second case, seawater conductivity linearly varies with depth z, with a depth-averaged conductivity of 3 S/m, 4 S/m, and 5 S/m (Figure 3A). The ambient geomagnetic field is $F_0 = 45000nT$, and the declination $\theta = 30°$ and inclination $I = 60°$.

Figures 3B–D show the ocean wave-induced electromagnetic fields with different seawater conductivity distributions. One can see that 1) maintaining a constant depth-averaged seawater conductivity but changing from a uniform to a linear distribution with depth results in an increase in the induced electromagnetic fields. Here, the variations in seawater conductivity distribution led to an increase of up to 25% in the electromagnetic fields; 2) for a fixed seawater conductivity distribution (i.e., a constant gradient of linear conductivity variation), changes in the depth-averaged seawater conductivity also affect the induced electromagnetic field. It is evident that the induced electromagnetic field increases with the increase in the depth-averaged seawater conductivity.

The effect of the seawater conductivity gradients

To investigate the effects of the seawater conductivity gradients, we consider the model with the same depth-averaged conductivity but different conductivity gradients. The depth-averaged conductivity gradient σ_g can be defined as

$$\sigma_g = \frac{1}{d}\int_0^d \left|\frac{d\sigma(z)}{dz}\right| dz. \tag{24}$$

Figure 4A shows the variation in seawater conductivity for depth-averaged conductivity gradients of 0.0025, 0.006, and 0.011. As shown in Figures 4B–D, the induced electromagnetic fields increase with the increase in the depth-averaged conductivity gradient.

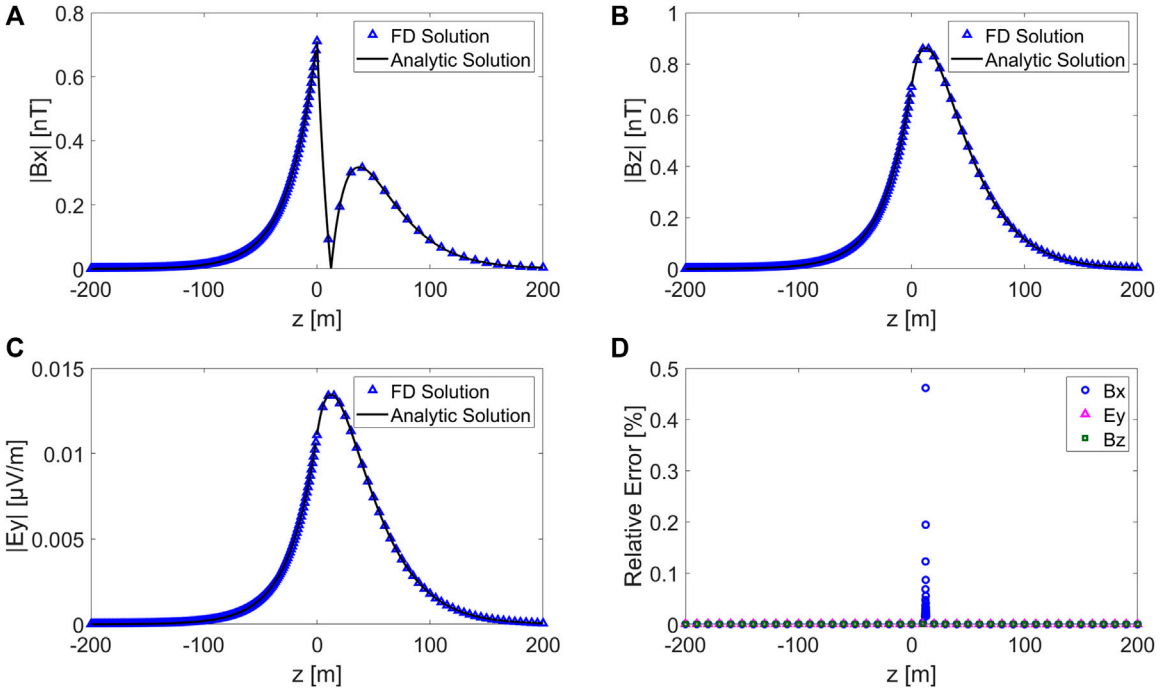

FIGURE 2
Amplitudes of electromagnetic fields induced by ocean waves; the blue triangles and the black solid line represent the FD results and analytic solution, respectively. Bx **(A)**, Bz **(B)**, Ey **(C)**, and relative errors **(D)**.

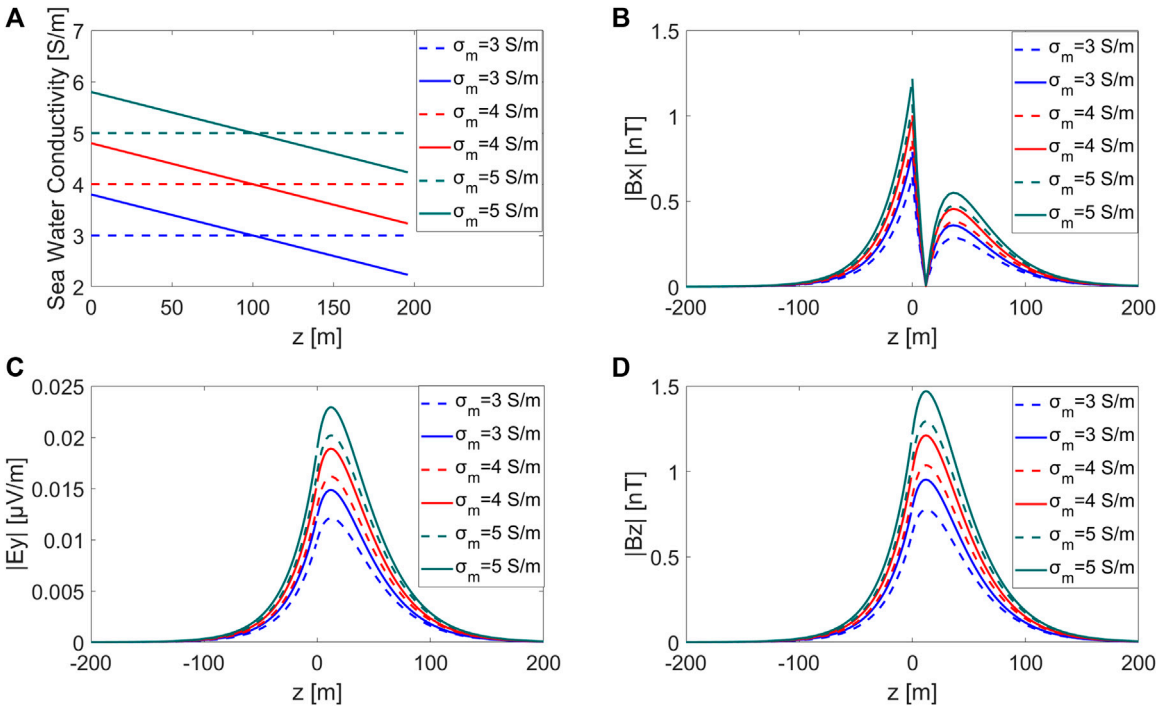

FIGURE 3
(A) Seawater conductivity profiles of six conductivity distributions; vertical profiles with different depth-averaged conductivity distributions are presented for **(B)** Bx, **(C)** Ey, and **(D)** Bz.

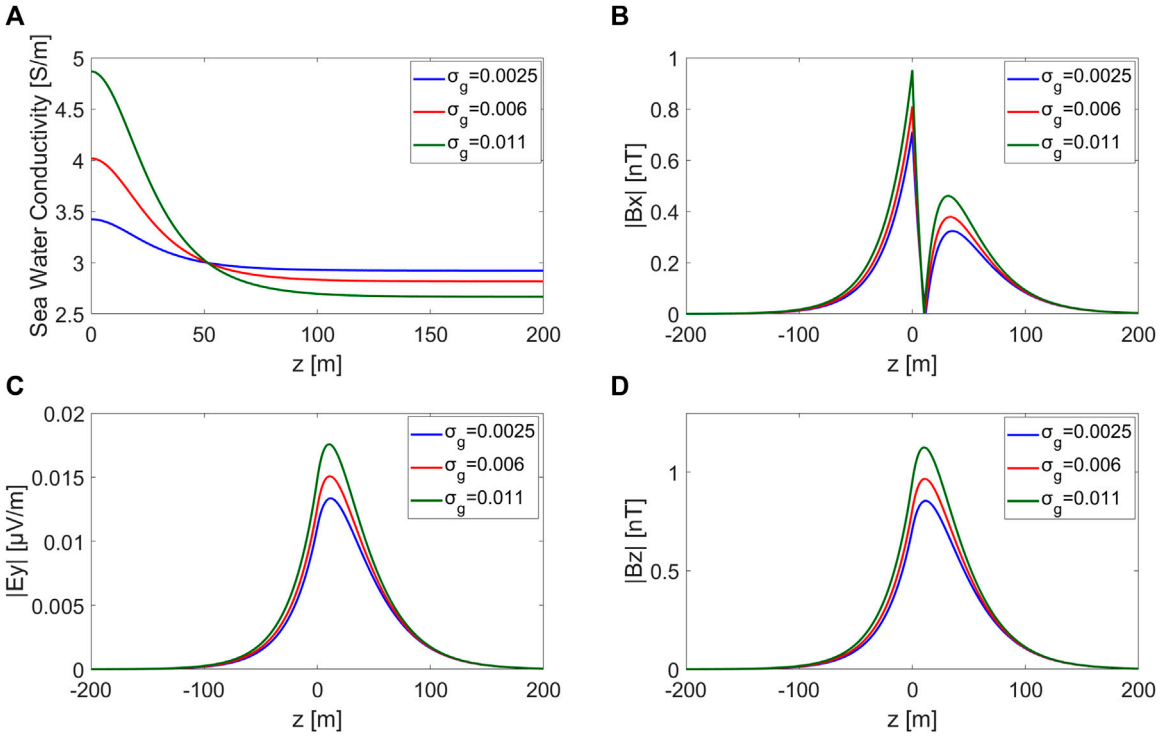

FIGURE 4
(A) Seawater conductivity with different depth-averaged conductivity gradients; **(B)** Bx, **(C)** Ey, and **(D)** Bz.

The effect of the thermocline

The thermocline is the transition layer between the warmer mixed water near the surface and the cooler deep water below. It plays an important role in marine ecology, meteorological forecasting, underwater communication, and aquaculture. In the body of the thermocline, there is a sudden temperature change. The temperature decreases rapidly from the mixed layer to the cooler deep layer.

The temperature t, salinity S, and pressure p in seawater affect the variations in seawater conductivity. According to the 1978 Practical Salinity Scale (Fofonoff and Millard, 1983), the seawater conductivity $C(S,t,p)$ can be expressed as

$$C(S,t,p) = C(35,15,0)R(S,t,p), \tag{25}$$

where $R(S,t,p)$ is the conductivity ratio, and $C(35,15,0)$ represents the conductivity of standard seawater at a salinity of 35‰, a temperature of 15°C, and standard atmospheric pressure (0 dbar), with a value of $4.2914 S/m$.

The conductivity ratio $R(S,t,p)$ can be written as

$$R(S,t,p) = \frac{1}{2A}\left[\sqrt{(B - Ar_tR_t)^2 + 4r_tR_tA(B+C)} - (B - Ar_tR_t)\right] \tag{26}$$

with

$$r_t = 0.6766097 + 0.0200564t + 1.104259 \times 10^{-4}t^2 - 6.9698 \times 10^{-7}t^3 + 1.0031 \times 10^{-9}t^4, \tag{27}$$

$$A = 0.4215 - 0.003107t,$$
$$B = 1 + 0.03426t + 4.464 \times 10^{-4}t^2,$$
$$C = (2.07 \times 10^{-5} - 6.37 \times 10^{-10}p + 3.989 \times 10^{-15}p^2)p. \tag{28}$$

The factor $R_t(S,t)$ can be calculated from the salinity S and the temperature t as

$$S = 0.008 + 0.0005c - (0.1692 + 0.0056c)R_t^{1/2} + (25.3851 - 0.0066c)R_t + (14.04941 - 0.0375c)R_t^{3/2} + (-7.0261 + 0.0636c)R_t^2 + (2.7081 - 0.0144c)R_t^{5/2} \tag{29}$$

with

$$c = \frac{t - 15}{1 + 0.0162(t - 15)}. \tag{30}$$

As a high linear correlation exists between temperature and conductivity in the thermocline, the conductivity in it may include the temperature dependence only and a constant salinity of 36 psu can be considered in Eq. 29 (Tyler et al., 2017; Zheng et al., 2018).

The thermocline largely depends on the seasons and latitudes. Figure 5 displays the variation in temperature and seawater conductivity in the thermocline for different latitudes (Figure 5A) and different seasons (Figure 5B). The temperature profiles vary at different latitudes as the surface water is warmer near the equator and colder at the poles. In low-latitude tropical regions, the sea surface is much warmer, leading to a highly pronounced thermocline, while in polar regions, the temperature is fairly constant at all depths. Seasons also have an impact on the

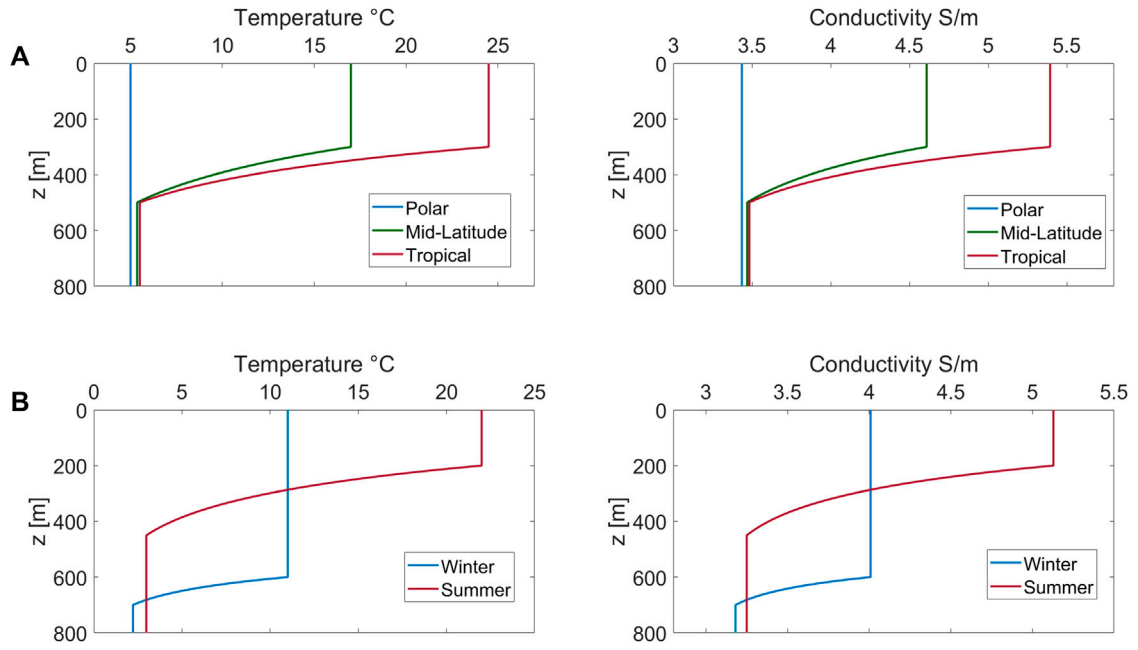

FIGURE 5
(A) Representative temperature and corresponding conductivity profiles for tropical, mid-latitude, and polar regions, and for **(B)** winter and summer.

TABLE 1 Geomagnetic field intensity, magnetic declination, and inclination vary with latitudes (polar, mid-latitude, and tropical regions) and seasons (summer and winter).

		Magnetic induction ntensity (nT)	Declination (°)	Inclination (°)
Latitude	Pola region	586873	−1.8	881
	Mid latitude	584233	−97	68.2
	Tropical region	42906.4	−21	26.9
Season	winter	584901	−11.2	687
	summer	58477.2	−111	687

vertical variation in seawater temperature and conductivity. In winter, the sea surface temperature is lower than that in summer, resulting in a thicker thermocline. In contrast, in summer, due to solar radiation, the thermocline is thinner and has more pronounced variations.

The geomagnetic field also varies with latitudes. The intensity of the magnetic field is generally higher near the magnetic poles and lower near the equator. At the magnetic equator, where the proximity to the geographic equator is high, the magnetic field lines intersect Earth's surface, resulting in a smaller magnetic inclination angle. However, as the latitude increases, the magnetic inclination angle gradually becomes larger (Table 1).

Figure 6 shows the electromagnetic fields in the thermocline for tropical, mid-latitude, and polar regions, and for winter and summer, respectively. Figure 6 shows that 1) compared to tropical and polar regions, the mid-latitude regions have the highest amplitude values of induced electromagnetic fields (Figure 6A). This is because tropical regions have relatively high seawater conductivity but low geomagnetic field values, while mid-latitude regions have slightly lower seawater conductivity than tropical regions but significantly higher geomagnetic field values; 2) due to the relatively insignificant seasonal variations in the geomagnetic field, the values of induced electromagnetic fields are larger in summer than those in winter (Figure 6B).

Numerical simulation of electromagnetic fields induced by ocean wave based on sea wave spectrums within inhomogeneous ocean

The motion of realistic ocean waves can be described as a stationary random process. The ocean waves can be simulated by the wave spectrum, which represents the statistical characteristic of ocean wave motion (Longuet-Higgins, 1962; Grainger et al., 2021). Thus, the height and velocity potential of the ocean waves can be simulated by linear superposition:

$$\eta(x,t) = \mathrm{Re}\sum_{k=1}^{N} a_k \exp[i(\omega_k t - p_k x - \epsilon_k)], \tag{31}$$

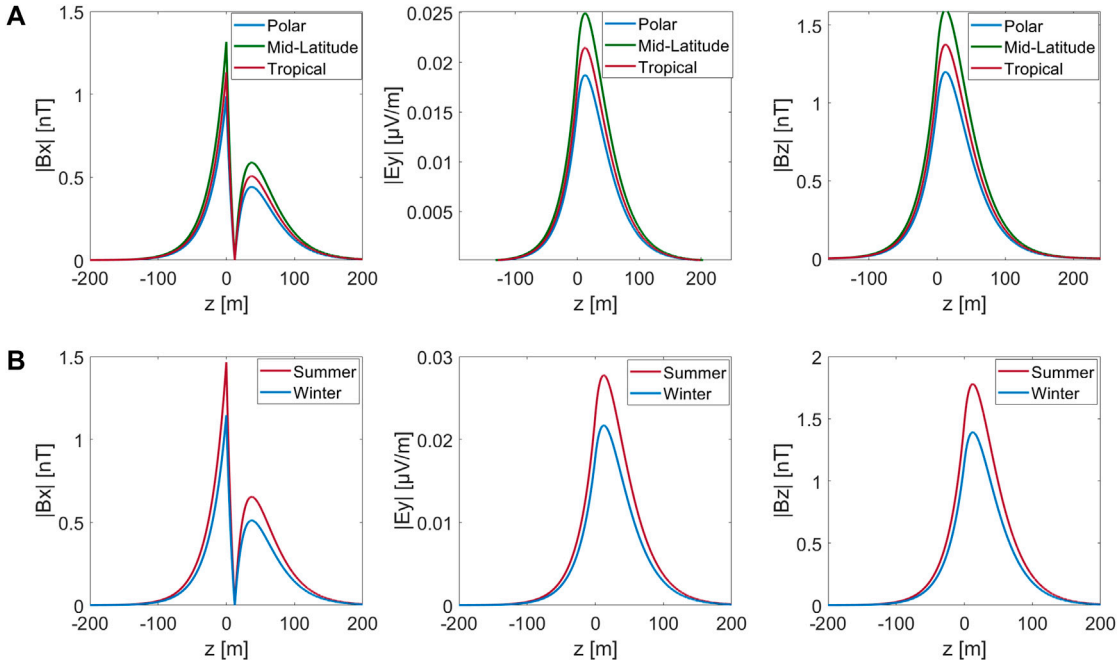

FIGURE 6
(A) Induced electromagnetic fields of ocean waves in thermoclines for tropical, mid-latitude, and polar regions and **(B)** for winter and summer, respectively.

$$\Phi(x,t)=\sum_{k=1}^{N}\frac{a_k g}{\omega}\frac{\cosh\left[p(d-z)\right]}{\cosh(pd)}\exp\left[i(\omega_k t-p_k x-\epsilon_k)\right], \quad (32)$$

where a_k, ω_k, and p_k are the amplitude, angular frequency, and wave number for each component of the ocean wave, respectively. N is the number of frequencies. The phase ϵ_k is randomly distributed within the interval $[0, 2\pi]$. The amplitude a_k can be expressed as (Zhu and Xia, 2014)

$$a_k=\sqrt{2S(w_k)\Delta\omega_k}, \quad (33)$$

where $S(w_k)$ is the spectrum of the ocean wave and $\Delta\omega_k$ is the interval of the angular frequency.

We consider the wave-induced electromagnetic field in a specific area of the South China Sea, taking into account the actual temperature, salinity, and density of seawater. The area is located at latitude 18°N and longitude 119.336°E. The water depth in this region is 294 m. The seawater conductivity can be calculated using Eqs 25–30. Figure 7 shows the distribution of temperature, salinity, and seawater conductivity in this area. The geomagnetic induction intensity in this region is 40,174.6 nT with a magnetic declination of 47° and a magnetic inclination of 1.1°.

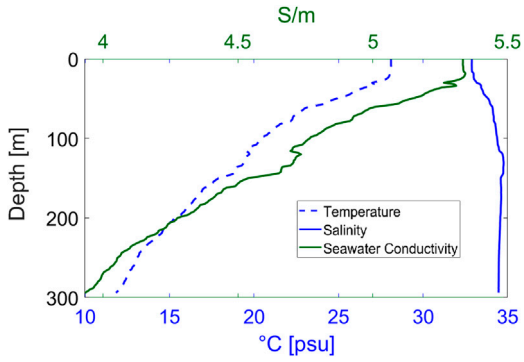

FIGURE 7
Distribution of temperature (the blue dashed line), salinity (the blue solid line), and seawater conductivity (the greed solid line) in a certain area of the South China Sea.

Electromagnetic fields induced by wind waves

The JONSWAP spectrum is commonly used to describe the spectrum of wind waves (Hasselmann et al., 1973):

$$S(\omega)=\frac{\alpha g^2}{\omega^5}\exp\left[-\frac{5}{4}\left(\frac{\omega_p}{\omega}\right)^4\right]\gamma^r \quad (34)$$

with

$$r=\exp\left[-\frac{(\omega-\omega_p)^2}{2\tau^2\omega_p^2}\right],\ \alpha=0.076\left(\frac{V_{10}^2}{gx}\right)^{0.22},\ \omega_p=22\left(\frac{g^2}{V_{10}x}\right)^{1/3},$$
$$\tau=\begin{cases}0.07\omega\leqslant\omega_p,\\ 0.09\omega>\omega_p,\end{cases} \quad (35)$$

where α is the energy scale factor, ω_p is the peak wave frequency, and γ is the peak shape parameter. V_{10} is the wind speed at a height of 10 m above the sea surface, and x is the distance over which the wind blows with a constant velocity, also called wind fetch.

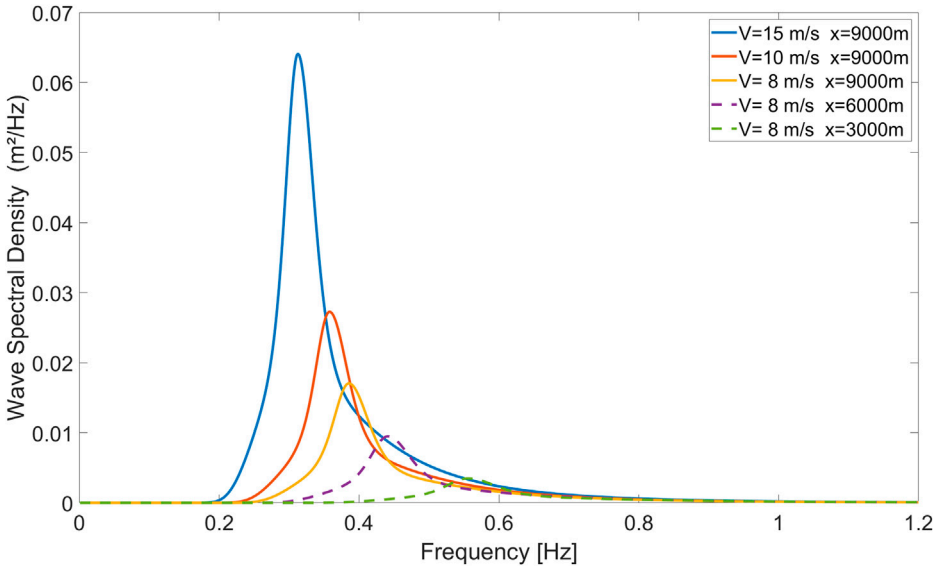

FIGURE 8
JONSWAP spectrum for different wind speeds and fetches V = 15 m/s and x = 9,000 m (the blue solid line); V = 10 m/s and x = 9,000 m (the red solid line); V = 8 m/s and x = 9,000 m (the yellow solid line); V = 8 m/s and x = 6,000 m (the purple dashed line); and V = 8 m/s and x = 3,000 m (the green dashed line).

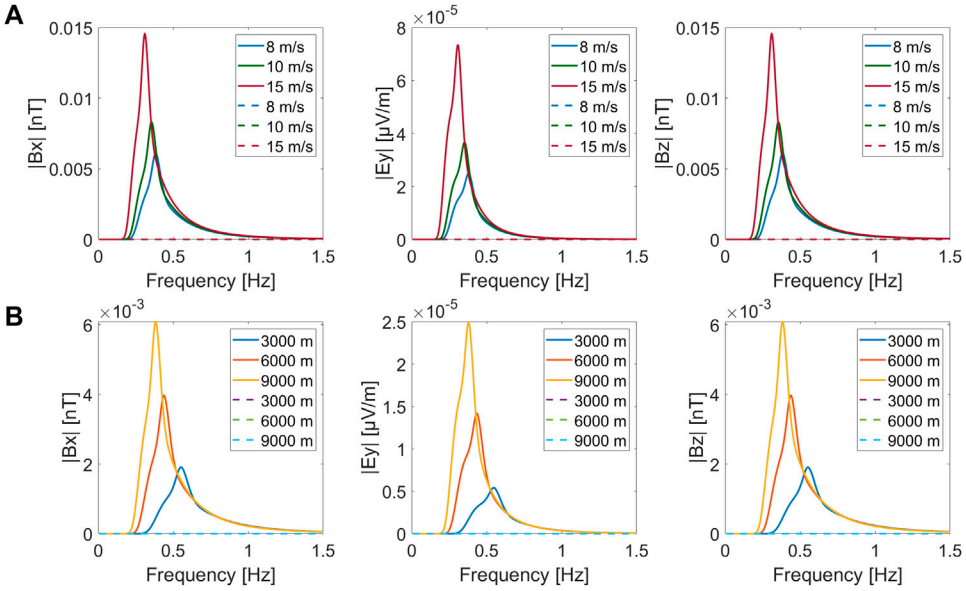

FIGURE 9
Electromagnetic fields generated with the **(A)** wind speed of 8 m/s, 10 m/s, and 15 m/s (a wind fetch of 9,000 m) and the **(B)** wind fetch of 3,000, 6,000, and 9,000 m (a wind speed of 8 m/s).

Figure 8 shows that with the increase in both the wind speed and wind fetch, the magnitude of the spectrum increases but the peak frequency decreases.

The wind-induced electromagnetic fields at the sea surface can be obtained by combining Eqs 20, 23, 32 with the JONSWAP spectrum (34) and are depicted in Figure 9. One can observe that 1) the amplitude of the induced electric and magnetic fields increases with the increase in wind speed; 2) the magnitude of the electrical and magnetic fields increases with the expansion of the wind fetch; 3) as the wind speed increases and the wind fetch expands, the dominant peak frequency gradually shifts toward lower frequencies; and 4) the wind-induced electromagnetic fields are considerably smaller in magnitude at the seafloor (dashed lines) than those near the sea surface (solid lines).

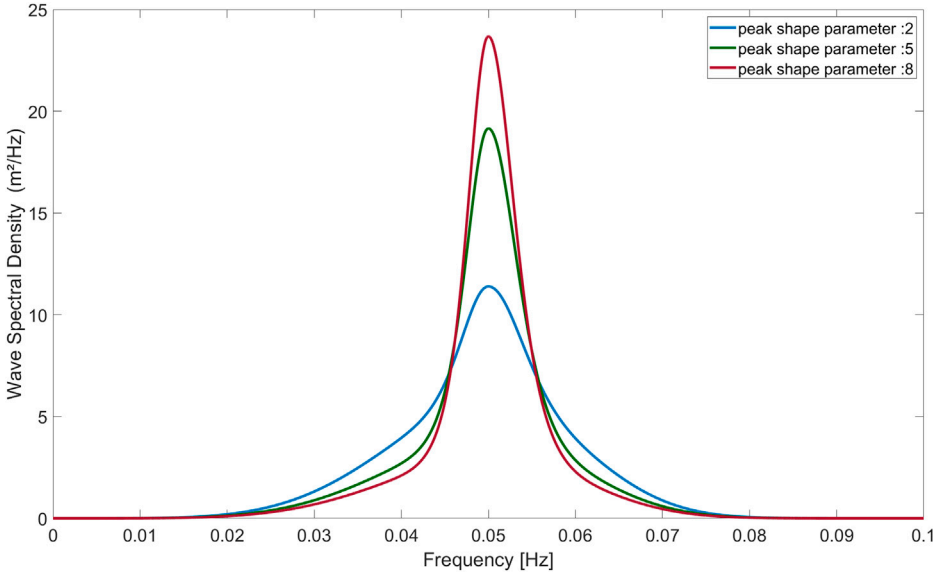

FIGURE 10
Swell spectrum for three different peak shape parameters γ_S = 2, 5, and 8, and H_S = 5 m, and ω_P = 0.3142 rad/s.

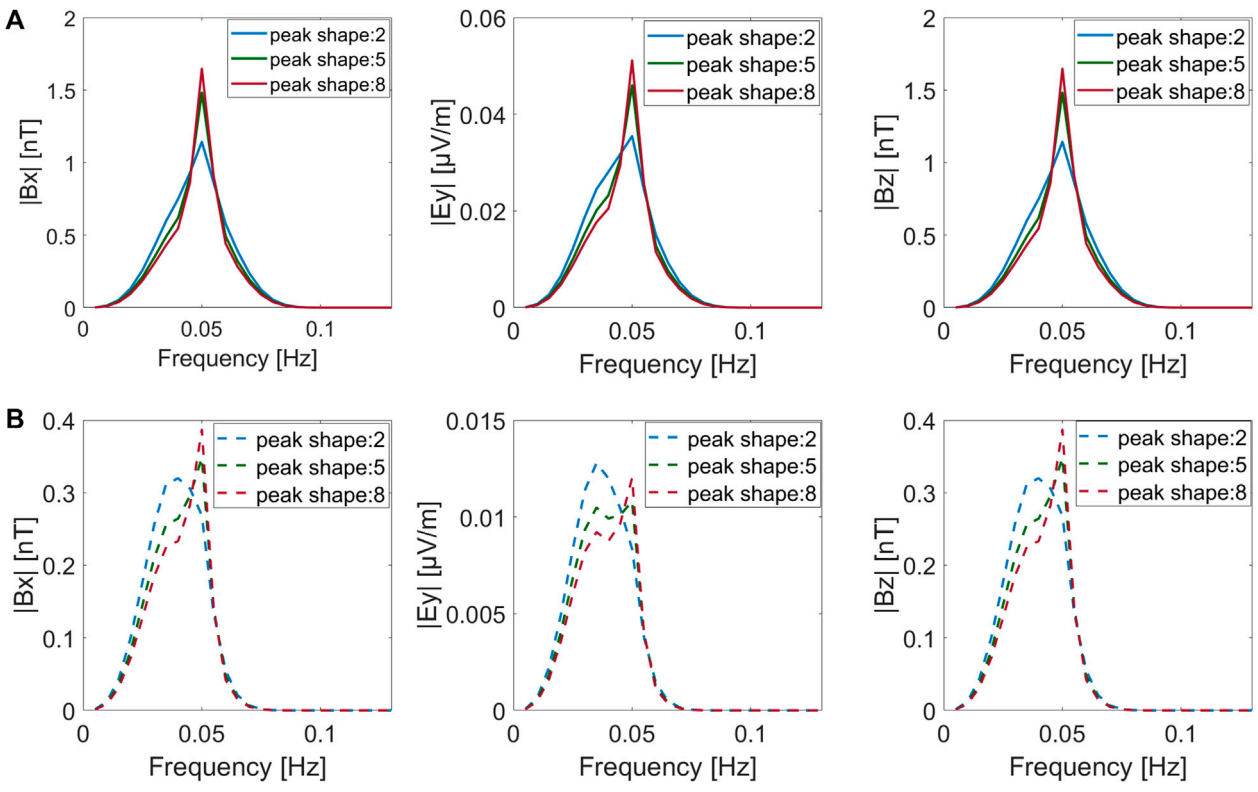

FIGURE 11
Electromagnetic field spectrum for peak shape parameters γ_S = 2, 5, and 8 at the sea surface **(A)** and seafloor **(B)**.

Electromagnetic fields induced by a swell

Wind waves travel in a great circle route after being generated, and after moving out of the area of the wind fetch, the waves are called swell waves and can travel thousands of kilometers. As short-wavelength waves carry less energy and dissipate faster, swell waves often have a relatively long wavelength (Gao et al., 2022). The swell spectrum is given by (Lucas and Guedes Soares, 2015)

TABLE 2 Parameters of mixed ocean waves; type 1: strong wind and weak swell type; type 2: equivalent wind and swell type; and type 3: weak wind and strong swell type.

	Type 1	Type 2	Type 3
$H_{s1}m$	2.51	3.81	4.5
$H_{s2}m$	4.5	3.35	2.51
$\omega_{p1}rad/s$	0.5067	0.5067	0.4909
$\omega_{p2}rad/s$	0.7953	0.7953	0.8963
λ1	1.4	3.3	3.3
λ2	3.3	1.38	1.4
category	$0.1 \le \frac{S_{m1}}{S_{m2}} < 0.67$	$0.67 < \frac{S_{m1}}{S_{m2}} \le 1.5$	$\frac{S_{m1}}{S_{m2}} > 0.15$

$$S(\omega) = \beta\left(\frac{\omega}{\omega_p}\right)^{-5} \exp\left[-1.25\left(\frac{\omega}{\omega_p}\right)^{-4}\right]\gamma_S{}^{r} \tag{36}$$

with

$$r = \exp\left[\frac{-(\omega-\omega_p)^2}{2\tau^2\omega_p^2}\right], \tau = \begin{cases} 0.07\omega \leqslant \omega_p \\ 0.09\omega > \omega_p \end{cases},$$
$$\beta = \frac{5H_s^2}{16\omega_p}\left[1.15 + 0.1688\gamma_S - \frac{0.925}{(1.909+\gamma_S)}\right]^{-1}, \tag{37}$$

where ω_p is the peak wave frequency, γ_S is the peak shape parameter, and H_s is the significant wave height. We assume $\omega_p = 0.3142rad/s$ and $H_s = 5m$. Figure 10 shows the spectrum of swell waves for three different peak shape parameters $\gamma_S = 2$, 5, and 8.

Figure 10 shows that with the increase in the shape peak parameter γ_S, the amplitude of the swell spectrum increases but results in a narrower band of the spectrum.

Figure 11 shows the electromagnetic fields generated by the ocean swell at both the sea surface (A) and seafloor (B). Figure 11 shows that 1) as the shape peak parameter γ_S increases, the magnitudes of the electromagnetic fields also increase at both the sea surface and seafloor; 2) compared to the spectrum of wind waves at the seafloor, the magnitudes of the swell spectrum are much larger for their low frequency ranges.

The electromagnetic fields induced by mixed ocean waves

In some cases, the realistic ocean waves are mixed with wind waves and swell, called mixed ocean waves. The former refers to wind waves in equilibrium with the local wind, while the latter is defined as the swell waves generated elsewhere and not significantly affected by the local wind at that time (Hwang et al., 2012; Garcia-Gabin, 2015).

In order to describe complicated sea states due to the coexistence of wind waves and ocean swell, a double-peaked spectrum is proposed by combining the wind wave system and the swell system (Guedes Soares, 1984, 1991; Rossi et al., 2021). Ochi and Hubble (1976) presented a double-peaked spectrum as a combination of two gamma distributions as follows:

$$S(\omega) = \frac{1}{4}\sum_{j=1}^{2}\frac{\left(\frac{4\lambda_j+1}{4}\omega_{pj}^4\right)^{\lambda_j}}{\Gamma(\lambda_j)}\frac{H_{sj}^2}{\omega^{4\lambda_j+1}}\exp\left[-\left(\frac{4\lambda_j+1}{4}\right)\left(\frac{\omega_{pj}}{\omega}\right)^4\right] \tag{38}$$

with

$$\Gamma(\lambda_j) = \int_0^{+\infty} s^{\lambda_j-1}e^{-s}ds\,(s>0), \tag{39}$$

where H_{sj}, ω_{pj}, and λ_j $(j = 1, 2)$ are the significant wave height, angular peak frequency, and spectral shape factor, respectively, for

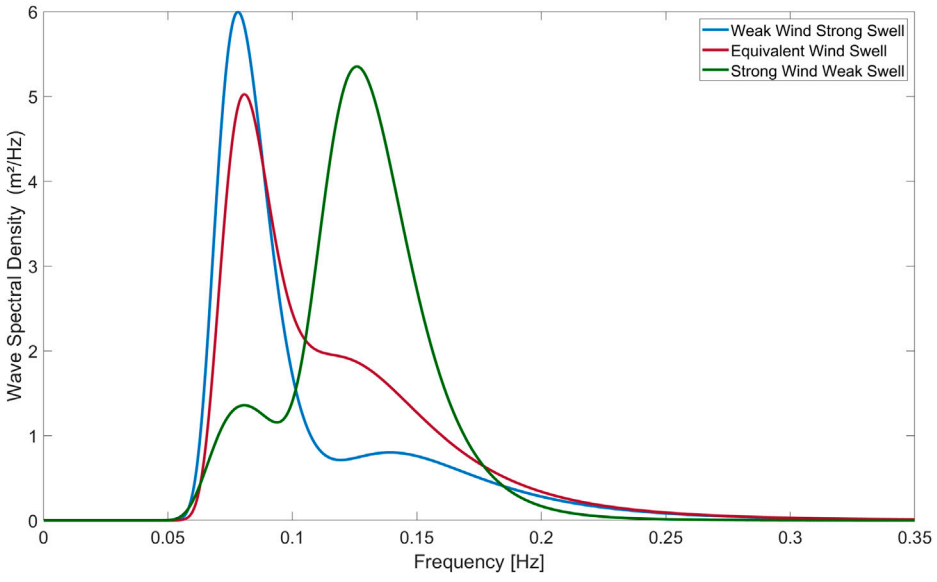

FIGURE 12
Double-peaked spectrum of the weak wind and strong swell type (the blue line), the equivalent wind and swell type (red line), and the strong wind and weak swell type (the green line).

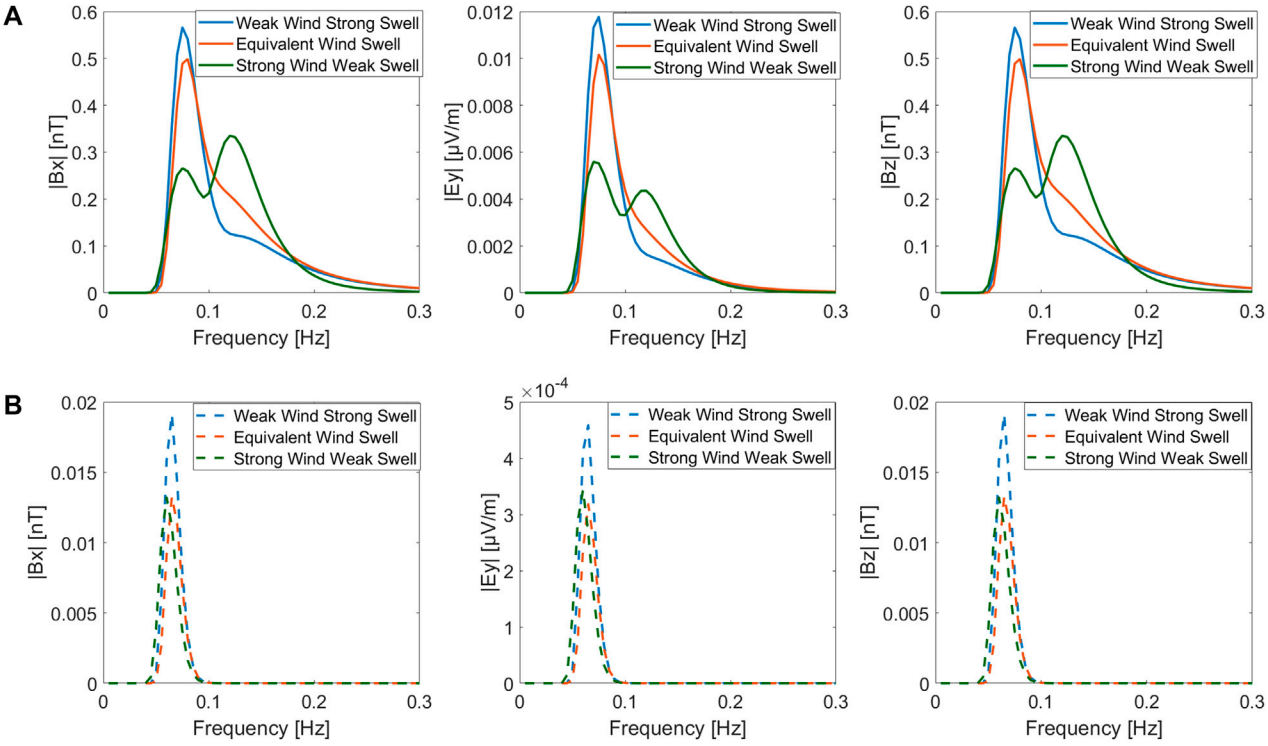

FIGURE 13
Electromagnetic fields induced by three types of mixed ocean waves at the sea surface **(A)** and seafloor **(B)**.

low- and high-frequency parts (known as swell and wind–sea components, respectively). The parameters H_{s1}, H_{s2}, ω_{p1}, ω_{p2}, λ_1, and λ_2 involved in Eq. 38 are determined for the appropriate initial values.

Due to the difference in the effect caused by the wind waves and swell, the spectrum of the mixed ocean waves can be divided into three types: the strong wind and weak swell type, weak wind and strong swell type, and equivalent wind and swell type. The classification of the three types can be determined by the 0^{th} spectral moment of the wind waves and swell, which are defined as Sm_1 and Sm_2, respectively (Cai et al., 2007):

$$Sm_1 = \frac{1}{4}\int_0^{\infty} \frac{\left(\frac{4\lambda_1+1}{4}\omega_{p1}^4\right)^{\lambda_1}}{\Gamma(\lambda_1)} \frac{H_{s1}^2}{\omega^{4\lambda_1+1}} \exp\left[-\left(\frac{4\lambda_1+1}{4}\right)\left(\frac{\omega_{p1}}{\omega}\right)^4\right] d\omega, \quad (40)$$

$$Sm_2 = \frac{1}{4}\int_0^{\infty} \frac{\left(\frac{4\lambda_2+1}{4}\omega_{p2}^4\right)^{\lambda_2}}{\Gamma(\lambda_2)} \frac{H_{s2}^2}{\omega^{4\lambda_2+1}} \exp\left[-\left(\frac{4\lambda_2+1}{4}\right)\left(\frac{\omega_{p2}}{\omega}\right)^4\right] d\omega. \quad (41)$$

Table 2 shows the parameters of the mixed ocean waves. Figure 12 shows that the energy in the spectrum of weak wind and strong swell type is usually concentrated at low frequencies, but the energy in the spectrum of the strong wind and weak swell type is usually concentrated at high frequencies. The energy distribution is more balanced in the spectrum of the equivalent wind and swell type.

The electromagnetic fields induced by three types of mixed ocean waves are shown in Figure 13. From Figure 13, we can see that 1) the three-type mixed wave spectrum can be easily recognized by the x- and z-components of the induced magnetic intensity strength spectrum observed at the sea surface (Figure 13A); 2) due to the high-frequency filtering effect of the ocean, the electromagnetic field spectra at the seafloor (Figure 13B) mainly retain the low-frequency information on the wave spectrum and may not reflect the realistic spectrum of the mixed ocean waves.

Conclusion

In this paper, we presented a finite difference algorithm for simulating ocean wave-induced electromagnetic fields with varying seawater conductivity. Our method allows us to simulate and investigate the influence of arbitrary variation in seawater conductivity on wave-induced electromagnetic fields. Our numerical examples show that seawater conductivity has a significant effect on wave-induced electromagnetic fields. We also investigated the effects of the thermocline on wave-induced electromagnetic responses at different latitudes and seasons. We observed the maximum amplitude of induced electromagnetic fields in the mid-latitude regions, while we observed the minimum amplitude of induced electromagnetic fields in the polar regions. This is mainly influenced by both the geomagnetic field and temperature of the thermocline at different latitudes. Furthermore, in mid-latitude regions, the thermocline conductivity exhibits seasonal variations, with a greater decrease during summer than that during winter, leading to a larger induced electromagnetic field. The latitude and seasonal variations in the geomagnetic field and seawater

conductivity are crucial for the accurate simulation of ocean wave-induced electromagnetic fields.

Moreover, we simulate the electromagnetic field spectra for wind waves, ocean swell, and mixed ocean waves in the inhomogeneous ocean. We find that the energy of the wind wave-induced electromagnetic field is predominantly concentrated in the high-frequency band, while the energy of the swell wave-induced electromagnetic field is mainly concentrated in the low-frequency band. Additionally, we simulate three types of mixed wave-induced electromagnetic fields based on the combination of wind and swell strengths, and analyze their characteristics.

Data availability statement

The original contributions presented in the study are included in the article/Supplementary Material; further inquiries can be directed to the corresponding author.

Author contributions

JG implemented the algorithms, drew the figures, and wrote the manuscript. YL led the research, supervised the study, and edited the manuscript. All authors contributed to the article and approved the submitted version.

Funding

This work was supported by the National Science Foundation of China (91958210 and U2241201).

Acknowledgments

The authors thank Ji Cai for helping in manuscript editing.

Conflict of interest

YL is a adjunct professor of the National Engineering Research Center of Offshore Oil and Gas Exploration.

The remaining author declares that the research was conducted in the absence of any commercial or financial relationships that could be construed as a potential conflict of interest.

Publisher's note

References

Ailliot, P., Maisondieu, C., and Monbet, V. (2013). Dynamical partitioning of directional ocean wave spectra. *Probabilistic Eng. Mech.* 33, 95–102. doi:10.1016/j.probengmech.2013.03.002

Cai, F., Liu, Q., and Miu, Q. (2007). *Study on numerical simulation of bi-spectrum wave*. Shanghai, China: The Chinese Society Of Naval Architects And Marine Engineers, 512–515.

Chave, A. D., and Luther, D. S. (1990). Low-frequency, motionally induced electromagnetic fields in the ocean: 1. Theory. *J. Geophys. Res.* 95, 7185. doi:10.1029/JC095iC05p07185

Chave, A. D. (1983). On the theory of electromagnetic induction in the Earth by ocean currents. *J. Geophys. Res. Solid Earth* 88, 3531–3542. doi:10.1029/JB088iB04p03531

Cieutat, J.-M., Gonzato, J.-Ch., and Guitton, P. "A general ocean waves model for ship design," in Proceedings of the Conference: Virtual Concept, Biarritz, France, November 2003.

Cox, C., Kroll, N., Pistek, P., and Watson, K. (1978). Electromagnetic fluctuations induced by wind waves on the deep-sea floor. *J. Geophys. Res.* 83, 431. doi:10.1029/JC083iC01p00431

Crews, A., and Futterman, J. (1962). Geomagnetic micropulsations due to the motion of ocean waves. *J. Geophys. Res.* 67, 299–306. doi:10.1029/JZ067i001p00299

Fofonoff, N. P., and Millard, R. C. (1983). *Algorithms for the computation of fundamental properties of seawater*. Paris, France: UNESCO. doi:10.25607/OBP-1450

Fraser, D. C. (1966). The magnetic fields of ocean waves. *Geophys. J. R. Astronomical Soc.* 11, 507–517. doi:10.1111/j.1365-246X.1966.tb03162.x

Gao, X., Ma, X., Ma, Y., Huang, X., Zheng, Z., and Dong, G. (2022). Spectral characteristics of swell-dominated seas with *in situ* measurements in the coastal seas of Peru and Sri Lanka. *J. Atmos. Ocean. Technol.* 39, 755–770. doi:10.1175/JTECH-D-21-0143.1

Garcia-Gabin, W. (2015). Wave bimodal spectrum based on swell and wind-sea components. I*FAC-PapersOnLine* 48, 223–228. doi:10.1016/j.ifacol.2015.10.284

Grainger, J. P., Sykulski, A. M., Jonathan, P., and Ewans, K. (2021). Estimating the parameters of ocean wave spectra. *Ocean. Eng.* 229, 108934. doi:10.1016/j.oceaneng.2021.108934

Guedes Soares, C. (1991). On the occurrence of double peaked wave spectra. *Ocean. Eng.* 18, 167–171. doi:10.1016/0029-8018(91)90040-W

Guedes Soares, C. (1984). Representation of double-peaked sea wave spectra. *Ocean. Eng.* 11, 185–207. doi:10.1016/0029-8018(84)90019-2

Håland, E., Flekkøy, E. G., and Måløy, K. J. (2012). Vertical and horizontal components of the electric background field at the sea bottom. *GEOPHYSICS* 77, E1–E8. doi:10.1190/geo2011-0039.1

Hasselmann, K., Barnett, T. P., Bouws, E., Carlson, H., Cartwright, D. E., Enke, K., et al. (1973). Hamburg, Germany: Deutches Hydrographisches Institut.Measurements of wind-wave growth and swell decay during the joint north sea wave project (JONSWAP)

Hwang, P. A., Ocampo-Torres, F. J., and García-Nava, H. (2012). Wind Sea and swell separation of 1D wave spectrum by a spectrum integration method. *J. Atmos. Ocean. Technol.* 29, 116–128. doi:10.1175/JTECH-D-11-00075.1

Irrgang, C., Saynisch, J., and Thomas, M. (2016). Impact of variable seawater conductivity on motional induction simulated with an ocean general circulation model. *Ocean. Sci.* 12, 129–136. doi:10.5194/os-12-129-2016

Larsen, J. C. (1971). The electromagnetic field of long and intermediate water waves. *J. Mar. Res.* 29.

Lilley, F. E. M., Hitchman, A. P., Milligan, P. R., and Pedersen, T. (2004a). Sea-surface observations of the magnetic signals of ocean swells. *Geophys. J. Int.* 159, 565–572. doi:10.1111/j.1365-246X.2004.02420.x

Lilley, F. E. M., Ted)and Weitemeyer, K. A. (2004b). Apparent aeromagnetic wavelengths of the magnetic signals of ocean swell. *Explor. Geophys.* 35, 137–141. doi:10.1071/EG04137

Longuet-Higgins, M. S. (1962). The directional spectrum of ocean waves, and processes of wave generation. *Proc. R. Soc. Lond. Ser. A, Math. Phys. Sci.* 265, 286–315. doi:10.1098/rspa.1962.0010

Lucas, C., and Guedes Soares, C. (2015). On the modelling of swell spectra. *Ocean. Eng.* 108, 749–759. doi:10.1016/j.oceaneng.2015.08.017

Miles, T., Dosso, H. W., and Ng, T. P. (1977). An analogue model for studying magnetic variations induced by ocean waves. *Phys. Earth Planet. Interiors* 14, 137–142. doi:10.1016/0031-9201(77)90150-9

Minami, T. (2017). Motional induction by tsunamis and ocean tides: 10 Years of progress. *Surv. Geophys.* 38, 1097–1132. doi:10.1007/s10712-017-9417-3

Minami, T., Schnepf, N. R., and Toh, H. (2021). Tsunami-generated magnetic fields have primary and secondary arrivals like seismic waves. *Sci. Rep.* 11, 2287. doi:10.1038/s41598-021-81820-5

Minami, T., and Toh, H. (2013). Two-dimensional simulations of the tsunami dynamo effect using the finite element method. *Geophys. Res. Lett.* 40, 4560–4564. doi:10.1002/grl.50823

Nielsen, U. D., and Dietz, J. (2020). Ocean wave spectrum estimation using measured vessel motions from an in-service container ship. *Mar. Struct.* 69, 102682. doi:10.1016/j.marstruc.2019.102682

Ochadlick, A. R. (1989). Measurements of the magnetic fluctuations associated with ocean swell compared with Weaver's Theory. *J. Geophys. Res.* 94 (16), 16237–16242. doi:10.1029/JC094iC11p16237

Ochi, M. K., and Hubble, E. N. (1976). Six-parameter wave spectra. *Coast. Eng. Proc.* 1, 17. doi:10.9753/icce.v15.17

Rasool, S., Muttaqi, K. M., and Sutanto, D. (2021). Modelling Ocean waves and an investigation of ocean wave spectra for the wave-to-wire model of energy harvesting. *Eng. Proc.* 12, 51. doi:10.3390/engproc2021012051

Rossi, G. B., Crenna, F., Berardengo, M., Piscopo, V., and Scamardella, A. (2021). Investigation on spectrum estimation methods for bimodal sea state conditions. *Sensors (Basel)* 21, 2995. doi:10.3390/s21092995

Ryabkova, M., Karaev, V., Guo, J., and Titchenko, Yu. (2019). A review of wave spectrum models as applied to the problem of radar probing of the sea surface. *J. Geophys. Res. Oceans* 124, 7104–7134. doi:10.1029/2018JC014804

Semkin, S. V., and Smagin, V. P. (2012). The effect of self-induction on magnetic field generated by sea surface waves. *Izv. Atmos. Ocean. Phys.* 48, 207–213. doi:10.1134/S0001433812020119

Shimizu, H., and Utada, H. (2015). Motional magnetotellurics by long oceanic waves. *Geophys. J. Int.* 201, 390–405. doi:10.1093/gji/ggv030

Techet, A. H. (2005). 13.42 design principles for ocean vehicles. https://ocw.mit.edu/courses/2-22-design-principles-for-ocean-vehicles-13-42-spring-2005/fea036f3255fa4824279668c7ff8c6cd_r1_lti.pdf.

Tyler, R. H., Boyer, T. P., Minami, T., Zweng, M. M., and Reagan, J. R. (2017). Electrical conductivity of the global ocean. *Earth, Planets Space* 69, 156. doi:10.1186/s40623-017-0739-7

Weaver, J. T. (1965). Magnetic variations associated with ocean waves and swell. *J. Geophys. Res.* 70, 1921–1929. doi:10.1029/JZ070i008p01921

Yaakobi, O., Zilman, G., and Miloh, T. (2011). Detection of the electromagnetic field induced by the wake of a ship moving in a moderate sea state of finite depth. *J. Eng. Math.* 70, 17–27. doi:10.1007/s10665-010-9410-z

Zhan, Y., and Pan, X. (2019). Propagation characteristics of electromagnetic wave in seawater channel for submerged buoy. *J. Comput. Commun.* 7, 72–81. doi:10.4236/jcc.2019.710007

Zheng, Z., Fu, Y., Liu, K., Xiao, R., Wang, X., and Shi, H. (2018). Three-stage vertical distribution of seawater conductivity. *Sci. Rep.* 8, 9916. doi:10.1038/s41598-018-27931-y

Zhu, X., and Xia, M. (2014). Magnetic field induced by wake of moving body in wind waves (Invited Paper). *PIER* 149, 109–118. doi:10.2528/PIER14070706

frontiers | Frontiers in Earth Science

TYPE Original Research
PUBLISHED 23 August 2023
DOI 10.3389/feart.2023.1230071

OPEN ACCESS

EDITED BY
Cong Zhou,
East China University of Technology, China

REVIEWED BY
Xian Zhang,
Central South University, China
Yoshiya Usui,
The University of Tokyo, Japan
Ikuko Fujii,
Meteorological College, Japan

*CORRESPONDENCE
Lili Zhang,
lilyzhang@mail.iggcas.ac.cn

RECEIVED 28 May 2023
ACCEPTED 08 August 2023
PUBLISHED 23 August 2023

CITATION
Chen H, Zhang L, Ren Z, Cao H and Wang G (2023), An automatic preselection strategy for magnetotelluric single-site data processing based on linearity and polarization direction. *Front. Earth Sci.* 11:1230071. doi: 10.3389/feart.2023.1230071

An automatic preselection strategy for magnetotelluric single-site data processing based on linearity and polarization direction

Hao Chen[1], Lili Zhang[2]*, ZhengYong Ren[1], Hui Cao[3] and Gang Wang[4]

[1]School of Geosciences and Info-Physics, Central South University, Changsha, China, [2]Key Laboratory of Petroleum Resource Research, Institute of Geology and Geophysics, Chinese Academy of Sciences, Beijing, China, [3]College of Geophysics, Chengdu University of Technology, Chengdu, China, [4]Energy and Deep Earth Exploration Laboratory, Institute of Geophysical and Geochemical Exploration, China Geological Survey, Langfang, China

The magnetotelluric response function can be severely disturbed by cultural electromagnetic noise. The preselection strategy is one of the effective ways to remove the influence of noise when calculating the response function. This study proposed three new parameters (the amplitude ratio predicted amplitude ratio and linear coherence (PLcoh) between the predicted and observed electric fields and the dispersion degree of the magnetic polarization direction (DD_{pol})) to detect noisy data, making the preselection strategy automatic. The first two were used to evaluate the linearity of binary linear regression to constrain incoherent noise, while the last was used to evaluate the magnetic polarization direction to constrain coherent noise. Finally, the technique is illustrated by applying it to two field datasets and comparing it with the previous studies. The results showed that these parameters can be used to effectively identify contaminated data, and a reliable response function can be obtained by using these parameters to extract high-quality data when intermittent noise contaminates field data.

KEYWORDS

magnetotelluric impedance, linearity, polarization direction, data processing, preselection

1 Introduction

The magnetotelluric (MT) method is an electromagnetic (EM) geophysical method used to infer the subsurface electrical conductivity from the natural geomagnetic and geoelectric fields obtained at the Earth's surface (Tikhonov, 1950; Cagniard, 1953). There is a linear relationship between the geoelectric and geomagnetic fields in the frequency domain, and it can be expressed as follows (Tikhonov and Berdichevsky, 1966):

$$\begin{pmatrix} E_x(\omega) \\ E_y(\omega) \end{pmatrix} = \begin{pmatrix} Z_{xx}(\omega)\, Z_{xy}(\omega) \\ Z_{yx}(\omega) Z_{yy}(\omega) \end{pmatrix} \begin{pmatrix} H_x(\omega) \\ H_y(\omega) \end{pmatrix}, \quad (1)$$

where $\boldsymbol{E}$ and $\boldsymbol{H}$ are the horizontal electric and magnetic field components at a specific frequency, respectively, ω denotes the angular frequency, and $\boldsymbol{Z}$ represents the MT impedance. The subscripts x and y denote two orthogonal directions. The conventional MT impedance estimator first transforms the time-series data into the frequency domain by the windowed Fourier transformation and then performs regression in the frequency domain to calculate the impedance (Jones et al., 1989; Smirnov, 2003; Chave and Jones, 2012). The least-squares (LS) estimator (Sims et al., 1971) is a basic method used for linear regression; it requires the magnetic field to be noise-free, and the residuals between the predicted and observed electric fields are uncorrelated and follow a multivariate normal probability distribution (Chave and Thomson, 1989). However, field data consist of natural sources and local cultural noise (Szarka, 1988; Junge, 1996), these assumptions often fail, and the LS estimator can be severely disturbed by cultural noise.

Methods to remove these disturbances are mainly based on robust statistical algorithms, remote reference processing, multistation analyses or time series modification. The robust statistical methods are based on data-adaptive weighting schemes, which aim to detect and reject outliers from a majority of well-behaved samples (Egbert and Booker, 1986; Chave and Thomson, 2004; 2003; 1989; Jones et al., 1989). These methods require reasonable proportions of normal data to yield reliable results, e.g., data with no more than 50% contamination (Smirnov, 2003). If a noise source is more persistent, it can easily result in a distribution of the majority of the data, which is wrong (Weckmann et al., 2005). The remote reference method requires simultaneously recorded EM fields from at least two sites. Remote reference processing uses cross-power spectra instead of auto-power spectra when performing regression based on the least-squares estimator (Goubau et al., 1978; Gamble et al., 1979). The remote reference method cannot always improve the results, as a successful application requires a horizontal magnetic field at a remote site without correlated noise. It is difficult to find a suitable reference site because cultural noise signals can be widespread and coherent over large areas (Weckmann et al., 2005), and we are faced with single-site robust processing. Moreover, MT researchers have proposed multistation analyses. Larsen et al. (1996) and Oettinger et al. (2001) proposed the signal-noise separation (SNS) method. SNS uses the remote magnetic field to estimate the interstation transform function as the separation tensor; they separated the local magnetic field into signal and noise parts and then calculated the impedance. Egbert (1997) proposed a robust multivariate errors-in-variables estimator (RMEV) to separate field data into signal and noise components using principal component analysis. A more recent application of the method is shown in Smirnov and Egbert (2012). Both the RMEV and SNS methods use a robust approach to their data processing. Those methods may be biased when the majority of the data are contaminated and the noise is coherent between the local and remote sites. In a strong noise environment, the time series modification method is also effective in suppressing the influence of noise (Chen et al., 2022; Li et al., 2022; Li et al., 2023; Li et al., 2018; Zhang et al., 2022; Zhang et al., 2021; Zhou et al., 2022; Wang et al., 2017; Kappler, 2012). These methods identify abnormal waveforms in the time domain and modify the original time series, and they are useful for data contaminated by strong noise with an abnormal waveform.

In a noisy EM environment, as an alternative method, it is practical to use a preselection strategy (Jones and Jödicke, 1984; Travassos and Beamish, 1988; Smirnov, 2003; Chave and Thomson, 2004; Weckmann et al., 2005; Platz and Weckmann, 2019) to reduce the EM noise to a level that the robust statistic method can handle. All of the studies, e.g., Platz and Weckmann (2019), Weckmann et al. (2005), and Garcia and Jones (2002), demonstrated substantially better performance for data-adaptive weighting schemes after prescreening. In theory, if the noise does not contaminate the local site all the time, we can extract high signal-to-noise ratio (SNR) data and obtain a reliable result. The multiple coherence (Jones and Jödicke, 1984; Travassos and Beamish, 1988; Egbert and Livelybrooks, 1996; Bendat and Piersol, 2011) and bivariate coherence (Ritter et al., 1998; Weckmann et al., 2005) are widely used to evaluate the data quality under the assumption that the dataset follows a linear relationship. In this research, we propose a new method, which performs similarly with multiple coherence and is superior to the bivariate coherence, to evaluate the linearity by comparing the similarity between the observed and predicted electric fields. The parameters based on the linearity are effective for detecting incoherent noise, but coherent noise may also have high linearity (Weckmann et al., 2005). In addition, Weckmann et al. (2005) showed the effectiveness of magnetic polarization direction (MPD) in visualizing coherent noise. However, their preselection strategy cannot be performed automatically. Platz and Weckmann (2019) attempted to perform data preselection automatically and used statistical information on the magnetic polarization direction (SMPD) to constrain coherent noise with strong polarization direction. They removed all the data whose polarization directions fall in a bin which is much higher than the threshold. However, the data fall in out of the bin also may correspond to the coherent noise. We proposed a new parameter based on the dispersion degree of the magnetic polarization direction (DD_{pol}) to identify the coherent noise, and the case study shows that it is superior to the criteria based on SMPD. The new parameters are tested on approximately 500 site data from the USArray project (Schultz et al., 2018; Kelbert, 2019) and data collected in China. Finally, two case studies are used to show the effectiveness of the parameters in detecting noisy data and the preselection strategy in improving the quality of the impedance tensor calculation.

The following sections are organized as follows. Section 2 introduces the new parameters proposed to detect noise. Section 3 shows the effectiveness of the parameters to detect noise and compares the new parameters with the previous study.

2 Parameters proposed for the preselection strategy

The method to obtain the spectra of EM fields in different frequencies is similar to the method used in the bounded influence remote reference processing (BIRRP) code (Chave and Thomson, 1989; Chave and Thomson, 2004; 2003). The time series is prewhited and divided into adjacent segments. These segments are cosine tapered before the Fourier transformation. Then, the Fourier coefficients are corrected for the influence of the instrument response. Next, selected frequencies within each segment are extracted to calculate the impedance tensor and uncertainty followed by the robust estimator created by Neukirch and García

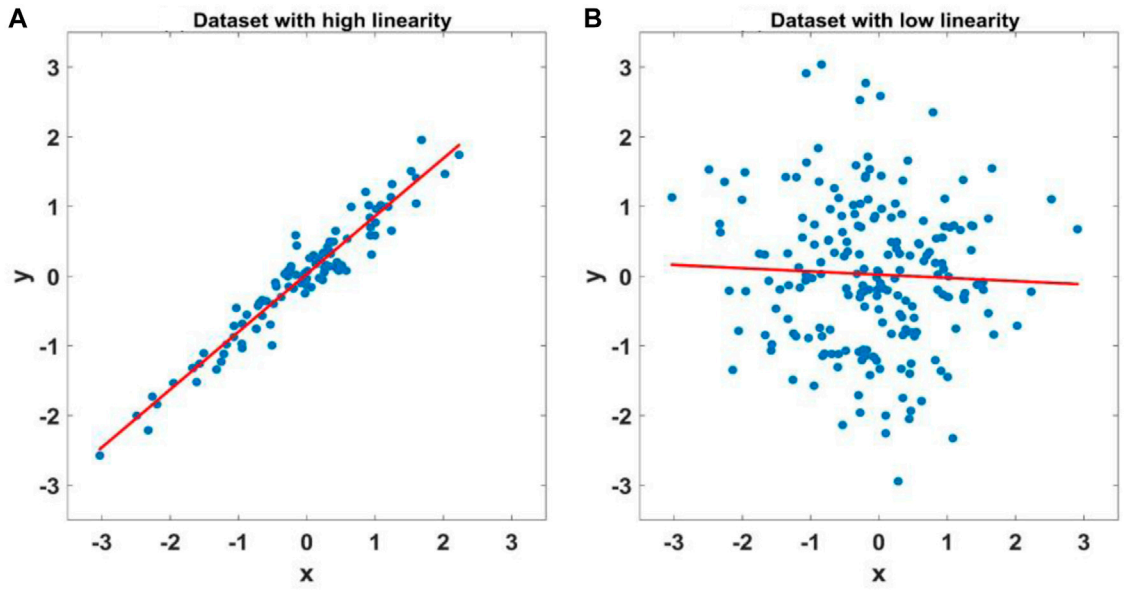

FIGURE 1
Single-input/single-output linear model ***y***=a****x***+b. ***x*** is the input, and ***y*** is the output. The blue points denote the observed data, and the red line is the model calculated by regression. The difference between the data with high linearity and low linearity is that most of the predicted values (a****x***+b) calculated by the model and the output (***y***) are similar, as shown in **(A)** and **(B)**.

(2014). At last, the segment length is variable, the previous steps are repeated to calculate the impedance in different frequencies. During data processing, one segment corresponds to one data in the frequency domain. In the following, we refer to one data as one event in the frequency domain. The key to obtaining a reliable impedance from the noisy site is detecting and removing the noise before the impedance estimation. This section introduces the parameters used to detect noisy events from the perspective of linearity and MPD.

2.1 Noise detection based on linearity

From the perspective of whether the data follow the linear relationship in Eq. 1, the field data (***E*** and ***H***) can be subdivided into three parts as follows:

$$\boldsymbol{E} = \{\boldsymbol{E}^{\boldsymbol{MT}}, \boldsymbol{E}^{\boldsymbol{HLN}}, \boldsymbol{E}^{\boldsymbol{LLN}}\}, \tag{2}$$

$$\boldsymbol{H} = \{\boldsymbol{H}^{\boldsymbol{MT}}, \boldsymbol{H}^{\boldsymbol{HLN}}, \boldsymbol{H}^{\boldsymbol{LLN}}\}, \tag{3}$$

where the superscript ***HLN*** denotes the data dominated by noise with high linearity, the superscript ***LLN*** denotes the data dominated by noise with low linearity, and the superscript ***MT*** denotes the high-quality data with high linearity. Noise with low linearity can be identified from the similarity between the observed electric field and that predicted by the linear relationship. It is similar to the single-input/single-output linear model to evaluate the linearity, as shown in Figure 1. The difference between the data with high linearity and low linearity is that most of the predicted and observed values of the output are similar.

Assuming the data are highly linear related, the observed electric field (***E***) should be similar to the predicted electric field ($\boldsymbol{E_p}$), where $\boldsymbol{E_p}$ =***ZH*** and ***Z*** are obtained by the least-squares estimator. We can identify noisy data with low linearity by comparing the measured electric field (***E***) and the predicted electric field ($\boldsymbol{E_p}$). The complex number has two properties: the amplitude and phase. In this study, we use the linear coherence defined by the phase difference between the predicted and observed electric fields to confirm the phase similarity and use the amplitude ratio between the predicted and observed electric fields to confirm the amplitude similarity.

The linear coherence (Lcoh) between two spectra A_i and B_i is defined by the cosine of the phase difference (PD) as follows:

$$\cos(\theta_i) = \mathrm{Re}\left(e^{j\left(\varphi_{A_i}-\varphi_{B_i}\right)}\right) = \mathrm{Re}\left(\frac{A_i\bar{B}_i}{|A_i||B_i|}\right), \tag{4}$$

where A_i and B_i denote the spectrum calculated from the i^{th} segment, $\bar{B}_i$ represents a conjugate of B_i, and θ_i denotes the angle of the phase difference (PD) between A_i and B_i. According to Euler's formula, Lcoh equals the real part of $e^{j(\varphi_{A_i}-\varphi_{B_i})}$. Re denotes the real part of the complex number. The value of Lcoh lies in the range of (−1,1). When the PD is close to 0 °, the Lcoh is high and close to 1. In this study, the predicted linear coherence (*P Lcoh*) between the measured electric field (***E***) and the predicted electric field ($\boldsymbol{E_p}$) is calculated as follows:

$$PLcoh = \mathrm{Re}\left(\frac{Y_{p_i}\bar{Y}_i}{|Y_{p_i}||Y_i|}\right), \tag{5}$$

where Y_{p_i} and Y_i are the predicted and measured electric fields corresponding to the i^{th} segment, and Y is associated with either E_x

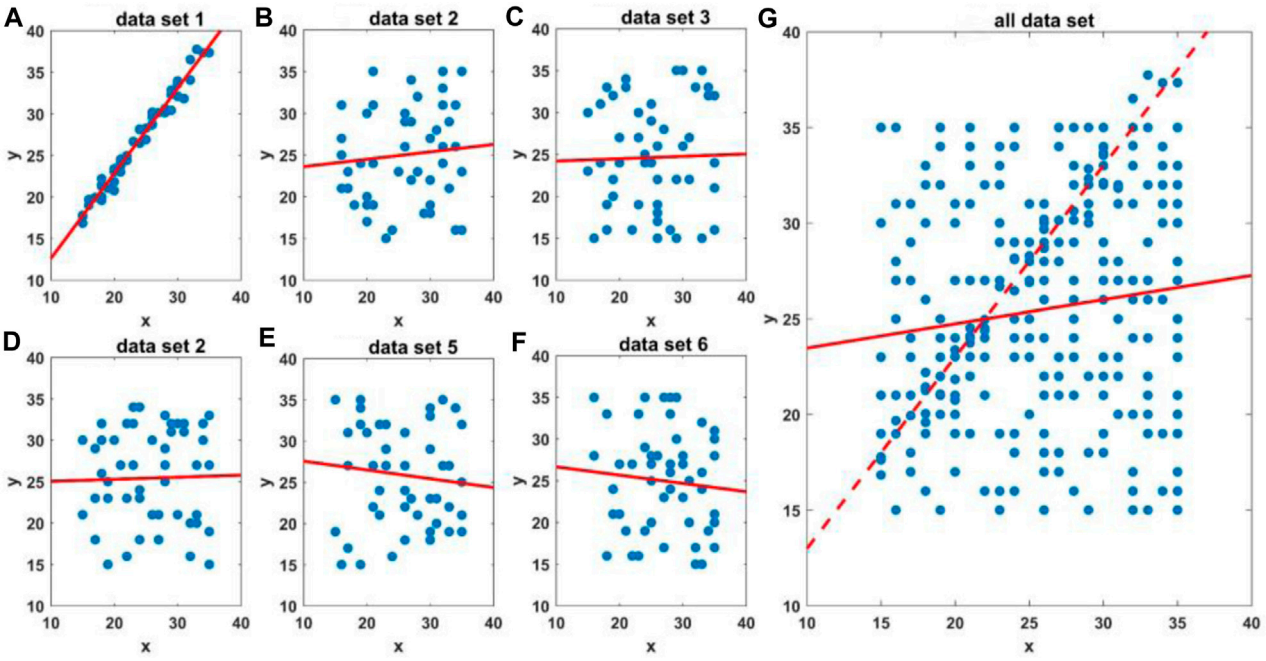

FIGURE 2
Single-input/single-output linear model ***y***=a****x***+b. **(A–F)** show the regression results for six datasets separately; each dataset has 50 points, and only dataset 1 has high linearity. The blue points denote the observed data, and the red line is the model calculated by regression. **(G)** shows the regression results for all the available data, including 300 points. The red solid line denotes the model calculated by all the available data, and the dashed line denotes the model calculated by dataset 1.

or E_y. The predicted electric field and the observed electric field should be similar when the linearity is high, and *PLcoh* should be close to 1.

The high predicted linear coherence can ensure the phase similarity. We also use the predicted amplitude ratio (*PAR*) to ensure the amplitude similarity, and it is defined as follows:

$$PAR = \begin{cases} \dfrac{|Y_{p_i}|}{|Y_i|}, |Y_{p_i}| < |Y_i|, or \\ \dfrac{|Y_i|}{|Y_{p_i}|}, |Y_i| < |Y_{p_i}|. \end{cases} \quad (6)$$

The *PAR* ranges from 0 to 1; the higher *PAR* is, the higher the similarity between the two spectra in terms of the amplitude.

There is a problem that the energy of the signal and noise changes with time, and the linearity may change. Suppose we perform regression with all the available data; the linearity may be low in the presence of a large amount of noise and provide misleading information. It is similar to the single-input/single-output linear model, as shown in Figure 2. There are six datasets, and only dataset 1 has high linearity. When we perform regression with all the available data, the linearity is low, and we cannot extract data with high linearity. To solve this problem, we subdivide the data into small groups and calculate the *PAR* and *PLcoh* values separately. We rename the predicted linear coherence and amplitude ratio as $PLcoh_{sz}$ and PAR_{sz}, where the subscript *SZ* means we calculate the predicted electric field ($\boldsymbol{E_p} = \boldsymbol{ZH}$) by the impedance ($\boldsymbol{Z}$) obtained by the subdivided data. In this research, the field data are subdivided into small groups with 20 samples when evaluating the linearity. It is necessary to divide the data into groups when evaluating linearity (see Supplementary Figures S2, S3).

2.2 Noise detection based on the magnetic polarization directions

Fowler et al. (1967) proposed the polarization direction, and Weckmann et al. (2005) showed the effectiveness of MPD in detecting coherent noise. The MPD (α_{H_i}) at a specific frequency is defined as follows:

$$\alpha_{H_i} = tan^{-1}\frac{2Re\left(H_{x_i}\bar{H}_{y_i}\right)}{|H_{x_i}|^2 - |H_{y_i}|^2} = tan^{-1}\frac{2\frac{|H_{y_i}|}{|H_{x_i}|}\cdot cos(\theta_i)}{1-\left(\frac{|H_{y_i}|}{|H_{x_i}|}\right)^2}, \quad (7)$$

where i (=1,2, . . . , N) is the number index of the event, H_{x_i} and H_{y_i} are the spectra of the magnetic field calculated from the i^{th} segment, and θ_i denotes the PD between H_{x_i} and H_{y_i}. The polarization direction is related to the PD and amplitude ratio (AR) between the two orthogonal fields. Various sources generate natural magnetic signals that vary in incident directions and energy, and the PD and AR between the two orthogonal fields vary with time; thus, the magnetic field has no preferred polarization direction (Weckmann et al., 2005). In contrast, the local EM noise source usually has a constant location; the incident direction and energy have similar properties that change with

TABLE 1 Classification of the data quality based on the linearity and MPD.

	Linearity	MPD
High-quality data	$PLcoh_{sz}$ >0.8; PAR_{sz} >0.8	DD_{pol} < 0.5
Incoherent noise	$PLcoh_{sz}$ < 0.8; or PAR_{sz} <0.8	DD_{pol} < 0.5
Coherent noise	$PLcoh_{sz}$ >0.8; PAR_{sz} >0.8	DD_{pol} > 0.5

time. Suppose there is a preferred polarization direction for the magnetic field; we can consider that the coherent noise contaminates the data. On the other hand, when incoherent noise contaminates the field data, the magnetic field has no preferred polarization direction. Therefore, the polarization direction for the magnetic field can only detect coherent noise.

To quantify the dispersion degree of MPD, the dispersion degree of the polarization directions (DD_{pol}) is proposed as follows:

$$DD_{pol} = \frac{N_{in}}{N}, \tag{8}$$

where N_{in} denotes the number of samples falling in the range of (m_i + 30 °, m_i-30 °). m_i is the median for each α_{H_i} with its surrounding 2k samples (k is set to 20 in this study), and it is calculated as follows:

$$m_i = \text{median}\left(\alpha_{H_{i-k}}, \alpha_{H_{i-k-1}}, \ldots, \alpha_{H_i}, \ldots, \alpha_{H_{i+k-1}}, \alpha_{H_{i+k}}\right). \tag{9}$$

When the polarization direction has a preferred direction, m_i approximately equal to the preferred direction. m_i is calculated by the surrounding 2k samples, and there are two sides; we hope half of the data is beyond a specific range, which means the threshold is set as 0.5; therefore, the expected value of DD_{pol} should be smaller than 0.5, and 1/3 is chosen in this research, which means the range is 60 ° (180 °× 1/3), and the specific range is set as (m_i + 30 °, m_i-30 °). If the polarization directions vary randomly from −90 ° to 90 °, DD_{pol} should be close to 1/3, and DD_{pol} increases when there is a preferred direction. DD_{pol} can be used to automatically detect coherent noise with a strong polarization direction.

3 Case studies for the preselection strategy

Usually, data dominated by incoherent noise do not have a stable relationship; therefore, the linearity should be low. We can identify the incoherent noise using the parameters $PLcoh_{sz}$ and PAR_{sz}. According to the linearity and MPD of the data, the data quality can be classified into three types, as shown in Table 1. Combining the linearity and the MPD, we can constrain both coherent and incoherent noise simultaneously.

The preselection strategy based on linearity and the MPD is tested on approximately 500 site data from the USArray project (Schultz et al., 2018; Kelbert, 2019) and data collected in China. It can improve the quality of the impedance tensor when intermittent noise contaminates the field data. Two typical field datasets are chosen to demonstrate the effectiveness of those parameters to identify noisy events. The location map is shown in Figure 3. The first data are contaminated by incoherent noise, which contains a geomagnetic storm, the energy from the natural EM signal increases significantly, and high signal-to-noise ratio (SNR) data appear during the storm. The second dataset is contaminated by coherent noise and incoherent noise simultaneously, the noise decreases during the local nighttime, and high SNR data appear.

3.1 Case study 1: Data contaminated by intermittent *incoherent noise*

The first case study used the data observed at TVN48 from the USArray project. The time-series data can be downloaded from the Incorporated Research Institutions for Seismology (IRIS) website.

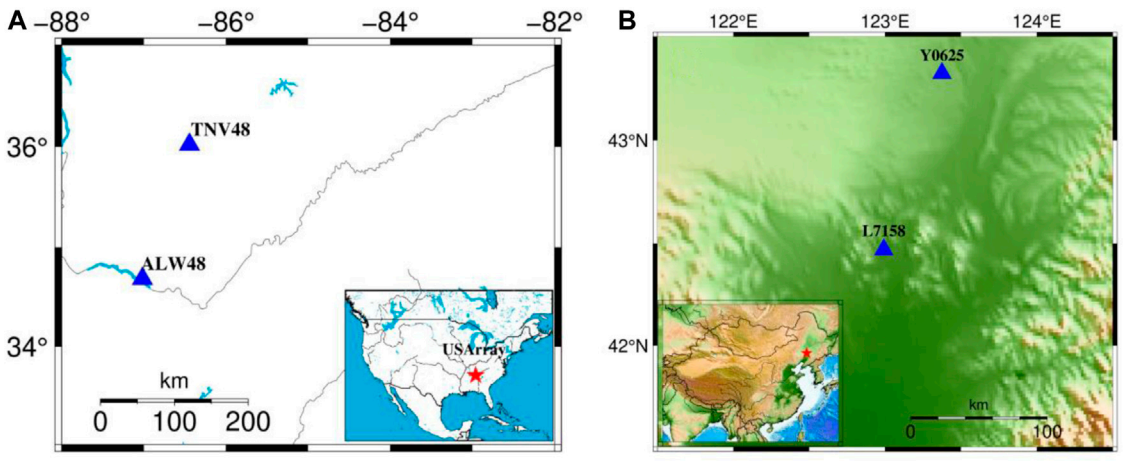

FIGURE 3
Location map of the field data. **(A)** shows the location of the first field data; the blue triangles denote the observation site. TNV48 is used as the locale site, and ALW48 is set as the remote reference site. The lower right corner in **(A)** shows the survey location of the USArray, and the red star denotes the location of site TNV48. **(B)** shows the location map of the second field data observed in China. Y0625 is the remote reference site, and L7-158 is the local site. The lower left corner in **(B)** shows the survey area in China, and the red star denotes the local site.

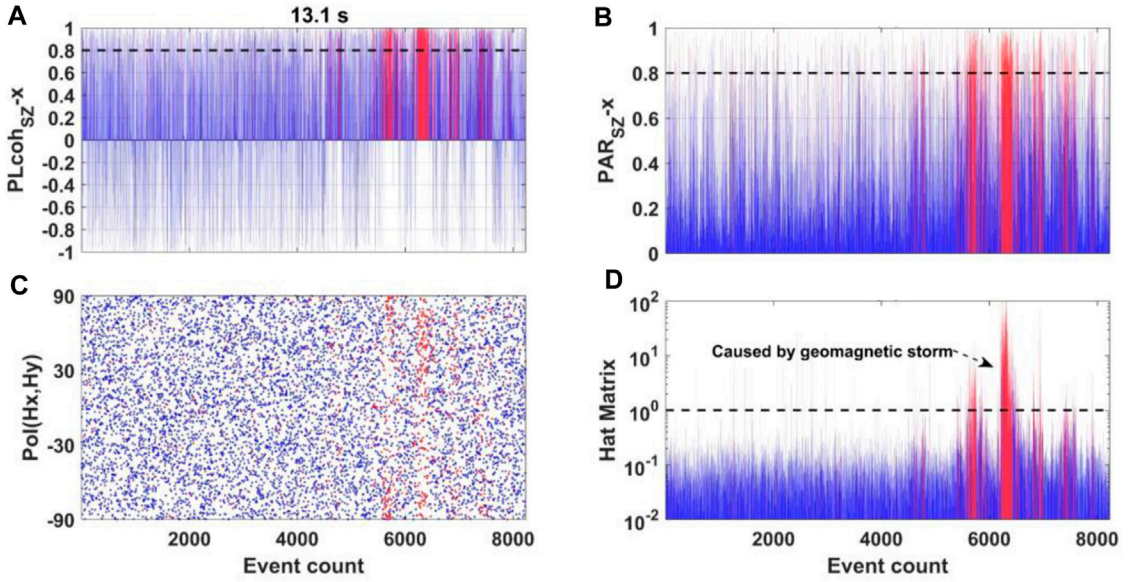

FIGURE 4
Parameters variation at TVN48 in the period of 13.1 s. The horizontal axis denotes the event count. Panels **(A, B)** show the variation in $PLcoh_{sz}$ and PAR_{sz} associated with E_x-component, respectively. The red color denotes the events in which both $PLcoh_{sz}$ and PAR_{sz} are higher than 0.8, and the other events are shown in blue. **(C)** shows the variation in the MPD. **(D)** shows the variation in the hat matrix's diagonal element, and the hat matrix's diagonal element is normalized by the expected value.

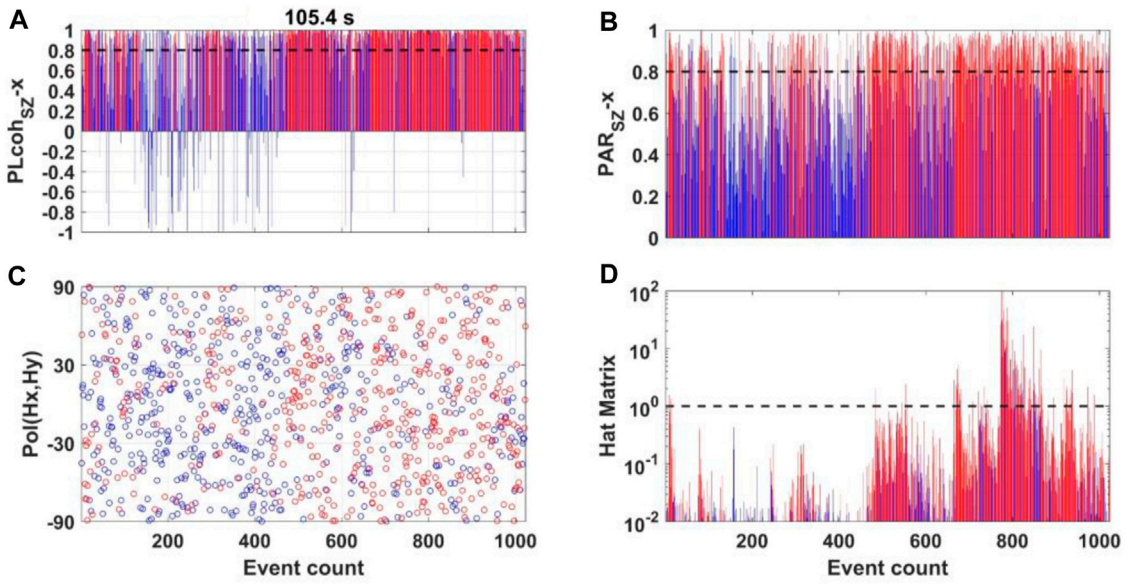

FIGURE 5
Parameters variation at TVN48 in the period of 105.4 s. **(A, B)** show the variation in $PLcoh_{sz}$ and PAR_{sz} associated with E_x-component, respectively. The red color denotes the events with high linearity, and the other events are shown in blue. **(C)** shows the variation in MPD. **(D)** shows the variation in the hat matrix's diagonal element.

The data sampling period is 1 s, and the used times-series data are observed from July 19 to 24 July 2015. First, we examine the variation in the parameters at different frequencies. Figure 4 shows the parameter variation in the period of 13.1 s. Figures 4A, B show the variation in $PLcoh_{sz}$ and PAR_{sz} associated with E_x-component, respectively. The events in which both $PLcoh_{sz}$ and PAR_{sz} are larger than 0.8 are shown in red, and the other is shown in blue. Red denotes an event with high linearity, and blue denotes an event with low linearity. Figure 4C shows that the MPD is scattered for all the events. Figure 4D shows the variation in the hat

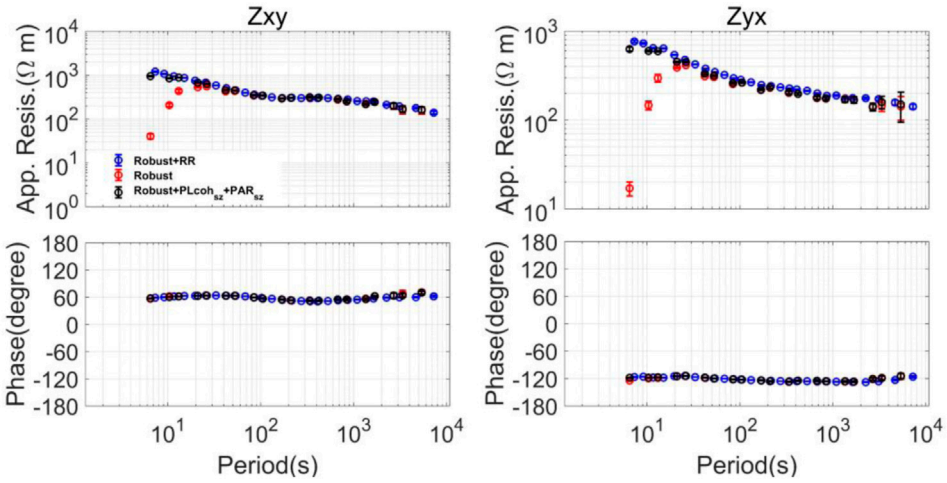

FIGURE 6
MT sounding curves calculated by the different methods using the data observed at site TNV48. The upper figures show the apparent resistivity, and the lower figures show the impedance phase. All the responses are estimated by a M-estimator. The blue curves denote the remote reference results. The red curves denote the single-site robust result. The black curves are calculated by the preselection strategy using $PLcoh_{sz}$ and PAR_{sz}, and the threshold is set to 0.8 for both $PLcoh_{sz}$ and PAR_{sz}. The apparent resistivity of the robust results is downbiased compared with other results between 5 and 20 s.

matrix's diagonal element. The hat matrix is an N by N matrix (N denotes the number of events) defined as follows (Chave and Thomson, 2004; 2003):

$$\boldsymbol{H}_{hat} = \boldsymbol{H}\left(\boldsymbol{H}^{\dagger}\boldsymbol{H}\right)^{-1}\boldsymbol{H}^{\dagger}, \tag{10}$$

where $\boldsymbol{H}$ represents N by two matrices of the horizontal magnetic field ($\boldsymbol{H}_x, \boldsymbol{H}_y$) at a specific frequency. The superscript † denotes the complex conjugate transpose. The expected value of the hat matrix's diagonal element is $2/N$. The variation in the diagonal elements of the hat matrix has the same trend as the magnetic field amplitude (Chen et al., 2022; Li et al., 2022; Li et al., 2023; Li et al., 2018; Zhang et al., 2022; Zhang et al., 2021). Therefore, we can use the hat matrix to visualize the energy variation in the magnetic field. Figure 4D shows that the red events have high energy. This is caused by the geomagnetic storm (see Supplementary Figure S1). Since the natural EM signal is relatively low in the dead band (0.1–10 s), local noise can easily influence it during non-storm periods. When there is a geomagnetic storm, the natural EM signal strength increases, and high SNR events appear. In conclusion, the blue events are dominated by incoherent noise in the period of 13.1 s, and $PLcoh_{sz}$ and PAR_{sz} can identify incoherent noise. Figure 5 shows the parameter variation in the period of 105.4 s. Most of the events have high linearity, and the MPD is scattered for all the events. This indicates that only a small part of the events are contaminated by incoherent noise. After analyzing the variation in the parameters in different periods, we found that most of the events are dominated by incoherent noise between 5 and 20 s.

Then, we compare the MT sounding curves calculated by the different methods, as shown in Figure 6. All of those responses are estimated by M-estimator (Egbert and Booker, 1986; Neukirch and García, 2014; Maronna et al., 2019). The result using the data preselection strategy with $PLcoh_{sz}$ and PAR_{sz} coincides with the remote reference result, and they are regarded as the true model. It shows that a reliable result can be obtained even if we do not use the remote site data by the preselection method. On the other hand, the apparent resistivity of the robust results is downbiased between 6 and 20 s. According to the analysis of Figure 4, more than half of the events are contaminated by incoherent noise. The underestimation of the apparent resistivity was probably attributed to the auto-power spectra of the noise in the denominator of the response function, which is a well-known limitation of the single-site data processing (Sims et al., 1971; Simpson and Bahr, 2005).

3.2 Comparison of the parameters used to evaluate the linearity

This subsection compares the performance of the related parameters used to evaluate linearity, e.g., multiple coherence (Travassos and Beamish, 1988; Egbert and Livelybrooks, 1996; Bendat and Piersol, 2011) and bivariate coherence (Ritter et al., 1998; Weckmann et al., 2005). All of those parameters can be indicators of the data quality under the assumption that the dataset follows a linear relationship.

Multiple coherence is defined as the ratio of the ideal output spectrum due to the measured inputs in the absence of noise to the total output spectrum, which includes the noise (Bendat and Piersol, 2011). In equation form, the multiple coherence associated with E_x is calculated as follows:

$$r_m^2 = 1 - \frac{E_{err_{x_i}}\bar{E}_{err_{x_i}}}{E_{x_i}\bar{E}_{x_i}}, \tag{11}$$

where $E_{err_{x_i}} = E_{p_{x_i}} - E_{x_i}, E_{p_{x_i}}$ *and* E_{x_i} denote the predicted and observed electric field calculated by the i^{th} segment. The bar denotes the conjugate of a complex number. Because the error between the predicted and observed electric field may be larger than the observed electric field. The right part of Eq. 11 may be a negative value. We take the square root of the absolute value of $1 - \frac{E_{err_{x_i}}\bar{E}_{err_{x_i}}}{E_{x_i}\bar{E}_{x_i}}$ as

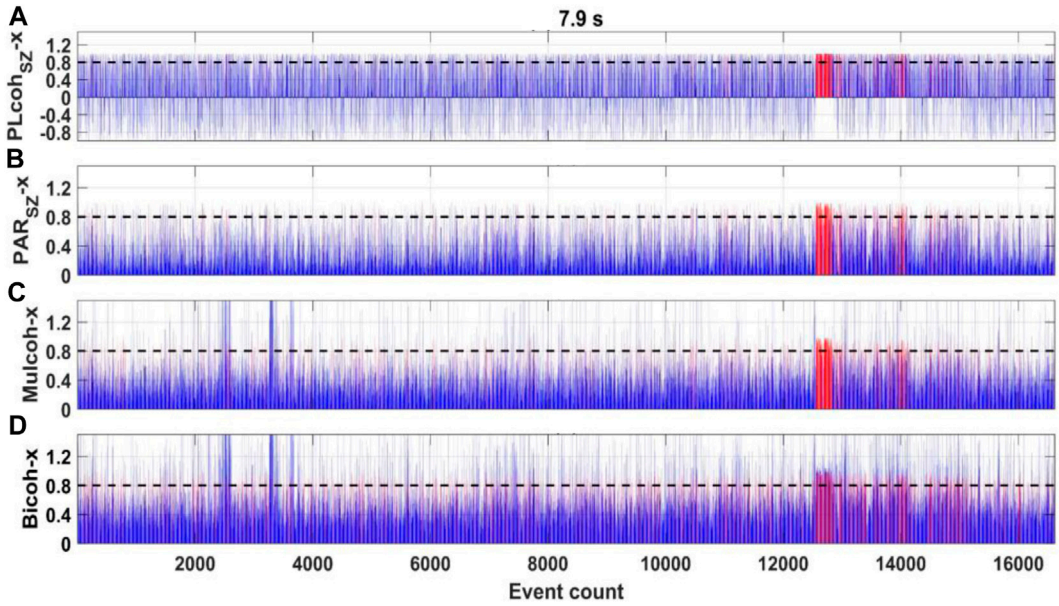

FIGURE 7
Parameters variation at TVN48 in the period of 7.9 s. The red color denotes the events in high linearity based on different parameters, and the other events are shown in blue. All the parameters are determined from the bivariate equations whose dependent variable is the E_x-component. **(A, B)** show the variation in $PLcoh_{sz}$ and PAR_{sz}. The high linearity events are in which both $PLcoh_{sz}$ and PAR_{sz} are higher than 0.8. **(C)** shows the variation in multiple coherence. The high linearity events are in which the multiple coherence is higher than 0.8 and smaller than 1. **(D)** shows the variation in bivariate coherence. The high linearity events are in which the bivariate coherence is higher than 0.8 and smaller than 1.

the multiple coherence (r_m), and regard the event, which r_m larger than 0.8 and smaller than 1, are in high linearity. The red events in Figure 7C show the event in high linearity based on the multiple coherence.

Bivariate coherence is defined as a function of the amplitude ratio and phase difference between the predicted and the observed electric field. In equation form, bivariate coherence associated with E_x is calculated as follows (Weckmann et al., 2005):

$$r_b^2 = \frac{Z_{xx}{}^{*}H_{x_i}\bar{E}_{x_i} + Z_{xy}{}^{*}H_{y_i}\bar{E}_{x_i}}{E_{x_i}\bar{E}_{x_i}} = \frac{E_{p_{x_i}}\bar{E}_{x_i}}{E_{x_i}\bar{E}_{x_i}} = \frac{\left|E_{p_{x_i}}\right|}{\left|E_{x_i}\right|} \cdot cos(\theta_i), \quad (12)$$

where E_{x_i}, H_{x_i} and H_{y_i} represent the *EM* field corresponding to the i^{th} segment. θ_i is the phase difference between $E_{p_{x_i}}$ *and* E_{x_i}. Because the predicted electric field may be larger than the observed electric field, and bivariate coherence may be larger than 1. We regard the event, which r_b larger than 0.8 and smaller than 1, are in high linearity. The red events in Figure 7D show the data in high linearity based on the bivariate coherence.

The comparison of the parameters used to evaluate the linearity is shown in Figure 7. First, the events are divided into groups that contain N samples, e.g., 20 samples. We calculate the predicted electric field for each group, separately. If the data quality is high, all of the parameters should be close to one under the assumption that the data follow a linear relationship. All of the parameters can identify the high-quality data corresponding to the magnetic storm. However, the parameters ($PLcoh_{sz}$ and PAR_{sz}) proposed in the research and multiple coherence perform better than bivariate coherence. Some parts of the high-quality events, which r_b larger but close to 1 are regarded as in low linearity based on the bivariate coherence. The MT sounding curves calculated by the different preselection strategies are shown in Figure 8. All of the preselection strategies can reduce the influence of noise compared with the robust result in Figure 6. While the apparent resistivity in Figure 8B around the period of 7.9 s is downbiased compared with other results in Figures 8A, C. It may be caused by some parts of the high-quality events being removed when using the bivariate coherence to prescreen data.

3.2 Case study 2: Data contaminated by intermittent *coherent Noise and incoherent noise*

The second case study uses data observed in northeastern China on 26 June 2020. Phoenix Geophysics Instruments were used to collect the MT time-series data. These data are provided by the Institute of Geophysical and Geochemical Exploration, China Geological Survey. Time-series data from 3:00 to 22:00 UTC were used in this case study. The sampling rate is 15 Hz. The observation area is in the GMT+8 time zone, and the local midnight time is approximately 16:00.

First, we examine the variation in the parameters at different frequencies. Figure 9 shows the variation in the period of 6.7 s. Red denotes events with high linearity, and blue denotes events with low linearity. The previous 2,500 events in the daytime have a preferred polarization direction of approximately −30 °, as shown in Figure 9C, and the polarization direction becomes scattered at nighttime (the events are approximately 2,500 to 4,000). This indicates that the daytime event is dominated by coherent noise, and most of the events have high linearity; in contrast, the event at nighttime is

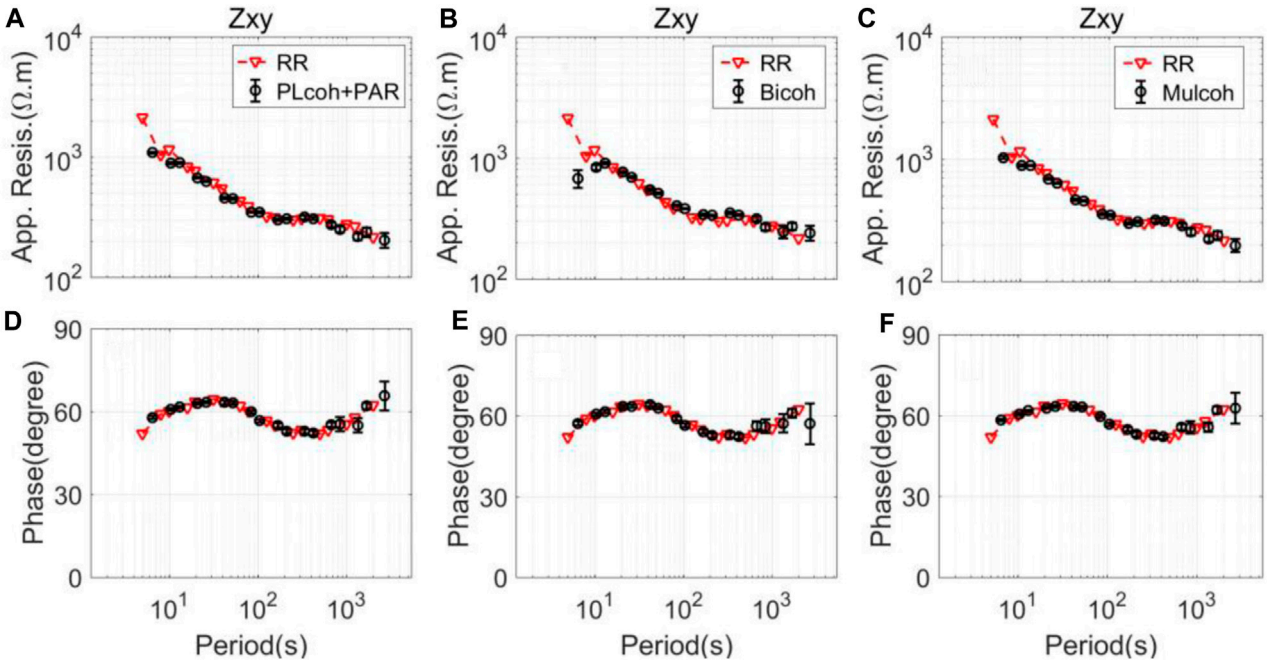

FIGURE 8
MT sounding curves calculated by the different preselection strategies corresponding to Z_{xy} component using the data observed at site TNV48. The upper figures show the apparent resistivity, and the lower figures show the impedance phase. The red curves denote the remote reference results. The black curves denote the result calculated by the different preselection strategies. **(A, D)** are calculated by the preselection strategy using $PLcoh_{sz}$ and PAR_{sz}. **(B, E)** are calculated by the preselection strategy using bivariate coherence. **(C, F)** are calculated by the preselection strategy using multiple coherence. The apparent resistivity in **(B)** at 7.9 s is downbiased compared with other results in **(A, C)**.

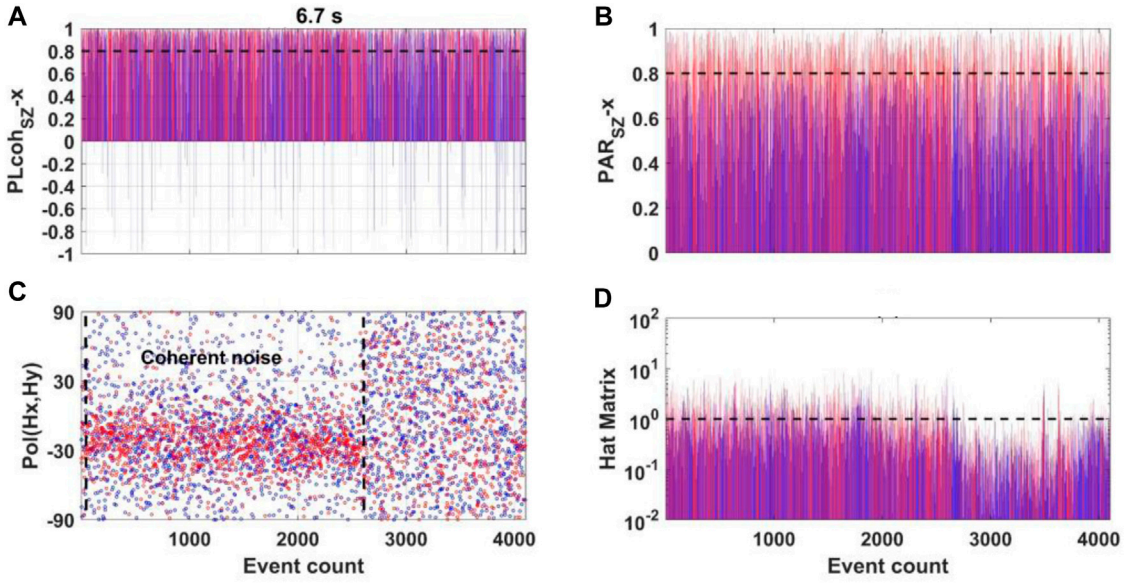

FIGURE 9
Parameters variation at L7-158 in the period of 6.7 s. **(A, B)** show the variation in $PLcoh_{sz}$ and PAR_{sz} associated with E_x-component, respectively. The red color denotes the events with high linearity, and the other events are shown in blue. **(C)** shows the variation in the MPD. **(D)** shows the variation in the hat matrix's diagonal element.

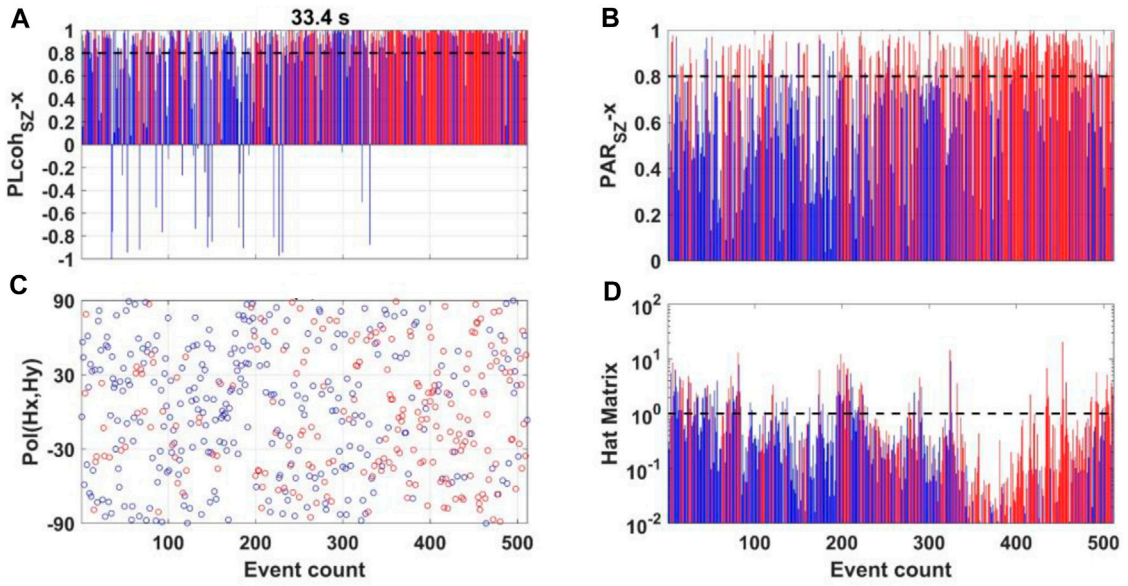

FIGURE 10
Parameters variation at L7-158 in the period of 33.4 s. **(A, B)** show the variation in $PLcoh_{sz}$ and PAR_{sz} associated with E_x-component, respectively. The red color denotes the events with high linearity, and the other events are shown in blue. **(C)** shows the variation in the MPD. **(D)** shows the variation in the hat matrix's diagonal element.

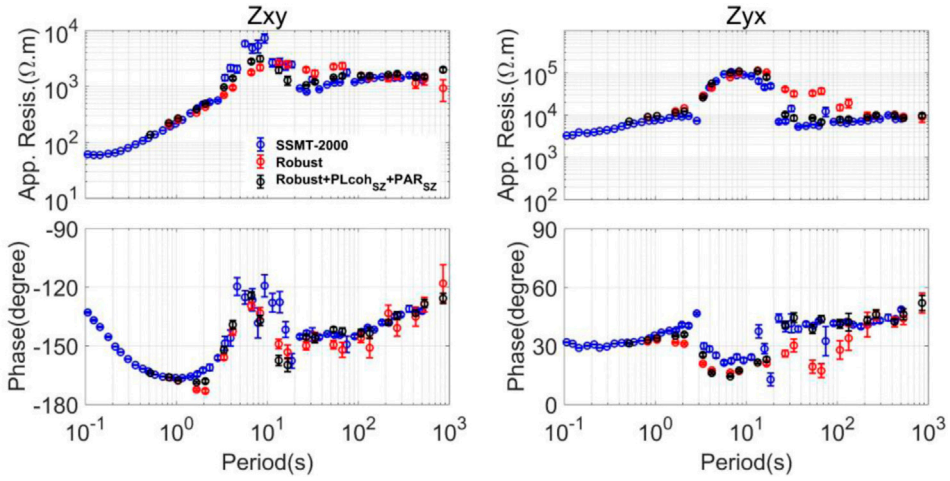

FIGURE 11
MT sounding curves calculated by the different methods using the data observed at site L7-158. SSMT-2000 is used to calculate the blue curves. SSMT-2000 is one of the standard Phoenix software sets. The robust single-site processing approach is used to calculate the red curves. The preselection strategy using $PLcoh_{sz}$ and PAR_{sz} is used to calculate the black curves.

relatively quiet. Figure 10 shows the variation in the period of 33.4 s. The previous 300 events in the daytime have low linearity, and the polarization direction is scattered. In contrast, the events during the nighttime between 300 and 500 have a high linearity, and the polarization direction is scattered. This indicates that the daytime event is dominated by incoherent noise and that the nighttime events are relatively quiet. After analyzing the parameter variation at different frequencies, we find that most of the events are dominated by coherent noise between 2 and 20 s and dominated by incoherent noise between 20 and 100 s. The field data are contaminated by coherent and incoherent noise simultaneously.

Then, we compare the MT sounding curves calculated by the different methods. First, we compare the result calculated by the SSMT-2000 and the results with and without the preselection strategy based on linearity, as shown in Figure 11. SSMT-2000 is one of the standard Phoenix software sets. After comparing all the results, we think all the impedance results are biased between 2 and 20 s, and there is a rapid rise and fall in the apparent resistivities. The

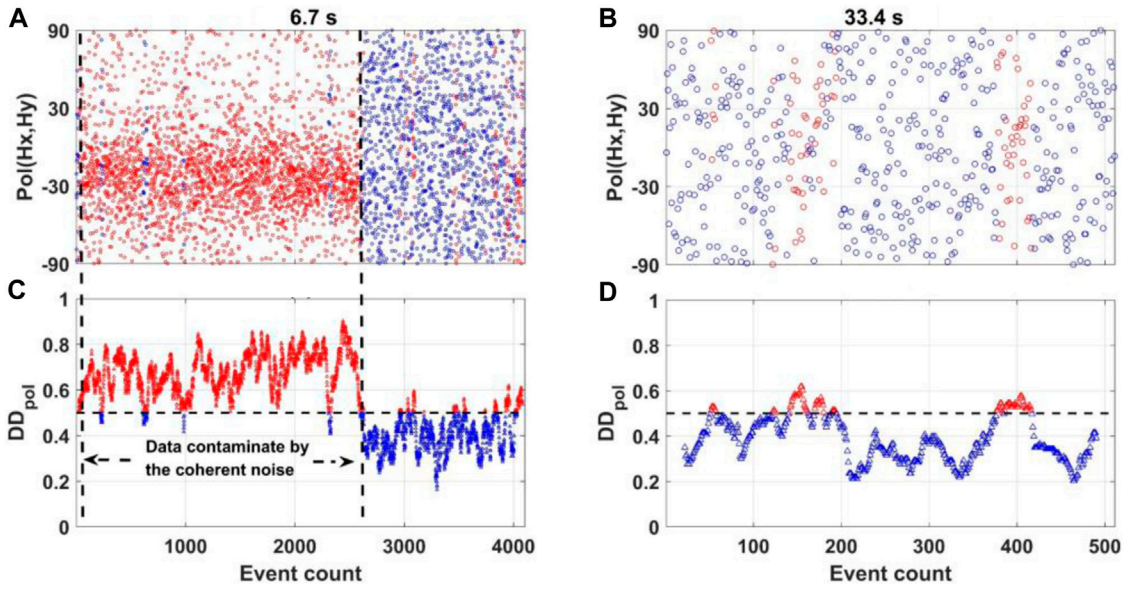

FIGURE 12
Variation in the polarization direction and the corresponding variation in DD_{pol} at 6.7 and 33.4 s. **(A, B)** show the variation in the polarization direction, and **(C, D)** show the corresponding dispersion degree. The horizontal axis denotes the event count. The red color denotes the events whose dispersion degrees are higher than 0.5, and the other events are shown in blue.

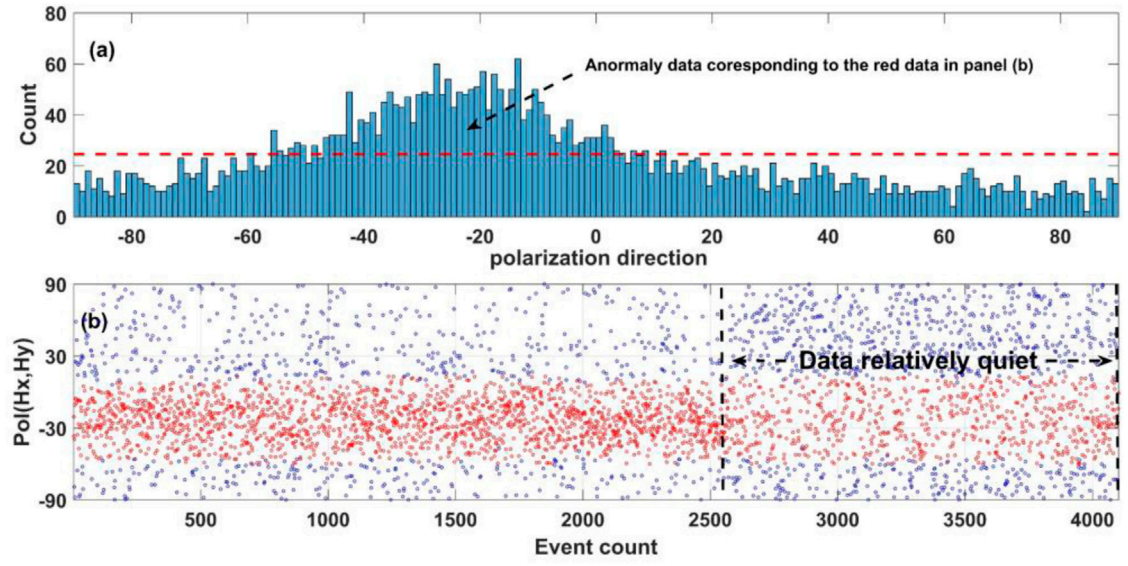

FIGURE 13
Histogram of the MPD and the corresponding variation in the MPD at site L7-158 in the period of 6.7 s. **(A)** shows the histogram of the MPD; the horizontal axis denotes the bins of the MPD, the vertical axis denotes the number falling in the corresponding bin, and the red dashed line denotes the threshold. **(B)** shows the variation in the MPD. The horizontal axis denotes the event count. The red color denotes the events that fall into a bin with a higher than expected value, and the other events are shown in blue. The quiet event may be removed at nighttime (the event from 2,500 to 4,000) and many of the events in the daytime remain based on the criteria of SMPD.

SSMT-2000 result coincides with the preselection strategy result between 20 and 100 s and changes smoothly. The single-site robust result is improved between 20 and 100 s after using the preselection strategy with $PLcoh_{sz}$ and PAR_{sz}. According to the data quality analysis in different periods, most of the events are contaminated by incoherent noise between 20 and 100 s, and $PLcoh_{sz}$ and PAR_{sz} are effective in removing incoherent noise. Most of the events are contaminated by coherent noise, which is highly linear, between

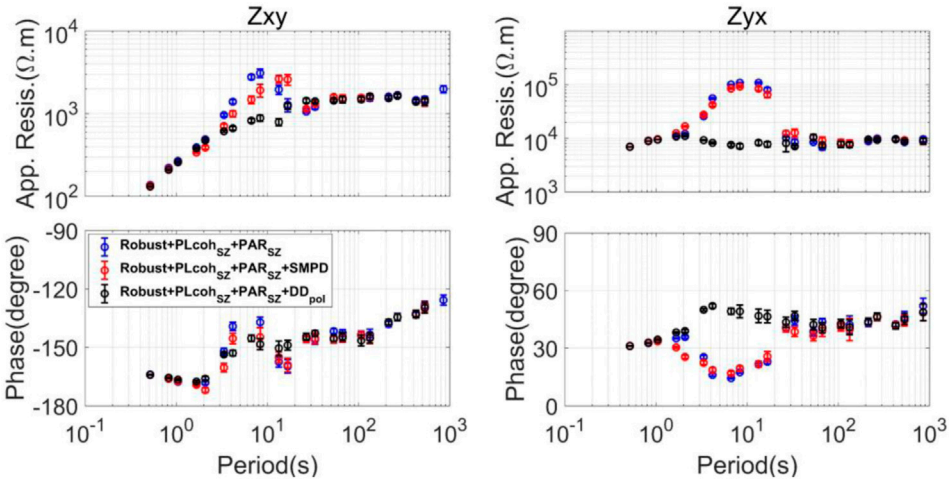

FIGURE 14
MT sounding curves calculated by the different preselection strategies using the data observed at site L7-158. The robust estimator combining $PLcoh_{sz}$, and PAR_{sz} for the preselection strategy is used to calculate the blue curves. The robust estimator combining $PLcoh_{sz}$, PAR_{sz} and SMPD for the preselection strategy is used to calculate the red curves. The robust estimator combining $PLcoh_{sz}$, PAR_{sz} and DD_{pol} for the preselection strategy is used to calculate the black curves.

2 and 20 s. We also try to use the remote reference method to improve the result but fail (see Supplementary Figure S5), and it needs a different strategy to suppress the noise.

Next, we try to use the information on MPD to constrain the coherent noise. Figure 12 shows the variation in the MPD and the corresponding variation in DD_{pol} in the periods of 6.7 and 33.4 s. The expected value of DD_{pol} is 1/3, and DD_{pol} increases when the polarization direction has a preferred direction. It shows that DD_{pol} is effective in differentiating the events with and without a preferred polarization direction.

We also compare the criteria proposed by Platz and Weckmann (2019) which is based on the statistical information on magnetic polarization direction (SMPD). They subdivided the polarization direction into 180 bins with a bin width of 1 °. In general, the polarization direction is randomly distributed in each bin. Therefore, the expected value ($\frac{Number\ of\ events}{180}$) is the same for each bin. They removed all the events whose polarization directions fall into bins that are much higher than the expected value. Figure 13 shows the statistical analyses of the polarization direction; the threshold k ($k = 1.5\sigma$) is used to detect abnormal values, where σ is the standard deviation (Chave and Thomson, 2003). The corresponding abnormal events are drawn in red. According to the criteria based on SMPD, the quiet event may be removed at nighttime (the event from 2,500 to 4,000) and many of the events in the daytime remain.

At last, we compare the MT sounding curves calculated by the different preselection strategies based on the information on MPD, as shown in Figure 14. The robust estimator combining $PLcoh_{sz}$, PAR_{sz} for the preselection strategy is used to calculate the blue curve, which prescreens the data only based on the linearity. The robust estimator combining $PLcoh_{sz}$, PAR_{sz} and SMPD for the preselection strategy is used to calculate the red curve. The criteria proposed by Platz and Weckmann (2019) do not improve the result, the rapid rise and rapid fall between 2 and 20 s remain. The robust estimator combining $PLcoh_{sz}$, PAR_{sz} and DD_{pol} for the preselection strategy is used to calculate the black curve, and the threshold for DD_{pol} is set to 0.5. The rapid rise and rapid fall between 2 and 20 s are removed. Comparing the two criteria between DD_{pol} and SMPD, most of the events in the daytime are removed based on the DD_{pol}, while many events in the daytime remain based on the SMPD, and those events in the daytime may also correspond to the coherent noise and dominate the regression, making the preselection strategy fail. This shows the superiority of DD_{pol} for detecting coherent noise with a strong magnetic polarization direction.

4 Conclusion

Robust single-site data processing may work well unless a large fraction of the data is quiet. On the other hand, the remote reference method may also fail to obtain a reliable result when the noise is correlated between local and remote sites. In a noisy EM environment, it is practical to use a preselection strategy to extract high signal-to-noise ratio (SNR) data, and a reliable response function can be obtained if the noise does not contaminate the local site all the time.

We proposed three new parameters for the preselection strategy from the perspectives of linearity and magnetic polarization, making the preselection process automatic. The predicted linear coherence ($\boldsymbol{PLcoh_{sz}}$) and amplitude ratio ($\boldsymbol{PAR_{sz}}$) are combined to evaluate the linearity. We compared the performance with related parameters, e.g., multiple coherence and bivariate coherence. It shows that new parameters proposed in this research ($\boldsymbol{PLcoh_{sz}}$ and $\boldsymbol{PAR_{sz}}$) perform similarly with multiple coherence and better than the bivariate coherence. Linearity can be a general criterion for detecting noisy data with low linearity, which corresponds to incoherent noise. However, coherent noise may also have high linearity (see Supplementary Figure S4). The dispersion degree

of the magnetic polarization direction (DD_{pol}) is proposed to detect coherent noise with a preferred polarization direction, which performs better than the criteria proposed by Platz and Weckmann (2019). It can quantify the polarization change over time. Suppose noise contaminates the local site intermittently; using those parameters may improve the quality of the response function.

Data availability statement

The time-series data from the USArray project are available from IRIS (http://ds.iris.edu/gmap/#network=_US-MT&planet=earth).

Author contributions

HaC processed the time-series data, created the results, and wrote the paper. HaC contributed approximately 50%. ZR, LZ, and HuC reviewed the paper and contributed approximately 30%; GW provided the MT field data and processed the time-series data with SSMT-2000 software. GW contributed approximately 20% to this work.

Funding

This research is financially supported by the National Natural Science Foundation of China (grants 41774086, 41930430), the Major Research plan of the National Natural Science Foundation of China (grant 92262303), and the Key Research Program of the Institute of Geology and Geophysics, Chinese Academy of Sciences (IGGCAS-201901).

Acknowledgments

We are grateful to the Institute of Geophysical and Geochemical Exploration, China Geological Survey, and USArray team members for providing the time-series data used in this study. The valuable comments and suggestions by three reviewers have greatly improved the manuscript. Finally, we thank Ruan Shuai and Hao Zhou for making meaningful comments on the paper's content.

Conflict of interest

The authors declare that the research was conducted in the absence of any commercial or financial relationships that could be construed as a potential conflict of interest.

The reviewer XZ declared a shared affiliation with the authors HC, ZR to the handling editor at time of review,

Publisher's note

All claims expressed in this article are solely those of the authors and do not necessarily represent those of their affiliated organizations, or those of the publisher, the editors and the reviewers. Any product that may be evaluated in this article, or claim that may be made by its manufacturer, is not guaranteed or endorsed by the publisher.

Supplementary material

The Supplementary Material for this article can be found online at: https://www.frontiersin.org/articles/10.3389/feart.2023.1230071/full#supplementary-material

References

Bendat, J. S., and Piersol, A. G. (2011). *Random data: Analysis and measurement procedures*. Hoboken, NJ, United States: John Wiley & Sons.

Cagniard, L. (1953). Basic theory of the magneto-telluric method of geophysical prospecting. *Geophysics* 18, 605–635. doi:10.1190/1.1437915

Chave, A. D., and Jones, A. G. (2012). *The magnetotelluric method: Theory and practice*. Cambridge, United Kingdom: Cambridge University Press.

Chave, A. D., and Thomson, D. J. (2003). A bounded influence regression estimator based on the statistics of the hat matrix. *J. R. Stat. Soc. Ser. C Appl. Stat.* 52, 307–322. doi:10.1111/1467-9876.00406

Chave, A. D., and Thomson, D. J. (2004). Bounded influence magnetotelluric response function estimation. *Geophys. J. Int.* 157, 988–1006. doi:10.1111/j.1365-246x.2004.02203.x

Chave, A. D., and Thomson, D. J. (1989). Some comments on magnetotelluric response function estimation. *J. Geophys. Res. Solid Earth* 94, 14215–14225. doi:10.1029/jb094ib10p14215

Chen, H., Mizunaga, H., and Tanaka, T. (2022). Influence of geomagnetic storms on the quality of magnetotelluric impedance. *Earth Planets Space* 74, 111–117. doi:10.1186/s40623-022-01659-6

Egbert, G. D., and Booker, J. R. (1986). Robust estimation of geomagnetic transfer functions. *Geophys. J. Int.* 87, 173–194. doi:10.1111/j.1365-246x.1986.tb04552.x

Egbert, G. D., and Livelybrooks, D. W. (1996). Single station magnetotelluric impedance estimation: coherence weighting and the regression M-estimate. *Geophysics* 61, 964–970. doi:10.1190/1.1444045

Egbert, G. D. (1997). Robust multiple-station magnetotelluric data processing. *Geophys. J. Int.* 130, 475–496. doi:10.1111/j.1365-246x.1997.tb05663.x

Fowler, R. A., Kotick, B. J., and Elliott, R. D. (1967). Polarization analysis of natural and artificially induced geomagnetic micropulsations. *J. Geophys. Res.* 72, 2871–2883. doi:10.1029/jz072i011p02871

Gamble, T. D., Goubau, W. M., and Clarke, J. (1979). Magnetotellurics with a remote magnetic reference. *Geophysics* 44, 53–68. doi:10.1190/1.1440923

Garcia, X., and Jones, A. G. (2002). Atmospheric sources for audio-magnetotelluric (AMT) sounding. *Geophysics* 67, 448–458. doi:10.1190/1.1468604

Goubau, W. M., Gamble, T. D., and Clarke, J. (1978). Magnetotelluric data analysis: removal of bias. *Geophysics* 43, 1157–1166. doi:10.1190/1.1440885

Jones, A. G., Chave, A. D., Egbert, G., Auld, D., and Bahr, K. (1989). A comparison of techniques for magnetotelluric response function estimation. *J. Geophys. Res. Solid Earth* 94, 14201–14213. doi:10.1029/jb094ib10p14201

Jones, A. G., and Jödicke, H. (1984). "Magnetotelluric transfer function estimation improvement by a coherence-based rejection technique," in *SEG technical program expanded abstracts 1984* (Houston, Texas, United States: Society of Exploration Geophysicists), 51–55.

Junge, A. (1996). Characterization of and correction for cultural noise. *Surv. Geophys.* 17, 361–391. doi:10.1007/bf01901639

Kappler, K. N. (2012). A data variance technique for automated despiking of magnetotelluric data with a remote reference. *Geophys. Prospect.* 60, 179–191. doi:10.1111/j.1365-2478.2011.00965.x

Kelbert, A. "Taking magnetotelluric data out of the drawer," in Proceedings of the AGU Fall Meeting Abstracts, San Franciso, CA, USA, December 2019, IN21A–01.

Larsen, J. C., Mackie, R. L., Manzella, A., Fiordelisi, A., and Rieven, S. (1996). Robust smooth magnetotelluric transfer functions. *Geophys. J. Int.* 124, 801–819. doi:10.1111/j.1365-246x.1996.tb05639.x

Li, G., Gu, X., Ren, Z., Wu, Q., Liu, X., Zhang, L., et al. (2022). Deep learning optimized dictionary learning and its application in eliminating strong magnetotelluric noise. *Minerals* 12, 1012. doi:10.3390/min12081012

Li, G., Wu, S., Cai, H., He, Z., Liu, X., Zhou, C., et al. (2023). IncepTCN: A new deep temporal convolutional network combined with dictionary learning for strong cultural noise elimination of controlled-source electromagnetic data. *Geophysics* 88, E107–E122. doi:10.1190/geo2022-0317.1

Li, J., Zhang, X., Gong, J., Tang, J., Ren, Z., Li, G., et al. (2018). Signal-noise identification of magnetotelluric signals using fractal-entropy and clustering algorithm for targeted de-noising. *Fractals* 26, 1840011. doi:10.1142/s0218348x1840011x

Maronna, R. A., Martin, R. D., Yohai, V. J., and Salibián-Barrera, M. (2019). *Robust statistics: Theory and methods (with R)*. Hoboken, NJ, United States: John Wiley & Sons.

Neukirch, M., and García, X. (2014). Nonstationary magnetotelluric data processing with instantaneous parameter. *J. Geophys. Res. Solid Earth* 119, 1634–1654. doi:10.1002/2013jb010494

Oettinger, G., Haak, V., and Larsen, J. C. (2001). Noise reduction in magnetotelluric time-series with a new signal–noise separation method and its application to a field experiment in the Saxonian Granulite Massif. *Geophys. J. Int.* 146, 659–669. doi:10.1046/j.1365-246x.2001.00473.x

Platz, A., and Weckmann, U. (2019). An automated new pre-selection tool for noisy Magnetotelluric data using the Mahalanobis distance and magnetic field constraints. *Geophys. J. Int.* 218, 1853–1872. doi:10.1093/gji/ggz197

Ritter, O., Junge, A., and Dawes, G. J. (1998). New equipment and processing for magnetotelluric remote reference observations. *Geophys. J. Int.* 132, 535–548. doi:10.1046/j.1365-246x.1998.00440.x

Schultz, A., Egbert, G. D., Kelbert, A., Peery, T., Clote, V., Fry, B., et al. (2018). Staff of the National Geoelectromagnetic Facility and their contractors (2006–2018). *USArray TA magnetotelluric Transf. Funct.*, doi:10.17611.DP/EMTF/USARRAY/TA

Simpson, F., and Bahr, K. (2005). *Practical magnetotellurics*. Cambridge, United Kingdom: Cambridge University Press.

Sims, W. E., Bostick, F. X., and Smith, H. W. (1971). The estimation of magnetotelluric impedance tensor elements from measured data. *Geophysics* 36, 938–942. doi:10.1190/1.1440225

Smirnov, M. Y., and Egbert, G. D. (2012). Robust principal component analysis of electromagnetic arrays with missing data. *Geophys. J. Int.* 190, 1423–1438. doi:10.1111/j.1365-246x.2012.05569.x

Smirnov, M. Y. (2003). Magnetotelluric data processing with a robust statistical procedure having a high breakdown point. *Geophys. J. Int.* 152, 1–7. doi:10.1046/j.1365-246x.2003.01733.x

Szarka, L. (1988). Geophysical aspects of man-made electromagnetic noise in the earth—a review. *Surv. Geophys.* 9, 287–318. doi:10.1007/bf01901627

Tikhonov, A. N., and Berdichevsky, M. N. (1966). Experience in the use of magnetotelluric methods to study the geological structures of sedimentary basins. *Izv. Acad. Sci. USSR Phys. Solid Earth* 2, 34–41.

Tikhonov, A. N. (1950). On determining electrical characteristics of the deep layers of the Earth's crust. *Dokl. Citeseer*, 295–297.

Travassos, J. M., and Beamish, D. (1988). Magnetotelluric data processing—a case study. *Geophys. J. Int.* 93, 377–391. doi:10.1111/j.1365-246x.1988.tb02009.x

Wang, H., Campanyà, J., Cheng, J., Zhu, G., Wei, W., Jin, S., et al. (2017). Synthesis of natural electric and magnetic Time-series using Inter-station transfer functions and time-series from a Neighboring site (STIN): applications for processing MT data. *J. Geophys. Res. Solid Earth* 122, 5835–5851. doi:10.1002/2017jb014190

Weckmann, U., Magunia, A., and Ritter, O. (2005). Effective noise separation for magnetotelluric single site data processing using a frequency domain selection scheme. *Geophys. J. Int.* 161, 635–652. doi:10.1111/j.1365-246x.2005.02621.x

Zhang, L., Ren, Z., Xiao, X., Tang, J., and Li, G. (2022). Identification and suppression of magnetotelluric noise via a deep residual network. *Minerals* 12, 766. doi:10.3390/min12060766

Zhang, X., Li, J., Li, D., Li, Y., Liu, B., and Hu, Y. (2021). Separation of magnetotelluric signals based on refined composite multiscale dispersion entropy and orthogonal matching pursuit. *Earth Planets Space* 73, 76–18. doi:10.1186/s40623-021-01399-z

Zhou, R., Li, T., Han, J., Liu, L., and Guo, Z. (2022). Research on magnetotelluric long-duration noise reduction based on adaptive sparse representation. *IEEE Trans. Geosci. Remote Sens.* 60, 1–13. doi:10.1109/tgrs.2022.3229362

frontiers | Frontiers in Earth Science

TYPE Methods
PUBLISHED 18 October 2023
DOI 10.3389/feart.2023.1183188

OPEN ACCESS

EDITED BY
Cong Zhou,
East China University of Technology, China

REVIEWED BY
Ying Liu,
China University of Geosciences Wuhan, China
Xiaoyue Cao,
Ministry of Education, China
Liang Zhang,
Guizhou University, China

*CORRESPONDENCE
Pengfei Zhao,
zhaopf@jlu.edu.cn

RECEIVED 09 March 2023
ACCEPTED 03 October 2023
PUBLISHED 18 October 2023

CITATION
Zhan Q, Liu C, Liu Y and Zhao P (2023), Data processing method for magnetotelluric sounding based on cepstral analysis.
Front. Earth Sci. 11:1183188.
doi: 10.3389/feart.2023.1183188

Data processing method for magnetotelluric sounding based on cepstral analysis

Qining Zhan, Cai Liu, Yang Liu and Pengfei Zhao*

College of Geo-exploration Science and Technology, Jilin University, Changchun, China

Magnetotelluric (MT) signals exhibit the characteristics of being weak and having a wide frequency band. The acquired field data are susceptible to various types of noise, which poses challenges in accurate identification and processing. Currently, there exist numerous MT data processing methods; however, they lack efficiency and physical meaning. To address this issue and improve the signal-to-noise ratio of the acquired data, this study proposes a MT data processing method based on cepstral analysis. By employing cepstral analysis on the MT data, the cepstrum is obtained, and an appropriate truncation position is selected for processing. The experimental results demonstrate that this method obtains smoother and more continuous apparent resistivity curves with fewer errors. Compared with other methods, the cepstral analysis method can effectively suppress different types of MT noise, and the method is simple and efficient with clear physical significance.

KEYWORDS

magnetotelluric, cepstral analysis, data processing, spectral smoothing, signal denoising

1 Introduction

The magnetotelluric (MT) method is an electromagnetic exploration method that was first proposed in the 1950s (Tikhonov 1950; Cagniard, 1953). Due to its advantages of low cost, simple construction, large detection depth, and high resolution of low-resistivity layers, the method is widely used in exploration geophysics. However, the natural MT signal is extremely weak, and its frequency band is extremely wide; this makes such signals with nonlinear and nonstationary characteristics more susceptible to interference by various noises (Wang and Wang, 2004a; Wang, 2004b). With the continuous advancement of human civilization, electromagnetic interference caused by human and industrial activities has become increasingly severe, resulting in a typical near-source effect in the collection of MT data in the field (Wei, 2002). Whether studying deep geological formations or exploring mineral resources, it is impossible to completely avoid the complex electromagnetic interference environment (Dong et al., 2012). Noise suppression is always an research hot spot in MT studies. To address this problem, geophysicists have proposed a series of techniques to obtain unbiased MT impedance data.

The traditional least squares method assumes that the input is not affected by noise and that the noise at the output follows a Gaussian distribution. The time series of MT data are assumed to be stationary. However, MT signals are actually nonstationary due to various factors, such as geomagnetic storms and anthropogenic noise. Due to the presence of measurement errors and non-unique sources, the data may contain large outliers, resulting in lower fitting accuracy (Gangi and Shapiro, 1979). In this regard, Gamble et al. (1979) proposed the remote reference method for the first time, which involves adding remote reference points and utilizing cross-power spectra instead of

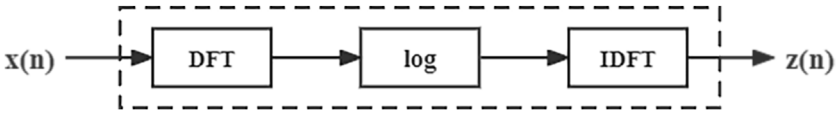

FIGURE 1
Cepstral analysis and processing flow.

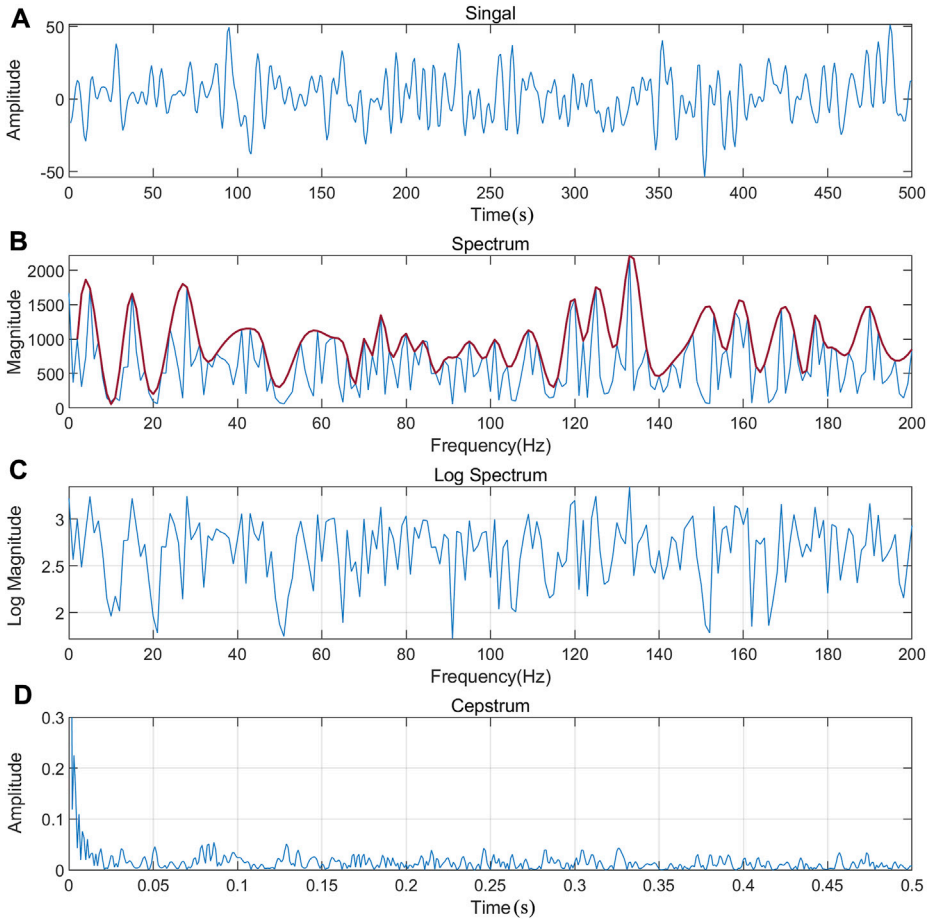

FIGURE 2
Schematic diagram of cepstral analysis. **(A)** signal and **(B)** spectrum. The red line is the envelope. **(C)** Log spectrum and **(D)** cepstrum.

auto-power spectra to suppress unrelated noise in MT data. However, its effectiveness in the low-frequency range is not optimal. Ritter et al.(1998) utilized indicators such as the transfer function between the magnetic field at measurement and reference points to determine the presence of noise in each data segment. They removed the segments with noise before the subsequent impedance estimation to eliminate their impact. To suppress non-Gaussian noise, the robust method has been widely applied for transfer function (TF) correction (Egbert and Booker, 1986; Chave et al., 1987; Chave and Thomson, 1989), where coefficients are weighted to eliminate the influence of outliers. Although this method can achieve smooth apparent resistivity and phase curves within a certain frequency band, its effectiveness is mainly limited to the high-frequency range. Satisfactory results are often challenging to obtain in the low-frequency range due to the limited sampling rate. Therefore, neither the remote reference method nor the robust estimation method can fully solve the challenges associated with processing MT data.

Consequently, several signal processing and inversion methods have been introduced into the field of MT data processing. Interpolation, filtering, and regularization techniques such as smoothing constraints have played crucial roles as preprocessing algorithms. Among these techniques, time- and frequency-domain filtering, such as the wavelet transform, provide a better description of signal

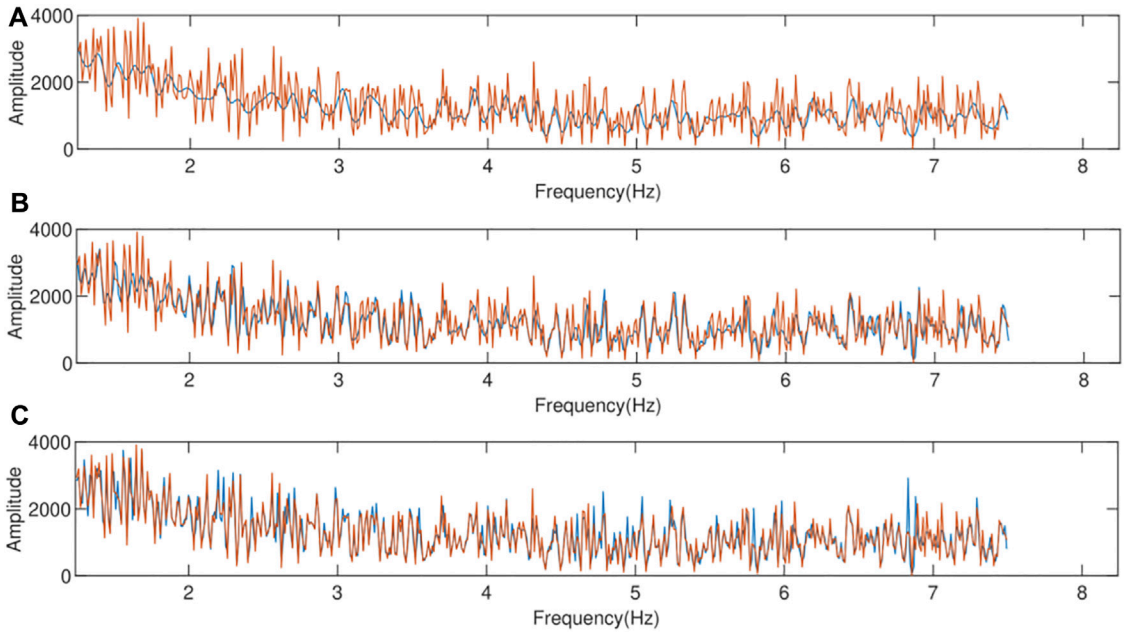

FIGURE 3
Comparison chart of amplitude spectrum before and after processing. **(A)**1/8 truncation: The red line is the original spectrum, and the blue line is the processed spectrum. **(B)** 2/8 truncation: The red line is the original spectrum, and the blue line is the processed spectrum. **(C)** 3/8 truncation: The red line is the original spectrum, and the blue line is the processed spectrum.

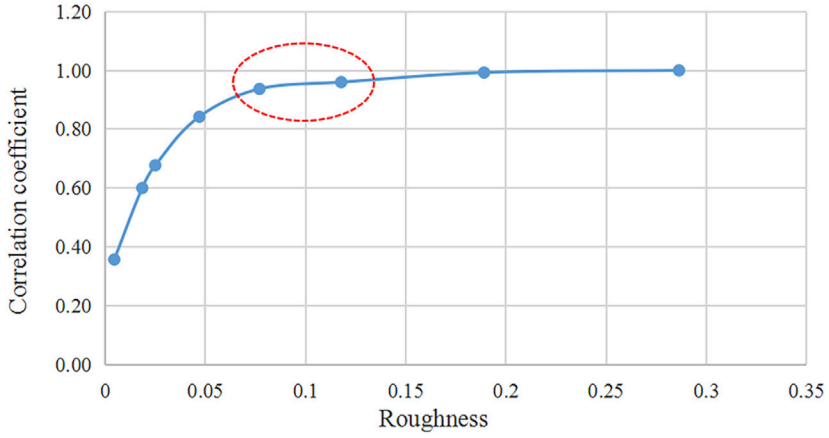

FIGURE 4
Correlation coefficient and roughness curves.

time–frequency distribution and different scales. However, these methods heavily rely on wavelet basis functions and are unable to capture local signal features (Trad and Jandyr, 2000; Garcia and Jones, 2008; Carbonari et al., 2017). Other methods include the Hilbert–Huang transform (Cai et al., 2009; Cai, 2014), the generalized S-transform (Jing et al., 2012), and mathematical morphological filtering (Tang et al., 2012). Furthermore, an effective estimation process is indispensable for obtaining the transfer function. Some researchers have applied artificial intelligence (Manoj and Nagarajan 2003), regularization optimization (Kim et al., 2018), nonparametric statistics (Constable et al. 1987; Chave and Thomson, 1989), and maximum likelihood estimation (Chave, 2017) as alternatives to robust estimation, achieving significant results. All these efforts aim to obtain high-quality transfer functions, which are essential for electromagnetic inversion, as the curves are expected to exhibit smooth trends due to the diffusive nature of the MT field (Weidelt, 1972). Therefore, regardless of the method used, the smoothness of the apparent resistivity and phase curves serves as an important criterion for evaluating the quality of

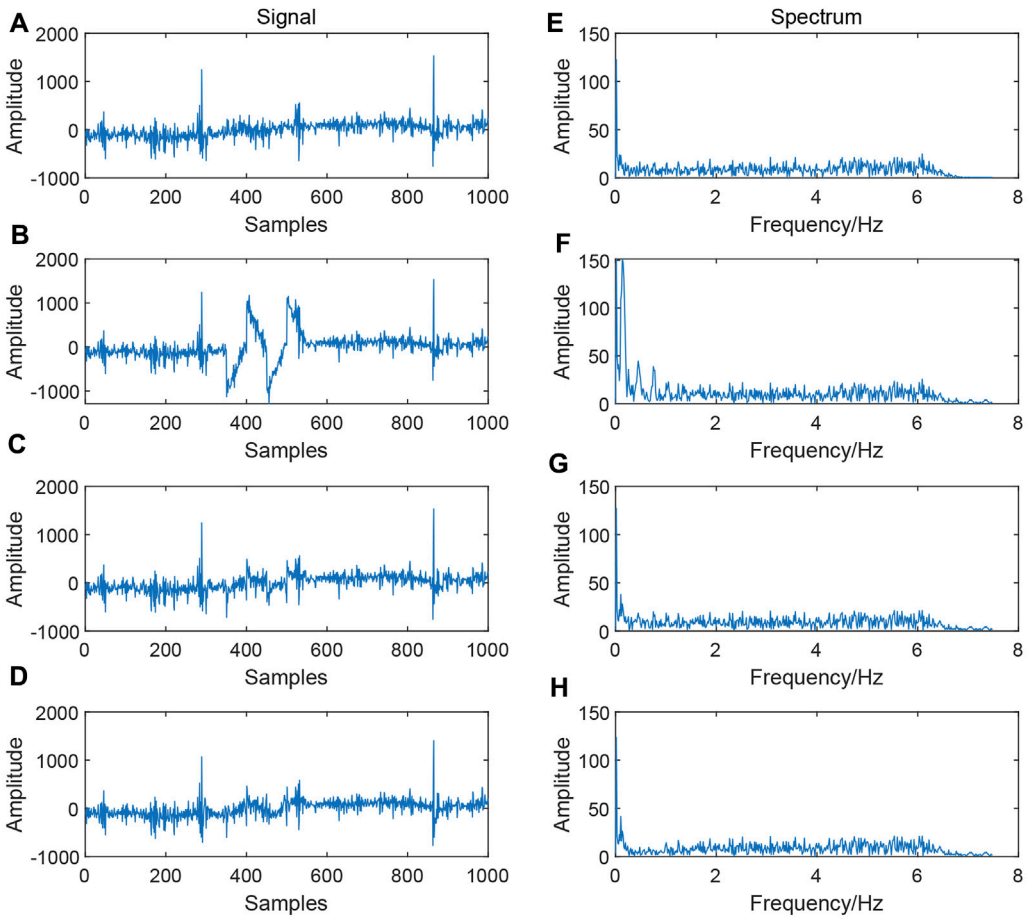

FIGURE 5
Comparison of simulated triangle wave denoising effects. **(A)** Original signal; **(B)** signal with triangular wave noise; **(C)** signal processed using the cepstrum method; **(D)** signal processed using the EMD method; **(E)** spectrum of the original signal; **(F)** spectrum of the signal with triangular wave noise; **(G)** signal spectrum processed using the cepstrum method; and **(H)** signal spectrum processed using the EMD method.

TABLE 1 Signal parameters.

Method	SNR	MSE	NCC
Cepstral analysis	8.98	44,500	0.94
EMD	5.12	64,014	0.84

processed data. By observing the acquired MT data, it is evident that the signals contain many periodic abnormal waveforms, such as square wave noise, triangular wave noise, and impulse noise. This leads to a degradation in the quality of the acquired data in the low-frequency range, resulting in non-smooth apparent resistivity curves. However, applying the aforementioned methods may result in excessive data loss of useful signals or the inability to remove a large amount of abnormal data in the low-frequency range. The cepstral analysis method proposed in this study utilizes homomorphic linear filtering to separate convolution signals. It can effectively suppress non-earth electromagnetic signals in the low-frequency range while preserving the genuine MT signals, thereby enhancing the signal-to-noise ratio of magnetotelluric soundings. Compared to methods such as empirical mode decomposition (EMD), it possesses clear physical significance and simple operation, which are particularly important for improving the inversion accuracy of MT data. This method essentially performs secondary spectrum analysis of the signal spectrum, providing a powerful tool for identifying complex periodic components in the signal spectrum (Li et al., 2006a). The term "cepstrum" was first introduced by Bogert (1963), along with various definitions emerging with the advent of the fast Fourier-transform (FFT) algorithm (Randall and Sawalhi, 2011). Currently, it has been widely applied in fields such as speech (Li et al., 2006b), acoustics (Zeng et al., 2011), mechanical fault diagnosis (Choi and Kim, 2007), and sound detection and classification (Li, 2012). In the field of geophysics, Wei and Li (2003) applied cepstral analysis to identify the characteristics of seismic sources and have effectively analyzed seismic and explosion events in recent years. By examining the differences in the unique morphology of explosion cepstral and the diversity of seismic cepstral, an effective approach was established for identifying the nature of seismic sources. This has opened up a new and effective method to identify seismic source types. Linear prediction cepstral coefficient feature extraction has also been

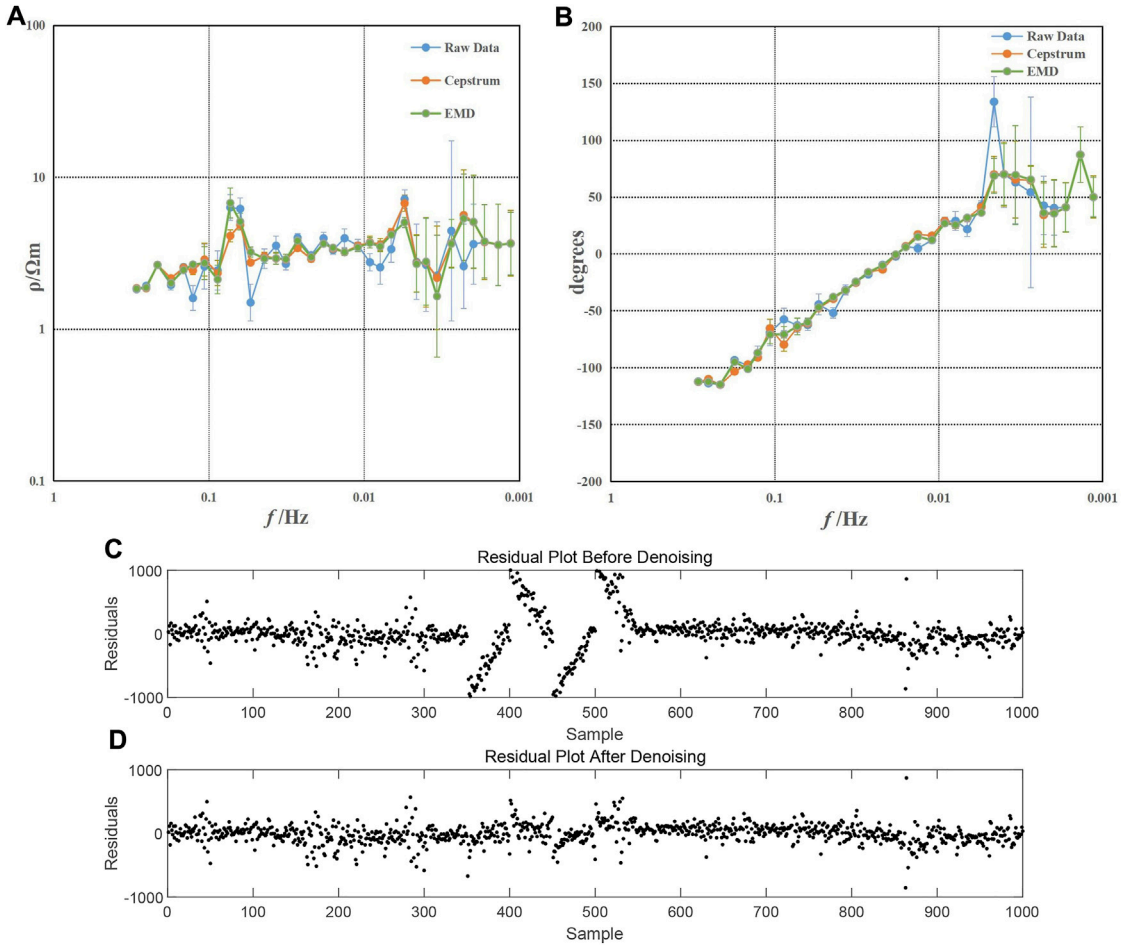

FIGURE 6
Apparent resistivity and phase curves and residual plots. **(A)** Apparent resistivity curve; **(B)** phase curve; **(C)** residual plot before denoising; and **(D)** residual plot after denoising.

used to decompose seismic data, obtaining seismic feature parameters that separate wavelets and reflection coefficients and providing a good description of geological boundary phenomena. This allows for a more detailed observation of geological features hidden in seismic data in different dimensions (Xie and Zheng, 2016). Previous studies indicate that cepstral analysis can be employed to separate convolution signals using linear filtering methods, thus identifying the desired characteristic information. However, its application in MT soundings is currently limited.

This study utilizes cepstral analysis to investigate denoising techniques for the time-series sequences of MT data. The experimental results demonstrate that this method is direct and straightforward. It improves not only the overall smoothness and continuity of the apparent resistivity curve but also significantly the data quality in the low-frequency range. Additionally, it provides clear physical significance, offering a more precise data foundation for subsequent inversion work, and the corresponding method can easily be extended to smoothing phase curves.

2 Principle of the algorithm

Further research on spectrum smoothing methods and signal denoising is presented in this study, especially by introducing a new method based on cepstral analysis. To address the multitude of noise types currently faced by MT, accurate identification proves challenging and the variety of processing methods lack an efficient and unified pipeline.

The processing flow is shown in Figure 1. The cepstrum based on the Fourier spectrum is defined as the inverse Fourier transform of the logarithmic spectrum. The specific step is to first apply the Fourier transform to signal (a) in Figure 2 to obtain signal (b). In Figure 2B, the red line forms an envelope representing the slow-varying signal, while the blue line represents the fast-varying signal. Mathematically, a slow signal and a fast signal can be expressed as the product of a low-frequency signal and a high-frequency signal. Then, the logarithm of the spectrum is taken. As we know from the previous step, the slow variable signal and the fast variable signal are coupled in the way of product, so after the logarithm is taken, the slow variable signal and the fast variable signal are coupled in the

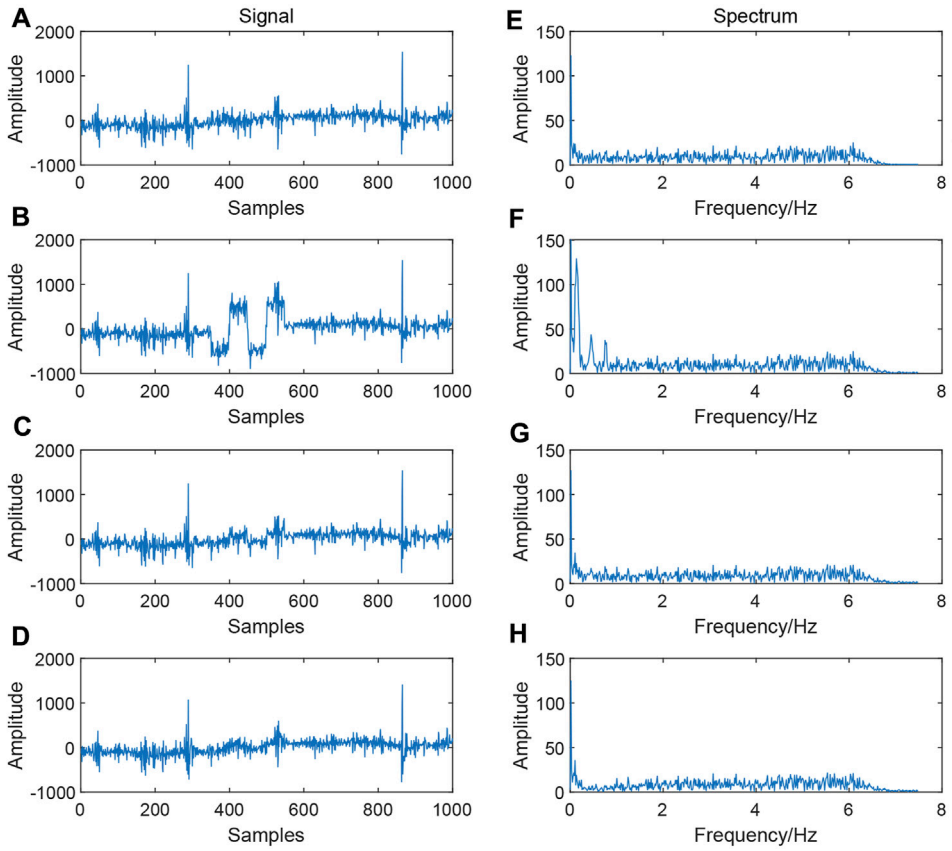

FIGURE 7
Comparison of simulated square wave denoising effects. **(A)** Original signal; **(B)** signal with square wave noise; **(C)** signal processed using the cepstrum method; **(D)** signal processed using the EMD method; **(E)** spectrum of the original signal; **(F)** spectrum of the square wave noise signal; **(G)** signal spectrum processed using the cepstrum method; and **(H)** signal spectrum processed using the EMD method.

TABLE 2 Signal parameters.

Method	SNR	MSE	NCC
Cepstral analysis	10.40	32,068	0.95
EMD	6.98	47,564	0.91

way of addition, as shown in Figure 2C. Finally, the inverse Fourier transform is taken so that the coupling of the high- and low-frequency signals after product variation addition can be separately analyzed. Next, the cepstrum (d) is processed in segments, and the required data are extracted by selecting the segment position, as shown in Figure 2.

The mathematical expression is

$$\boldsymbol{Z}(\mathbf{n}) = \boldsymbol{F}^{-1}[\boldsymbol{log}(\boldsymbol{X}(\boldsymbol{n}))], \tag{1}$$

where $Z(n)$ represents the cepstrum and $X(n)$ is the spectrum. $X(n)$ after Fourier change in the $X(t)$ signal can be expressed as

$$\boldsymbol{X}(\boldsymbol{n}) = \int_{-\infty}^{+\infty} \boldsymbol{x}(\boldsymbol{t}) \boldsymbol{exp}^{-j2\pi nt}\, \boldsymbol{dt}\,. \tag{2}$$

From the aforementioned equation, it can be seen that the signal retains the amplitude and phase information after the Fourier variation. The cepstrum defined by the Fourier spectrum is further divided into real cepstrum and complex cepstrum.

Then, the signal, through Fourier variation, can be expressed as

$$\boldsymbol{X}(\boldsymbol{n}) = \boldsymbol{A}(\boldsymbol{n})\, \boldsymbol{exp}\left(\boldsymbol{j}\varnothing(\boldsymbol{n})\right). \tag{3}$$

So there is

$$\boldsymbol{ln}(\boldsymbol{X}(\boldsymbol{n})) = \boldsymbol{ln}(\boldsymbol{A}(\boldsymbol{n})) + \boldsymbol{j}\varnothing(\boldsymbol{n}), \tag{4}$$

where $A(n)$ is the continuous amplitude spectrum of the analysis signal and $\varnothing(n)$ is the continuous phase spectrum.

When $X(n)$ retains only the real part, the real cepstrum is defined as

$$\boldsymbol{Z}(\mathbf{n}) = \boldsymbol{F}^{-1}[\boldsymbol{ln}(\boldsymbol{A}(\boldsymbol{n}))]. \tag{5}$$

It can be found that in the calculation of the cepstrum, real cepstral analysis actually involves zeroing the phase spectrum, which is the "inverse Fourier transform of the logarithmic amplitude spectrum." Therefore, we need to add back the lost phase when

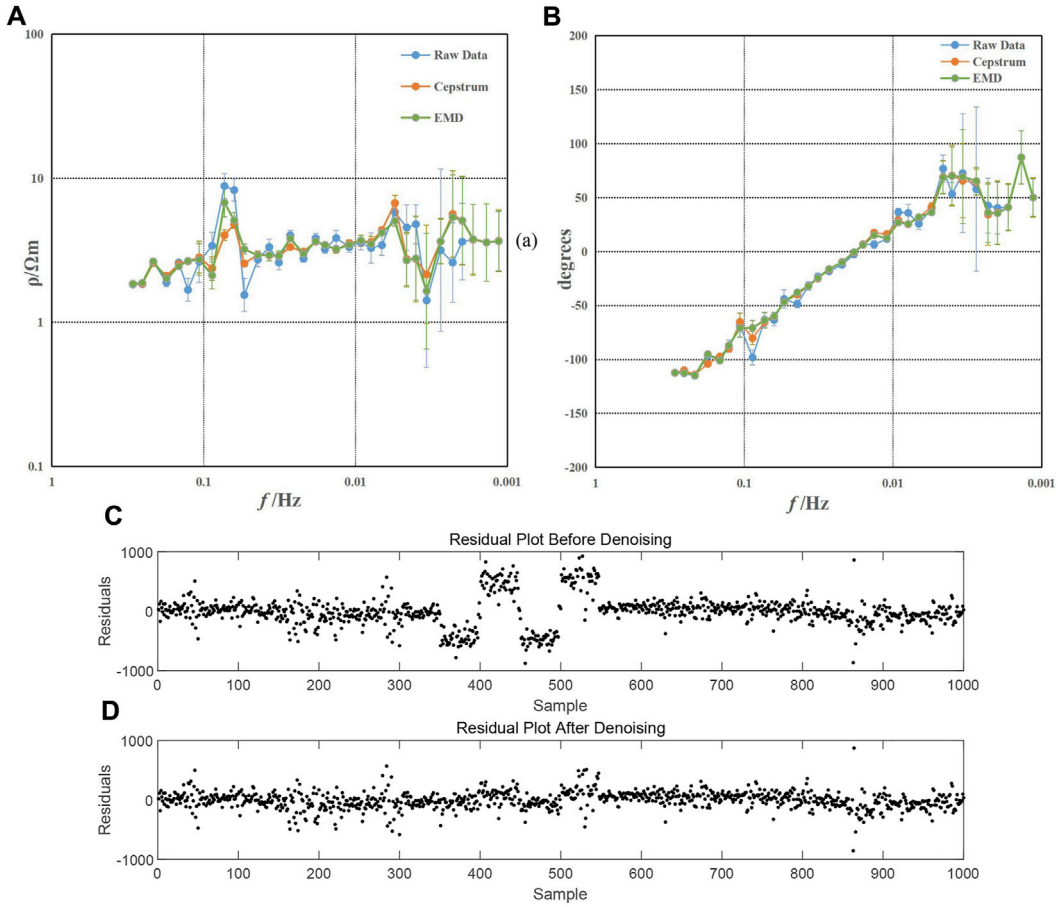

FIGURE 8
Apparent resistivity and phase curves and residual plots. **(A)** Apparent resistivity curve; **(B)** phase curve; **(C)** residual plot before denoising; and **(D)** residual plot after denoising.

rebuilding the signal after segmental cepstrum; this restoration is crucial for the calculation of the apparent resistivity.

3 Simulation

To demonstrate the effect of the cepstral analysis method, we selected high-quality spectral curves from the measured MT data for easy addition of various types of noise for comparison. First, we verified the impact of different selections of the cepstral cutoff point on the smoothness of the amplitude spectrum. The selected data were processed, and Figures 3A–C depicts the partial amplitude spectrum before and after processing with different cepstral segment positions, with the post-processing amplitude spectrum in blue and the pre-processing amplitude spectrum in yellow. The amplitude spectrum becomes smoother than before the processing by truncating the cepstrum. The change in the truncation position directly affects the smoothness of the amplitude spectrum. However, determining an appropriate truncation point still relies on other parameters. In this study, we have acquired different spectrum smoothness levels and correlations by adjusting the cepstral truncation position. Figure 4 displays the results derived from these two parameters, where the *y*-axis represents the correlation coefficient of the spectrum before and after processing and the *x*-axis signifies the roughness of the spectrum. We seek points with a lower degree of roughness on the curve with a high auto-correlation coefficient to serve as truncation points for the processing, as indicated by the range within the red circle in the figure. This provides a basis for the subsequent selection of the cutoff location.

To demonstrate the denoising effect of the cepstral analysis, we add square waves, triangular waves, and impulse noise to the simulation data from 400 to 600 sampling points. We processed the simulation data using the cepstral analysis method. During the procedure, we truncated the latter half of the cepstrum, retaining only the preceding half. By reconstructing the signal, we obtained the processed spectral curves for comparison and further analysis.

Figure 5 shows the comparative analysis of the simulated signal before and after adding triangular wave noise. Figure 5A depicts a segment of the original signal without noise, while Figure 5B portrays the signal with triangular wave-like noise. Figures 5C, D depict the signals processed using the methodology proposed in this study and the EMD method, respectively. Figures 5E–H represent the corresponding spectrum. In

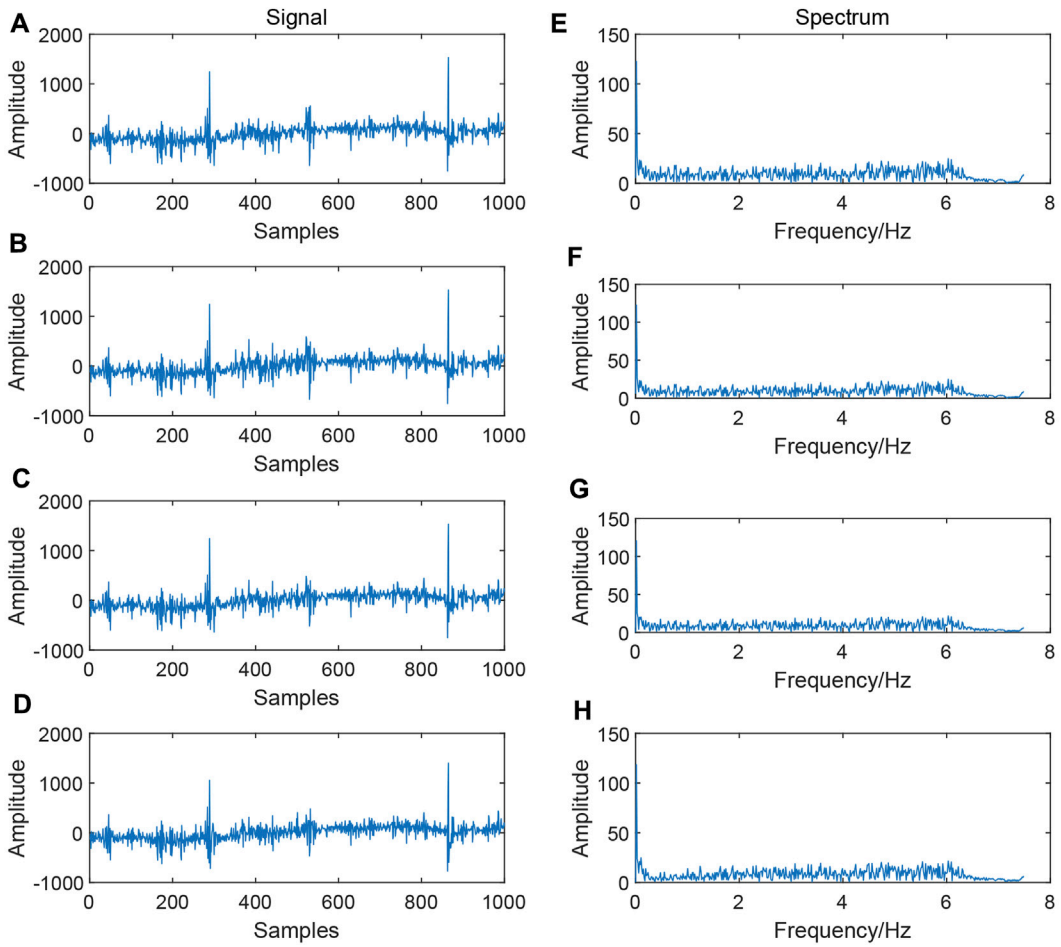

FIGURE 9
Comparison of denoising effects of simulated Gaussian noise. **(A)** Original signal; **(B)** signal with Gaussian noise; **(C)** signal processed using the cepstrum method; **(D)** signal processed using the EMD method; **(E)** spectrum of the original signal; **(F)** spectrum of the Gaussian sound signal; **(G)** signal spectrum processed using the cepstrum method; and **(H)** signal spectrum processed using the EMD method.

TABLE 3 Signal parameters.

Method	SNR	MSE	NCC
Cepstral analysis	17.06	604	0.99
EMD	8.08	4,234	0.94

Figure 5B, it is evident that the triangular wave-like noise is effectively suppressed using the cepstral analysis and EMD methods. The spectrum on the right further shows that the frequency-domain characteristics of the triangular wave, as shown in Figure 5F, have been substantially eliminated in Figures 5G, H. To further compare the effectiveness of the two methods, we introduce parameters such as signal-to-noise ratio (SNR), mean square error (MSE), and normalized cross-correlation (NCC) (Table 1). The results indicate that the data processed using the cepstral analysis method display a higher SNR and cross-correlation and lower error, underscoring the superior performance of this method. To facilitate the calculation of apparent resistivity and phase, the simulation data were extended to 54,000 points for computation. Figure 6A shows the apparent resistivity curves derived from the noise-added data using two different methods, while Figure 6B shows the phase curves. In Figure 6, the yellow curve represents the apparent resistivity and phase curves obtained through the cepstral method, while the green curve is derived from the EMD method. Upon comparison, it is evident that within the 0.005–0.01 Hz range, the yellow curve is smoother and has fewer errors. Comparing Figures 6C, D it can be seen that the residual map after denoising is closer to 0, effectively removing the noise. This further validates the effectiveness of the methodology presented in this study.

Figure 7 shows the comparison of signal processing before and after adding square wave noise. Figure 7A shows a segment of the original signal without noise, while Figure 6B shows the signal with square wave-like noise. Figures 7C, D demonstrate the signal processed using the cepstral analysis and EMD methods, repectively. Figures 7E–H each depict the corresponding spectrum. From Figure 7B, it can be observed that the square wave-like noise was effectively eliminated using the cepstral analysis and EMD methods. From the spectrum on the right,

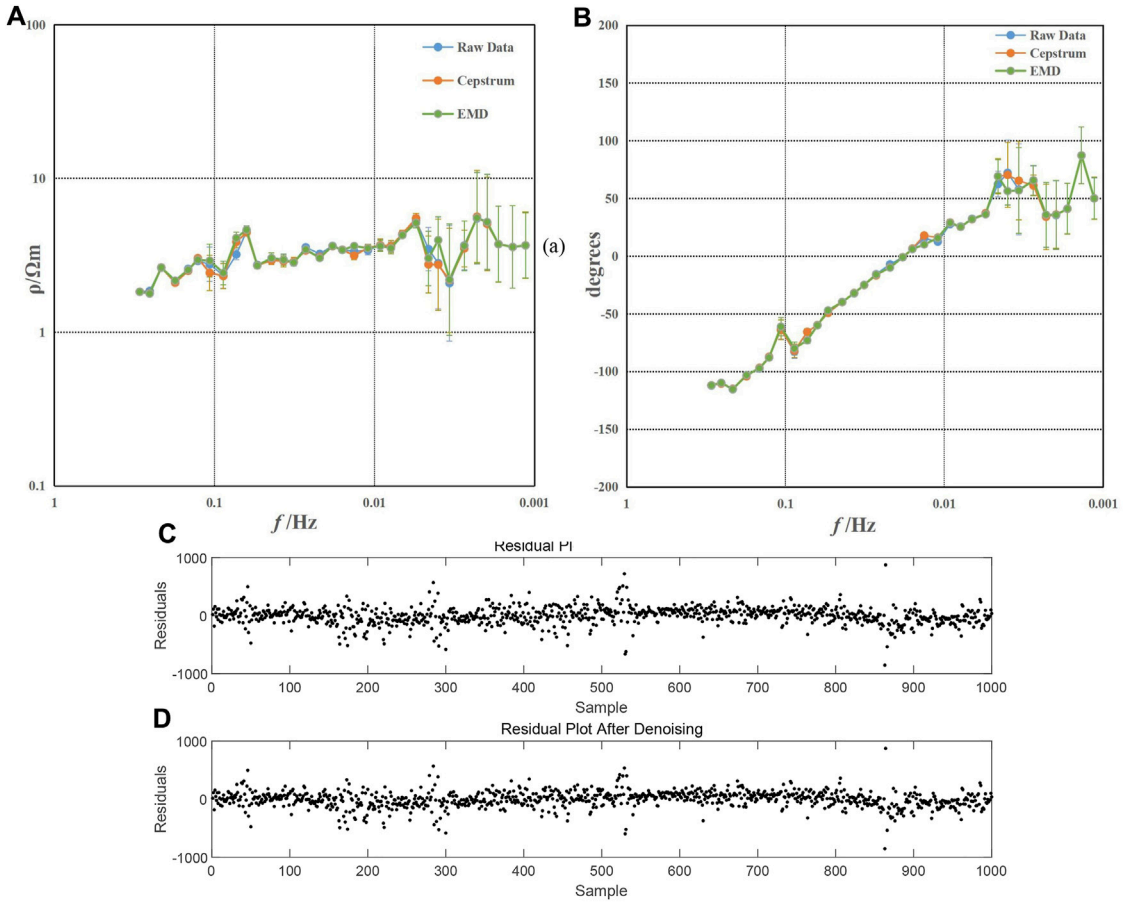

FIGURE 10
Apparent resistivity and phase curves and residual plots. **(A)** Apparent resistivity curve; **(B)** phase curve; **(C)** residual plot before denoising; and **(D)** Residual plot after denoising.

Figures 6H, 7G show that the spectral characteristics of the square wave in Figure 7F have been essentially eliminated. The results in Table 2 indicate that the data processed using the cepstral analysis method display a higher SNR and NCC and a lower MSE, underscoring the superior performance of this method.

Figure 8A shows the apparent resistivity curves derived from the noise-added data using two different methods, while Figure 8B shows the phase curves. In Figure 8, both methods have effectively suppressed noise, resulting in smoother apparent resistivity curves. However, at the 0.1 Hz mark in Figure 8A, the two increasing frequency points are more prominently addressed using the method proposed in this study, showing a more significant decline. Comparing Figures 8C, D, it can be seen that the residual map after denoising is closer to 0, effectively removing the noise.

Figure 9 shows the comparison of signal processing before and after adding Gaussian noise. Figure 9A shows a segment of the original signal without noise, while Figure 9B shows the signal with Gaussian noise. Figures 9C, D represent the signals processed using the cepstral analysis and EMD methods, respectively. Figures 9E–H show the corresponding spectrum. By comparing Figure 9B, the Gaussian noise was effectively suppressed using the cepstral analysis and EMD methods. Although we cannot observe the spectral characteristics of the noise being eliminated from the spectrum as in Figures 5, 7, we can still compare the results using parameters such as signal-to-noise ratio, mean square error, and normalized cross-correlation (Table 3). The results indicate that the data processed using the cepstral analysis method display a higher SNR and NCC and a lower MSE, indicating the superior performance of the cepstral analysis method.

Figure 10A shows the apparent resistivity curves derived from the noise-added data using two different methods, while Figure 10B shows the phase curves. In Figure 10, it is challenging to determine whether the noise has been effectively suppressed, both from the waveform and apparent resistivity and phase curves. The residual plots of Figures 10C, D also fail to observe the difference. Compared to the noise of triangular and square waves, the method proposed in this study does not perform well when addressing noise whose waveform and spectrum closely resemble the signal.

Based on the analysis and discussion in this section, it becomes evident that the cepstral analysis method proposed in this study outperforms the EMD method in effectively suppressing various types of noise present in the signals. The application of cepstral

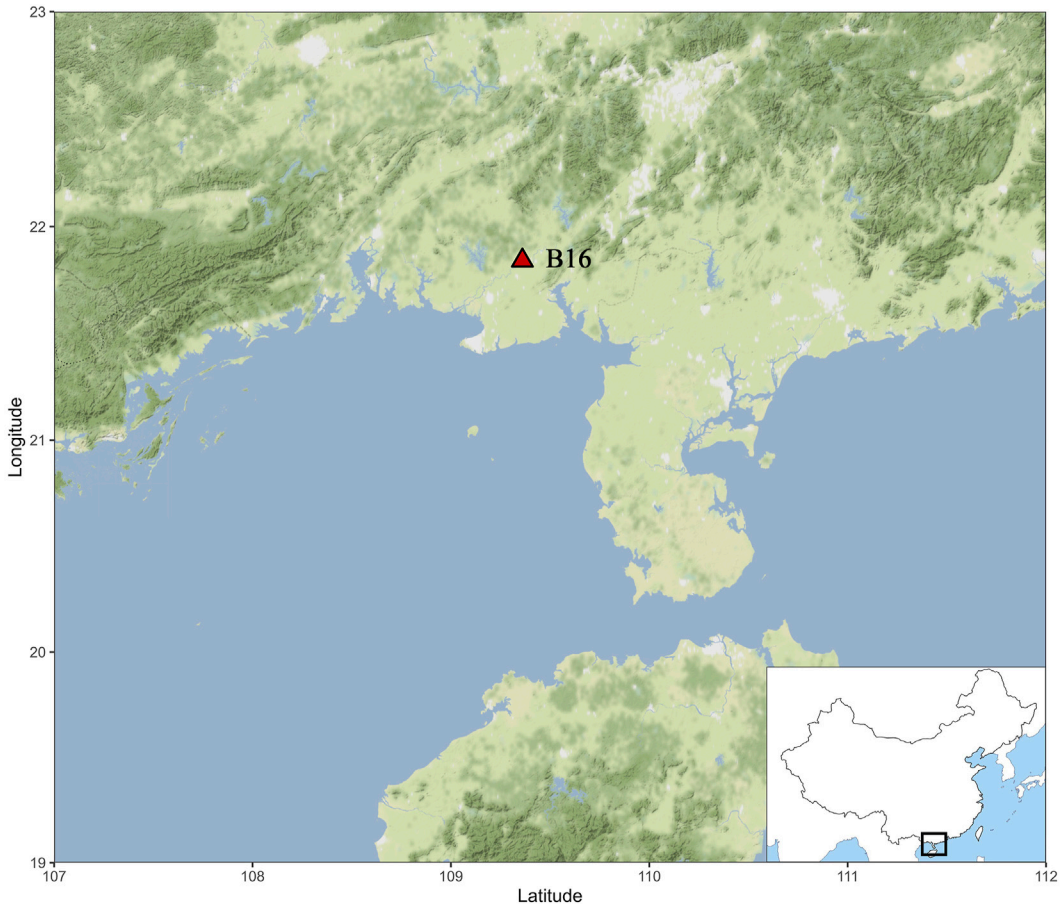

FIGURE 11
Map showing the location of site B16.

analysis leads to enhanced smoothness in the spectrum, resulting in improved overall performance.

4 Data processing

To further verify the validity of the proposed method, we selected three measuring points for detailed analysis and discussion. The high-frequency portion of these data is of good quality, while the low-frequency band has noise interference and poor-quality apparent resistivity curves. These characteristics facilitate our subsequent analysis and validation. We used V5-2000 for data acquisition and SSMT-2000 software for apparent resistivity and phase calculations, and we employed the robust method produced by Phoenix Geophysics Limited, Toronto, Canada.

The MT site BH16 is located near the Hepu Industrial Zone, where industrial noise may have an impact on the quality of the signals. The location of the site BH16 is shown in Figure 11. Figures 12A, B depict the apparent resistivity curves in the Rxy and Ryx directions for the site BH16 obtained using three different methods. Given the lower quality of data in the low-frequency range, Figures 12C, D provide a clearer comparison by showcasing the apparent resistivity curves for frequencies less than 0.01 Hz.

Figure 12 shows the apparent resistivity curves of the MT site BH16 obtained from the original data, the EMD method, and the proposed method. Figures 12A, C represent the Rxy direction, while Figures 12B, D represent the Ryx direction. The blue curve has poor continuity and smoothing of apparent resistivity, which represents the original data. Within the frequency range of 0.1–0.008 Hz, the apparent resistivity curve appears relatively smooth with a small range of errors. However, in the frequency range of 0.008–0.0005 Hz, the data of approximately 12 frequency points are completely distorted. At approximately 0.0005 Hz, the apparent resistivity curve shows significant fluctuations with large errors. In Figure 12C, the apparent resistivity in the Rxy direction reaches a minimum value close to 0.1 Ω·m and a maximum value close to 60 Ω·m. In Figure 12D, the apparent resistivity in the Ryx direction reaches a minimum value close to 0.9 Ω·m and a maximum value close to 70 Ω·m. Because of noise interference, the time–frequency characteristics cannot reflect the true typical features of the subsurface.

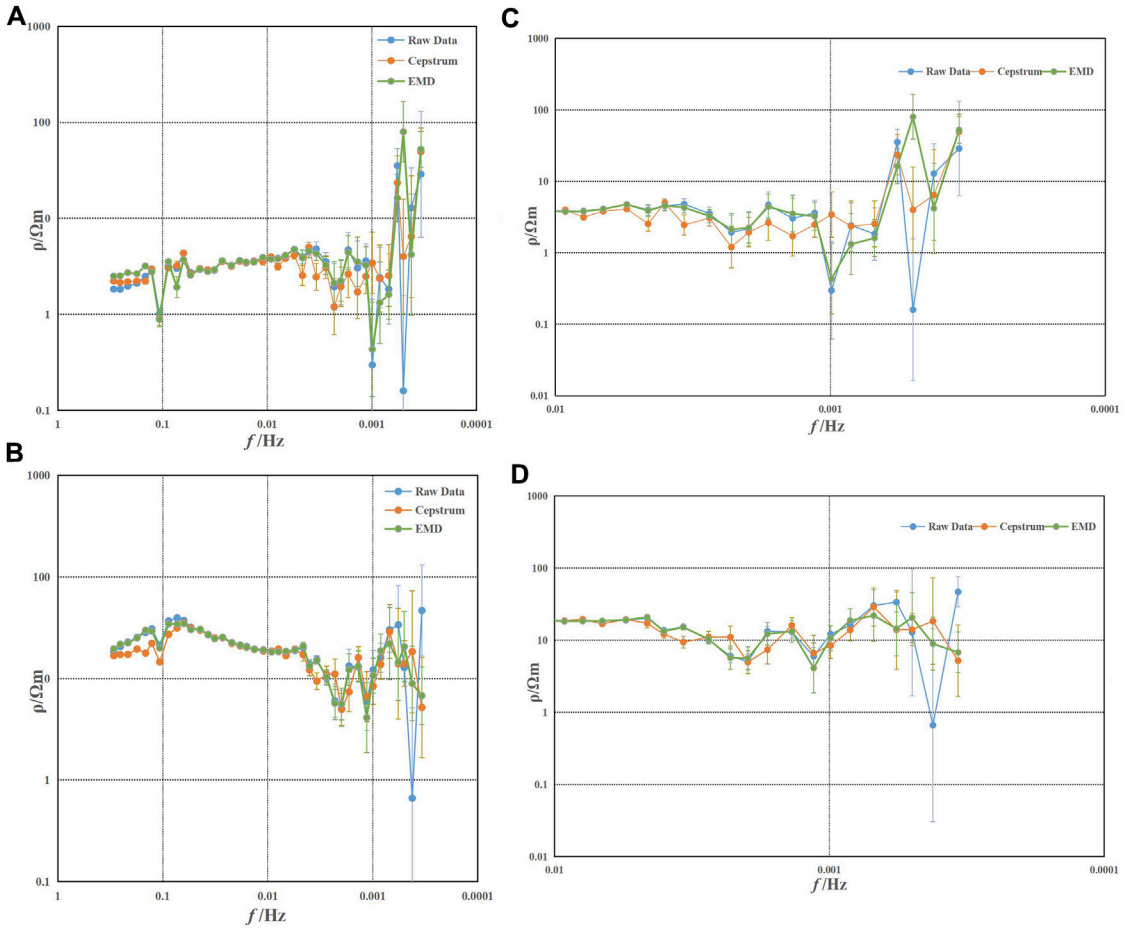

FIGURE 12
Apparent resistivity curve of site BH16. **(A)** Rxy; **(B)** Ryx; **(C)** part of Rxy; and **(D)** part of Ryx.

The yellow curve in Figure 12 represents the apparent resistivity curve of the MT site BH16 processed using the proposed cepstral method. The green curve demonstrates the process of decomposing the original signal into various scale components using the EMD method, extracting the approximate single component of each intrinsic mode function from high to low frequencies, and then reconstructing the signal by removing the high-frequency IMF component. Comparing the three curves in the low-frequency range, it can be observed that both methods effectively suppress noise interference to some extent. However, the proposed method obtains more significant results with relatively smoother apparent resistivity curves. Particularly in the Rxy direction, the sudden frequency drops near 0.001 Hz and 0.0008 Hz tend to approach normal levels, and the errors in the low-frequency range are reduced, resulting in relatively stable numerical values.

Figures 14, 15 show data obtained from Xiwuqi, Inner Mongolia, in close proximity to Gaorihan Town, with surrounding agricultural households and frequent livestock passing through, generating anthropogenic noise that may impact signal quality. The location of the point is shown in Figure 13.

Figures 14A, B depict the apparent resistivity curves in the Rxy and Ryx directions for the site MT086, obtained using three different methods. In the high-frequency range, the signal strength is relatively weak. The proposed method in this paper tends to de-truncate the high-frequency noise and retain the low-frequency trend when dealing with the cepstrum of the signal. Therefore, it is easy to increase the errors in the high-frequency band if it is processed too much, so in case of poor quality of this band, manual adjustments are usually needed. For the low-frequency band, the cepstrum analysis method is used. Figures 14C, D provide a clearer comparison by showcasing the apparent resistivity curves for frequencies less than 0.01 Hz.

Figure 14 shows the apparent resistivity curves of the MT site MT086 obtained from the original data, processed using EMD, and processed using the cepstral method. Figures 14A, C represent the Rxy direction, while Figures 14B, D represent the Ryx direction. In Figure 14C, the overall smoothness of the blue apparent resistivity curve is poor, which represents

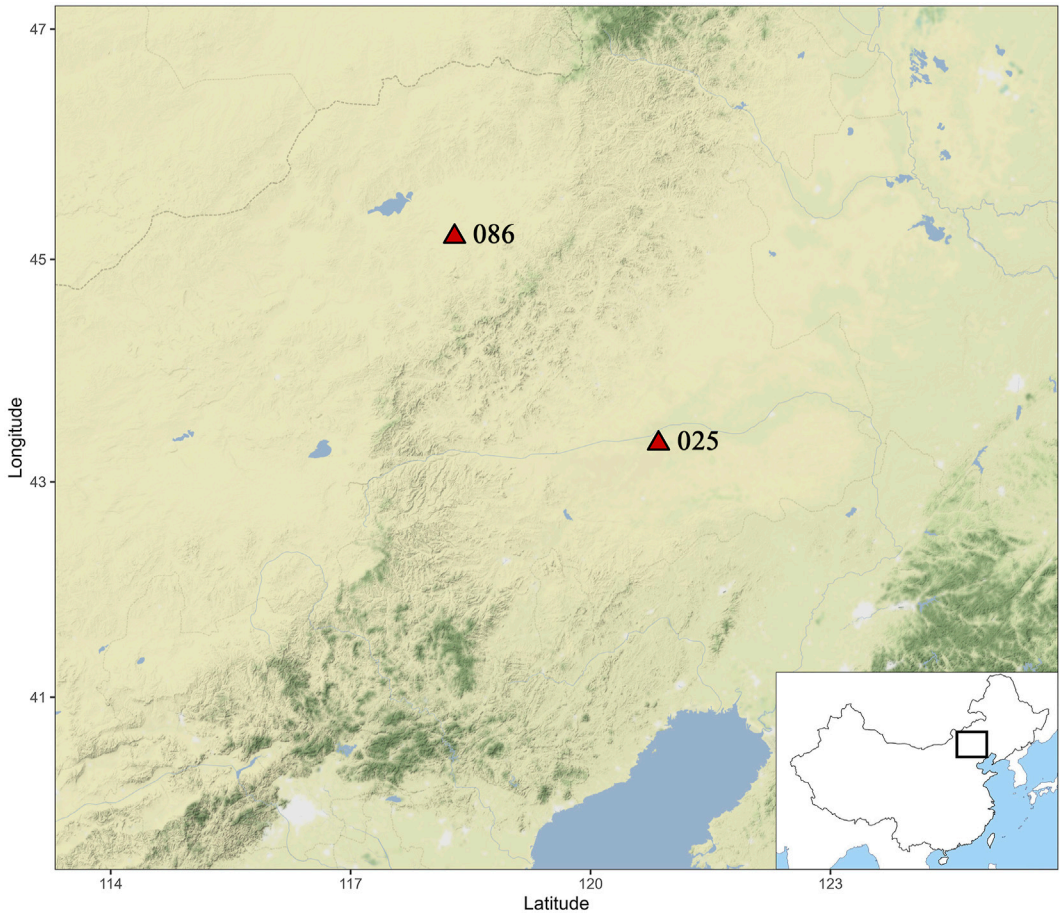

FIGURE 13
Map showing the locations of sites 025 and 086.

the original data, and there are significant variations in the low-frequency range. Within the frequency range of 0.08 Hz–0.001 Hz, the curve appears smooth with small errors. However, in the frequency range of 0.001 Hz–0.0005 Hz, the data from approximately four frequency points are completely distorted. At approximately 0.0008 Hz, the resistivity rapidly drops to approximately 0.9 Ω·m, followed by significant fluctuations in the resistivity curve. At 0.0008 Hz, the resistivity sharply decreases to 0.1 Ω·m. Due to noise interference, the time–frequency characteristics of this MT site fail to reflect the true typical subsurface features.

The yellow curve in Figure 14 represents the apparent resistivity curve obtained using the cepstral analysis method, while the green curve represents the apparent resistivity curve obtained using the EMD method. In the low-frequency range, the EMD method does not obtain significant improvement around the distorted frequency point near 0.0006 Hz, but it reduces the magnitude of the drop to some extent (Figure 14C). However, in the Ryx direction, the EMD method shows inferior results (Figure 14D). In contrast, the proposed method in this study demonstrates more significant effects, thus successfully suppressing noise interference in the low-frequency range (approximately 0.0006 Hz). Overall, the resulting apparent resistivity curve appears smooth, with a reduction in error values for several high fluctuation frequency points, resulting in relatively stable numerical values.

Figures 15A, B depict the apparent resistivity curves in the Rxy and Ryx directions for the site MT025 obtained using three different methods. In the high-frequency range, the signal strength is relatively weak, and adjustments are typically made manually. Figures 15C, D provide a clearer comparison by showcasing the apparent resistivity curves for frequencies less than 0.01 Hz.

Figure 15 shows the apparent resistivity curves of the MT site MT025 obtained from the original data and processed using the EMD cepstral methods. Figures 15A, C represent the Rxy direction, while Figures 15B, D represent the Ryx direction. In Figure 15C, the overall smoothness of the blue apparent resistivity curve is poor, which represents the original data, and the overall continuity of the resistivity curve shape is also poor. There are significant variations

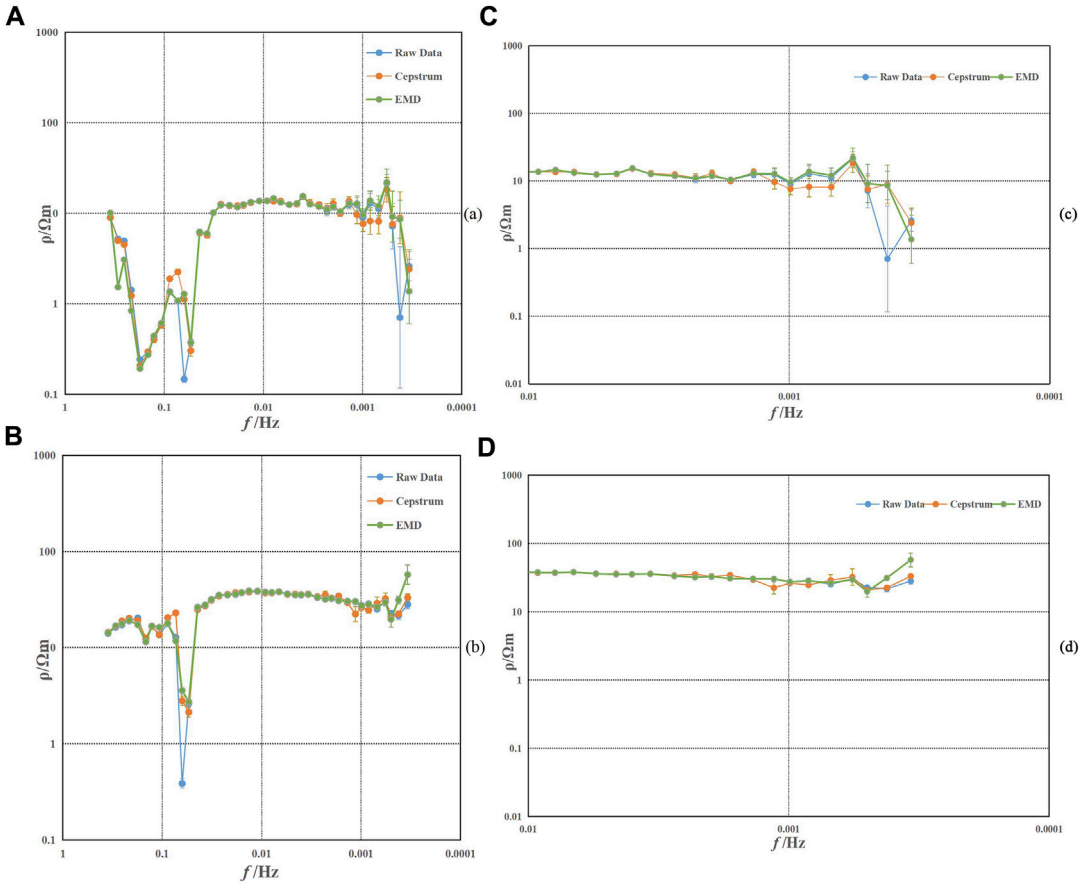

FIGURE 14
Apparent resistivity curve of site MT086. **(A)** Rxy; **(B)** Ryx; **(C)** part of Rxy; and **(D)** part of Ryx.

in resistivity in the low-frequency range. The resistivity curve appears relatively smooth within the frequency range of 0.01–0.001 Hz. However, in the frequency range of 0.001–0.0005 Hz, data from approximately four frequency points are completely distorted. At approximately 0.0008 Hz, there is a rapid drop followed by an increase at approximately 0.0005 Hz. Because of noise interference, the time–frequency characteristics of this MT site fail to reflect the true typical subsurface features.

The yellow curve in Figure 15 represents the apparent resistivity curve obtained using the cepstral analysis method. The green curve represents the apparent resistivity curve obtained using the EMD method. Comparing the low-frequency range in Figure 15C, the EMD method shows little improvement at a few distorted frequency points. In contrast, the proposed method in this study shows more significant effects in the low-frequency range. It improves all four distorted frequency points at approximately 0.0006 Hz, although there is a slight performance decrease in the front part of the curve. Overall, the resulting apparent resistivity curve appears relatively smooth, with a reduction in error values at several significant fluctuation frequency points, resulting in relatively stable numerical values.

5 Conclusion and discussion

To apply cepstral analysis to the processing of MT data, this study selected three sets of field-collected MT data. The process of cepstral analysis involves homomorphic deconvolution of the data, transforming the multiplicative signal into an additive signal, and then separating the noise through filtering in the cepstral domain. The key to denoising is the selection of the truncation position and the choice of filtering. Choosing a truncation position that is too large may result in the loss of useful information, while selecting a position that is too small may not effectively suppress the noise. The selection of an appropriate filter depends on the characteristics of the data. The results of this study demonstrate that, compared to traditional methods such as robust and EMD, the proposed method in this study shows better performance in handling MT data. The processed apparent resistivity curves exhibit smoother and more continuous characteristics, particularly in the low-frequency range, where the quality of the curves is significantly improved with a substantial reduction in errors. Furthermore, this method has been introduced for the first time in the processing of MT data, offering a novel approach with clear physical significance and a simple pipeline, providing a new

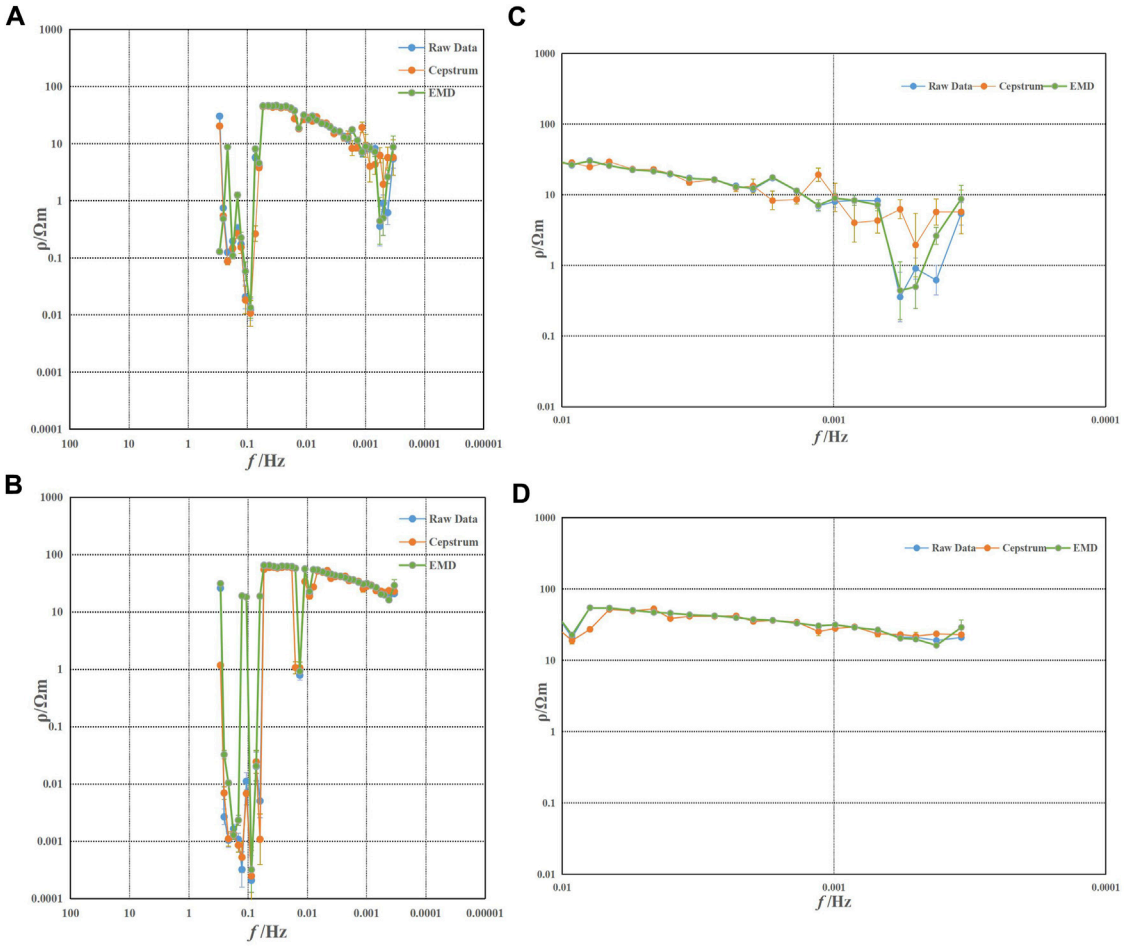

FIGURE 15
Apparent resistivity curve of site MT025. **(A)** Rxy; **(B)** Ryx; **(C)** part of Rxy; and **(D)** part of Ryx.

direction for future MT data processing. However, it also has limitations because the spectral envelope of the signal approaches that of the noise, which is not effective in successfully suppressing the noise. This method calculates the cepstrum based on the amplitude spectrum of the data, and the quality of the phase curve has not been significantly improved, leaving room for further improvement. The determination of the optimal truncation position still requires iterative experiments. Therefore, future research can explore the integration of adaptive algorithms to dynamically select the optimal truncation position based on the quality of the apparent resistivity and amplitude spectrum curves, further enhancing the data quality. Nonetheless, additional experimental validation and verification of this theory are required. It is crucial to process and invert a larger dataset of MT data to gain a more comprehensive understanding of the MT profiles and underground structures, which will be the focus of future work.

Data availability statement

The data analyzed in this study are subjected to the following licenses/restrictions: Group project. Requests to access these datasets should be directed to QZ, 292800073@qq.com.

Author contributions

All authors listed have made a substantial, direct, and intellectual contribution to the work and approved it for publication.

Conflict of interest

The authors declare that the research was conducted in the absence of any commercial or financial relationships that could be construed as a potential conflict of interest.

Publisher's note

References

Bogert, B. P. (1963). "The quefrency alanysis of time series for echoes: cepstrum, pseudoautocovariance, cross-cepstrum and saphe cracking," in *Proc. Symposium time series analysis* (Wuhan, China: Scientific Research Publishing), 209–243.

Cagniard, L. (1953). Basic theory of the magneto-telluric method of geophysical prospecting. *Geophysics* 18, 605–635. doi:10.1190/1.1437915

Cai, J.-H., Tang, J.-T., Hua, X.-R., and Gong, Y.-R. (2009). An analysis method for magnetotelluric data based on the Hilbert–Huang Transform. *Explor. Geophys.* 40, 197–205. doi:10.1071/eg08124

Cai, J. (2014). A combinatorial filtering method for magnetotelluric time-series based on Hilbert–Huang transform. *Explor. Geophys.* 45, 63–73. doi:10.1071/eg13012

Carbonari, R., D'Auria, L., Rosa Di Maio, and Petrillo, Z. (2017). Denoising of magnetotelluric signals by polarization analysis in the discrete wavelet domain. *Comput. Geosciences* 100, 135–141. doi:10.1016/j.cageo.2016.12.011

Chave, A. D., Thomson, D. J., and Ander, M. E. (1987). On the robust estimation of power spectra, coherences, and transfer functions. *J. Geophys. Res. Solid Earth* 92, 633–648. doi:10.1029/jb092ib01p00633

Chave, A. D., and Thomson, D. J. (1989). Some comments on magnetotelluric response function estimation. *J. Geophys. Res. Solid Earth* 94, 14215–14225. doi:10.1029/jb094ib10p14215

Chave, A. D. (2017). Estimation of the magnetotelluric response function: the path from robust estimation to a stable maximum likelihood estimator. *Surv. Geophys.* 38, 837–867. doi:10.1007/s10712-017-9422-6

Choi, Y.-C., and Kim, Y.-H. (2007). Fault detection in a ball bearing system using minimum variance cepstrum. *Meas. Sci. Technol.* 18, 1433–1440. doi:10.1088/0957-0233/18/5/031

Constable, S. C., Parker, R. L., and Constable, C. G. (1987). Occam's inversion: a practical algorithm for generating smooth models from electromagnetic sounding data. *Geophysics* 52, 289–300. doi:10.1190/1.1442303

Dong, S., Li, T., Chen, X., Wei, W., Gao, R., Lv, Q., et al. (2012). Progress of deep exploration in mainland China. *Chin. J. Geophys.* 55, 3884–3901. doi:10.6038/j.issn.0001-5733.2012.12.002

Egbert, G. D., and Booker, J. R. (1986). Robust estimation of geomagnetic transfer functions. *Geophys. J. Int.* 87, 173–194. doi:10.1111/j.1365-246x.1986.tb04552.x

Gamble, T. D., Goubau, W. M., and Clarke, J. (1979). Magnetotellurics with a remote magnetic reference. *Geophysics* 44, 53–68. doi:10.1190/1.1440923

Gangi, A. F., and Shapiro, J. N. (1979). A propagating algorithm for determining nth-order polynomial, least-squares fits; discussion and reply. *Geophysics* 44, 1588–1591.

Garcia, X., and Jones, A. G. (2008). Robust processing of magnetotelluric data in the AMT dead band using the continuous wavelet transform. *Geophysics* 73, F223–F234. doi:10.1190/1.2987375

Jing, J.-En, Wei, W.-Bo, Chen, H.-Y., and Jin, S. (2012). Magnetotelluric sounding data processing based on generalized S transformation. *Chin. J. Geophys.* 55, 4015–4022.

Kim, G.-S., Cho, G.-R., Jong-Nam, K., Yong-Chol, P., Sung-Hyon, Ri, and Hu, X.-Y. (2018). 'Constrained smoothness optimization of bootstrapped transfer functions for handling noisy MT data. *J. Appl. Geophys.* 155, 226–231. doi:10.1016/j.jappgeo.2018.05.018

Li, H., Zheng, H., and Tang, L. (2006a). Application of order cepstrum to bearing fault diagnosis. *J. Data Acquis. Process.* 21, 454–458.

Li, X. (2012). *Research on feature extraction and classification of ship noise and whale sound*. Harbin, China: Harbin Engineering University.

Li, Y., Sun, X., and Zhou, T. (2006b). Research on digital audio watermark bsaed on complex cepstrum transform. *Comput. Eng.* 32, 145–147.

Manoj, C., and Nagarajan, N. (2003). The application of artificial neural networks to magnetotelluric time-series analysis. *Geophys. J. Int.* 153, 409–423. doi:10.1046/j.1365-246x.2003.01902.x

Randall, R. B., and Sawalhi, N. (2011). A new method for separating discrete components from a signal. *Sound Vib.* 45, 6.

Ritter, O., Junge, A., and Dawes, G. J. K. (1998). New equipment and processing for magnetotelluric remote reference observations. *Geophys. J. Int.* 132, 535–548. doi:10.1046/j.1365-246x.1998.00440.x

Tang, J.-T., Jin, Li, Xiao, X., Zhang, L.-C., and Qing-Tian, L. V. (2012). Mathematical morphology filtering and noise suppression of magnetotelluric sounding data. *Chin. J. Geophys.* 55, 1784–1793.

Tikhonov, A. N. (1950). On determining electrical characteristics of the deep layers of the Earth's crust. *Dokl. Akad. Nauk. SSSR*, 295–297.

Trad, D. O., and Jandyr, M. (2000). Wavelet filtering of magnetotelluric data. *Geophysics* 65, 482–491. doi:10.1190/1.1444742

Wang, J.-ying (2004b). Discussion on the non-minimum phase of magnetotelluric signals. *Prog. Geophys.* | *Prog Geophys* 19, 216–221.

Wang, S., and Wang, J. (2004a). Application of higher-order statistics in magnetotelluric data processing. *Chin. J. Geophys.* 47, 1046–1053. doi:10.1002/cjg2.584

Wei, F., and Li, M. (2003). Cepstrum analysis of source character. *Acta Seismol. Sin.* 25, 47–54.

Wei, W.-Bo (2002). New advance and prospect of magnetotelluric sounding (MT) in China. *Prog. Geophys.* | *Prog Geophys* 17, 245–254.

Weidelt, P. (1972). 'The inverse problem of geomagnetic induction. *Z. Geophys.* 38, 257–289.

Xie, T., and Zheng, X. (2016). 'Seismic facies analysis based on linear prediction cepstrum coefficients. *Chin. J. Geophys.* 59, 4266–4277.

Zeng, Z., Li, Y., and Liu, X. (2011). Study on feature extraction of ship radiated noise based on higher order spectrum and cepstrum. *Comput. Simul.* 28, 5–9.

frontiers | Frontiers in Earth Science

TYPE Original Research
PUBLISHED 18 October 2023
DOI 10.3389/feart.2023.1183191

OPEN ACCESS

EDITED BY
Cong Zhou,
East China University of Technology, China

REVIEWED BY
Nian Yu,
Chongqing University, China
Bo Han,
China University of Geosciences Wuhan, China
Arkoprovo Biswas,
Banaras Hindu University, India

*CORRESPONDENCE
Guihang Shao,
shaoguihang@ouc.edu.cn

RECEIVED 09 March 2023
ACCEPTED 27 July 2023
PUBLISHED 18 October 2023

CITATION
Zhu Y, Shao G, Wang X and Zhang W (2023), A rapid 3D magnetotelluric forward approach for arbitrary anisotropic conductivities in the Fourier domain.
Front. Earth Sci. 11:1183191.
doi: 10.3389/feart.2023.1183191

A rapid 3D magnetotelluric forward approach for arbitrary anisotropic conductivities in the Fourier domain

Yuzhen Zhu[1], Guihang Shao[1,2]*, Xiudong Wang[1] and Wenyan Zhang[1]

[1]Shandong Provincial Research Institute of Coal Geology Planning and Exploration, Jinan, China, [2]College of Marine Geosciences, Ocean University of China, Qingdao, China

Previous studies have shown that anisotropy generally exists in geological bodies such as sedimentary rocks and fault zones, and more and more attention has been paid to the arbitrary conductivity media in surveys with the magnetotelluric sounding method. With the breakthrough development of computer hardware technology, large-scale 3D magnetotelluric modeling in anisotropic media has gradually become possible. At present, there are 3D magnetotelluric field simulation algorithms based on finite differences or finite elements for arbitrary anisotropic conductivity. In order to solve the common computational efficiency problems of the existing algorithms, we proposed a rapid 3D magnetotelluric forward approach for arbitrary anisotropic conductivity in the Fourier domain. Through the 2D Fourier transform, the governing equation can be converted from the space domain to the Fourier domain, thereby greatly reducing the calculation amount of the numerical simulation and improving the calculation efficiency. Then, the classical 1D anisotropy model is used to verify the correctness and the computational efficiency. Finally, the 3D anisotropic models of land and ocean are calculated, and the influence characteristics of the anisotropic medium on the magnetotelluric response are analyzed. The proposed algorithm will be used in the inverse imaging technique for large-scale 3D anisotropic data in future studies.

KEYWORDS

Fourier domain, 3D modeling, anisotropic conductivity, magnetotelluric, parallel algorithm

1 Introduction

Since its establishment in the 1950s, the magnetotelluric (MT) method has gradually become an important geophysical prospecting method after 70 years of development. The MT method uses the natural variable electromagnetic field as the field source and finally obtains the underground electrical structure through qualitative analysis or inverse interpretation of the transfer function of the induced electromagnetic field. It is well known that the conductivity of subsurface media often exhibits anisotropy. Laboratory observations and studies have shown that gneiss and other types of rocks have significant electrical conductivity anisotropy (Parkhomenko, 1967; Keller, 1982; Andréa and Li, 2022; Li et al., 2022; Yin et al., 2022). During the development of magnetotellurics, the research on anisotropy included all aspects of data analysis, forward modeling, and inversion. The early simulation of anisotropy mainly used analytical solutions to solve 1D models (Kovacikova

and Pek, 2002; Pek and Santos, 2002; Okazaki et al., 2016), but due to its narrow application range, it was gradually replaced by numerical simulation methods.

With the improvement in the performance of computing equipment and the improvement in computing methods, researchers have successively carried out the simulation of 3D anisotropic magnetotelluric field (Liu et al., 2018; Yu et al., 2018; Rivera-Rios et al., 2019; Xiao et al., 2019; Guo et al., 2020; Ye et al., 2021; Zhou et al., 2021; Luo et al., 2022; Li et al., 2023). At present, the 3D electromagnetic numerical simulation methods mainly include the integral equation method (IEM), the finite difference method (FDM), the finite volume method (FVM), and the finite element method (FEM). The integral equation method only discretizes the anomalous body region, so the dimension of the obtained linear equations is small. In the early stage of electromagnetic calculation, due to the limitation of computer memory and calculation speed, the integral equation method was only widely used in the calculation of a simple 3D geoelectric model. The finite difference method is a numerical simulation method that was earlier applied to the calculation of electromagnetic fields. Saraf et al. (1986) used the finite-difference method to realize the numerical simulation of the TM mode of the magnetotelluric structure with perpendicular anisotropy. Pek and Verner (1997) implemented a 2D magnetotelluric numerical algorithm for arbitrary anisotropic media based on the finite difference method and analyzed the magnetotelluric response characteristics in a specific anisotropic model. Han et al. (2018) implemented a 3D arbitrary anisotropic magnetotelluric forward algorithm based on the finite difference method and analyzed the influence of inclined anisotropic blocks on the magnetotelluric field. Yu et al. (2018) also implemented a 3D arbitrary anisotropic magnetotelluric forward algorithm based on finite differences and analyzed the influence of a specific 3D model on the magnetotelluric phase. The finite volume method is similar to the finite difference method. The grid of the finite volume method can be a regular grid or an irregular grid. Because of this property, the finite volume method is widely used in the calculation of fluid mechanics. However, the finite volume method is not as widely used in electromagnetic calculations as other numerical methods. The finite element method can simulate complex terrain and has received more and more attention in recent years. Reddy and Rankin (1975) implemented a 2D anisotropic magnetotelluric forward algorithm with three principal axis conductivities and a strike angle based on the finite element method. Li (2002) implemented a 2D magnetotelluric forward algorithm for arbitrary anisotropic media based on the finite element method. Li and Pek (2008) added adaptive unstructured mesh technology to the 2D anisotropic finite element numerical solution algorithm, which improved the calculation accuracy and efficiency. Cao et al. (2018) realized the magnetotelluric forward algorithm of the 3D anisotropic model based on the adaptive finite element. Xiao et al. (2019) derived the finite element equations of 3D anisotropic media by using vector potential functions and realized the forward algorithm. Zhou et al. (2021) integrated divergence correction technology into the numerical simulation of magnetotelluric 3D anisotropic vector finite element, which improved the iterative solution accuracy of linear equations.

However, since 3D calculation involves the solution of large linear equations, the increase in unknowns of anisotropic media increases the scale of linear equations, resulting in the problems of large calculation and time consumption in a 3D anisotropic numerical simulation. Most research on the 3D anisotropic forward modeling algorithm is only to achieve corresponding numerical simulation, and there is a lack of algorithm research aimed at improving the efficiency of forward modeling. The spatial wavenumber mixed domain simulation method based on vector potential is a newly proposed simulation method, which has been applied in gravity, magnetic, and control source electromagnetic methods (Dai et al., 2018; Dai et al., 2019a; Dai et al., 2019b; Dai et al., 2021; Dai et al., 2022); these works of research show that using this method can effectively reduce the computing memory and computation time. In this paper, a Fourier domain simulation method is used for 3D anisotropic magnetotelluric simulation. First, the Coulomb gauge is used to transform the anisotropic electromagnetic field equations into vector and scalar governing equations. The 3D partial differential equation in the space domain is transformed into a 1D ordinary differential equation in the Fourier domain by using the 2D Fourier transform. Then, the Galerkin method is used to transform the Fourier domain equations into finite element equations and the Chase method is used to solve the equations. Finally, the 2D Fourier inverse transform is performed on the solution in the Fourier domain to obtain the electromagnetic fields in the space domain. This method transforms the space domain equation into the Fourier domain, reduces the solution dimension, and improves the calculation efficiency. The proposed algorithm can be used for other electromagnetic methods for anisotropic media in future studies.

2 Basic theory

2.1 Frequency domain Maxwell's equations in anisotropic media

In the frequency domain, assuming that the time constant is $e^{-i\omega t}$, the electromagnetic field in the conductivity anisotropic medium satisfies the following Maxwell equations (Weiss and Newman, 2000):

$$\nabla\times \mathbf{E} = i\omega\mu_0\mathbf{H} \tag{1}$$

$$\nabla\times \mathbf{H} = (\boldsymbol{\sigma} - i\omega\varepsilon)\mathbf{E} \tag{2}$$

In formulas 1–2, ω is the angular frequency, i is the imaginary number unit, μ_0 is the magnetic permeability in a vacuum, $\boldsymbol{\sigma}$ is any anisotropic conductivity tensor, ε is the permittivity, $\mathbf{E}$ is the electric field strength, and $\mathbf{H}$ is the magnetic field strength. $\mathbf{B} = \mu_0\mathbf{H}$ is the magnetic induction intensity, and it is described by the relationship between magnetic permeability and magnetic field strength $\mathbf{H}$. For the natural low-frequency electromagnetic field (10^{-3}~10^{4} Hz) studied in this paper, the displacement current term can be ignored. Among them, any 3×3 anisotropic conductivity tensor can be expressed as follows:

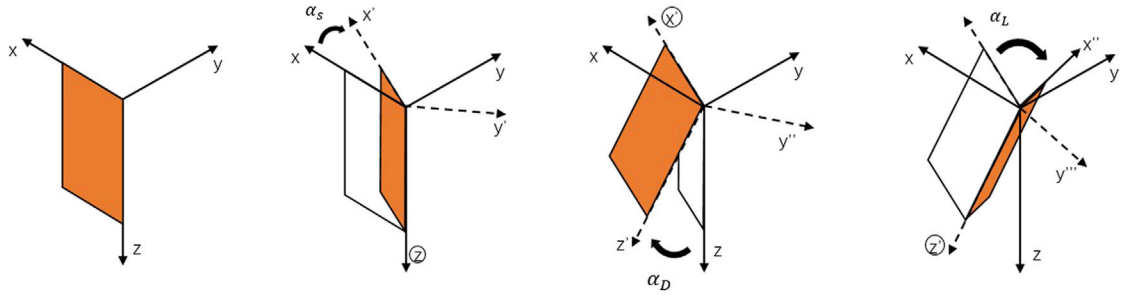

FIGURE 1
Schematic diagram of Euler rotation (Pek and Santos, 2002).

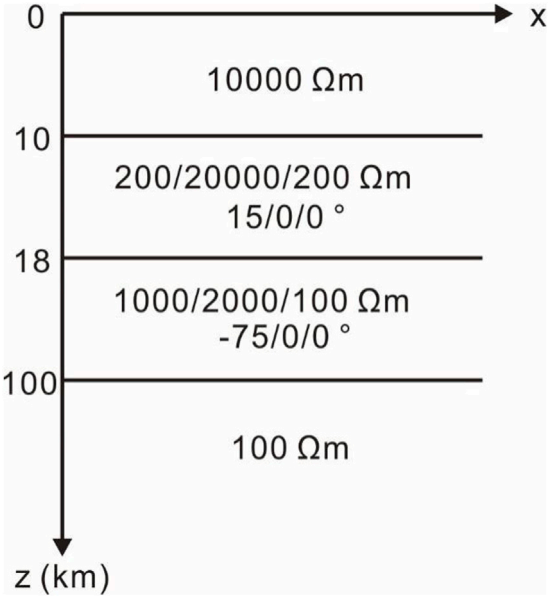

FIGURE 2
Schematic diagram of the 1D model.

$$\boldsymbol{\sigma} = \begin{bmatrix} \sigma_{xx} & \sigma_{xy} & \sigma_{xz} \\ \sigma_{yx} & \sigma_{yy} & \sigma_{yz} \\ \sigma_{zx} & \sigma_{zy} & \sigma_{zz} \end{bmatrix} \tag{3}$$

In the actual formation medium, these two tensors can be rotated to establish the relationship with the main coordinate axis. For the conductivity tensor, here are three main coordinate axes conductivity σ_x, σ_y, σ_z, and anisotropy strike angle (α_s), anisotropy dip angle (α_d), and anisotropy deflection angle (α_l) represent.

$$\boldsymbol{\sigma} = \begin{bmatrix} \sigma_{xx} & \sigma_{xy} & \sigma_{xz} \\ \sigma_{yx} & \sigma_{yy} & \sigma_{yz} \\ \sigma_{zx} & \sigma_{zy} & \sigma_{zz} \end{bmatrix} = R_s^T R_d^T R_l^T \begin{bmatrix} \sigma_x & 0 & 0 \\ 0 & \sigma_y & 0 \\ 0 & 0 & \sigma_z \end{bmatrix} R_l R_d R_s \tag{4}$$

where,

$$R_s = \begin{bmatrix} \cos\alpha_s & \sin\alpha_s & 0 \\ -\sin\alpha_s & \cos\alpha_s & 0 \\ 0 & 0 & 0 \end{bmatrix} \tag{5}$$

$$R_d = \begin{bmatrix} \cos\alpha_d & 0 & \sin\alpha_d \\ 0 & 0 & 0 \\ -\sin\alpha_d & 0 & \cos\alpha_d \end{bmatrix} \tag{6}$$

$$R_l = \begin{bmatrix} 0 & 0 & 0 \\ 0 & \cos\alpha_l & \sin\alpha_l \\ 0 & -\sin\alpha_l & \cos\alpha_l \end{bmatrix} \tag{7}$$

In Eqs 5–7, α_s, α_d and α_l, are three Euler rotation angles (Pek and Santos, 2002). Any anisotropic conductivity can be obtained from the principal axis conductivity in the x, y, and z directions, and by Euler rotation, transformation is obtained, as shown in Figure 1.

2.2 Vector-scalar-position governing equations based on coulomb gauge

According to the relationship between magnetic vector potential and electric scalar potential (Biro and Preis, 1989)

$$\mathbf{B} = \nabla\times \mathbf{A} \tag{8}$$

$$\mathbf{E} = \mathrm{i}\omega\mathbf{A} - \nabla\Phi \tag{9}$$

Substituting Eqs 8–9 into Eqs 1–2, and introducing the vector identity $\nabla\times(\nabla\times\mathbf{A}) = \nabla(\nabla\cdot\mathbf{A}) - \nabla^2\mathbf{A}$ and the Coulomb gauge $\nabla\cdot\mathbf{A} = 0$ (Everett and Schultz, 1996), we can get the coupled equations of vector potential and scalar potential equations (LaBrecque et al., 1999; Haber et al., 2000; Varilsuha and Candansayar, 2018)

$$\begin{cases} \nabla^2\mathbf{A} + \boldsymbol{k}^2\mathbf{A} - \mu_0\boldsymbol{\sigma}\nabla\Phi = 0 \\ \nabla\cdot(\boldsymbol{\sigma}\nabla\Phi) - \mathrm{i}\omega\nabla\cdot(\boldsymbol{\sigma}\mathbf{A}) = 0 \end{cases} \tag{10}$$

The equations are relatively complete in theory, and the physical meaning is relatively clear, and at this time, the vector position and the scalar position have unique solutions.

Vector potential and scalar potential based on the Coulomb gauge are expressed as

$$\begin{cases} \mathbf{A} = \mathbf{A^p} + \mathbf{A^s} \\ \Phi = \Phi^{\mathbf{p}} + \Phi^{\mathbf{s}} \end{cases} \tag{11}$$

where $\mathbf{A^p}$, $\mathbf{A^s}$ are the vector potential of the primary field and the vector potential of the secondary field, and $\Phi^{\mathbf{p}}$, $\Phi^{\mathbf{s}}$ are the scalar

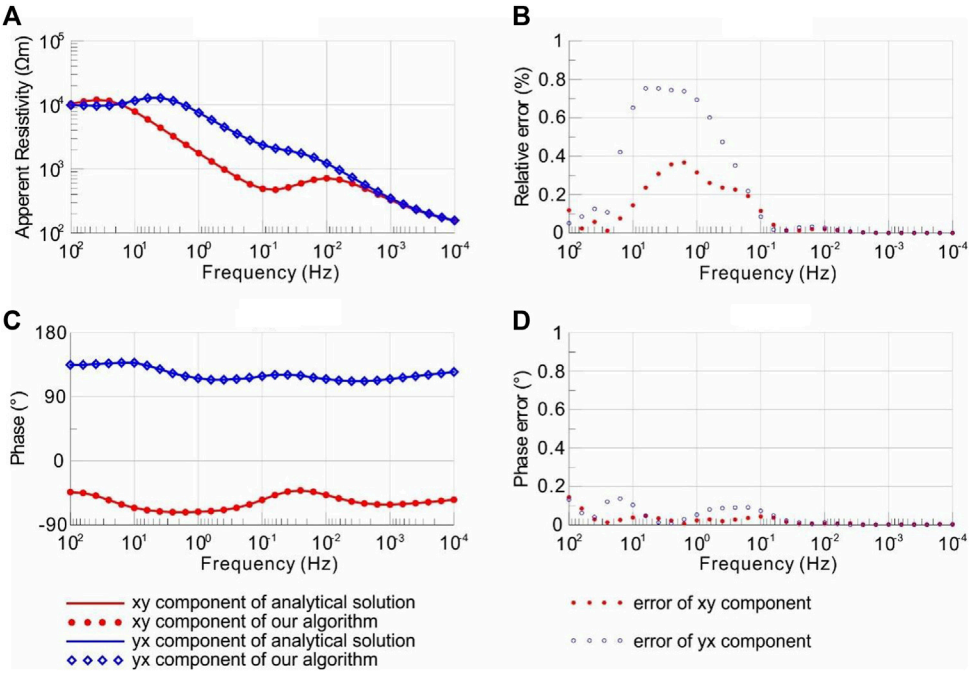

FIGURE 3
Comparison of apparent resistivity and phase calculation results. **(A)** Apparent resistivity, **(B)** phase, **(C)** relative error of apparent resistivity, and **(D)** error of phase.

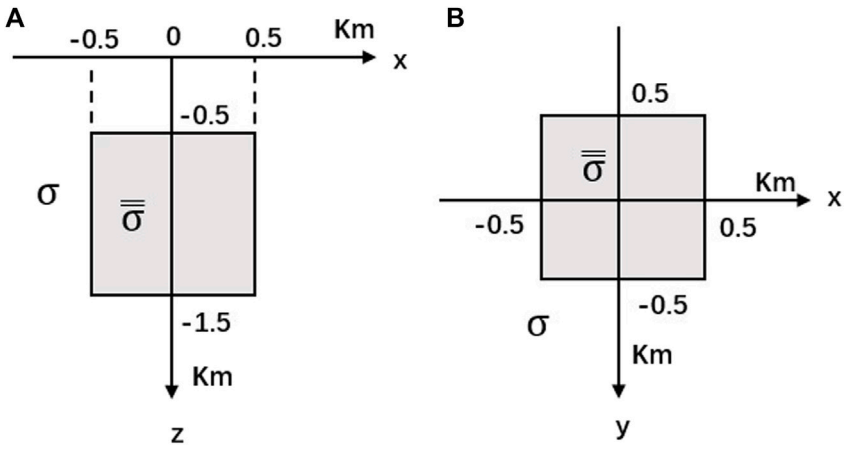

FIGURE 4
3D land anisotropy model: **(A)** section view along the x-axis and **(B)** plan view.

potential of the primary field and the scalar potential of the secondary field, respectively.

$$\begin{cases} \boldsymbol{k}^2 = \boldsymbol{k}_p^2 + \boldsymbol{k}_s^2 \\ \boldsymbol{\sigma} = \boldsymbol{\sigma}_p + \boldsymbol{\sigma}_s \end{cases} \tag{12}$$

where $\boldsymbol{k}_p^2$ is the product of the admittance tensor and resistivity corresponding to the primary field, $\boldsymbol{\sigma}_p$ is the conductivity tensor corresponding to the primary field, $\boldsymbol{k}_s^2$ is the product of the admittance tensor and resistivity corresponding to the secondary field and $\boldsymbol{\sigma}_s$ is the conductivity corresponding to the secondary field rate tensor. According to the principle of superposition, the coupling equations satisfied by the secondary field vector potential and scalar potential are

$$\begin{cases} \nabla^2 \mathbf{A}^s + \boldsymbol{k}_p^2 \mathbf{A}^s - \mu_0 \boldsymbol{\sigma}_p \nabla \Phi^s = -\mu_0 \boldsymbol{\sigma}_s \mathbf{E} \\ \nabla \cdot \left(\boldsymbol{\sigma}_p \nabla \Phi^s \right) - \mathrm{i}\omega \nabla \cdot \left(\boldsymbol{\sigma}_p \mathbf{A}^s \right) = \nabla \cdot \left(\boldsymbol{\sigma}_s \mathbf{E} \right) \end{cases} \tag{13}$$

Many scholars (Haber et al., 2000; Badea et al., 2001; Jahandari and Farquharson, 2015) used numerical methods to solve the above Eq. 10 or (13) and achieved good results. However, the conventional numerical methods require a large

TABLE 1 The comparison of the memory and time obtained with the five algorithms.

Algorithm	Mesh Num.	Degrees of freedom	Calculation area (km^3)	Memory (GB)	Time cost s)
SFE	463680	1391040	57.2 × 56.8 × 40	51.3	561
SFE1E	338336	1015008	6 × 6 × 4	29.3	255
TFE	463680	1391040	57.2 × 56.8 × 40	51.2	549
TFETE	338336	1015008	6 × 6 × 4	33.3	263
MSWD	**9895936**	**39583744**	**57.2 × 56.8 × 40**	**14**	**45**
MSWD	**338336**	**1353344**	**6 × 6 × 4**	**4.1**	**11**

It can be seen from Table 1 that the algorithm in this paper (MSWD), which is marked by bold values, cost less computing memory and time.

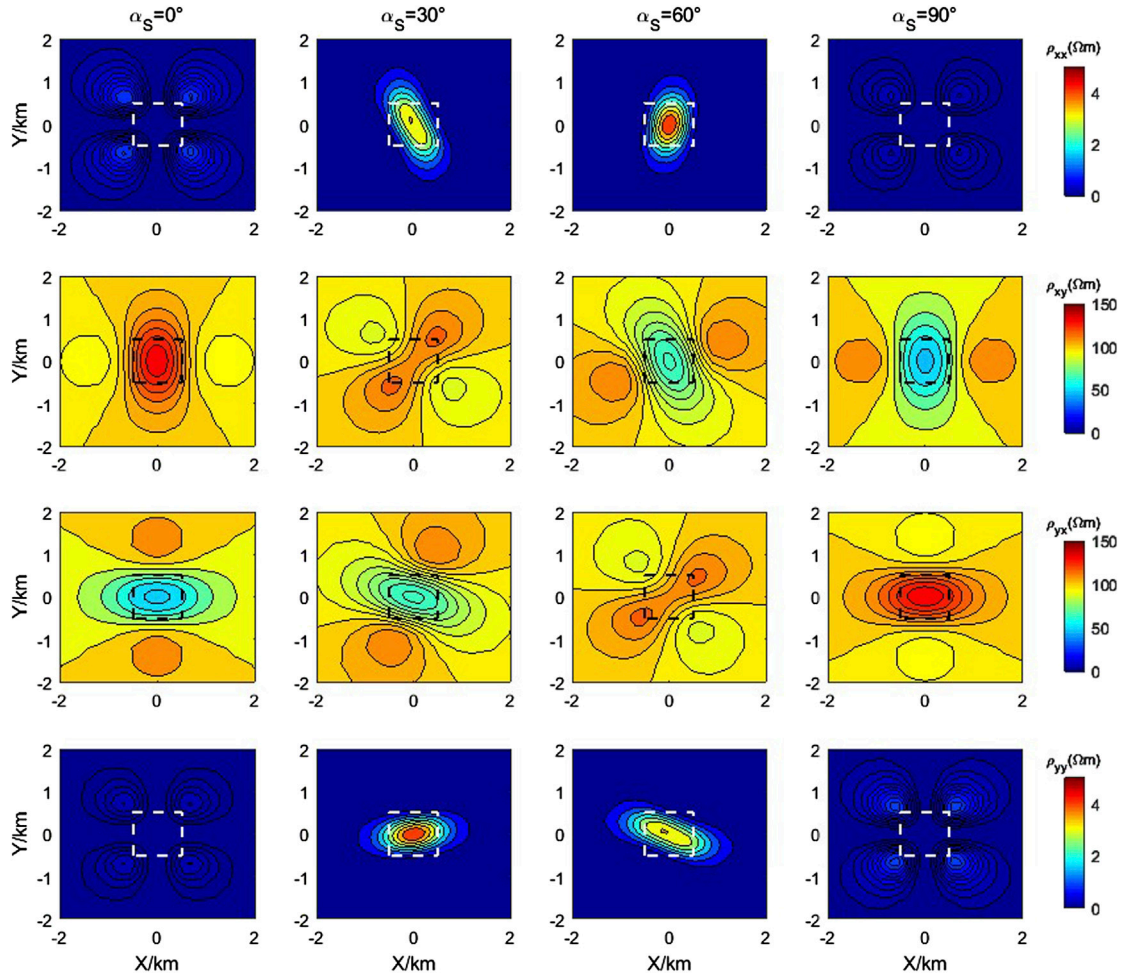

FIGURE 5
Apparent resistivity plan at different strike angles at 0.1Hz.

amount of calculation and storage due to the large sparse matrix linear equations (Varilsuha and Candansayar, 2018), especially for any anisotropic medium. In order to decrease the computation and storage load, how to solve the governing equations of vector potential and scalar potential is particularly important. This paper intends to use a rapid 3D numerical simulation method in the Fourier domain (Dai et al., 2022), and this method performs a 2D Fourier transform of Equation 13 along the horizontal directions, a 3D partial differential equation in the space domain is transformed into multiple 1D coupled ordinary differential equations in the Fourier domain, and the coupling between different wave

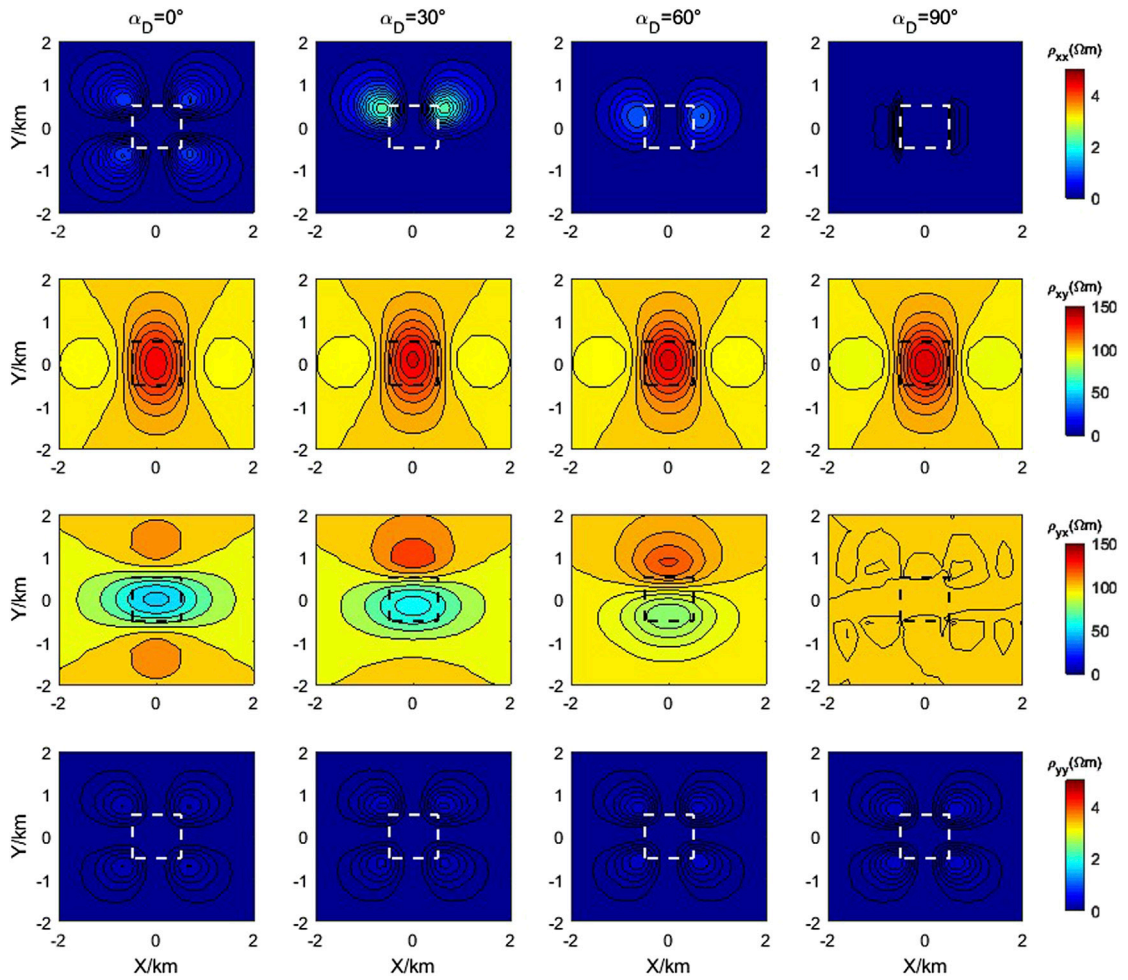

FIGURE 6
Apparent resistivity plan at different angles α_D at 0.1Hz.

numbers' ordinary differential equations are independent of each other and have a high degree of parallelism.

2.3 Vector and scalar potential ordinary differential equation in fourier domain

We wrote formula (13) in component form and expanded

$$\begin{cases} \dfrac{\partial^2 A_x^s}{\partial x^2}+\dfrac{\partial^2 A_x^s}{\partial y^2}+\dfrac{\partial^2 A_x^s}{\partial z^2}+\boldsymbol{k}_p^2 A_x^s-\mu_0\hat{\boldsymbol{y}}_p\dfrac{\partial \Phi^s}{\partial x}=-\mu_0\boldsymbol{j}_x^s \\ \dfrac{\partial^2 A_y^s}{\partial x^2}+\dfrac{\partial^2 A_y^s}{\partial y^2}+\dfrac{\partial^2 A_y^s}{\partial z^2}+\boldsymbol{k}_p^2 A_y^s-\mu_0\hat{\boldsymbol{y}}_p\dfrac{\partial \Phi^s}{\partial y}=-\mu_0\boldsymbol{j}_y^s \\ \dfrac{\partial^2 A_z^s}{\partial x^2}+\dfrac{\partial^2 A_z^s}{\partial y^2}+\dfrac{\partial^2 A_z^s}{\partial z^2}+\boldsymbol{k}_p^2 A_z^s-\mu_0\hat{\boldsymbol{y}}_p\dfrac{\partial \Phi^s}{\partial z}=-\mu_0\boldsymbol{j}_z^s \\ \hat{\boldsymbol{y}}_p\left(\dfrac{\partial^2 \Phi^s}{\partial x^2}+\dfrac{\partial^2 \Phi^s}{\partial y^2}+\dfrac{\partial^2 \Phi^s}{\partial z^2}\right)+\dfrac{\partial \Phi^s}{\partial z}\dfrac{\partial \hat{\boldsymbol{y}}_p}{\partial z}-\mathrm{i}\omega A_z^s\dfrac{\partial \hat{\boldsymbol{y}}_p}{\partial z} \\ =\dfrac{\partial \boldsymbol{j}_x^s}{\partial x}+\dfrac{\partial \boldsymbol{j}_y^s}{\partial y}+\dfrac{\partial \boldsymbol{j}_z^s}{\partial z} \end{cases} \tag{14}$$

where A_x^s, A_y^s and A_z^s are the three components of the secondary field vector potential, $\boldsymbol{j}_x^s=\hat{\boldsymbol{y}}_s E_x^0$, $\boldsymbol{j}_y^s=\hat{\boldsymbol{y}}_s E_y^0$, $\boldsymbol{j}_z^s=\hat{\boldsymbol{y}}_s E_z^0$ are the current density tensors, and E_x^0, E_y^0 and E_z^0 are the background fields.

For formula (14), a 2D Fourier transform is used along the x and y direction

$$\begin{cases} \dfrac{\partial^2 \tilde{A}_x^s}{\partial z^2}+\left(\boldsymbol{k}_p^2-k_x^2-k_y^2\right)\tilde{A}_x^s+\mathrm{i}k_x\mu_0\hat{\boldsymbol{y}}_p\tilde{\Phi}^s=-\mu_0\tilde{\boldsymbol{j}}_x^s \\ \dfrac{\partial^2 \tilde{A}_y^s}{\partial z^2}+\left(\boldsymbol{k}_p^2-k_x^2-k_y^2\right)\tilde{A}_y^s+\mathrm{i}k_y\mu_0\hat{\boldsymbol{y}}_p\tilde{\Phi}^s=-\mu_0\tilde{\boldsymbol{j}}_y^s \\ \dfrac{\partial^2 \tilde{A}_z^s}{\partial z^2}+\left(\boldsymbol{k}_p^2-k_x^2-k_y^2\right)\tilde{A}_z^s-\hat{\boldsymbol{y}}_p\mu_0\dfrac{\partial \tilde{\Phi}^s}{\partial z}=-\mu_0\tilde{\boldsymbol{j}}_z^s \\ \left(\hat{\boldsymbol{y}}_p\dfrac{\partial^2 \tilde{\Phi}^s}{\partial z^2}+\dfrac{\partial \hat{\boldsymbol{y}}_p}{\partial z}\dfrac{\partial \tilde{\Phi}^s}{\partial z}-\hat{\boldsymbol{y}}_p\left(k_x^2+k_y^2\right)\tilde{\Phi}^s\right)+ \\ \mathrm{i}\omega\left(\mathrm{i}k_x\hat{\boldsymbol{y}}_p\tilde{A}_x^s+\mathrm{i}k_y\hat{\boldsymbol{y}}_p A_y^s-\hat{\boldsymbol{y}}_p\dfrac{\partial \tilde{A}_z^s}{\partial z}\right)-\mathrm{i}\omega\tilde{A}_z^s\dfrac{\partial \hat{\boldsymbol{y}}_p}{\partial z} \\ =-\mathrm{i}k_x\tilde{\boldsymbol{j}}_x^s-\mathrm{i}k_y\tilde{\boldsymbol{j}}_y^s+\dfrac{\partial \tilde{\boldsymbol{j}}_z^s}{\partial z} \end{cases} \tag{15}$$

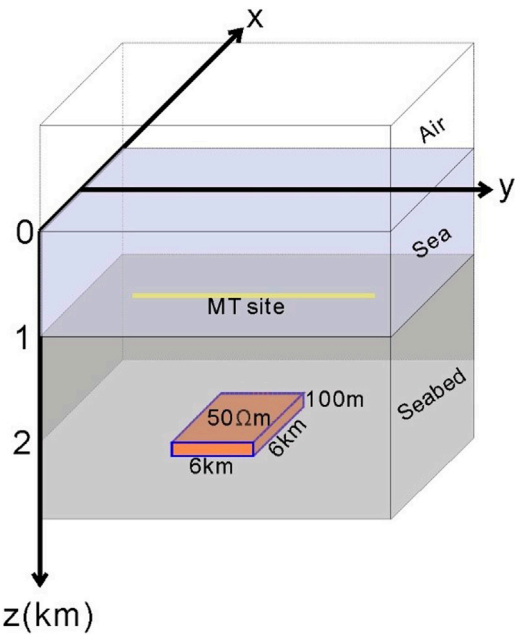

FIGURE 7
Schematic diagram of 3D anisotropic ocean model.

where k_x and k_y are the wavenumbers in the space wavenumber domain, $\tilde{A}_x^s$, $\tilde{A}_y^s$ and $\tilde{A}_z^s$ are the three components of the secondary field vector potential in the Fourier domain, and $\tilde{\Phi}^s$ are the secondary field scalar potential in the Fourier domain, $\tilde{j}_x^s$, $\tilde{j}_y^s$ and $\tilde{j}_z^s$ are the current densities in the Fourier domain, respectively.

Using a 2D Fourier transform to transform the 3D partial differential coupling Eq. 14 into 1D ordinary differential coupling Eq. 15, thus decomposing a super-large-scale problem into multiple small problems and greatly reducing the anisotropy Medium simulation requires computing time and storage, and the ordinary differential equations between different wave numbers are independent of each other, which has a high degree of parallelism.

2.4 Boundary conditions

In a homogeneous medium, according to the Helmholtz equation and the Coulomb gauge $\nabla \cdot \mathbf{A} = 0$ satisfied by the electric field vector $\mathbf{E}$, combined with the relationship between the vector potential $\mathbf{A}$, the scalar potential Φ and the electromagnetic field, and the lower and upper boundary conditions of the vector potential $\tilde{\mathbf{A}}$, scalar potential $\tilde{\Phi}$ in the Fourier domain can be obtained

$$\begin{cases} \dfrac{\partial \tilde{A}_x^s}{\partial z} = -s\tilde{A}_x^s + \dfrac{(t-s)}{\omega}k_x\tilde{\Phi}^s \\ \dfrac{\partial \tilde{A}_y^s}{\partial z} = -s\tilde{A}_y^s + \dfrac{(t-s)}{\omega}k_y\tilde{\Phi}^s \\ \dfrac{\partial \tilde{A}_z^s}{\partial z} = \mathrm{i}k_x\tilde{A}_x^s + \mathrm{i}k_y\tilde{A}_y^s \\ \dfrac{\partial \tilde{\Phi}^s}{\partial z} = -t\tilde{\Phi}^s \end{cases} \tag{16}$$

$$\begin{cases} \dfrac{\partial \tilde{A}_x^s}{\partial z} = s\tilde{A}_x^s - \mathrm{i}k_x\tilde{A}_z^s + \dfrac{sk_x\tilde{\Phi}^s}{\omega} \\ \dfrac{\partial \tilde{A}_y^s}{\partial z} = s\tilde{A}_y^s - \mathrm{i}k_y\tilde{A}_z^s + \dfrac{sk_y\tilde{\Phi}^s}{\omega} \\ \dfrac{\partial \tilde{A}_z^s}{\partial z} = \mathrm{i}k_x\tilde{A}_x^s + \mathrm{i}k_y\tilde{A}_y^s \\ \dfrac{\partial \tilde{\Phi}^s}{\partial z} = \mathrm{i}\omega\tilde{A}_z^s \end{cases} \tag{17}$$

2.5 Finite element method

Eq. 15 is the coupled ordinary differential equation satisfied by the vector and scalar potentials in the Fourier domain, and Eqs 16, 17 are the lower and upper boundary conditions, respectively. For Eqs 15–17 boundary value problems, this paper intends to use the one-dimensional finite element method based on quadratic interpolation

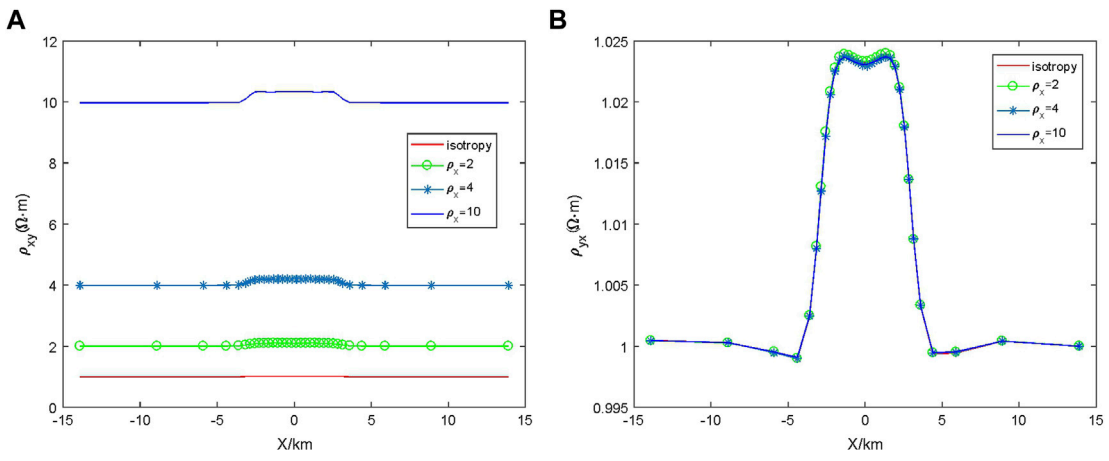

FIGURE 8
Effect of ρ_x on apparent resistivity: **(A)** xy component and **(B)** yx component.

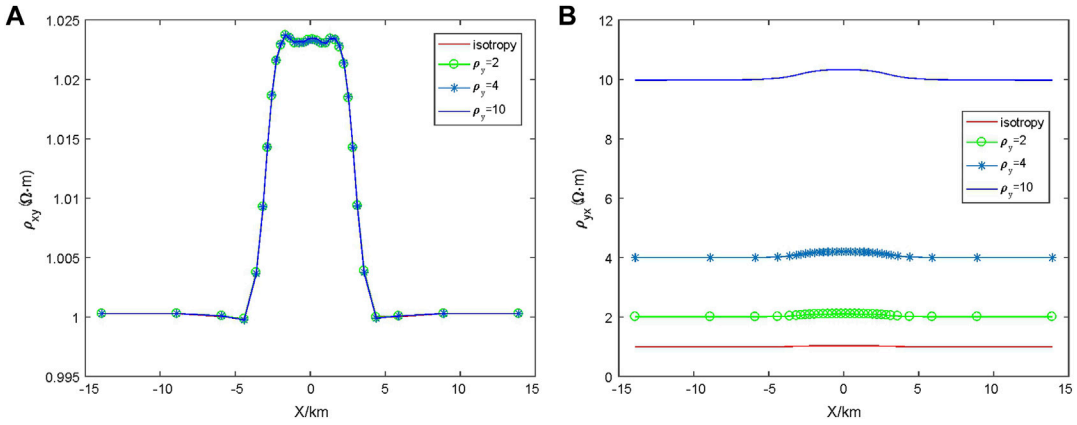

FIGURE 9
Effect of ρ_y on apparent resistivity: **(A)** xy component and **(B)** yx component.

to solve them. Using the Galerkin method to transform the boundary value problem of Eqs 15–17 into finite element equations

$$\begin{cases}
\sum_{e=1}^{Ne}\int_e\left(-\frac{\partial\tilde{A}_x^s}{\partial z}\frac{\partial N_i}{\partial z}+\left(k_p^2-k_x^2-k_y^2\right)N_i\tilde{A}_x^s+\mathrm{i}k_x\mu_0\sigma_pN_i\tilde{\Phi}^s+N_i\mu_0\tilde{j}_x^s\right)\mathrm{d}z\\
+\sum_{e=1}^{Ne}\int_s N_i\frac{\partial\tilde{A}_x^s}{\partial z}n_z\mathrm{d}z=0\\
\sum_{e=1}^{Ne}\int_e\left(-\frac{\partial\tilde{A}_y^s}{\partial z}\frac{\partial N_i}{\partial z}+\left(k_p^2-k_x^2-k_y^2\right)N_i\tilde{A}_y^s+\mathrm{i}k_y\mu_0\sigma_pN_i\tilde{\Phi}^s+N_i\mu_0\tilde{j}_y^s\right)\mathrm{d}z\\
+\sum_{e=1}^{Ne}\int_s N_i\frac{\partial\tilde{A}_y^s}{\partial z}n_z\mathrm{d}z=0\\
\sum_{e=1}^{Ne}\int_e\left(-\frac{\partial\tilde{A}_z^s}{\partial z}\frac{\partial N_i}{\partial z}+\left(k_p^2-k_x^2-k_y^2\right)N_i\tilde{A}_z^s-\mu_0\sigma_pN_i\frac{\partial\tilde{\Phi}^s}{\partial z}+N_i\mu_0\tilde{j}_z^s\right)\mathrm{d}z\\
+\sum_{e=1}^{Ne}\int_s N_i\frac{\partial\tilde{A}_z^s}{\partial z}n_z\mathrm{d}z=0\\
\sum_{e=1}^{Ne}\int_e\left(-\sigma_p\frac{\partial\tilde{\Phi}^s}{\partial z}\frac{\partial N_i}{\partial z}+N_i\frac{\partial\hat{y}_p}{\partial z}\frac{\partial\tilde{\Phi}^s}{\partial z}-\sigma_p\left(k_x^2+k_y^2\right)N_i\tilde{\Phi}^s\right)\mathrm{d}z+\\
\sum_{e=1}^{Ne}\int_e\left(-\mathrm{i}\omega N_i\frac{\partial\hat{y}_p}{\partial z}\tilde{A}_z^s+\mathrm{i}k_xN_i\tilde{j}_x^s+\mathrm{i}k_yN_i\tilde{j}_y^s-N_i\frac{\partial\tilde{j}_z^s}{\partial z}\right)\mathrm{d}z+\\
\sum_{e=1}^{Ne}\int_s\sigma_pN_i\frac{\partial\tilde{\Phi}^s}{\partial z}n_z\mathrm{d}z=0
\end{cases}\tag{18}$$

where Ne is the number of vertical unit subdivisions, $N_i\,(i=j,p,m)$ is the quadratic interpolation function of the eth unit and the ith node (Xu, 1994). For Eq. 18, there are mainly seven types of integrals (Dai et al., 2022); the overall synthesis of each unit integral can be obtained as a diagonal equation system with a bandwidth of 23

$$\mathbf{Ku}=\mathbf{P}\tag{19}$$

where $\mathbf{K}$ is a 23-diagonal matrix, $\mathbf{P}$ is the source term, and $\mathbf{u}$ is the Fourier domain vector and scalar potential to be obtained. Linear Eq. 19 can be quickly solved using the chasing method. The numerical simulation method adopted in this paper transforms the 3D problem into multiple independent 1D problems, which fundamentally change the characteristics and solution methods of the governing equation. Compared with the iterative solution method and the direct solution method, the pursuit method has the advantage of solving ordinary differential equations; its high parallelism greatly reduces the simulation time and memory consumption.

The other components of the electromagnetic field in the Fourier domain can be obtained through the relationship between the magnetic vector potential and the electric scalar potential and the electromagnetic field (8)~(9). The electromagnetic field in the space domain can be obtained by the 2D inverse Fourier transform of the electromagnetic field in the Fourier domain (Dai et al., 2022).

2.6 Compact operator iteration scheme

For the above formula (18), the solution obtained by the finite element method is the Born approximate solution, and it is difficult to achieve stable convergence or even divergence by direct iteration. For the convergence problem, here, the scalar iteration format for stable convergence in isotropic media is extended as tensor form (Gao, 2005; Dai et al., 2022).

$$\mathbf{E}^{(n)}=\boldsymbol{\alpha}\mathbf{E}^{(n)}+\boldsymbol{\beta}\mathbf{E}^{(n-1)}\tag{20}$$

where $\boldsymbol{\alpha},\boldsymbol{\beta}$ is the tensor related to the background field conductivity $\boldsymbol{\sigma}_b$, the difference $\Delta\boldsymbol{\sigma}$ between the abnormal bulk conductivity and the background field conductivity is calculated as follows:

$$\boldsymbol{\alpha}=\frac{2\boldsymbol{\sigma}_b}{2\boldsymbol{\sigma}_b+\Delta\boldsymbol{\sigma}}\tag{21}$$

$$\boldsymbol{\beta}=\frac{\Delta\boldsymbol{\sigma}}{2\boldsymbol{\sigma}_b+\Delta\boldsymbol{\sigma}}\tag{22}$$

2.7 Apparent resistivity and phase

Assuming that the ground electromagnetic fields excited by two linearly independent field sources are E_{x1}, E_{y1}, H_{x1}, H_{y1} and E_{x2},

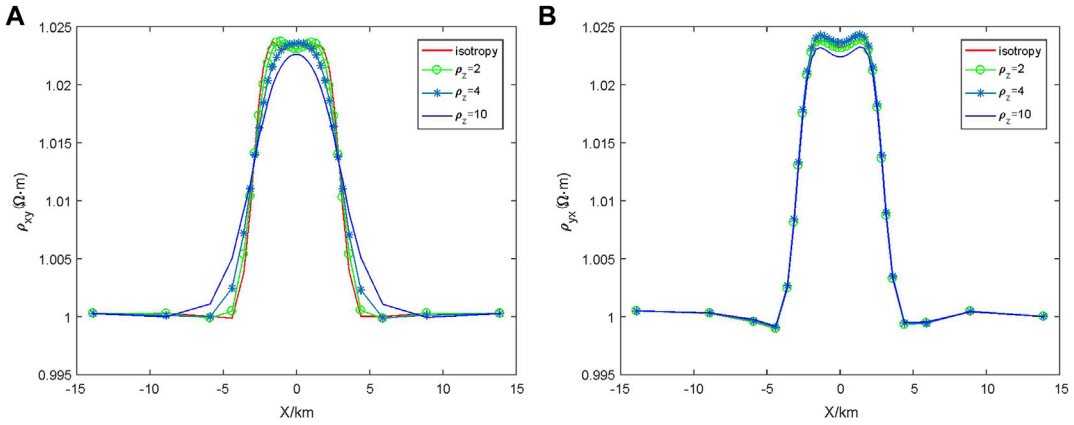

FIGURE 10
Effect of ρ_z on apparent resistivity: **(A)** xy component and **(B)** yx component.

E_{y2}, H_{x2}, H_{y2}, respectively, the impedance tensors of *XX*, *XY*, *YX*, and *YY* polarization modes can be obtained.

$$Z_{xx} = \frac{E_{x1}H_{y2} - E_{x2}H_{y1}}{H_{x1}H_{y2} - H_{x2}H_{y1}} \tag{23}$$

$$Z_{xY} = \frac{E_{x2}H_{x1} - E_{x1}H_{x2}}{H_{x1}H_{y2} - H_{x2}H_{y1}} \tag{24}$$

$$Z_{yx} = \frac{E_{y1}H_{y2} - E_{y2}H_{y1}}{H_{x1}H_{y2} - H_{x2}H_{y1}} \tag{25}$$

$$Z_{yy} = \frac{E_{y2}H_{x1} - E_{y1}H_{x2}}{H_{x1}H_{y2} - H_{x2}H_{y1}} \tag{26}$$

Then, according to the apparent resistivity and phase formulas, we can get

$$\rho_{ij} = \frac{|Z_{ij}|^2}{\omega\mu}, \varphi_{ij} = \arg(Z_{ij}) \quad (i, j = x, y) \tag{27}$$

3 Numerical experiments

3.1 Calculation accuracy and time-consuming comparison

In order to verify the accuracy of the algorithm proposed in this paper, the one-dimensional anisotropic medium model in the article by Rasmussen (1988) was used to compare the calculation results. This one-dimensional model was used as a test model by Pek and Santos (2002) and Han et al. (2018). The model is divided into four layers: the second and third layers are anisotropic media and the first and bottom layers are isotropic media (Figure 2). The first layer of the model has a resistivity of 10000Ω·m and a thickness of 10km; the depths of the second and third layers are 18 km and 100 km, respectively, and the principal axis resistivity is 200/20000/200Ω·m and 1000/2000/1000Ω·m, respectively; the Euler rotation angle α_s is 15° and −75°, respectively, and the angles α_d and α_l are both zero. The bottom layer is an isotropic medium with a resistivity of 100Ω·m.

The number of grid nodes calculated by our algorithm is 101×101×81, and the number of air layers is set to 10. The frequency used in the forward modeling is 31 frequency points taken at logarithmic intervals from 0.0001 Hz to 100 Hz. The calculated numerical solution is compared with the one-dimensional analytical solution given by Pek and Santos (2002) (Figure 3). The relative error and phase error of apparent resistivity are calculated, as shown in Figure 4. It can be seen that the relative error of apparent resistivity is less than 1%, and the error of phase is less than 0.2°. Therefore, the calculation accuracy of this algorithm satisfies the requirements of magnetotelluric simulation.

The 3D numerical simulation algorithm in this paper has the feature of high parallelism, and its calculation time and memory cost will not increase exponentially with the number of mesh nodes but will increase approximately linearly. This feature is suitable for the numerical simulation of large-scale complex 3D models.

The algorithms in this paper are written in Fortran 95 language, and the calculation platform is Intel(R) Xeon(R) CPU3.1G, 64GB RAM, 16CPUs, which is basically the same configuration as in Zhang et al. (2017). According to the 3D model by Zhang et al. (2017), we design a model with a mesh number of 119×65×38 (the grid nodes number is 120×66×39) to test the calculation efficiency and memory usage of the algorithm in this paper.

Zhang et al. (2017) used four algorithms: 1) algorithm based on total field finite element (TFE); 2) algorithm based on secondary field finite element (SFE); 3) algorithm based on total field finite element and infinite element (TFEIE); 4) algorithm based on the secondary field finite-element and infinite element (SFEIE). The SFE and TFE algorithms adopt the truncated boundary condition, and the electric field on the boundary is assumed to be zero, so a larger calculation area (57.2×56.8×40 km^3) is needed, while a smaller calculation area (6×6×4 km^3) can be set for the SFEIE and TFEIE algorithms. For comparison, we also designed a model with a larger calculation area (57.2×56.8×40 km^3), and the grid nodes number is 256×256×151. Table 1 lists the calculation memory and calculation time of the algorithm in this paper (MSWD) and the four algorithms of Zhang et al. (2017).

The algorithm (MSWD) proposed in this paper has a high degree of parallelism, and its forward modeling speed is 1–2 orders of magnitude faster than the traditional finite element method, and it consumes less memory.

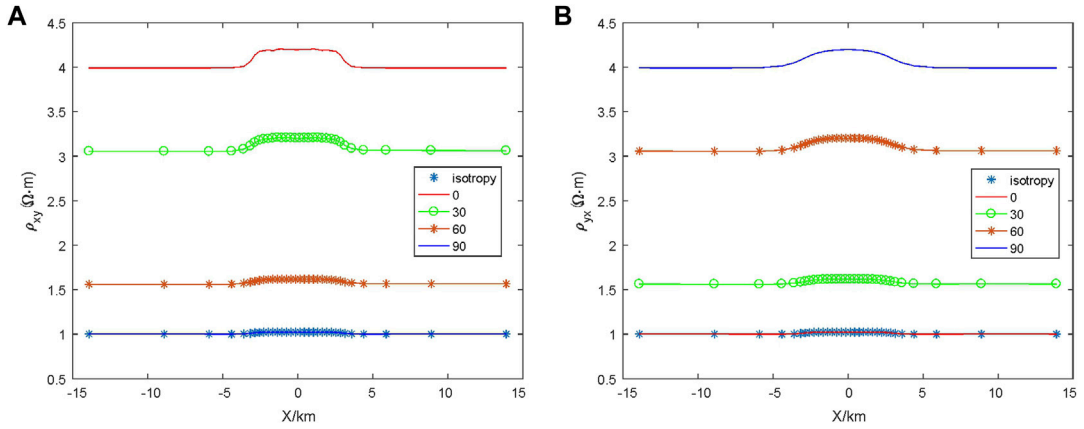

FIGURE 11
Effect of α_d on apparent resistivity: **(A)** xy component and **(B)** yx component.

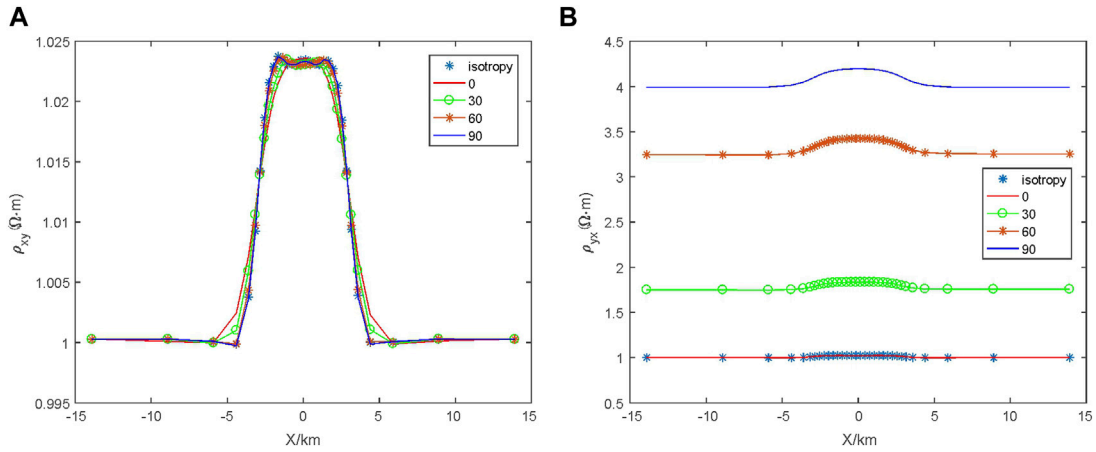

FIGURE 12
Effect of α_s on apparent resistivity: **(A)** xy component and **(B)** yx component.

The calculation advantage of the algorithm (MSWD) in this paper is more obvious in the model with numerous meshes.

3.2 The 3D anisotropic land model

Referring to the model by Xiao et al. (2019), an anisotropic 3D anomalous body model with a size of 1 km × 1 km × 1 km was selected as shown in Figure 4, in which the top surface of the anomalous body is 0.5 km away from the surface. For comparison, the surrounding rock around the abnormal body is set as an isotropic medium with a resistivity of 100 Ωm.

First of all, we studied the horizontal anisotropy, and the main axis resistivity of the 3D anisotropic anomalous body is taken as 1000, 10, and 100, the Euler rotation angle α_d and α_l are 0°, and the angle α_s is taken as 0°, 30°, 60°, and 90°. In this paper, the cuboid unit is used to divide the grid of the research area, and a total of 96×96×80 (97×97×81 grid nodes) grid units are discretized, and the number of air layers is five. The forward modeling result of the finite element method at a frequency of 0.1 Hz is shown in Figure 5.

Figure 5 contains 16 sub-figures; from left to right are the results of taking the α_s values of 0°, 30°, 60°, and 90°, and from top to bottom are the apparent resistivity of XX mode, XY mode, YX mode, and YY mode. These figures show that when α_s=0°, the apparent resistivity of the XY mode at the abnormal body position mainly depends on the spindle resistivity ρ_x, and the apparent resistivity of the YX mode at the abnormal body position depends on the spindle resistivity ρ_y. With the change of α_s, the apparent resistivity changes of XY mode and YX mode also rotate accordingly. When α_s=90°, the apparent resistivity of the XY mode at the abnormal body position is mainly related to the spindle resistivity ρ_y, and the apparent resistivity of the YX mode at the abnormal body position is related to the spindle resistivity ρ_x. It shows that when the main axis resistivity is constant and the α_s changes, the apparent resistivity of both the XY mode and YX mode changes, and the directionality of apparent resistivity imaging is related to the α_s.

We then studied the tilt anisotropy, and the 3D anomalous body model is the same as above; the main axis resistivity is still 1000, 10, and 100; however, this time, the Euler rotation angle sum is 0°, and the Euler rotation angle is 0°, 30°, 60°, and 90°. The calculation frequency is also 0.1Hz, and the forward simulation results are shown in Figure 6.

Figure 6 includes 16 subgraphs, which are arranged in the same way as mentioned above. From the apparent resistivity imaging in the figure, it can be seen that no matter how the Euler rotation angle α_d changes, the apparent resistivity ρ_{xy} does not change. This is because the Euler rotation angle α_d changes around the x-axis, so the resistivity ρ_x of the anomaly position does not change, indicating that the apparent resistivity ρ_{xy} is only related to the principal axis resistivity ρ_x. However, the apparent resistivity ρ_{yx} changes with the change in the Euler rotation angle. When the Euler rotation angle $\alpha_d = 90°$, the resistivity in the y direction of the abnormal body position is 10. At this time, a large low-resistance anomaly appears at the abnormal body position. When the Euler rotation angle is applied, the resistivity of the abnormal body position in the y direction is equal to the principle axis resistivity ρ_z which is 100. At this time, the apparent resistivity of the abnormal body position is almost consistent with the surrounding rock area within the allowable range of error, which is also the main axis anisotropic; the off-diagonal elements of the anisotropic conductivity tensor matrix are zero. When the Euler rotation angle α_d changes from 0° to 90°, the apparent resistivity near the position of the abnormal body increases, since the principal axis resistivity is ρ_z is larger than ρ_y, this means the component in the y direction is related to the principal axis resistivity ρ_y and ρ_z. In addition, the apparent resistivity imaging of the XX mode and YY mode shows that the apparent resistivity change of XX mode is related to YX mode when the tilt anisotropy occurs, and the imaging of YY mode is similar to that of XY mode.

3.3 3D anisotropy ocean model

In order to verify the influence of resistivity anisotropy on the magnetotelluric response in the seabed model, this paper improves the marine oil and gas reservoir model designed by Li and Dai (2011) with resistivity anisotropy of surrounding rock, as shown in Figure 7. The air resistivity is $10^8\Omega$m; the resistivity of seawater is 0.3Ωm, and the thickness of seawater is 1000 m; the seabed is the anisotropic medium, and an isotropic high-resistivity oil and gas reservoir exists at 1000 m below the seabed, with a resistivity of 50Ωm; the length and width are 6000 m, and the thickness is 100 m. The research frequency is 0.25Hz, and the electromagnetic-receiving devices are placed on the seabed −14 km–14 km.

3.3.1 Influence of ρ_x

In the resistivity anisotropic medium model shown in Figure 7, it is assumed that $\rho_y = \rho_z = 1.0$ Ωm in the anisotropic medium layer is constant, and its influence on the electromagnetic response is studied by changing the resistivity of the main coordinate axis ρ_x as 1 Ωm, 2 Ωm, 4 Ωm, and 10 Ωm. The calculation results are shown in Figure 8. From the calculation results, it can be seen that the influence of ρ_x on the xy component of the apparent resistivity is more obvious than that of the yx component.

3.3.2 Influence of ρ_y

In the anisotropic resistivity medium model shown in Figure 7, it is assumed that the resistivity of the principal axis of the anisotropic medium layer $\rho_x = \rho_z = 1.0$ Ωm remains unchanged, and the effect of the resistivity of the principal coordinate axis on the electromagnetic response is studied by changing the resistivity of the principal coordinate axis ρ_y as 1 Ωm, 2 Ωm, 4 Ωm, and 10 Ωm. The calculation results are shown in Figure 9. From the calculation results, it can be seen that the influence of ρ_y on the yx component of the apparent resistivity is more obvious than the xy component.

3.3.3 Influence of ρ_z

In the anisotropic resistivity medium model shown in Figure 7, it is assumed that the resistivity of the principal axis of the anisotropic medium layer $\rho_x = \rho_y = 1.0$ Ωm remains unchanged, and the effect of the resistivity of the principal coordinate axis on the electromagnetic response is studied by changing the resistivity of the principal coordinate axis ρ_z as 1 Ωm, 2 Ωm, 4 Ωm, and 10 Ωm. The calculation results are shown in Figure 10. From the calculation results, it can be seen that ρ_z has an influence on both the xy component and the yx component of the apparent resistivity. Relatively speaking, the influence range of the xy component is larger than that of the yx component.

3.3.4 Influence of α_d

In the resistivity anisotropic medium model shown in Figure 7, it is assumed that the resistivity of the principal axis of the anisotropic dielectric layer is $\rho_x = \rho_y = 1.0$ Ωm and $\rho_z = 4\Omega$m ; the effect on the electromagnetic response is studied by changing the anisotropic dip angle α_d as 0°, 30°, 45°, 60°, and 90°. According to the different angles of anisotropy, it can be divided into three types. When $\alpha_d = 0°$, it is called transverse isotropy vertical (TIH); when α_d =30°, 45°, and 60°, it is called transverse isotropy dip (TID); when $\alpha_d = 90°$, it is called transverse isotropy horizontal (TIV). The calculation results are shown in Figure 11. From the calculation results, we can see that α_d has an influence on both the xy component and the yx component of the apparent resistivity. Relatively, the influence range of the xy component is larger than that of the yx component.

3.3.5 Influence of α_s

In the resistivity anisotropic medium model shown in Figure 7, it is assumed that the resistivity of the principal axis of the anisotropic layer is $\rho_x = 4\Omega$m and $\rho_y = \rho_z = 1.0$ Ωm; the effect on the electromagnetic response is studied by changing the anisotropic strike angle α_s as 0°, 30°, 45°, 60°, and 90°. The calculation results are shown in Figure 12. From the calculation results, it can be seen that α_s has a greater influence on the yx component of the apparent resistivity than the xy component.

4 Conclusion

In this paper, from the perspective of improving the calculation efficiency of 3D anisotropic magnetotelluric numerical simulation, a Fourier domain anisotropic 3D magnetotelluric simulation algorithm is proposed. This algorithm transforms the space domain equation into the Fourier domain, reduces the solution dimension, and improves the calculation efficiency. A one-dimensional model is used to test the correctness of the algorithm, and a land model and a group of ocean models are calculated using this algorithm, The influence characteristics of resistivity anisotropy on the magnetotelluric response function in different models are discussed respectively.

Data availability statement

The raw data supporting the conclusion of this article will be made available by the authors, without undue reservation.

Author contributions

YZ did most of the forward method study. GS did most of the data process and analysis work. XW and WZ did the numerical experience work. All authors contributed to the article and approved the submitted version.

Funding

This paper is supported by the 2022-2023 key scientific research project of the Shandong Coalfield Geology Bureau (LUMEIDIKEZI 2022-19; LUMEIDIKEZI 2022-60) and Shandong Provincial Natural Science Foundation (ZR2023QD084).

Conflict of interest

The authors declare that the research was conducted in the absence of any commercial or financial relationships that could be construed as a potential conflict of interest.

Publisher's note

All claims expressed in this article are solely those of the authors and do not necessarily represent those of their affiliated organizations, or those of the publisher, the editors and the reviewers. Any product that may be evaluated in this article, or claim that may be made by its manufacturer, is not guaranteed or endorsed by the publisher.

References

Andréa, D., and Li, Y. (2022). Understanding the effect of 1-D dipping anisotropic conductivity on the response and interpretation of magnetotelluric data. *Geophys. J. Int.* 3 (3), 1948–1965. doi:10.1093/gji/ggac166

Badea, E. A., Everett, M. E., Newman, G. A., and Biro, O. (2001). Finite element analysis of controlled-source electromagnetic induction using Coulomb-gauged potentials. *Geophysics* 66 (3), 786–799. doi:10.1190/1.1444968

Biro, O., and Preis, K. (1989). On the use of the magnetic vector potential in the finite-element analysis of three-dimensional eddy currents. *IEEE Trans. Magnetics* 25 (4), 3145–3159. doi:10.1109/20.34388

Cao, X., Yin, C., Zhang, B., Huang, X., Liu, Y., and Cai, J. (2018). A goal-oriented adaptive finite-element method for 3D MT anisotropic modeling with topography. *Chin. J. Geophys. (in Chinese)* 61 (6), 2618–2628. doi:10.6038/cjg2018L0068

Dai, S., Li, K., Zhou, Y., and Chen, L. (2019a). "Large-scale 3D forward modeling of magnetic anomaly in a mixed space-wavenumber domain," in *GEM 2019 xi'an: International workshop and gravity, electrical & magnetic methods and their applications, chenghu, China*.

Dai, S., Ling, J., Chen, Q., Li, K., Zhang, Q., Zhao, D., et al. (2021). Numerical modeling of 3D DC resistivity method in the mixed space-wavenumber domain. *Applied Geophysics* 18 (3), 361–374. doi:10.1007/s11770-021-0904-4

Dai, S., Zhao, D., Wang, S., Li, K., and Jahandari, H. (2022). Three-dimensional magnetotelluric modeling in a mixed space-wavenumber domain. *Geophysics* 87, E205–E217. doi:10.1190/geo2021-0216.1

Dai, S., Zhao, D., Wang, S., Xiong, B., Zhang, Q., Li, K., et al. (2019b). Three-dimensional numerical modeling of gravity and magnetic anomaly in a mixed space-wavenumber domain. *Geophysics* 84 (4), G41–G54. doi:10.1190/geo2018-0491.1

Dai, S., Zhao, D., Zhang, Q., Li, K., Chen, Q., and Wang, X. (2018). Three-dimensional numerical modeling of gravity anomalies based on Poisson equation in space-wavenumber mixed domain. *Applied Geophysics* 15 (3-4), 513–523. doi:10.1007/s11770-018-0702-9

Everett, M., and Schultz, A. (1996). Geomagnetic induction in a heterogenous sphere: azimuthally symmetric test computations and the response of an undulating 660-km discontinuity. *Journal of Geophysical Research Solid Earth* 101 (B2), 2765–2783. doi:10.1029/95jb03541

Gao, G. (2005). *Simulation of borehole electromagnetic measurements in dipping and anisotropic rock formations and inversion of array induction data*. University of Texas.

Guo, Z., Egbert, G., Dong, H., and Wei, W. (2020). Modular finite volume approach for 3Dmagnetotelluric modeling of the earth medium with general anisotropy. *Physics of the Earth and Planetary Interiors* 309, 106585. doi:10.1016/j.pepi.2020.106585

Haber, E., Ascher, U., Aruliah, D., and Oldenburg, D. (2000). Fast simulation of 3D electromagnetic problems using potentials. *Journal of Computational Physics* 163 (1), 150–171. doi:10.1006/jcph.2000.6545

Han, B., Li, Y., and Li, G. (2018). 3D forward modeling of magnetotelluric fields in general anisotropic media and its numerical implementation in Julia. *Geophysics* 83 (4), F29–F40. doi:10.1190/Geo2017-0515.1

Jahandari, H., and Farquharson, C. (2015). Finite-volume modelling of geophysical electromagnetic data on unstructured grids using potentials. *Geophysical Journal International* 202 (3), 1859–1876. doi:10.1093/gji/ggv257

Keller, G. (1982). *Handbook of physical properties of rocks*. Boca Raton: CRC Press, 414. doi:10.1201/9780203712115

Kovacikova, S., and Pek, J. (2002). Generalized Riccati equations for 1-D magnetotelluric impedances over anisotropic conductors Part I: plane wave field model. *Earth, Planets and Space* 54, 473–482. doi:10.1186/bf03353038

Labrecque, D., Morelli, G., Daily, W., Ramirez, A., and Lundegard, P. (1999). *Occam's inversion of 3-D electrical resistivity tomography*. Society of Exploration Geophysicists. doi:10.1190/1.9781560802154.ch37

Li, B., Han, T., Fu, L., and Yan, H. (2022). Pressure effects on the anisotropic electrical conductivity of artificial porous rocks with aligned fractures. *Geophysical Prospecting* 70 (4), 790–800. doi:10.1111/1365-2478.13184

Li, G., Wu, S., Cai, H., He, Z., Liu, X., Zhou, C., et al. (2023). IncepTCN: a new deep temporal convolutional network combined with dictionary learning for strong cultural noise elimination of controlled-source electromagnetic data. *Geophysics* 88 (4), E107–E122. doi:10.1190/geo2022-0317.1

Li, Y. (2002). A finite-element algorithm for electromagnetic induction in two-dimensional anisotropic conductivity structures. *Geophysical Journal International* 148 (3), 389–401. doi:10.1046/j.1365-246x.2002.01570.x

Li, Y., and Dai, S. (2011). Finite element modelling of marine controlled-source electromagnetic responses in two-dimensional dipping anisotropic conductivity structures. *Geophysical Journal International* 185 (2), 622–636. doi:10.1111/j.1365-246X.2011.04974.x

Li, Y., and Pek, J. (2008). Adaptive finite element modelling of two-dimensional magnetotelluric fields in general anisotropic media. *Geophysical Journal International* 175 (3), 942–954. doi:10.1111/j.1365-246X.2008.03955.x

Liu, Y., Xu, Z., and Li, Y. (2018). Adaptive finite element modelling of three-dimensional magnetotelluric fields in general anisotropic media. *Journal of Applied Geophysics* 151, 113–124. doi:10.1016/j.jappgeo.2018.01.012

Luo, T., Hu, X., Chen, L., and Xu, G. (2022). Investigating the magnetotelluric responses in electrical anisotropic media. *Remote Sensing* 14 (10), 2328–2346. doi:10.3390/rs14102328

Okazaki, T., Oshiman, N., and Yoshimura, R. (2016). Analytical investigations of the magnetotelluric directionality estimation in 1-D anisotropic layered media. *Physics of the Earth and Planetary Interiors* 260, 25–31. doi:10.1016/j.pepi.2016.09.002

Parkhomenko, E. I. (1967). *Electrical properties of rocks*. New York: Plenum Press.

Pek, J., and Santos, F. A. M. (2002). Magnetotelluric impedances and parametric sensitivities for 1-D anisotropic layered media. *Computers & Geosciences* 28 (28), 939–950. doi:10.1016/s0098-3004(02)00014-6

Pek, J., and Verner, T. (1997). Finite-difference modelling of magnetotelluric fields in two-dimensional anisotropic media. *Geophys. J. Int.* 128, 505–521. doi:10.1111/j.1365-246x.1997.tb05314.x

Rasmussen, T. (1988). Magnetotellurics in southwestern Sweden: evidence for electrical anisotropy in the lower crust. *Journal of Geophysical Research Solid Earth* 93 (B7), 7897–7907. doi:10.1029/JB093iB07p07897

Reddy, I. K., and Rankin, D. (1975). Magnetotelluric response of laterally inhomogeneous and anistotropic media. *Geophysics* 40, 1035–1045. doi:10.1190/1.1440579

Rivera-Rios, A. M., Zhou, B., Heinson, G., and Krieger, L. (2019). Multi-order vector finite element modeling of 3D magnetotelluric data including complex geometry and anisotropy. *Earth Planets and Space* 71 (1), 92–25. doi:10.1186/s40623-019-1071-1

Saraf, P. D., Negi, J. G., and Cerv, V. (1986). Magnetotelluric response of a laterally inhomogeneous anisotropic inclusion. *Phys. Earth Planet. Inter.* 43, 196–198. doi:10.1016/0031-9201(86)90046-4

Varilsuha, D., and Candansayar, M. E. (2018). 3D magnetotelluric modeling by using finite-difference method: comparison study of different forward modeling approaches. *Geophysics* 83 (2), WB51–WB60. doi:10.1190/geo2017-0406.1

Weiss, C. J., and Newman, G. A. (2000). *Electromagnetic induction in a fully 3D anisotropic Earth*. SEG Technical Program Expanded Abstracts, 351–354. doi:10.1190/1.1816064

Xiao, T., Huang, X., and Wang, Y. (2019). Three-dimensional magnetotelluric modelling in anisotropic media using the A-phi method. *Exploration Geophysics* 50 (1), 31–41. doi:10.1080/08123985.2018.1564274

Xu, S. (1994). *The finite element method in geophysics (in Chinese)*. Beijing: Science Press.

Ye, Y., Du, J., Liu, Y., Ai, Z., and Jiang, F. (2021). Three-dimensional magnetotelluric modeling in general anisotropic media using nodal-based unstructured finite element method. *Computers & Geosciences* 148, 104686. doi:10.1016/j.cageo.2021.104686

Yin, X., Ma, Z., Xiang, W., and Zong, Z. (2022). Review of fracture prediction driven by the seismic rock physics theory (I): effective anisotropic seismic rock physics theory. *Geophysical Prospecting for Petroleum (in Chinese)* 61 (2), 183–204. doi:10.3969/j.issn.1000-1441.2022.02.001

Yu, G., Xiao, Q., Zhao, G., and Li, M. (2018). Three-dimensional magnetotelluric responses for arbitrary electrically anisotropic media and a practical application. *Geophysical Prospecting* 66 (9), 1764–1783. doi:10.1111/1365-2478.12690

Zhang, L., Tang, J., and Ren, Z. (2017). Forward modeling of 3D CSEM with the coupled finite-infinite element method based on the second field. *Chinese Journal of Geophysics (in Chinese)* 60 (9), 3655–3666. doi:10.6038/cjg20170929

Zhou, J., Hu, X., Xiao, T., Cai, H., Li, J., Peng, R., et al. (2021). Three-dimensional edge-based finite element modeling of magnetotelluric data in anisotropic media with a divergence correction. *Journal of Applied Geophysics* 189, 104324–104334. doi:10.1016/j.jappgeo.2021.104324

Frontiers in Earth Science

Investigates the processes operating within the major spheres of our planet

Advances our understanding across the earth sciences, providing a theoretical background for better use of our planet's resources and equipping us to face major environmental challenges.

Discover the latest Research Topics

See more →

Frontiers

Avenue du Tribunal-Fédéral 34
1005 Lausanne, Switzerland
frontiersin.org

Contact us

+41 (0)21 510 17 00
frontiersin.org/about/contact